

A METHODOLOGY FOR INCORPORATING GEOMECHANICALLY-BASED  
FAULT DAMAGE ZONES MODELS INTO RESERVOIR SIMULATION

A DISSERTATION

SUBMITTED TO THE DEPARTMENT OF GEOPHYSICS

AND THE COMMITTEE ON GRADUATE STUDIES

OF STANFORD UNIVERSITY

IN PARTIAL FULFILLMENT OF THE REQUIREMENTS

FOR THE DEGREE OF


DOCTOR OF PHILOSOPHY

Pijush Kanti Paul

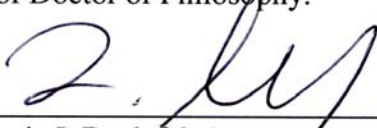
December 2007

© Copyright by Pijush Kanti Paul 2008  
All Rights Reserved

I certify that I have read this dissertation and that, in my opinion, it is fully adequate in scope and quality as dissertation for the degree of Doctor of Philosophy.

  
\_\_\_\_\_  
(Mark D. Zoback) Principal Advisor

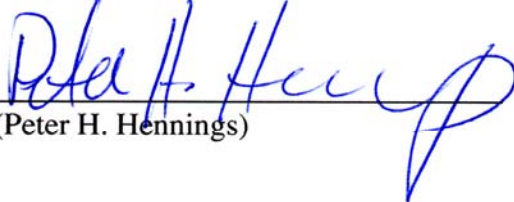
I certify that I have read this dissertation and that, in my opinion, it is fully adequate in scope and quality as dissertation for the degree of Doctor of Philosophy.

  
\_\_\_\_\_  
(Louis J. Durlofsky)

I certify that I have read this dissertation and that, in my opinion, it is fully adequate in scope and quality as dissertation for the degree of Doctor of Philosophy.

  
\_\_\_\_\_  
(Gary Mavko)

I certify that I have read this dissertation and that, in my opinion, it is fully adequate in scope and quality as dissertation for the degree of Doctor of Philosophy.

  
\_\_\_\_\_  
(Peter H. Hennings)

Approved for the University Committee on Graduate Studies.





# ABSTRACT

Efficient modeling of sub-surface heterogeneities is a requisite for successfully managing a reservoir or drilling a well. These heterogeneities can be of different scales and can affect different reservoir parameters. In this thesis, I present my contributions to modeling the heterogeneities associated with reservoir scale faults and implementing them into reservoir simulation, and modeling stress and rock strength heterogeneities to drill a stable wellbore in a complex environment.

In the fault damage zone modeling study for a field in the Timor Sea, I present a methodology to incorporate geomechanically-based fault damage zones into reservoir simulation. In the studied field, production history suggests that the mismatch between actual production and model prediction is due to preferential fluid flow through the damage zones associated with the reservoir scale faults, which is not included in the baseline petrophysical model. I analyzed well data to estimate stress heterogeneity and fracture distributions in the reservoir. Image logs show that stress orientations are homogenous at the field scale with a strike-slip/normal faulting stress regime and maximum horizontal stress oriented in NE-SW direction. Observed fracture zones in wells are mostly associated with well scale fault and bed boundaries. These zones do not show any anomalies in production logs or well test data, because most of the fractures are not optimally oriented to the present day stress state, and matrix permeability is high enough to mask any small anomalies from the fracture zones. However, I found that fracture density increases towards the reservoir scale faults,

indicating high fracture density zones or damage zones close to these faults, which is consistent with the preferred flow direction indicated by interference and tracer test done between the wells.

It is well known from geologic studies that there is a concentration of secondary fractures and faults in a damage zone adjacent to larger faults. Because there is usually inadequate data to incorporate damage zone fractures and faults into reservoir simulation models, in this study I utilized the principles of dynamic rupture propagation from earthquake seismology to predict the nature of fractured/damage zones associated with reservoir scale faults. The implemented workflow can be used to more routinely incorporate damage zones into reservoir simulation models. Applying this methodology to a real reservoir utilizing both field and well scale observations, I found that damage intensity gradually decreases away from faults, and if the secondary features associated with the damage zones are optimally oriented for shear failure in the present day stress state, they may affect the permeability of the reservoir in both the horizontal and vertical directions. I verified the modeling results with both field (outcrop) scale and well scale observations from a number of studies and show that dynamic rupture propagation gives a reasonable first order approximation of damage zones and can be incorporated into reservoir simulation models. Using fluid simulation in a fine-scale model that included the discrete secondary features of a damage zone, I demonstrated that the permeability anisotropy due to a damage zone exists due to increased permeability along the strike of the fault and in the vertical direction. However, there is no significant change in the permeability of the damage zone in a direction perpendicular to the strike of the parent faults in the studied field.

Faults are generally curved and oriented in multiple directions in a reservoir, so often they are not aligned with the simulation grid. Based on the complexity of fault geometry, a simulation grid may have complex cell geometry adjacent to the faults. I present a methodology to implement the effects of damage zones in the simulation grid, which are generally located in fault adjacent grid blocks. To incorporate the fault-related effects of permeability anisotropy in the simulation grid, I used the strike

and dip of faults with reference to the grid axes. The relative effects of the dimension of the damage zone are incorporated using the normalized damage zone width with respect to cell volume and surface area. The absolute value of permeability anisotropy is then defined by several iterations of history matching with the observed production data of the studied field. Inclusion of damage zones into simulation model shows a significant improvement in history matching of production and injection data with respect to the base reservoir simulation model (petrophysical model with no damage zones). Analyzing the uncertainty of the damage zone modeling in the reservoir simulation by testing multiple equiprobable models, I found that uncertainty ranges are compact; indicating the robustness of the modeling and implementation techniques and the improved model should better predict the production behavior.

In a wellbore stability study of the SAFOD (San Andreas Fault Observatory at Depth) research borehole, I demonstrate that analysis of wellbore failures associated with stress and rock strength heterogeneities in the upper part of the hole led to the accurate prediction of strength and stress at depth, as evidenced by the successful drilling through an active trace of San Andreas Fault (SAF). I present a methodology to calibrate the rock strength and stress model using geophysical logs and other borehole measurements, which allowed me to predict the mud weight required to drill through the SAF. As logging-while-drilling (LWD) acoustic caliper data and real-time hole volume calculations both showed that relatively little failure occurred while drilling through the SAF, the predicted mud weight was successful in drilling a stable borehole. However, a six-arm caliper log run after drilling was completed indicates that there was deterioration of the borehole with time, presumably caused by fluid penetration around the borehole. Resistivity logs at multiple depths of investigation during and after drilling indicate appreciable fluid penetration around the borehole, reducing the effectiveness of the drilling mud and failing the wellbore. Finite Element Modeling (FEM) of mud penetration into the fractured medium around the borehole shows wellbore failure with time, and leads support to my hypothesis.

# ACKNOWLEDGMENTS

First and foremost, I would like to acknowledge my Ph.D. advisor, Prof. Mark Zoback, for giving me great research opportunities and providing a nice working environment. Thank you, Mark, for being such a wonderful mentor and teacher. Your large encouragements and support even for my small achievements helped me to move forward enthusiastically. I also regard you as a person with high family values and great time management, and I tried to learn some of these things from your life. I want to thank my committee, Lou Durlinsky, Gary Mavko, and Peter Hennings for their thoughtful discussions and comments that helped focus my research.

I am thankful to Tapan Mukerji and Mohammad Karimi-Fard for guiding me in several part of my research. I want to thank Paul Hagin for being supportive and encouraging, and also for your friendly advice on my research. Paul, I also want to thank you for reading my Ph.D. manuscript. I want to thank Milt Enderline from ConocoPhillips, for mentoring me during my internships and challenging me with various research questions, which broadened my view about research.

I am deeply thankful to Tara Illich for being so helpful. I would like to acknowledge the wonderful staff of our department; things could be tougher around here without their help. Thanks especially to Susan, for supporting our research needs and also caring for us like a mother.

I want to thank Department of Geophysics and Stanford Rock Physics and Borehole consortium for funding my research. I would also like to thank the CEES facility at Stanford, which allowed me to include some advanced computational results in my research. I want to thank ConocoPhillips Ltd. for providing data and their reservoir simulator for the research. I would like to thank GeoMechanics International for providing their softwares for my research. I want to acknowledge other softwares (organizations) used during my research: Tetgen (WIAS), Triangle (CS, UCB), Flowgrid (Schlumberger), GoCad (Earth Decision), and Poly3D (IGEOSS).

I am fortunate to be a part of Stress and Crustal Mechanics group, which gave me opportunity to know many talented people, working in a broad range of research projects. I would like to acknowledge these people for their support, friendship and also giving some wonderful time in between the research work: Lourdes Colmenres, Alvin Chan, Naomi Boness, Ellen Malman, Hannah Ross, Amie Lucier, Amy Day-Lewis, Laura Chiaramonte, John Vermynen, Hiroki Sone, and Charley Weiland. I would also like to thanks Prof. Norm Sleep and Prof. George Thompson, for their useful comments during our group seminars.

I have made many friends and colleagues during my stay at Stanford. Without mentioning any individual name, because I fear that I may miss some of the names, I want to thank all of you for giving me such a wonderful time at Stanford. I enjoyed all the moments of sports, outdoors, movies, chatting and dinning etc with you which helped me to relax in between the research.

I would like to give a special thanks to Misha who has been so supportive and understanding in these busy years. I am incredibly thankful for your endless love and encouragement, which motivated me to work with ease in every condition.

I want to thank, God, for giving me extra strength and guidance whenever I needed. Last, but not the least, I would like to thank my Mum, Dad, Brother, and Sister for your love, support and believing in me that I can achieve great things.

# TABLE OF CONTENTS

<b>ABSTRACT .....</b>	<b>V</b>
<b>ACKNOWLEDGMENTS.....</b>	<b>VIII</b>
<b>TABLE OF CONTENTS .....</b>	<b>X</b>
<b>LIST OF TABLES.....</b>	<b>XIII</b>
<b>LIST OF FIGURES.....</b>	<b>XIV</b>
<b>CHAPTER 1 - INTRODUCTION.....</b>	<b>1</b>
1.1    OVERVIEW AND MOTIVATION.....	1
1.2    THESIS OUTLINE .....	2
REFERENCES.....	5
<b>CHAPTER 2 - WELLBORE STABILITY STUDY OF THE SAFOD BOREHOLE THROUGH THE SAN ANDREAS FAULT .....</b>	<b>6</b>
2.1    ABSTRACT.....	6
2.2    INTRODUCTION.....	7
2.3    THE SAN ANDREAS FAULT AND THE SAFOD LOCATION.....	8
2.4    THE SAFOD DRILLING PLAN.....	10
2.5    BOREHOLE STABILITY AND LITHOFACIES FOR PHASE-1 .....	12
2.6    STRESS ANALYSIS .....	15
2.7    UCS MODELING .....	19
2.8    MODELING OF PHASE-1 BOREHOLE FAILURES .....	25
2.9    MUD WEIGHT PREDICTION FOR PHASE-2 .....	27
2.10   QUANTITATIVE RISK ANALYSIS TO DRILL A STABLE BOREHOLE THROUGH THE SAF .....	29
2.11   BOREHOLE STABILITY DURING PHASE-2 THROUGH THE SAF .....	30
2.12   TIME DEPENDENT FAILURE .....	33
2.13   MODELING OF TIME DEPENDENT FAILURE .....	37
2.14   CONCLUSIONS .....	40
REFERENCES.....	40
<b>CHAPTER 3 - GEOMECHANICAL MODELING, PETROPHYSICS, AND WELL SCALE ANALYSIS OF A FIELD IN THE TIMOR SEA .....</b>	<b>43</b>
3.1    ABSTRACT.....	43

3.2	INTRODUCTION.....	44
3.3	REGIONAL TECTONIC SETTING AROUND THE STUDY AREA .....	45
3.3.1	<i>Stress variations within the study area.....</i>	46
3.4	ROCK STRENGTH AND PETROPHYSICAL PROPERTIES OF THE RESERVOIR .....	50
3.5	STRESS MAGNITUDES .....	53
3.6	FRACTURE ANALYSIS AT WELL SCALE.....	58
3.7	FLUID FLOW THROUGH THE FRACTURED ZONE.....	61
3.7.1	<i>Effect of stress in fluid flow and critical stress hypothesis.....</i>	63
3.8	WELL SCALE FRACTURE DENSITY AND DISTANCE FROM THE RESERVOIR SCALE FAULTS.....	66
3.9	CONCLUSIONS .....	69
	REFERENCES.....	69
<b>CHAPTER 4 - MODELING FAULT DAMAGE ZONES USING A DYNAMIC RUPTURE PROPAGATION METHOD.....</b>		<b>73</b>
4.1	ABSTRACT.....	73
4.2	INTRODUCTION.....	74
4.3	THE FORMATION, GROWTH, AND DEVELOPMENT OF FAULTS .....	76
4.4	MODELING OF THE DAMAGE ZONE DURING THE FAULT GROWTH USING A DYNAMIC RUPTURE PROPAGATION TECHNIQUE.....	79
4.4.1	<i>The mechanics of dynamic rupture propagation (Freund, 1979).....</i>	79
4.4.2	<i>The dynamic circular-shear-crack model (Madariaga, 1976).....</i>	83
4.4.3	<i>Combining the dynamic circular-shear-crack solution (Madariaga, 1976) with the dynamic rupture propagation solution (Freund, 1979).....</i>	87
4.5	THE MECHANISM OF THE GROWTH OF ELASTIC-BRITTLE FRACTURES .....	88
4.6	METHODOLOGY TO ESTIMATE DAMAGE ZONE WIDTH USING DYNAMIC RUPTURE PROPAGATION.....	91
4.6.1	<i>The structural model of the CS field.....</i>	91
4.6.2	<i>The historical stress regimes and the input parameters to estimate the damage zone width</i>	94
4.6.3	<i>Rupture source and propagation along a fault plane.....</i>	98
4.6.4	<i>Fracture density and failure plane directions within the damage zone.....</i>	99
4.6.5	<i>Monte Carlo Simulation of the input parameters.....</i>	102
4.7	DAMAGE ZONE MODELING OF THE NOJIMA FAULT: WELL SCALE CALIBRATION OF THE RUPTURE PROPAGATION TECHNIQUE .....	106
4.7.1	<i>Location of the Nojima Fault and the scientific boreholes.....</i>	107
4.7.2	<i>Input parameter and model of the Nojima fault .....</i>	109
4.7.3	<i>Modeling results and comparison with the observed data .....</i>	113
4.8	DAMAGE ZONE WIDTH FOR THE FAULTS FROM THE CS FIELD.....	115
4.9	CONCLUSIONS .....	119
4.10	APPENDIX .....	120
4.10.1	<i>Damage zone prior to faulting.....</i>	120
4.10.2	<i>Damage zone during slip along existing faults.....</i>	124
	REFERENCES.....	127
<b>CHAPTER 5 - IMPLEMENTATION OF PERMEABILITY ANISOTROPY ASSOCIATED WITH DAMAGE ZONES IN RESERVOIR SIMULATION .....</b>		<b>131</b>
5.1	ABSTRACT.....	131
5.2	INTRODUCTION.....	132
5.3	FIELD PRESSURE BEHAVIOR AND PROJECT MOTIVATION.....	134
5.4	PERMEABILITY ANISOTROPY DUE TO THE DAMAGE ZONES .....	136
5.4.1	<i>3D study.....</i>	136
5.4.2	<i>2D study.....</i>	141
5.5	DESCRIPTION OF GEOCELLULAR MODEL .....	143
5.6	INITIAL CONDITIONS AND FLUID PROPERTIES FOR RESERVOIR SIMULATION .....	149

5.7	DESCRIPTION OF UPSCALED MODEL AND IMPLEMENTATION OF PERMEABILITY CHANGES DUE TO DAMAGE ZONE .....	156
5.7.1	<i>Implementation of the damage zone in the upscaled grid.....</i>	<i>160</i>
5.8	HISTORY MATCHING .....	173
5.8.1	<i>Reservoir pressure .....</i>	<i>175</i>
5.8.2	<i>Water production.....</i>	<i>181</i>
5.8.3	<i>Uncertainty in the simulation response due to damage zone modeling.....</i>	<i>188</i>
5.8.4	<i>Uncertainty due to methods of anisotropy distribution in the simulation model.....</i>	<i>192</i>
5.8.5	<i>Uncertainty due to fracture density of damage zone in the simulation model.....</i>	<i>196</i>
5.9	DISCUSSIONS AND CONCLUSIONS.....	199
	REFERENCES .....	200



# LIST OF TABLES

<i>Number</i>	<i>Page</i>
Table 4.1: Mean and range of the input parameters used for Monte Carlo Simulation.....	103
Table 4.2: Parameters used to define dimension and properties of the Nojima Fault.....	110
Table 5.1: $\Delta P$ and $k^*$ for the different cases of 2D fine scale fluid simulations .....	140
Table 5.2: coefficients a and b for reservoir facies.....	145
Table 5.3: Water properties used during the simulation.....	155
Table 5.4: Initial hydrocarbon fluid composition used during the simulation.....	155
Table 5.5: Qualitative history matching with BHP and water production rate.....	174

# LIST OF FIGURES

<i>Number</i>	<i>Page</i>
Fig 2.1: Location map of the SAFOD borehole.....	9
Fig 2.2: A schematic of the SAFOD well trajectory.....	11
Fig. 2.3: A simplified lithology column of the SAFOD borehole.....	13
Fig. 2.4: Calipers showing borehole enlargements during Phase-1 drilling.....	14
Fig. 2.5: S1, S2 and S3 profiles with depth and lower hemisphere stereo plots .....	16
Fig. 2.6: Three principal stresses, $S_1$ , $S_2$ , $S_3$ , and pore pressure, $P_p$ , on the well trajectory plane.....	17
Fig. 2.7: Modified stress model around the SAFOD borehole.....	19
Fig. 2.8: (a) Caliper versus density (b) Caliper versus $V_p$ .....	21
Fig. 2.9: Transition from intact rock to heavily jointed rock mass with increasing sample size .....	22
Fig. 2.10: Deterministic modeling of breakout width for constant uniaxial compressive strength.....	24
Fig. 2.11: Modeling of borehole failures during Phase-1 drilling of the SAFOD borehole.....	25
Fig. 2.12: Modeling of borehole failures during Phase-1 drilling using different mud weights. ....	26
Fig. 2.13: Modified stress model for principal stresses, $S_2$ and $S_3$ .....	28
Fig. 2.14: Mud weight predictions for (a) 45 deg and (b) 60 deg breakout width. ....	29
Fig. 2.15: (a) QRA at the San Andreas Fault zone (~3300m) (b) the sensitivity analysis. ....	30
Fig. 2.16: LWD acoustic calipers through the San Andreas Fault. ....	31
Fig. 2.17: Comparison of actual mud volume with volumes from the bit size and LWD calipers .....	33
Fig. 2.18: Six arm wireline calipers show deterioration of the borehole with time .....	34
Fig. 2.19: LWD calipers, wireline calipers and resistivity logs with multiple depths of investigation.....	36
Fig. 2.20: A triangular mesh of the schematic model for the area around the borehole. ....	37
Fig. 2.21: Pressure front with time from the borehole wall .....	38
Fig. 2.22: The zone around the SAFOD borehole where fractures may slip due to mud penetration.....	39
Fig. 3.1: Regional tectonic and location map of the study area .....	46
Fig. 3.2: Structural map of the CS field .....	47

Fig. 3.3: Dip line section (AB) of the CS field shows that the large faults striking in ENE direction.....	48
Fig. 3.4: Schematic of tensile fractures and breakouts aoround a vertical borehole.....	49
Fig. 3.5: Stress-induced wellbore breakouts and tensile wall fractures in the CS field.....	49
Fig. 3.6: Lithology and petrophysical logs of formation section for the well - CSU2.....	52
Fig. 3.7: Confining stress versus axial stress at failure for core samples from Formation-1 .....	53
Fig. 3.8: XLOT in well CSP2 at 2078m MD shows $S_3$ gradient $\sim 1.65$ SG .....	55
Fig. 3.9: XLOT in well CSP2 at 3315m MD shows $S_3$ gradient $\sim 1.61$ SG. ....	55
Fig. 3.10: Stress polygon of the CS field indicating $S_{Hmax}$ gradient is $\sim 21 \pm 2$ ppg at well CSU2. ....	57
Fig. 3.11: Present day stress profiles: $S_v$ , $S_{Hmax}$ , $S_{hmin}$ , and pore pressure.....	58
Fig. 3.12: Core image from well CSB2 showing high angle fractures .....	59
Fig. 3.13: A fracture zone associated with a fault in well CSU2 shows rotation in $S_{Hmax}$ orientation.....	60
Fig. 3.14: The stereographic plot shows a southerly dipping fractures in well CSU2.....	61
Fig. 3.15: Petrophysical model and production logs in the fractured zone of well CSU2.....	62
Fig. 3.16: Well test model in the fractured zone of well CSU2.....	63
Fig. 3.17: (a) Critically stressed fractures on a Mohr circle and (b) some field examples .....	65
Fig. 3.18: (a) Stereoplot of CFF and (b) 3D Mohr diagram in the fractured zone of well CSU2.....	65
Fig. 3.19: Fracture locations in MD vs. the cumulative number of fractures in wells of the CS field.....	67
Fig. 3.20: The slop of fracture locations in MD vs. the cumulative number of fractures in wells.....	68
Fig. 3.21: Fracture density vs. the distance from the reservoir scale faults in the CS field. ....	68
Fig. 4.1: Evolutionary steps of a mature fault damage zone.....	75
Fig. 4.2: Stress concentartion at the tip of a propagating fault .....	78
Fig. 4.3: The width of the process zone vs. the length of the fault .....	78
Fig. 4.4: (a) Plane (y-z) and (b) a 3D view of a body containing a crack configuration .....	81
Fig. 4.5: The geometry of the problem where the fault is contained in the x-z plane.....	84
Fig. 4.6: Rupture front motion for a spontaneous initially circular crack.....	86
Fig. 4.7: Tip of a shear crack in mode II and mode III deformation.....	89
Fig. 4.8: Dip angle (a) at reservoir depth and (b) above reservoir depth of the reservoir scale faults. ....	92
Fig. 4.9: Archaic time dip slip movement on the reservoir scale faults at reservoir depth.....	93
Fig. 4.10: Stereonet shows the Coulomb Failure Function (CFF) values for all possible faults .....	94
Fig. 4.11: (a) P-wave velocity and (b) Rupture velocity profiles along a reservoir scale fault.....	97
Fig. 4.12: Rock strength profile along a reservoir scale fault.....	97
Fig. 4.13: Rupture propagation pattern along a fault in the CS field.....	98
Fig. 4.14: The coordinate system for dynamic rupture modeling along the fault.....	99
Fig. 4.15: Stress profiles during rupture propagation at (a) $0^\circ$ (b) $45^\circ$ (c) $90^\circ$ from the fault plane.....	101
Fig. 4.16: (a) Cross section view and (b) Map view of the damage zone.....	102
Fig. 4.17: Monte Carlo simulation of the damage zone modeling.....	104
Fig. 4.18: Four simulations of the damage zone modeling of fault in the CS field .....	105

Fig. 4.19: (a) The mean and (b) the standard deviation of the damage zone width .....	106
Fig. 4.20: Location map of the Nojima Fault and epicenter of the M 6.9 1995 Kobe earthquake.....	108
Fig. 4.21: Schematic diagram of the Nojima fault in the vicinity of GSJ and NIED boreholes .....	109
Fig. 4.22: A cross sectional view and rupture propagation pattern on the Nojima fault.....	111
Fig. 4.23: (a) P-wave velocity and (b) Rupture velocity profiles along the Nojima fault.....	112
Fig. 4.24: Rock strength profile along the Nojima fault .....	113
Fig. 4.25: (a) Mean and (b) standard deviation of the damage zone width along the Nojima fault.....	114
Fig. 4.26: Comparison of estimated and observed damage zone width along the Nojima fault.....	115
Fig. 4.27: (a) Mean and (b) standard deviation of damage zone width along the EW trending faults of the CS field. ....	117
Fig. 4.28: (a) Mean and (b) standard deviation of damage zone width along the NS trending faults of the CS field. ....	118
Fig. 4.29: Plots of Acoustic Emission (AE) locations for a Berea Sandstone sample under confining stress.....	121
Fig. 4.30: Stress-Strain relations for pure elastic and viscoelastic damage models.....	122
Fig. 4.31: Cauchy's tetrahedron with traction vector.....	126
Fig. 5.1: Fluid conductivity from well interference and tracer tests between the wells of the CS field.....	135
Fig. 5.2: Well description map and simulation response of three wells using the base model .....	136
Fig. 5.3: Discrete fractures associated with the fault damage zone within the model.....	137
Fig. 5.4: The fine scale unstructured grid (a) without damage zone and (b) with damage zone.....	138
Fig 5.5: At steady state, simulation shows a linear flow between the Injector and Producer .....	140
Fig 5.6: A 2D grid with damage zone width (~60m) and fracture density of ~0.8 fractures/m. ....	141
Fig 5.7: Permeability parallel and perpendicular to fault for different fracture density.....	143
Fig. 5.8: Geocellular model of the CS field. ....	144
Fig. 5.9: Porosity and permeability distribution of the reservoir quality facies .....	146
Fig. 5.10: $k_v$ vs. $k_h$ measurements showing all data point pairs .....	147
Fig. 5.11: Porosity distribution on a reservoir layer of geocellular model.....	147
Fig. 5.12: $k_h$ distribution on a reservoir layer of the geocellular model.....	148
Fig. 5.13: $k_v$ distribution on a reservoir layer of the geocellular model.....	148
Fig. 5.14: Field wide gas and water gradient from the pressure tests in the CS field .....	149
Fig. 5.15: Irreducible water saturation vs. Klinkenberg corrected permeability data .....	151
Fig. 5.16: Initial water saturation at reservoir depth in the CS field. ....	151
Fig. 5.17: $S_{g_r}$ vs. permeability-porosity ratio in the CS field.....	152
Fig. 5.18: Average water relative permeability at residual gas saturation from core data .....	153
Fig. 5.19: Oil-water and Oil-gas relative permeability used during the simulation. ....	154
Fig. 5.20: Upscaling ratio of the reservoir simulation grid.....	157
Fig. 5.21: Depth of layer-18 of the upscaled model.....	157

Fig. 5.21: Porosity of the reservoir section (layer-18) of the upscaled model.....	158
Fig. 5.22: Horizontal permeability ( $k_h$ ) of the reservoir section (layer-18).....	159
Fig. 5.23: Vertical permeability ( $k_v$ ) of the reservoir section (layer-18).....	159
Fig. 5.24: Anisotropy in a generalized grid cell adjacent to a fault in the reservoir simulation model. ....	160
Fig. 5.26: Projected values of (a) strike and (b) dip of the reservoir scale faults on simulation grid.....	162
Fig. 5.27: Projected values of (a) mean and (b) standard deviation of the damage zone width on the simulation grid.....	163
Fig. 5.28: Estimated values of normalized damage zone intensity on the upscaled grid.....	165
Fig. 5.29: Estimated values of normalized permeability factor in X-direction on the upscaled grid.....	166
Fig. 5.30: Estimated values of normalized permeability factor in Y-direction on the upscaled grid.....	167
Fig. 5.31: Estimated values of normalized permeability factor in Z-direction on the upscaled grid.....	167
Fig. 5.32: Actual permeability multiplier in X-direction on the upscaled grid.....	169
Fig. 5.33: Actual permeability multiplier in Y-direction on the upscaled grid.....	170
Fig. 5.34: Actual permeability multiplier in Z-direction on the upscaled grid.....	170
Fig. 5.35: Modified permeability in the X-direction ( $k_x$ ) of the simulation model.....	171
Fig. 5.36: Modified permeability in the Y-direction ( $k_y$ ) of the simulation model.....	172
Fig. 5.37: Modified permeability in the Z-direction ( $k_z$ ) of the simulation model.....	172
Fig. 5.38: Production and Gas Injection wells of the CS field.....	174
Fig. 5.39: Comparison of observed BHP, simulated BHP from the base model, and history matched BHP for the wells shown in Fig. 5.2.....	175
Fig. 5.39: Bottom Hole Pressure (BHP) history match of the injector well CSI2.....	176
Fig. 5.41: Bottom Hole Pressure (BHP) history match of injector CSI3.....	177
Fig. 5.42: Bottom Hole Pressure (BHP) history match of production well CSP3.....	178
Fig. 5.43: Bottom Hole Pressure (BHP) history match of production well CSP4.....	179
Fig. 5.44: Bottom Hole Pressure (BHP) history match of production well CSP1.....	179
Fig. 5.45: Bottom Hole Pressure (BHP) history match of production well CSP7.....	180
Fig. 5.46: Bottom Hole Pressure (BHP) history match of production well CSP8.....	181
Fig. 5.47: Water production history match of production well CSP8.....	182
Fig. 5.48: Water production history match of production well CSP7.....	183
Fig. 5.49: Water production history match of production well CSP5.....	184
Fig. 5.50: Water production history match of production well CSP6.....	184
Fig. 5.51: Water production history match of production well CSP1.....	185
Fig. 5.52: Water production history match of production well CSP4.....	185
Fig. 5.53: Water production history match of production well CSP2.....	186
Fig. 5.54: Water production history match of production well CSP3.....	187
Fig. 5.55: History matching of the cumulative water production of the CS field.....	188
Fig. 5.56: BHP response from the 20 equiprobable models with damage zones for injector CSI3.....	190

Fig. 5.57: BHP response from the 20 equiprobable models with damage zones for producer CSP4 .....	190
Fig. 5.58: BHP response from the 20 equiprobable models with damage zones for producer CSP7 .....	191
Fig. 5.59: Cumulative water production from the 20 equiprobable damage zone models of the CS field .....	191
Fig. 5.60: BHP response from two anisotropy distribution methods for injector CSI3 .....	194
Fig. 5.61: BHP response from two anisotropy distribution methods for producer CSP4 .....	194
Fig. 5.62: BHP response from two anisotropy distribution methods for producer CSP7 .....	195
Fig. 5.63: Cumulative water production from two anisotropy distribution methods of the CS field .....	195
Fig. 5.64: BHP response from three fracture density models for injector CSI3 .....	197
Fig. 5.65: BHP response from three fracture density models for producer CSP4.....	197
Fig. 5.65: BHP response from three fracture density models for producer CSP7.....	198
Fig. 5.67: Cumulative water production from three fracture density models of the CS field .....	198

## Chapter 1

# INTRODUCTION

### 1.1 Overview and motivation

This thesis is focused on defining stress and reservoir heterogeneities at different scales and their applications in drilling and reservoir management. It is composed of two separate studies: first, a wellbore stability study in a complex environment, and second, a methodology to implement heterogeneities associated with reservoir scale faults into reservoir simulation. These studies are distinct in their principal objective but both of them employ a methodology of analyzing and implementing stress and geological heterogeneities of different scales in order to improve drilling into the sub-surface, and add value to methods for developing and managing a complex reservoir.

In the first study, I aim to present a methodology that allows one to drill a stable borehole in an environment with complex stress heterogeneity and a lack of sufficient information to define an earth model. Hundreds of wells are drilled every year to extract oil, gas, and ground water from the sub-surface. Depending on the location and complexity of the environment, the average cost of drilling a well ranges from several hundred thousands to several millions of US dollars. Hence, reducing the number of lost wells due to wellbore stability problems will definitely make a huge difference to drilling industry. A lot of wells drilled in the industry for an exploration purpose are in

an unknown environment so a proper wellbore stability study is required to secure successful drilling. In this study I present a workflow for developing a wellbore stability model for such complex and unknown scenarios with a case study of drilling through the San Andres Fault.

The second study is aimed at presenting a methodology to implement secondary fractures associated with reservoir scale faults into reservoir simulation. Reservoirs with faults and fractures are generally more complex to manage than a matrix dominated reservoir. Studies done by Produced Water Management Asia suggest that ~90% of the produced water during oil and gas production come from fractured reservoir and the cost of handling this water is ~\$30-\$40 billion/year. There are other known problems involved with fractured reservoirs such as rapid decline in reservoir pressure, poor recovery, and underperformance by wells etc, which make these reservoirs more challenging. Some of these problems are associated with the highly anisotropic permeability caused by fracture patterns in the reservoir. In this study, I present a technique for modeling anisotropic permeability due to fractures associated with reservoir scale faults using data from a field from the Timor Sea. I also discuss a methodology to implement these fractures into a reservoir simulation model, which can be used for reservoir management.

## **1.2 Thesis outline**

In addition to this Introduction, this thesis contains five chapters. Chapter 2 covers the wellbore stability study, and chapters 3, 4, and 5 cover the study related to implementing fractures associated with the reservoir scale faults into a reservoir simulation model. As this thesis covers variety of topics, if you are interested in wellbore stability and/or SAFOD, read chapter 2 first. If your interest is reservoir simulation, read chapter 5 and for development of geomechanical model of damage zone using dynamic rupture propagation concept, read chapter 4. Chapter 3 has a good overview of stress and fracture analysis at well and field scales in the field being studied.



Chapter 2, **Wellbore stability study of the SAFOD borehole through the San Andreas Fault**, discusses the wellbore stability problems during the first phase of drilling of the SAFOD (San Andreas Fault Observatory at Depth) borehole and predicts the mud weight to successfully drill the second phase, which drilled through the SAF (San Andreas Fault). The main challenges were the unknown stresses and rock strength along the drilling trajectory. Hence, to estimate the mud weight to be used for drilling the San Andreas Fault zone, I present a workflow to calibrate the stress model and uniaxial compressive strength (UCS) with the observed borehole failures and other borehole observations during the first phase of drilling. The logging while drilling (LWD) caliper data during the second phase of drilling shows a successful drilling through the SAF using the estimated mud weights but wireline calipers were enlarged at the top section of the borehole indicating failure with time. I use FEM (Finite Element Modeling) to explain the borehole failures with time.

In the Chapter 3, **Geomechanical modeling, petrophysics, and well scale analysis of a field in the Timor Sea**, I estimate stress orientations and magnitudes at several well locations and build a geomechanical framework of the study area. I also discuss the petrophysical model of the reservoir section and analyze fractures at the well scale to find their contribution to fluid production. To estimate stress orientations and fracture distributions, I analyze image logs and calibrated log derived rock strength with lab measurements. Then I use density logs, leak-off tests, and frictional faulting theory to define the present day stress state in the reservoir. I analyze production logs, core permeability measurements, and well test data to define the relationship between fluid flow and fracture units at well scale and then study the fracture units under the present day stress field to project the role of geomechanics in fluid flow.

Chapter 4, **Modeling fault damage zones using a dynamic rupture propagation method**, discusses the evolutionary concepts of reservoir scale shear faults and associated damage zones containing secondary fractures. These damage zones are created during the three stages of faulting: prior to faulting, during fault growth, and during slip along the existing fault. Lockner et al. (1992) and Vermilye

and Scholz (1998) show that the damage zones from a pre-faulting stage are very narrow and can be ignored for reservoir scale faults. In this study, I present a methodology to model the damage zone for a propagating fault using the dynamic rupture propagation technique (Madariaga, 1976; Kostov, 1964; Virieux and Madariaga, 1982; Harris, 2004) used in earthquake seismology. Damage zones due to slip on existing faults create splay fractures at the tips of the existing fault, which can be modeled using established numerical techniques (Thomas, 1993) to estimate the stress perturbation due to slip on the faults.

I use the data from the study area to explain my methodology of modeling damage zones using the rupture propagation concept and verify this technique by comparing the results with outcrop data from analogous faults of same size. To further verify this technique, I model the damage zone of the Nojima Fault and compare the results of rupture propagation technique with the core data.

In the Chapter 5, **Implementation of permeability anisotropy associated with damage zones in reservoir simulation**, I discuss fine scale upscaling experiments to show the effects of the damage zone in the permeability anisotropy of a grid block of reservoir simulation model. Then I use the nature of permeability anisotropy of the grid block to incorporate the effect of the damage zones in the reservoir simulation model, which is a non-orthogonal grid with corner point geometries. The main challenges for incorporating damage zone into a reservoir simulation model are presented by the truncated and non-orthogonal grid blocks adjacent to the fault, which are required to honor the actual shape of the faults. I discuss a workflow to implement the effects of permeability anisotropy due to damage zones in the base simulation model. I also quantify the effects using history matching of the production and injection data and estimate the uncertainties associated with the damage zone modeling and implementation in the reservoir simulation.

## References

- Lockner, D.A., Byerlee, J.D., Kuksenko, V., Ponomarev, A., and Sidorin, A., 1992, Observations of quasi-static fault growth from acoustic emissions, *Fault mechanics and transport properties of rocks*, international Geophysics Series, 51, p-3-31, Academic Press, san Diego, CA.
- Vermilye, J. M., and Scholz, C. H., 1998, The process zone; a microstructural view of fault growth. *Journal of Geophysical Research*, 103, 12223-12237.
- Madariaga, R., 1976, Dynamics of an expanding circular fault, *Bulletin of Seismological Society of America*, 66, 639-666.
- Kostov, B. V., 1964, Selfsimilar problems of propagation of shear cracks, *J. Appl. Math. Mech.*, 28, 1077-1087.
- Thomas, A. L., 1993, Poly3d: a three-dimensional, polygonal element, displacement discontinuity boundary element computer program with applications to fractures, faults, and cavities in the earth's crust: Master thesis, Stanford University, Stanford, California, U.S.A., 69.
- Virieux, J., and Madariaga, R., 1982, Dynamic faulting studied by finite difference method, *Bull. of the Seis. So. of America*, 72, 345-369.
- Harris, R. A., and Day, S. M., 1997, Effects of a low-velocity zone in a dynamic rupture, *Bull. Seismol. Soc. Am.*, 87, 167-1280.

## Chapter 2

# **WELLBORE STABILITY STUDY OF THE SAFOD BOREHOLE THROUGH THE SAN ANDREAS FAULT**

*Part of this chapter was written as a paper with Mark Zoback and has been accepted by SPE (SPE 102781)*

### **2.1 Abstract**

This chapter presents a wellbore stability study of the SAFOD (San Andreas Fault Observatory at Depth) research borehole located in Parkfield, central California. In the summer of 2005, the SAFOD borehole was successfully drilled through an active trace of San Andreas Fault (SAF) in an area characterized by fault creep and frequent microearthquakes. In this study we report how the analysis of wellbore failures in the upper part of the hole, geophysical logs and a model for stress gradients in the vicinity of the fault were used to estimate the mud weights required to successfully drill through the fault. As logging-while-drilling (LWD) acoustic caliper data and real-time hole volume calculations both showed that relatively little failure occurred while drilling through the SAF, the predicted mud weight was successful in drilling a stable borehole. However, a six-arm caliper log run after drilling was

completed indicates that there was deterioration of the borehole with time, which appears to be caused by fluid penetration around the borehole. The LWD resistivity measurements show that essentially no fluid penetration occurred as the hole was being drilled. Because of this, the mud weight used was capable of maintaining a stable wellbore. However, the resistivity data obtained after drilling shows appreciable fluid penetration thus negating the effectiveness of the mud weight. Using Finite Element Modeling (FEM) we show that mud penetration into the fractured medium around the borehole causes failure with time.

## 2.2 Introduction

Drilling perturbs the stress state around a well and wellbore stability problems can occur when the near-wellbore stresses substantially exceed the strength of the rock. Excessive instability around the wellbore can be suppressed by choosing an optimally stable borehole orientation and sufficiently high mud weight. However, some wellbore failure types such as key seating does not cause instability in the borehole but can exacerbate an already unstable borehole.

As described below, drilling through the SAF was done in various phases. In this chapter, we discuss an analysis of wellbore failures during the first phase of drilling, which was used to predict the mud weight required to successfully drill the second phase, through the SAF. The main challenges during the SAFOD drilling were the unknown stress field and rock strength along the drilling trajectory. Hence, to estimate the mud weight to be used for drilling the San Andreas Fault zone, we first calibrate the stress model around the SAF (Chery et al.) with the observed borehole failures and minifrac test data during the first phase of drilling. Then we estimate and calibrate uniaxial compressive strength (UCS) of the rock by modeling the borehole failures.

LWD caliper data during the second phase of drilling shows a successful drilling through the SAF using the estimated mud weights but wireline calipers were enlarged at the top section of the borehole indicating failure with time. We use FEM modeling

to show the borehole failure with time. Block theory (Goodman, 1989; Goodman and Shi, 1985) used for the stability of underground openings suggests that only the removable blocks of the top section fail due to gravity but the lower section remains in gauge despite having removable blocks. Using this theory we explain why the time dependent enlargement of the SAFOD borehole is restricted to only the top section of the hole.

### **2.3 The San Andreas Fault and the SAFOD location**

The San Andreas Fault (SAF) is a transform fault that is the principal zone of deformation accommodating relative motion between the Pacific and North American Plates. The Pacific Plate moves  $\sim 48\text{mm/yr}$  to the northwest relative to the North American Plate. The SAFOD well is located at Parkfield, halfway between San Francisco and Los Angeles (Fig. 2.1). The drillsite is on a segment of the San Andreas Fault that moves through a combination of aseismic creep and repeating micro earthquakes. In the vicinity of the drillsite, the slip rate on the SAF is approximately half the plate rate, the remainder of plate motion being accommodated by slip on other faults.



Fig 2.1: The SAFOD borehole is located at Parkfield on a segment of the SAF that shows aseismic creep and repeating micro earthquakes.

The SAFOD project has the following goals: to establish an observatory to directly monitor earthquake nucleation at depth within the fault zone; to measure physical properties of the fault zone and exhume fault zone rocks for laboratory studies; and to make comprehensive downhole measurements of stress, pore pressure, temperature and other parameters. The SAFOD borehole is located on the west side of the San Andreas Fault where the bedrock is mostly granitic. The formations encountered on the east side of the San Andreas principally consist of Great Valley formation. The fault zone itself is presumed to consist of crushed breccias and fault gouges. The width of the zone of intense deformation at depth (i.e., the SAF itself), as well as that of the damage zone surrounding the fault, were unknown prior to drilling.

## 2.4 The SAFOD drilling plan

The SAFOD project was carried out in multiple phases. As shown in Fig. 2.2, a vertical Pilot Hole, located 1.8km to the southwest of the SAF, was drilled in 2002 and encountered granitic rock at ~850m as predicted by geophysical data. The design of the main SAFOD borehole was to drill vertically at the same drillsite as the Pilot Hole to a depth of ~1.5km and then drill a deviated hole through the fault zone in the vicinity of microearthquakes ( $M \sim 2$  and smaller) located by Thurber et al.(2004). In summer 2004, Phase-1 was completed to a measured depth (MD) of 3048m. After the Phase-1 borehole was logged, cased and cemented, a seismic study in the borehole improved knowledge of subsurface velocities and the location of the target microearthquakes. Utilizing this information, Phase-2 was carried out in the summer of 2005. The study reported here describes how we used data from Phase-1 to predict an optimum mud weight for drilling through the SAF in Phase-2. Conventional rotary drilling was used for Phases 1 and 2 and extensive cuttings samples were collected, sophisticated real-time gas sampling was done and comprehensive geophysical logging was carried out. Having obtained this information through the SAF zone, multilateral core holes were drilled through the fault zone in summer of 2007 (Phase-3). The approximate locations of the multilaterals are shown in Fig. 2.2.



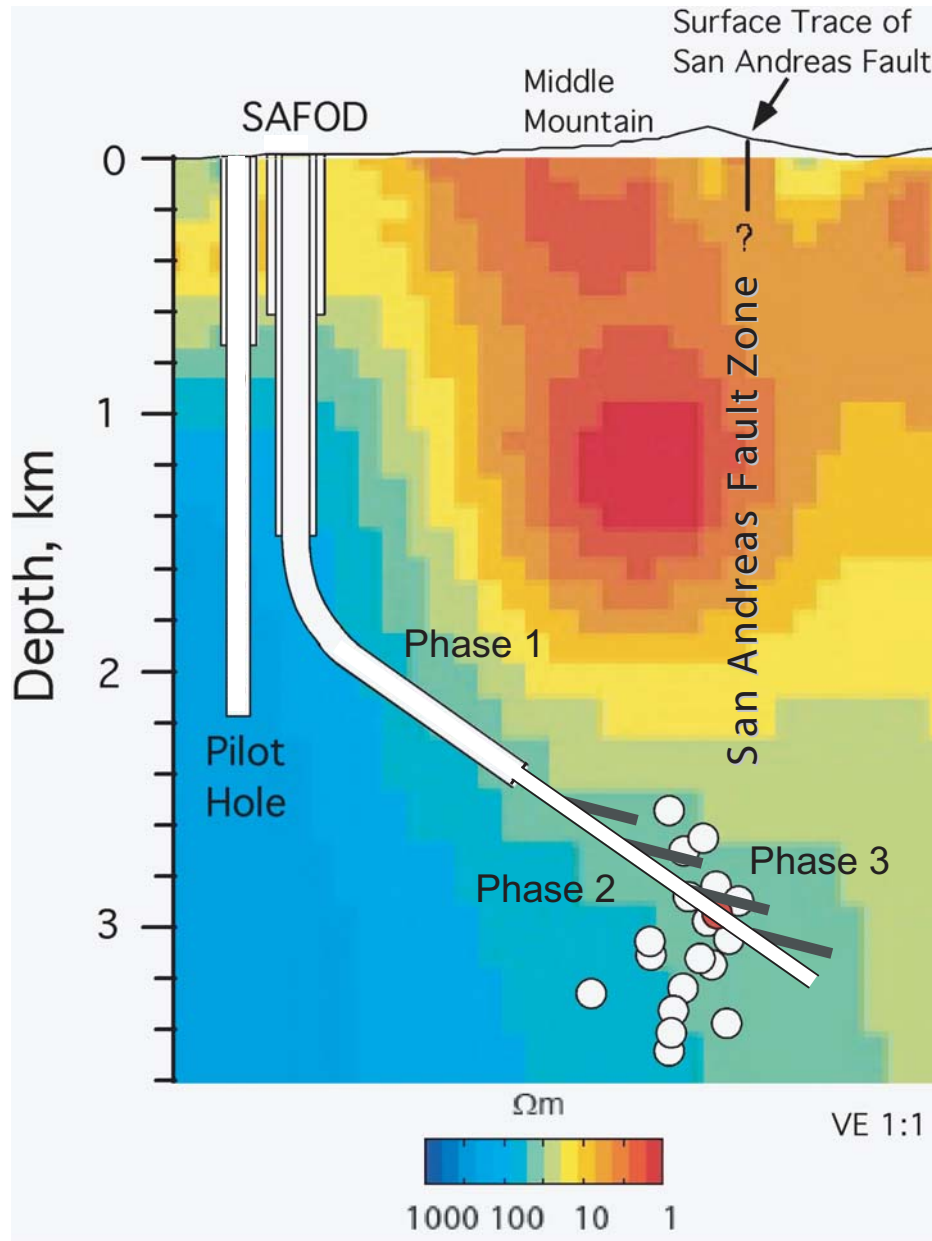


Fig 2.2: A schematic of the SAFOD well trajectory superimposed on resistivity section determined from inversion of active source MT data (Unsworth, 2004).

The vertical section of the Phase-1 borehole was mostly drilled with a bit size of 17-1/2" and casing with 13-3/8" casing. The deviated interval of the well (from 1.5km to 3km, MD) was drilled with a bit size of 12-1/4" and completed with 9-5/8" casing. The maximum deviation of the hole 54° was achieved with a build rate of 2.5° per 30 meters. Phase-2 was drilled from 3.05km (MD) to 3.8km (MD) with an 8-1/2" bit and completed with 7" casing (Zoback, 2006).

## 2.5 Borehole stability and Lithofacies for Phase-1

As interpreted from well-log analysis, three major lithofacies intersected by the SAFOD well during Phase-1 (Boness and Zoback, 2005). As shown in Fig. 2.3, the first 800m consists of weathered Tertiary/Quaternary sediments. This is followed by fractured granite and granodiorite to a depth of 1926m (MD), and below that sedimentary rocks were encountered down to 3048m. This sedimentary section is interpreted to be made up of arkosic sandstone with interbedded shale and conglomerate. These sedimentary rocks were not predicted by geological or geophysical models before drilling. Borehole resistivity image logs (FMI) indicate numerous natural fractures and faults throughout the entire interval drilled, as well as bedding in the sedimentary section. In conjunction with the other geophysical logs and cuttings analysis, a number of faults and brecciated zones were identified.

In general, there were relatively few problems during Phase-1 drilling even in the fault zones, although a number of trips were needed to wash and ream the hole at several depths. In Fig. 2.4, maximum and minimum diameters calculated from either the density caliper and FMI dual caliper log are presented to show the overall condition of the hole. The hole size in the sedimentary zone above 850m (that was logged only from 650-850m) is enlarged on all sides of the borehole. There is a slight improvement in hole condition in the upper, weathered granite, but most of the granite/granodiorite section is generally in gauge. The granodiorite section from 1440m to 1920m shows only a slight enlargement of the borehole diameter. In the fault zone at 1920m at the granite/sediment contact, we observe significant hole enlargements, again on all sides of the hole. Significant hole enlargements are also seen in the sedimentary section below 1926m, especially at some depth intervals. Better hole conditions are observed in the sandstone interval starting at 2682m.

At depths below 1440m, a detailed analysis of FMI caliper data with respect to the orientation of the well reveals orientation of borehole elongations that are  $\sim 10^\circ$  anticlockwise from the top and bottom of the hole (Fig. 2.4). The fact that the borehole

enlargements are close to the top and bottom of the hole suggests that they might be caused by key seating. This will be analyzed in more detail below.

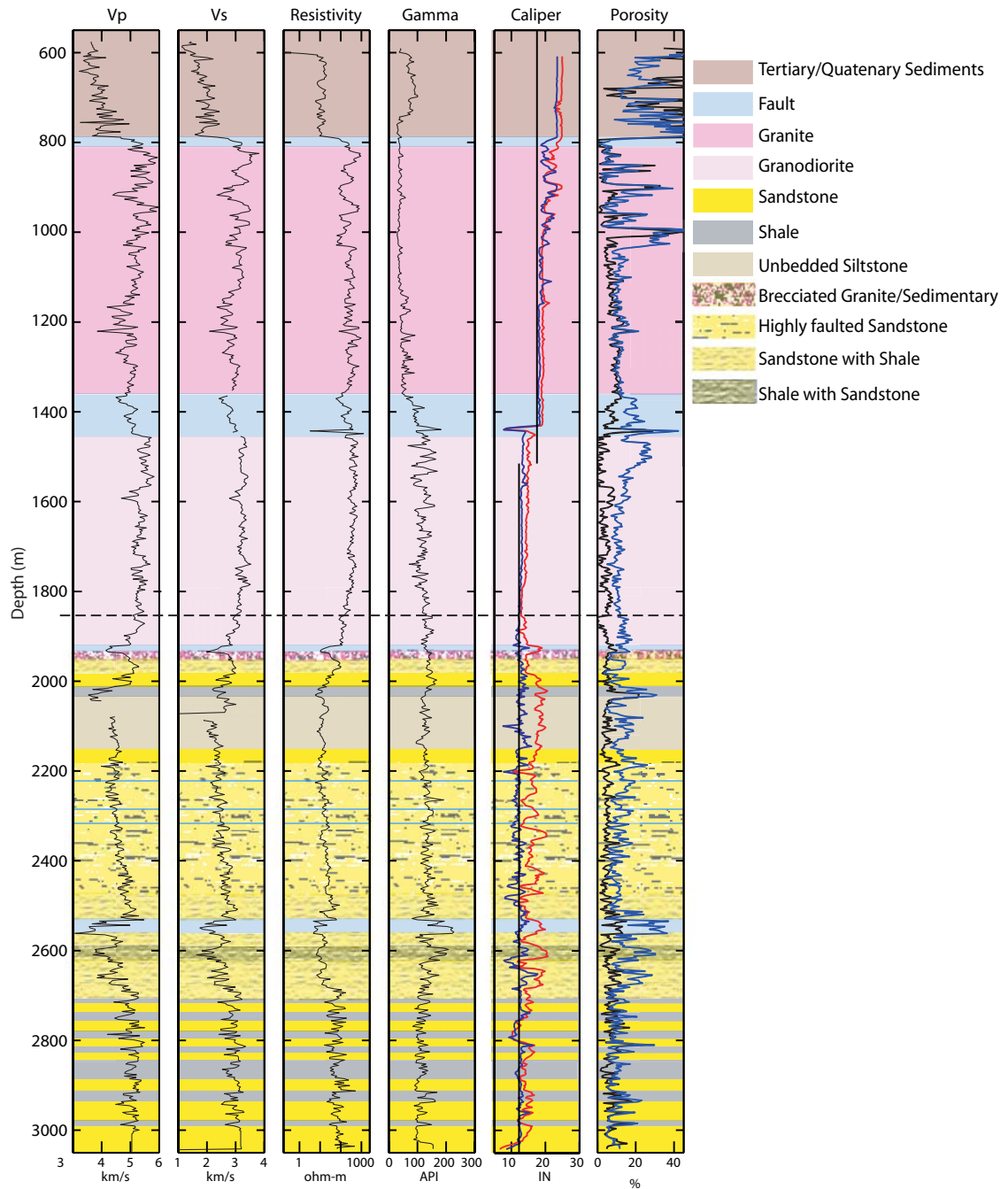


Fig. 2.3: A simplified lithology column calculated using petrophysical logs collected during the Phase-1 drilling of the SAFOD borehole (Boness and Zoback, 2006)

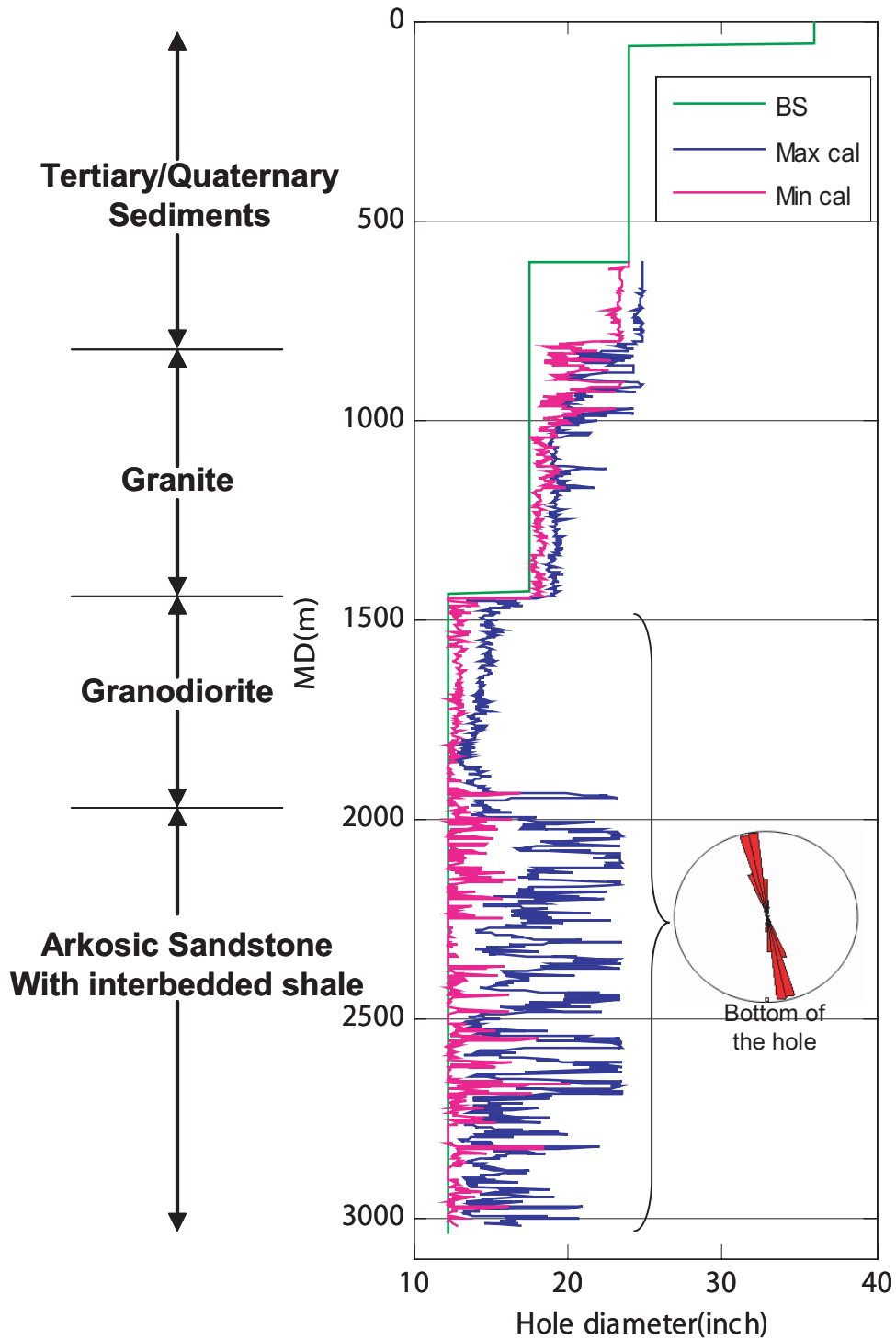


Fig. 2.4: Maximum and minimum caliper show borehole enlargements during Phase-1 drilling. Below 1440 m, borehole is elongated at  $\sim 10^\circ$  anticlockwise tilt from the top of the hole.

## 2.6 Stress Analysis

The San Andreas Fault (SAF) has been described as having low frictional strength because many in situ stress measurements show a high angle between the maximum horizontal stress and the strike of the fault (Zoback et al., 1987; Mount and Suppe, 1987; Townend and Zoback, 2004; Provost and Houston, 2003; Hickman and Zoback, 2004) and the absence of frictionally generated heat (Brune et al., 1969; Lachenbruch and Sass, 1980). We developed a preliminary stress distribution model for the well trajectory based on a geodynamic model of Chery et al. (Fig. 2.5) that proposes that the SAF has a very low intrinsic friction coefficient  $\sim 0.1$  (Chery et al., 2004). The possibility that the fault is characterized by anomalously high pore pressure (Rice, 1992), would, in effect produce very similar results but has proven to be not relevant as no evidence for high pore pressure was found during drilling. The Chery et al. model divides the region into a near field (NF, within  $\sim 5$  km of the fault) and the core of the fault zone (FZ) itself. The model predicts how stress magnitudes and the orientation of  $S_{Hmax}$  vary with depth and distance to the fault. This model predicts that the shear stress on planes parallel to the fault zone is very low and varies strongly with both distance to the fault and depth.

In the near field (NF), Chery et al. (2004) proposed that the minimum principal stress is equal to the vertical stress ( $S_3 \approx S_v$ ), where  $S_v$  corresponds to the vertical stress. The maximum principal stress is two times of the vertical stress ( $S_1 = 2 * S_3 \approx S_{Hmax}$ ), where  $S_{Hmax}$  is the maximum horizontal stress. The intermediate principal stress,  $S_2 \approx S_{hmin}$  (minimum horizontal stress), which is close to  $S_3$  or vertical stress such that the stress state implies a strike-slip/reverse faulting regime. The maximum principal stress,  $S_1$ , is oriented  $N30^\circ E$ , which is at high angle to the SAF. The minimum and maximum principal stresses are in a vertical plane almost perpendicular to the SAF and cause reverse faulting on faults striking parallel to the SAF (Zoback et al., 1987). However, the calculated normal stress acting on the fault zone (FZ) is close to  $S_1$ . Within the fault zone, all three principal stresses are predicted to be close to twice the lithostatic stress,  $S_v$ , (*i.e.*,  $S_1 \approx S_2 \approx S_3 \approx 2 * S_v$ ). A theoretical model by Rice also

supports this dramatic change in the value of  $S_3$  from the near field to fault zone but using the high pore pressure concept (Rice, 1992).

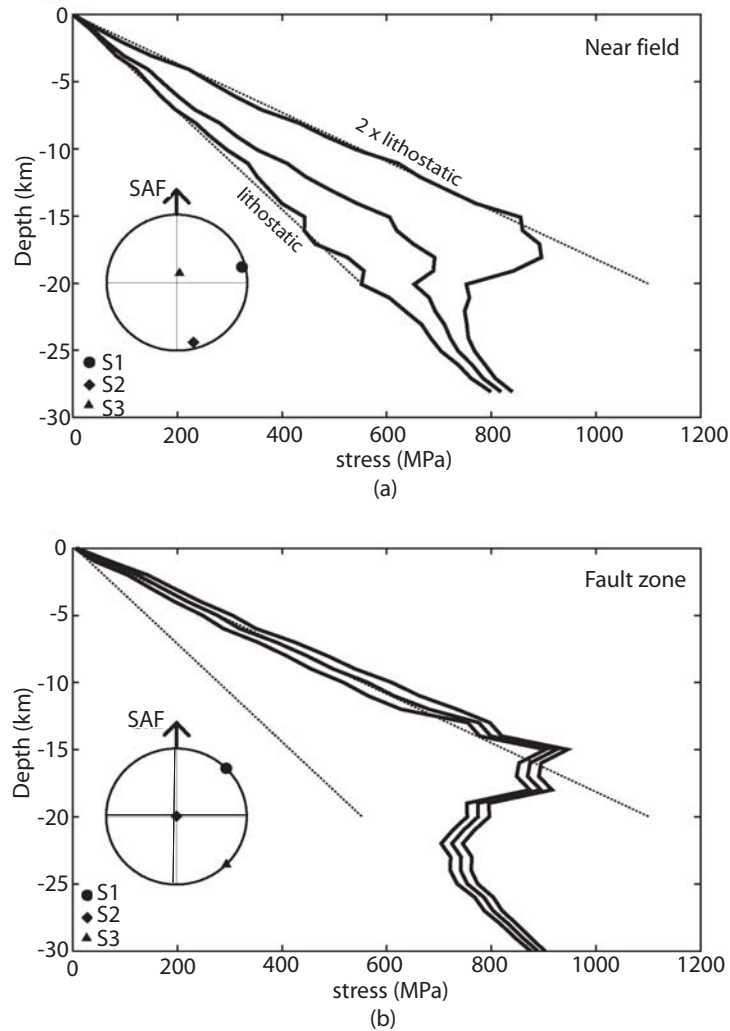


Fig. 2.5:  $S_1$ ,  $S_2$  and  $S_3$  profiles with depth and lower hemisphere stereo plots evaluated at 4km depth for (a) near field and (b) fault zone. (Chery et al. 2004)

For this study we obtained the lithostatic stress from density logs and other densities derived from gravity models in the drillsite area. The Chery et al. model was then used to estimate principal stresses in the near field and fault zone from the lithostatic stress gradient. We used linear interpolation to define the distribution of the stress between the near field and fault zone and assumed a 300m thick fault zone that is symmetric about the surface trace of the fault. Stress and pore pressure models in the well trajectory plane are shown in Fig. 2.6. To be consistent with the observations

made in the pilot hole (Hickman and Zoback, 2004), the azimuth of  $S_{Hmax}$  varies with depth. The high value for  $S_3$  predicted by the Chery et al. model was supported by a minifrac test done at MD 3028.5m (the bottom of the casing set after completion of Phase-1) that was carried out at the onset of Phase-2 operations. At the maximum pressure obtainable ( $\sim 10$  MPa above the vertical stress), it was not possible to extend a hydraulic fracture in the highly fractured rock, implying that  $S_3$  was appreciably above the overburden.

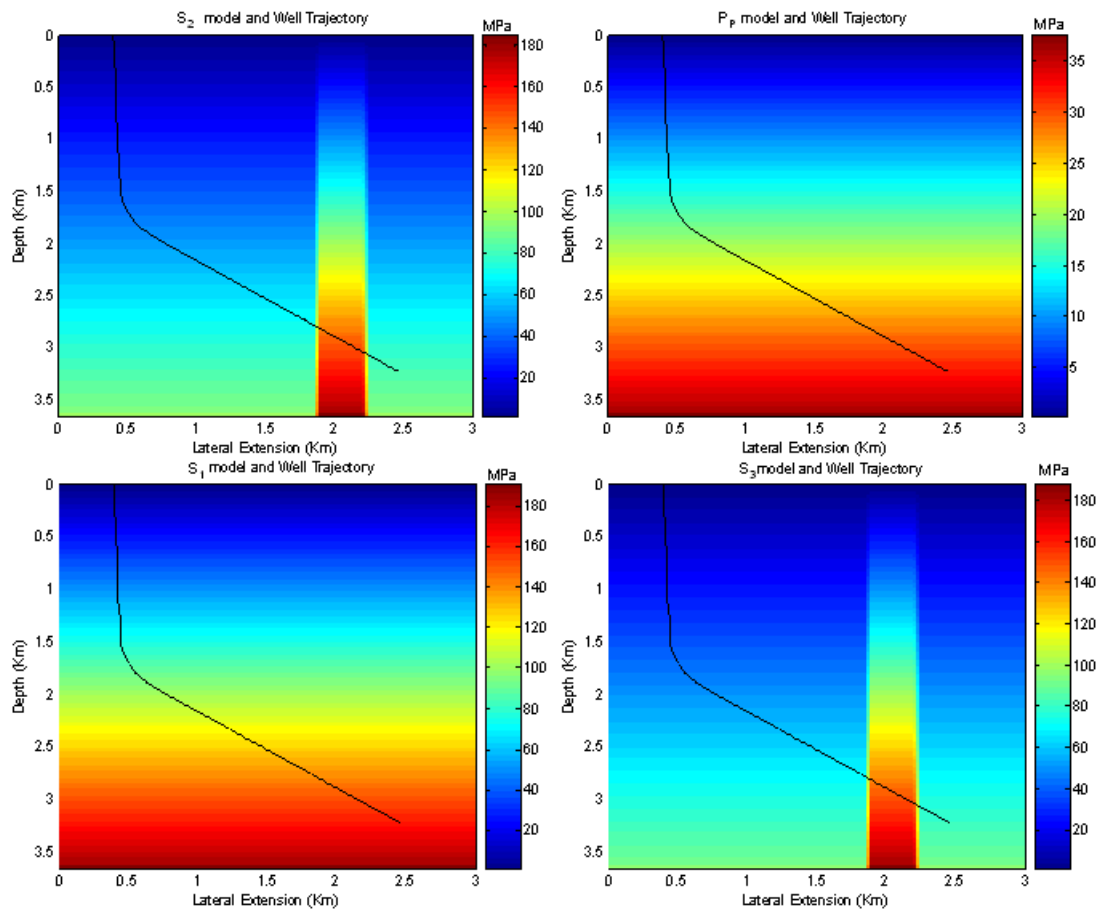


Fig. 2.6: Three principal stresses,  $S_1$ ,  $S_2$ ,  $S_3$ , and pore pressure,  $P_p$ , on the well trajectory plane. Black line shows the well path. The anomalous zone in  $S_2$  and  $S_3$  model at 1.8 km of lateral distance shows the San Andreas Fault zone.

The Chery et al. study was carried out after the Pilot Hole was drilled but before Phase-1 drilling. Three observations obtained during Phase-1 led us to slightly revise the preliminary stress model shown in Fig. 2.6. First, analysis of breakouts and drilling-induced tensile fractures and dipole sonic logs in the Phase-1 borehole

indicates a maximum horizontal stress orientation of N35°E (Boness and Zoback, 2006), which was ~5°E from that in the preliminary stress model. Second, as a result of modifying the velocity model in the vicinity of the San Andreas, there was shift in the microearthquake locations to the SW. The result of this is that when Phase-1 drilling was completed, it was clear that the bottom of the hole was close to the active fault zone. Third, the minifrac measurement noted above that shows extraordinarily high values of  $S_3$  at the bottom of the Phase-1 (>10 MPa above  $S_v$ ) independently confirms the fact that the active fault is to the SW of the surface trace and close to the end of Phase-1 drilling.

To constrain stress magnitudes in the arkosic rocks drilled during Phase-1, Fig. 2.7 is a wellbore stability analysis for wells of any orientation at a measured depth of 2220m using the methodology described in Peska and Zoback (1995). Radial distance from the center of each figure represents well deviation at a given azimuth. The figure on the left shows the orientation of a breakout (if it were to form) in a “looking down the hole” coordinate system. The figure on the right shows the magnitude of rock strength required to prevent failures larger than 60 degrees. The black arrows show the orientation of  $S_{Hmax}$ . The azimuth and orientation of the SAFOD borehole is shown in each figure. Note that the stress model used ( $S_1 \sim 101$  MPa,  $S_2 \sim 91$  MPa,  $S_3 \sim 50$  MPa, and Azimuth of  $S_1 \sim N35^\circ E$ ) predicts a breakout orientation that is 10° degrees counter clockwise from the top and bottom of the hole, exactly the same as what was observed in the caliper data (Fig. 2.4). This exercise shows, therefore, that the observed hole enlargements are stress-induced wellbore breakouts, not key seats although key seating may exacerbate the depth of the failure zones away from the borehole wall. Although this modified stress model now can be used to constrain in situ rock strength (Zoback et al., 1998) in the Phase-1 wellbore in the context of the observed failures (Fig. 2.4), in the next section we also utilize geophysical logs to constrain rock strength.



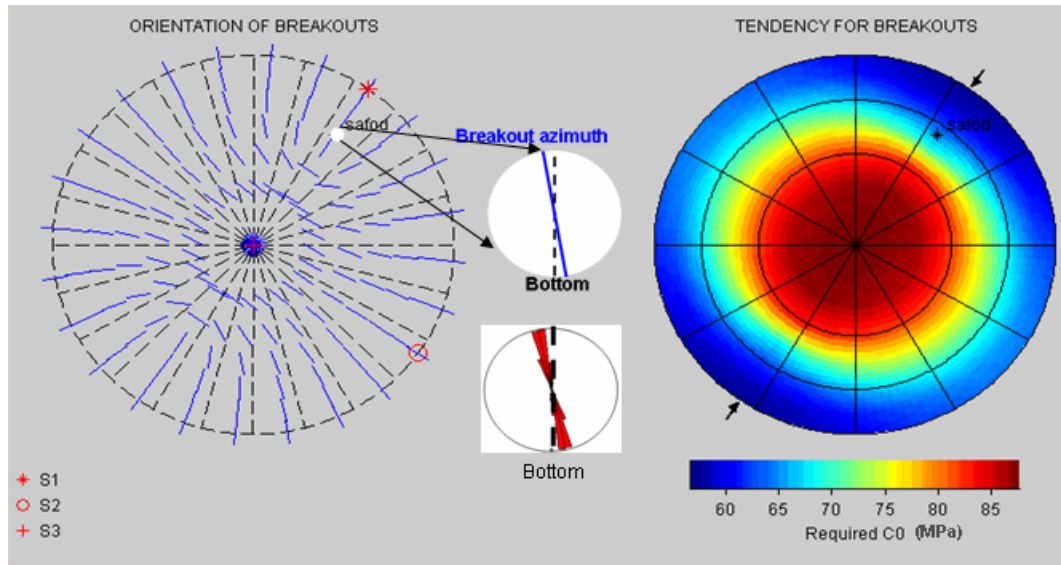


Fig. 2.7: Modified stress model with  $S_{Hmax}$  azimuth of 35 deg,  $S_{Hmax} \approx 2 \cdot S_v$ ,  $S_{hmin} \approx 1.82 \cdot S_v$ ,  $S_v \approx$  lithostatic gradient ( $\sim 0.025$  MPa/m) is able to model breakout azimuth (blue), which matches the orientation of observed borehole enlargements (red).

## 2.7 UCS Modeling

In cases such as this where no laboratory rock strength measurements are available, we estimate rock strength by calibrating a best fit rock strength model to the nature and severity of borehole failures. For the granite and granodiorite section between 853-1926m, we used a rock strength model (Eq. 2.1) of the type proposed by Annor and Jackson (1987) which uses P-wave velocity measured from sonic logs to calculate rock strength. This deterministic model was later calibrated for the granite around the SAFOD well by Hickman and Zoback (2004) using Pilot Hole data.

$$UCS = 129 + 0.0145V_p \quad (2.1)$$

where UCS is in MPa and  $V_p$  is in m/s.

To deal with the uncertainty in rock strength in the diverse sedimentary rocks that were drilled, we compared observed borehole failures with those predicted using several rock strength models (Chang et al., 2004). These rock strength models represent a range of sedimentary environments having different values of porosity,

cementation factor, clay percentage, and rock strength. We found that a coarse grained sandstone model with conglomerates (Eq. 2.2) proposed by Moos et al. (1999) gives the best correlation in this case. We used single and dual arm caliper data to assess the actual borehole condition.

$$UCS = 1.745 \times 10^{-9} \rho V_p^2 - 21 \quad (2.2)$$

where UCS is in MPa,  $\rho$  is in  $\text{kg/m}^3$ , and  $V_p$  is in m/s.

We found, however, that the above described sedimentary strength model tended to underestimate the magnitude of well failure indicating overestimation of the rock strength or underestimation of stress magnitudes. We believe that the rock is actually weaker than predicted by Eq. 2.2 because of pre-existing damage and micro-cracks in the rock (Hoek and Brown, 1997, 1980; Hongliang and Ahrens, 1994; Hu and Huang, 1993). Variations of sonic velocity are incapable of completely predicting the zones of increased wellbore failures nor do density measurements indicate increased porosity in those zones (Fig. 2.8). Resistivity images and other logs also show no increase of porosity in the failed zone. In this context, we argue that the rock weakness is caused at least in part by damage to the rock such that the overall porosity and bulk properties are unchanged.

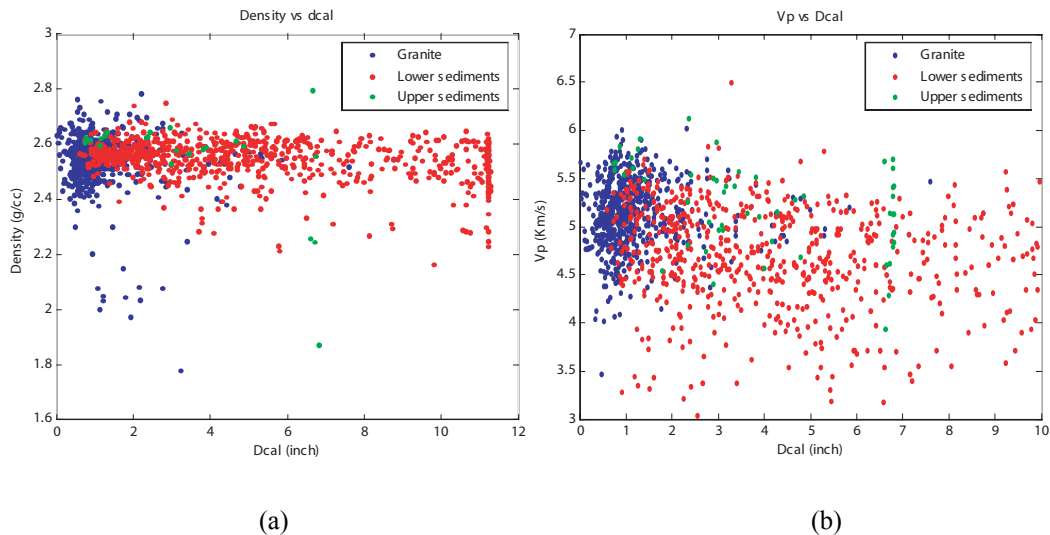


Fig. 2.8: (a) Caliper versus density shows density is constant around 2.6 for whole range of caliper measurements (b) Caliper versus Vp shows a slight decrease in velocity with the increasing borehole width.

To incorporate the effect of damage on the rock strength, we use the empirical criterion proposed by Hoek and Brown (1980) shown in Eq. 2.3. It suggests that strength of a rock mass depends on the scale of the damage. A heavily jointed rock mass behaves like an intact rock at fine scale but at larger scale behaves like an isotropic assemblage of interlocking angular particles (Fig. 2.9). Hence, the rock mass will be much weaker at large scale than fine scale. Experimental studies by Brown (1970) shows that a number of failure modes are possible in jointed rock. Chappell (1974) found that the internal distribution of stresses within the jointed rock mass can be very complex. Laboratory experiments on intact and jointed rock mass shows a non-linear behavior between principal stresses with shear or normal stresses at failure (Hoek and Brown, 1980).

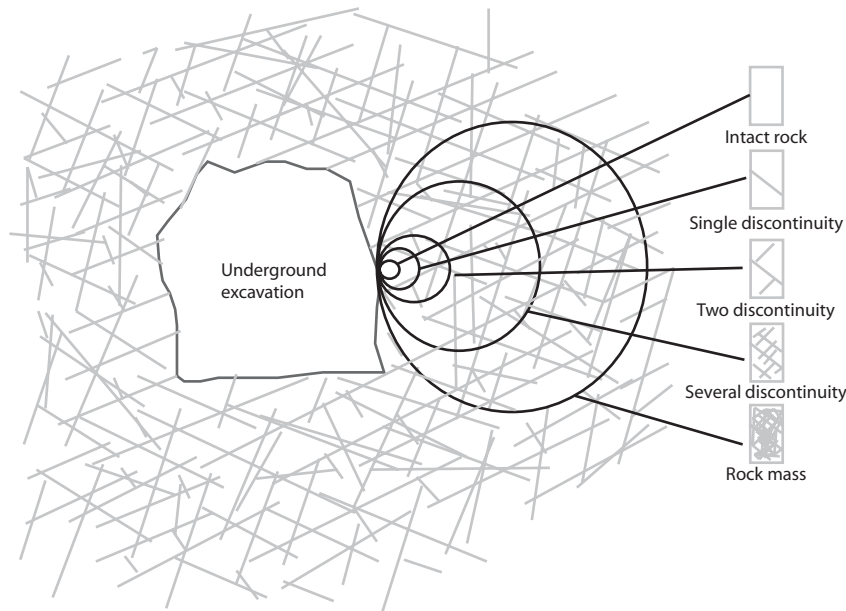


Fig. 2.9: Transition from intact rock to heavily jointed rock mass with increasing sample size (modified from Hoek, 1980; published with permission from ASCE).

Uniaxial compressive strength ( $UCS_f$ ) of a jointed rock mass is related to uniaxial compressive strength (UCS) of the intact rock by Eq. 2.3.

$$UCS_f = \sqrt{s * UCS^2} \quad (2.3)$$

The parameter 's' in Eq. 2.3 depends on interparticle tensile strength and the degree of particle interlocking. For an intact rock material  $s=1.0$ , for a damaged rock  $0 < s < 1$ , and for a completely granulated rock aggregate,  $s=0$ . 's' decreases as the degree of prior fracturing of the rock mass increases because of the greater degree of freedom made available to individual pieces of rock material. Thus, depending on the amount of damage, 's' may vary from 0 to 1 for different rock types. Laboratory tests on jointed samples of andesite and granite suggest a minimum value as low as 0.0002 for 's' (Jaeger, 1970). For anisotropic rocks, 's' varies with the orientation ( $\beta$ ) of the planes of weakness to the maximum principal stress direction by Eq. 2.4. (Hoek, 1964; Donath, 1964; McLamore and Gray, 1967).

$$s = 1 - P_1 \exp(-\zeta)^4, \quad (2.4)$$

where  $\zeta = (\beta - \beta_s) / (P_2 + P_3\beta)$ ,  $\beta_s$  = value of  $\beta$  at which 's' is minimum, and  $P_1$ ,  $P_2$ , and  $P_3$  are constants.

To determine the value of compressive strength of the jointed rock using Eq. 2.3, we have used the UCS of intact rock calculated from Eqs. 2.1 and 2.2 with a value of 's'. In general, 's' can be determined on laboratory core samples. In this study we used an empirical approach to estimate the value of 's' using the dual caliper measurements. To get an initial approximate value of 's', we will assume that if both calipers show that the entire hole is enlarged, or a washout, we will assume that breakout width  $\geq 180^\circ$ . If one caliper pairs shows large enlargement but the other shows an in gauge hole, then we assume a breakout width  $< 180^\circ$ . If both calipers are in gauge, we assume that the hole has not failed.

In Fig. 2.10 we show the predicted width of breakouts in the SAFOD Phase-1 borehole using the stress model defined above for constant rock strengths that vary between 20 and 90 MPa. For rock strengths of 90 MPa no wellbore failure is seen. When rock strength is  $\sim 80$  MPa, only a small amount of failure is observed in the interval 1500-1800m. Conversely, when strength is as low as 50 MPa, the prediction would be that the entire well below 1300m would be washed out. One can see, therefore, that realistic rock strengths would appear to be approximately 60-70 MPa for the assumed stress state. The calculated value of 's' is that which "corrects" the log-derived strength to values to be consistent with those estimated from the overall nature of wellbore failure as shown graphically in Fig. 2.11. For the Tertiary/Quaternary section, we found  $s \sim 1$  because rock strength predicted by geophysical logs is low enough to model the failure observed during Phase-1 drilling. In granite/granodiorite section, we found  $s \sim 1$ , indicating a strong rock, which is consistent with the stable borehole. Fig. 2.11 show borehole failure modeling results for  $s=1$  (intact rock),  $s=0.85$  ( $\sim 8\%$  weaker than intact rock), and  $s=0.7$  ( $\sim 16\%$  weaker than intact rock) in sedimentary section below 1926m. Weakness introduced by values  $s=1$  and  $s=0.7$  under predict and over predict the borehole failure. However, with  $s \sim 0.85$  modeled failures are consistent with the actual failure.

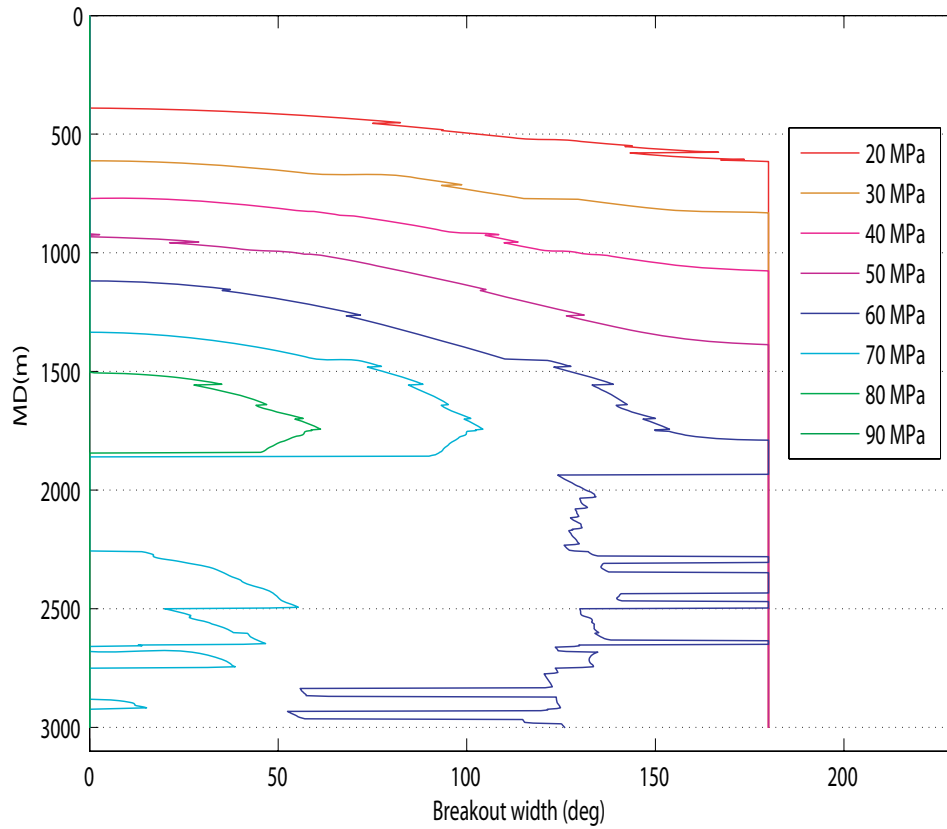


Fig. 2.10: At 1920m to 2804m (MD) of the SAFOD well trajectory, deterministic modeling indicates uniaxial compressive strength of  $\sim 60\text{-}70$  MPa for a rock, which gives breakout width  $\sim 90^\circ$  using mud weight of Phase-1 drilling.

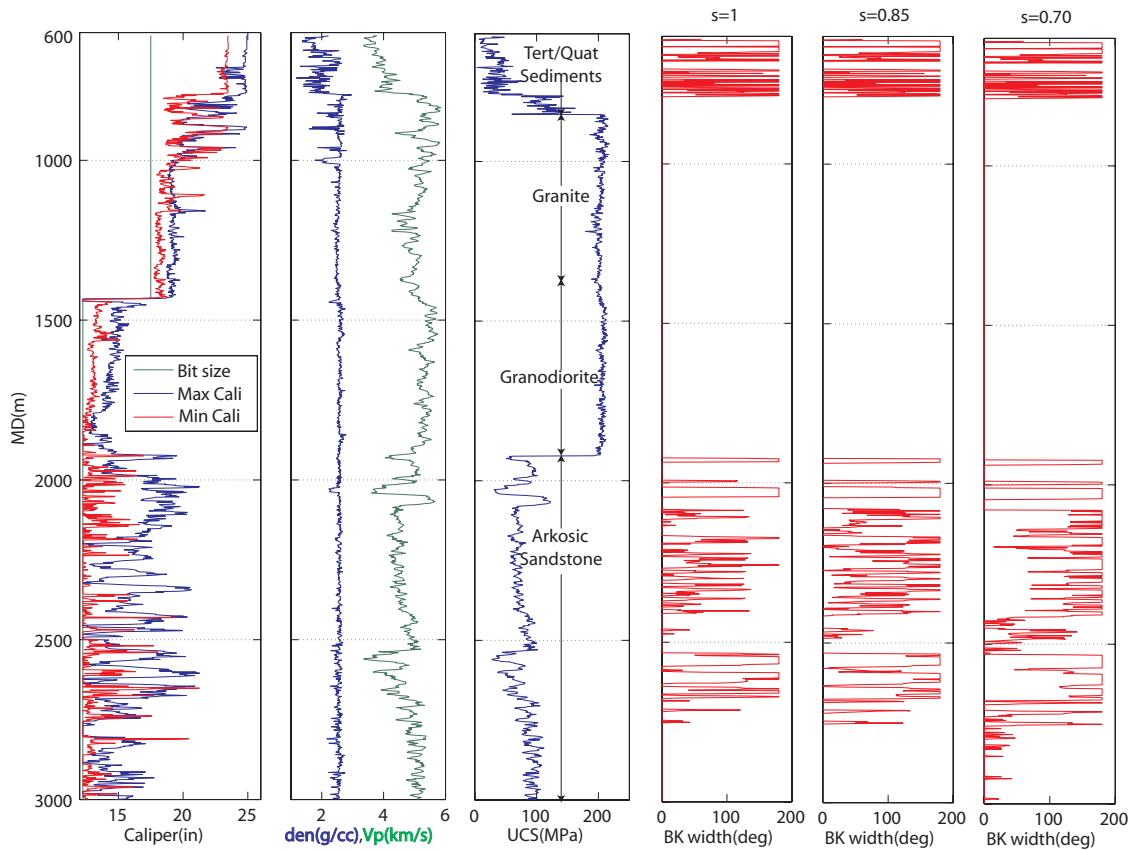


Fig. 2.11: Column 1: maximum and minimum calipers; column 2: density and P-wave velocity logs used for rock strength estimation; column 3: estimated uniaxial rock strength; column 4, 5, and 6: predicted breakout width with used mud weight using  $s=1$ ,  $s=0.85$ , and  $s=0.7$  in the sedimentary section below 1920m, and  $s=1$  for granite, granodiorite, and tertiary sediments above 1920m. With  $s \sim 0.85$  modeled borehole failures matches relatively well with the actual borehole failure in the sedimentary section below 1920m (column 1).

## 2.8 Modeling of Phase-1 borehole failures

To evaluate how well the technique described above predicts the degree of wellbore failure observed we compare the predicted failure width with the actual wellbore failures from the maximum and minimum calipers. We define the breakout width from observed calipers by assuming breakout width less than  $90^\circ$ , if one caliper is gauged and other is enlarged. Fig. 2.11 shows the minimum and maximum caliper data (column 1), the predicted strength profile (column 3) and the theoretical breakout width for  $s = 1$ , 0.85 and 0.7 in the sedimentary section below 1920m and  $s=1$  for sections above 1920m (columns 4, 5, 6). Overall, we see a very good correlation for

$s \sim 0.85$  in the section below 1920m. The model predicts the observed washouts in the Tertiary/Quaternary sediments at shallow depth. In the granite and granodiorite interval above 1926m, the borehole was observed to be generally stable which is what is also predicted by the model. In the sandstone section interval below 1926m, the breakouts are mostly predicted to be between of  $90^\circ$  to  $120^\circ$  width which matches with the caliper logs fairly well although there are some intervals where there is both a predicted and observed greater amount of failure.

Based on the analysis above, the mud weight used during drilling the deeper sedimentary section in Phase-1 ( $\sim 10$ ppg) was about 1ppg less than that which would have resulted in significantly less hole enlargement (Fig. 2.12). While a modest improvement in wellbore stability would have been achieved with an increase in mud weight of 0.5ppg, an increase of 1ppg would have resulted in significant improvements.

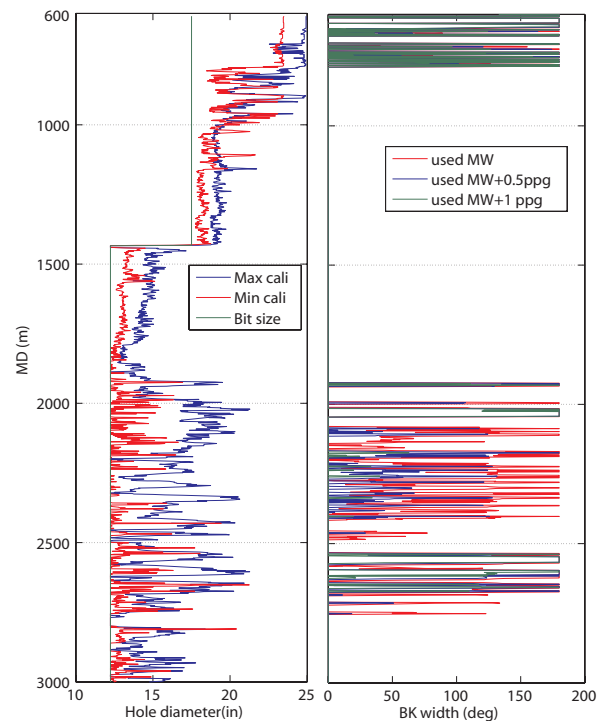


Fig. 2.12: Column 1: maximum and minimum calipers; column 2: predicted breakout width with rock strength (for  $s \sim 0.85$ ) for used mud-weight, and 0.5 ppg and 1 ppg higher mud-weights. An increase of  $\sim 1$  ppg in mud-weight shows significant improvement in the borehole failure.



## 2.9 Mud weight prediction for Phase-2

Using the analysis presented above, we estimated the mud weight that should be used during Phase-2 drilling in four steps. First, we extrapolated the stress model down to the total depth along the proposed well trajectory. Fig. 2.13 shows the modified stress models for  $S_2$  and  $S_3$  based on the observations made during Phase-1. Models for  $S_1$  and  $P_p$  (both within and outside the fault zone) remain the same as that described by Chery et al. (2004). Both a minifrac test done at the end of Phase-1 at MD of 3028m, (where  $S_3 > 10\text{MPa}$ ), and another minifrac test done on the vertical section of the well at MD of  $\sim 1470\text{m}$  indicate that the stress profile follows a reverse/strike slip fault state (Hickman and Zoback, 2004) as used in Chery et. al.'s model. We also assumed that the within the fault zone, stresses follow the Chery et. al. model. Then we used breakout analysis (Fig. 2.7) in between the two minifrac test intervals outside the fault zone to modify the stress profile from the preliminary model. The modified values for  $S_2$  and  $S_3$  (Fig. 2.13) show increased values of both stresses over a broad region in compare to the preliminary model. In the second step, we extrapolated rock strength along the well trajectory. To estimate the intact rock strength using Eq. 2.2, we used the P-wave velocity data for the rocks to be drilled using a three dimensional seismic tomography model (Thurber et al., 2004). We observed in Phase-1 that an average bulk density of  $2.68\text{ g/cm}^3$  characterized the sedimentary rocks. This value was used for Phase-2. To convert intact rock strength to in situ rock strength (incorporating damage to the rocks with varying intensity), we consider a wide range for the factor 's' in Eq. 2.3, that goes from 0.5 to 1.0. In other words we assumed the rock strength was either unaffected by damage ( $s=1$ ) or reduced by approximately 30% ( $s=0.5$ ). Recall that there was only a 8% decrease ( $s=0.85$ ) in the sedimentary rocks drilled in Phase-1.

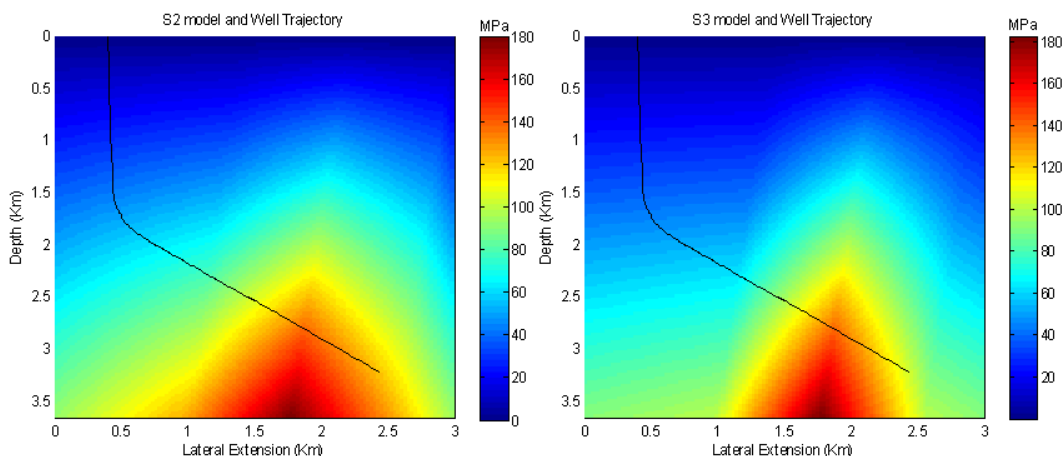


Fig. 2.13: Modified stress model for principal stresses,  $S_2$  and  $S_3$  through the San Andreas Fault. Pore pressure and  $S_1$  remain same as Chery et al. model (Fig. 2.6).

The third step of the analysis was to calculate the mud weight required to drill Phase-2 utilizing a range of ‘s’ values. Fig. 2.14a and b show the predicted mud weight to prevent borehole failures greater than  $45^\circ$  and  $60^\circ$  breakout width respectively. In fact, both assumptions are quite conservative as many wells are drilled successfully with breakouts widths that exceed  $60^\circ$ . For the mean case ( $s \sim 0.74$ ), the minimum mud weight required to prevent  $60^\circ$  breakout is  $\sim 11.7$  ppg in the fault zone and  $\sim 10.8$ - $11.4$  ppg in zones away from the fault zone. For a weaker rock ( $s \sim 0.5$ ), the required mud weights are  $\sim 12.3$  ppg for the fault zone and  $\sim 11.1$ - $12.1$  ppg away from the fault.

The fourth step of our study was to do a quantitative risk analysis (QRA) to formally incorporate the uncertainties in the extrapolated stress and rock strength values. In this way we could estimate the importance of these parameters for the prediction of minimum mud weight values.

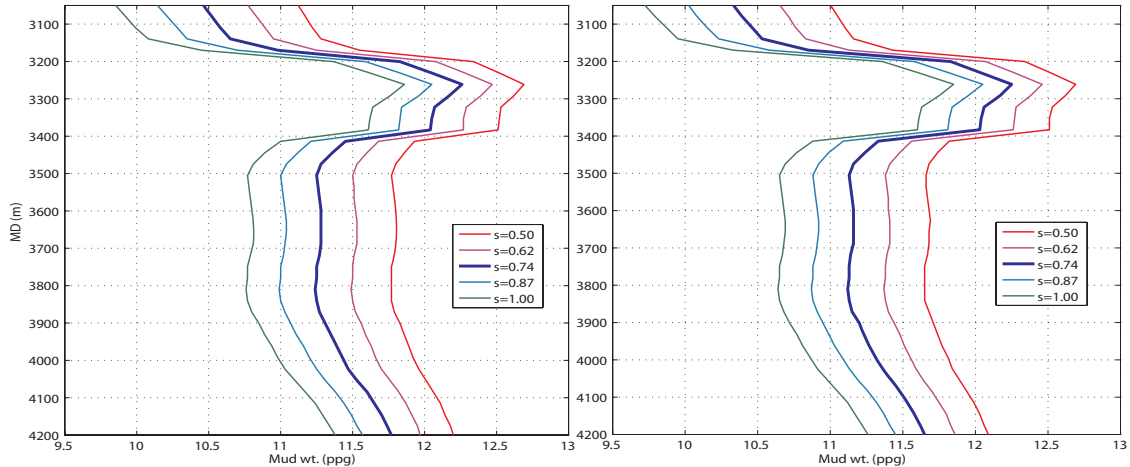
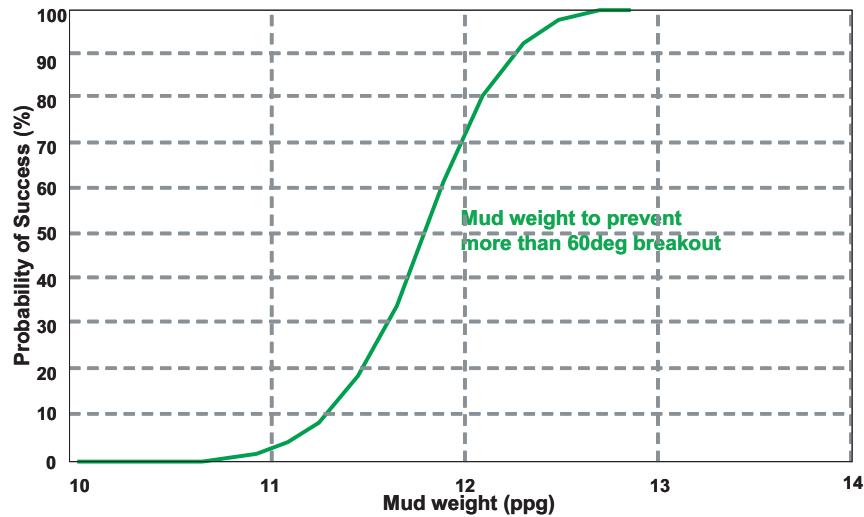


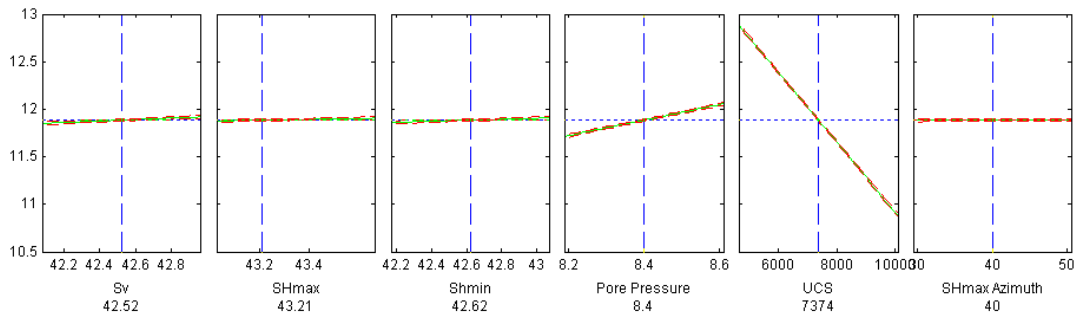
Fig. 2.14: Mud weight predictions using estimated rock strength and stress model for (a) 45 deg and (b) 60 deg breakout width. The analysis shows a minimum mud weight  $\sim 11.2$  ppg (no damage,  $s=1$ ) to 12.3 ppg (30% weaker than undamaged rock,  $s=0.5$ ) is required to drill through the San Andreas Fault with a breakout width of  $\sim 60^\circ$ .

## 2.10 Quantitative Risk Analysis to drill a stable borehole through the SAF

QRA allows us to incorporate uncertainty in the most expected value of the various parameters used in this study to give the probability of success using a particular mud weight (Moos et al., 2003; Ottesen et al., 1999). Analysis will be done for a maximum breakout width of  $60^\circ$ . We allow for 10% uncertainty in stress magnitudes, a range of azimuths of the maximum horizontal stress between  $N30^\circ E$  and  $N50^\circ E$ , and a variation of rock strengths that corresponds to values of  $s$  ranging from 0.5 to 1.0. The QRA analysis shows in Fig. 2.15a that for a mud weight of  $\sim 11.8$  ppg there is a 50% chance of success (the breakout width not exceeding  $60^\circ$ ). For a mud weight of 12.3 ppg there is a 90% chance of success. In Fig. 2.15b we see that rock strength (UCS) defines the uncertainty range of the estimated mud weight to drill a stable borehole with  $60^\circ$  breakout width. Hence, it is the most important parameter needed to drill a stable borehole through the fault zone. Hence, even with a mud weight of  $\sim 12$  ppg, intervals of extremely weak rock could still be problematic.



(a)



(b)

Fig. 2.15: (a) QRA at the San Andreas Fault zone ( $\sim 3300\text{m}$ ) the probability of success (to drill with  $60^\circ$  breakout width) as a function of mud weight. (b) The sensitivity analysis shows rock strength is the most sensitive parameter controlling the mud weight required to drill a stable hole through the fault zone. Stress and pore pressure are in ppg. UCS is in psi and  $S_{H\text{max}}$  azimuth is in degrees.

## 2.11 Borehole stability during Phase-2 through the SAF

Phase-2 drilling and logging showed that the San Andreas Fault zone (a zone of damaged rock encompassing several currently active fault traces) extends from  $\sim 3180\text{-}3420\text{m}$ . The arkosic sandstones drilled through in the lower part of Phase-1 extend to a depth of  $3160\text{m}$ . Below that depth, the formations encountered were mostly siltstones and claystones associated with the Great Valley formation. These rocks strike sub-

parallel to the San Andreas Fault and mostly dip to the SW, such that the wellbore trajectory is roughly orthogonal to the bedding (Boness and Zoback, 2006).

The range of mud weights shown in Fig. 2.16 were obtained from the analysis described above to achieve the desired degree of wellbore stability (breakouts that do not exceed 60° width) for the range of uncertainties in ‘s’ illustrated in Fig. 2.14. As can be seen this results in a range of recommended mud weights between 10.2 and 12.2 ppg. The mud weights actually used during drilling are also shown in Fig. 2.16. As can be seen, the initial mud weight was 9.8 ppg and increased gradually with depth and was mostly within the range of mud weights indicated by the analysis described above.

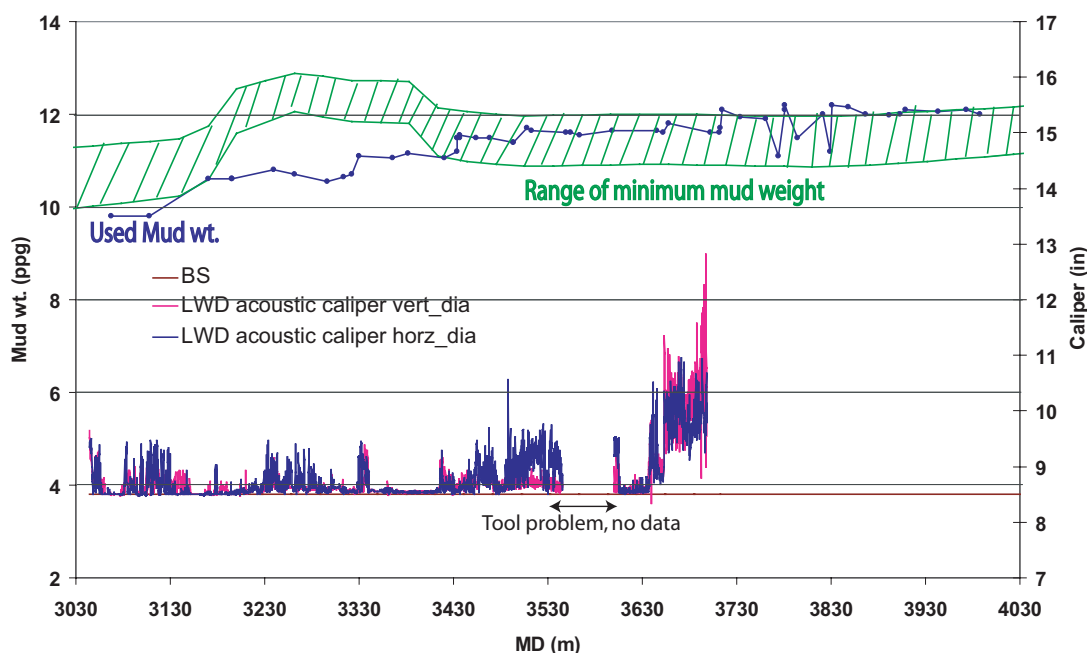


Fig. 2.16: Through the San Andreas Fault, LWD acoustic calipers show relatively little borehole failure in Phase-2 drilling when drilled with a mud weight close to predicted mud weight. Below 3650m, LWD shows onset of significant failure. A possible explanation may be underestimation of rock strength on the NE of the fault zone that is used to predict the range of minimum mud weight window.

Fig. 2.16 also shows the vertical and horizontal wellbore diameters as determined from acoustic caliper data obtained using logging while drilling (LWD). LWD data was obtained from 3050 to 3700m and a problem with the tool resulted in no data from 3550 to 3600m. Note that at depths above 3630m the hole is in good shape. The horizontal diameter is very close to the bit size and the vertical dimension

shows only modest increases in hole size at a few depths. Hence, the mud weight predicted using the analysis above did a good job of maintaining wellbore stability during drilling most of the interval shown.

Another source of data that confirms this conclusion is the volume of mud in the hole as it was being drilled (Fig. 2.17). Hole volume is calculated assuming a cylindrical shaped borehole with variable diameter, defined by calipers with measured depth. Mud volume is estimated by correcting the hole volume for the volume of drilling assembly in the hole. Note that the actual mud volume is the same as that predicted for an in-gauge hole to ~3450m. However, the cumulative hole volume calculated from the LWD caliper data below 3450m show that the hole volume should have been essentially equivalent to that corresponding to an in-gauge hole to 3550m. This implies that the increase in hole volume seen in the interval between 3450-3550m was occurring up the hole (above the acoustic caliper located 14 m above the bit). Hence, there seems to be a degree of time-dependent failure of the hole at depths above 3450m at the time the hole was in gauge as it was being drilled from 3450-3550m. Time-dependent hole failure is discussed in more detail in the next section.

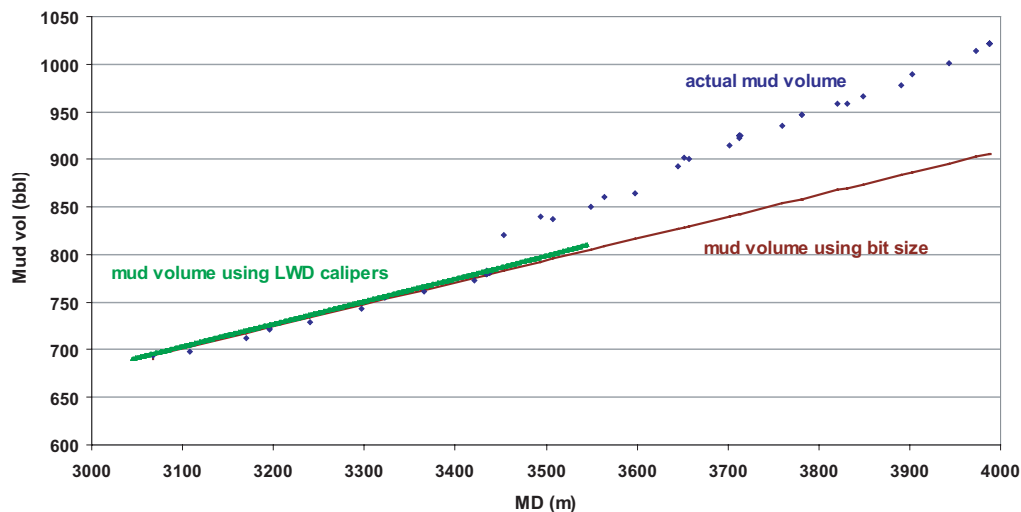


Fig. 2.17: A good match of the actual mud volume to mud volume estimates from the bit size and the LWD calipers indicates that the hole was relatively in good shape while drilling for the interval above 3440 m. LWD mud volume indicates good hole till 3550m (MD) while deviation of the actual mud volume from the bit size mud volume at this interval suggests a time dependent failures at interval above 3550m. Higher actual mud volume slope than bit size mud volume slope indicates onset of significant hole failure below 3550m.

Between 3630m and 3700m, the acoustic caliper data (and hole volume data) show the onset of significant hole enlargements. In the acoustic caliper data, a moderate washout (approximately 2-3") is observed (Fig. 2.16). In the hole volume data (Fig. 2.17) we see an increase of volume with depth in excess of that expected if the hole was in gauge. Hence, we seem to be using a mud weight that is too low. One reason for this might be the fact that because the SAF was crossed at MD of ~3300m (TVD of ~2800m), the strength analysis described above (based on the sedimentary section drilled during Phase-1 to the southwest of the San Andreas Fault) might have resulted in an underestimate of the strength of the Great Valley formation on the NE side of the fault.

## 2.12 Time dependent failure

Once Phase-2 drilling was completed at a MD of 3980m, a six arm caliper log was run (Fig. 2.16). Surprisingly, this log showed very large hole enlargements, even

in the interval from 3050-3650m where the LWD (and hole volume) data show that the hole was in gauge as it was being drilled. Thus, the enlarged calipers indicate deterioration of the borehole with time. Time dependent hole failure is clear for the depths covered by the LWD data as a direct comparison between Fig. 2.17 and Fig. 2.18. The time dependent failure of the borehole was so severe that there are depth intervals where one (or two) of the calipers are fully extended. As shown in the inset of Fig. 2.18 (a superposition of all the caliper data looking down the hole) the borehole seems to be primarily enlarged on the top of the hole. The blue symbols represent the tool position in the hole as determined using the algorithm described by Jarosinski (1998). The fact that the hole enlargements appear to be on the top of the hole might, in part, be an artifact of the logging tool being near the bottom of the deviated well and the fact that the hole failure might have caused there to be a cuttings bed on the bottom of the hole.

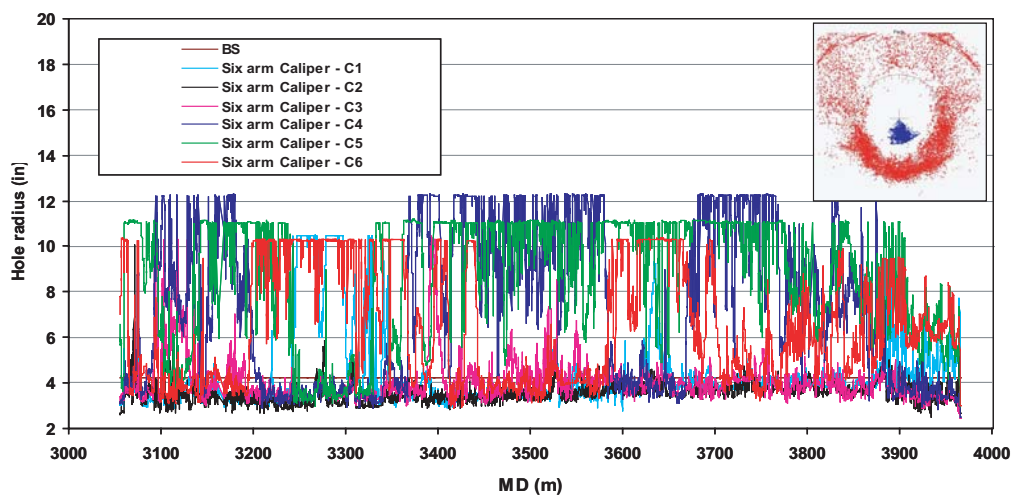


Fig. 2.18: Six arm wireline calipers show deterioration of the borehole with time. In the right up corner, centralized six-arm caliper pads are plotted in a borehole coordinate system. Borehole shape is highly extended at the top and top corners, consistent with key seating and failure in weak planes rather than borehole breakouts.

The processes responsible for the time dependent hole failure are not known. One possibility is that time dependent chemical reactions between the water based mud and the clays in shaly rocks decreased rock strength with time. However, the time



dependent increase in hole size is seen over the entire depth range drilled in Phase-2, including the arkosic rocks extending to 3180m. Moreover, such interactions are not known to be a significant problem in oil and gas wells drilled with water based mud in the Great Valley formation. The most likely possibility is time-dependent mud penetration into the rock surrounding the borehole. Fig. 2.19 shows LWD calipers and resistivity logs with multiple depths of investigation (track 1 and 2), and wireline calipers and resistivity logs (track 3 and 4), which were measured after several days of LWD logs when drilling was completed. There is almost no separation in LWD resistivity logs but wireline resistivity logs from different depths of investigation are separated, indicating mud fluid penetration into the formation with time. This would result from inadequate membrane efficiency potentially made worse by the numerous fractures in these formations. Below MD 3750m in Fig. 2.19, wireline calipers indicate that hole is relatively better which matches with minimal separation between the resistivity logs. This happened either because of the very low permeability of the formation or an insufficient time for mud fluid to penetrate into the formation. Fluid penetration around the well would increase pore pressure and reduce the effectiveness of mud weight to stabilize the hole and could cause cavitation of the rock surrounding the wellbore. In the next section, we present a FEM (Finite Element Modeling) exercise to show the mud penetration into the formation and the change of pore pressure with time. Increase in the pore pressure promotes shear failure on the fracture planes which leads to enlargement of the borehole. Because the hole is highly deviated and the wellbore seems to be principally enlarged on the top, key seating could also be a source of erosion of the wellbore wall, especially on the top of the hole. In reality, it could be the combination of these processes that were responsible for the time dependent hole failure.

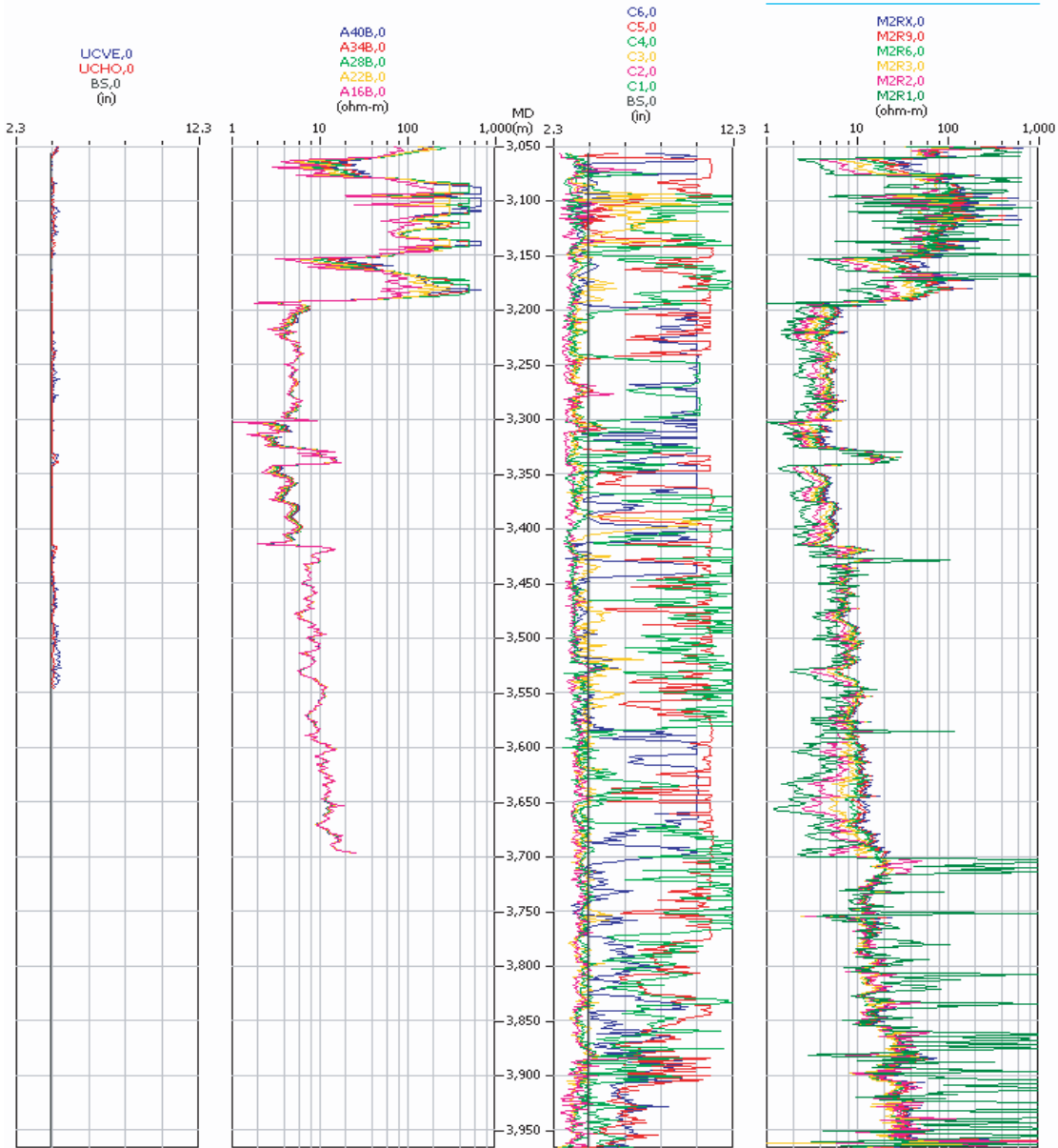


Fig. 2.19: LWD calipers (track 1) and resistivity logs with multiple depths of investigation (track 2) indicate a stable borehole and no fluid penetration around the borehole. Wireline resistivity logs (track 4) measured a few days after the LWD logs show separation between them, indicating mud penetration into the formation which may cause failure in the borehole as observed by the wire line calipers (track 3).

## 2.13 Modeling of time dependent failure

This modeling exercise shows mud penetration into the formation with time. It uses finite element modeling on a schematic model (Fig. 2.20) of the area surrounding the borehole with the realistic values for fracture permeability ( $\sim 1\text{mD}$ ) and matrix permeability ( $\sim 0.004\text{mD}$ ) for tight sandstones (Durrast et al., 2002). The borehole mud pressure of  $\sim 33\text{MPa}$  (used during drilling) and formation pore pressure of  $\sim 29\text{MPa}$  (estimated by in-situ measurements) are used as initial boundary conditions for the modeling.

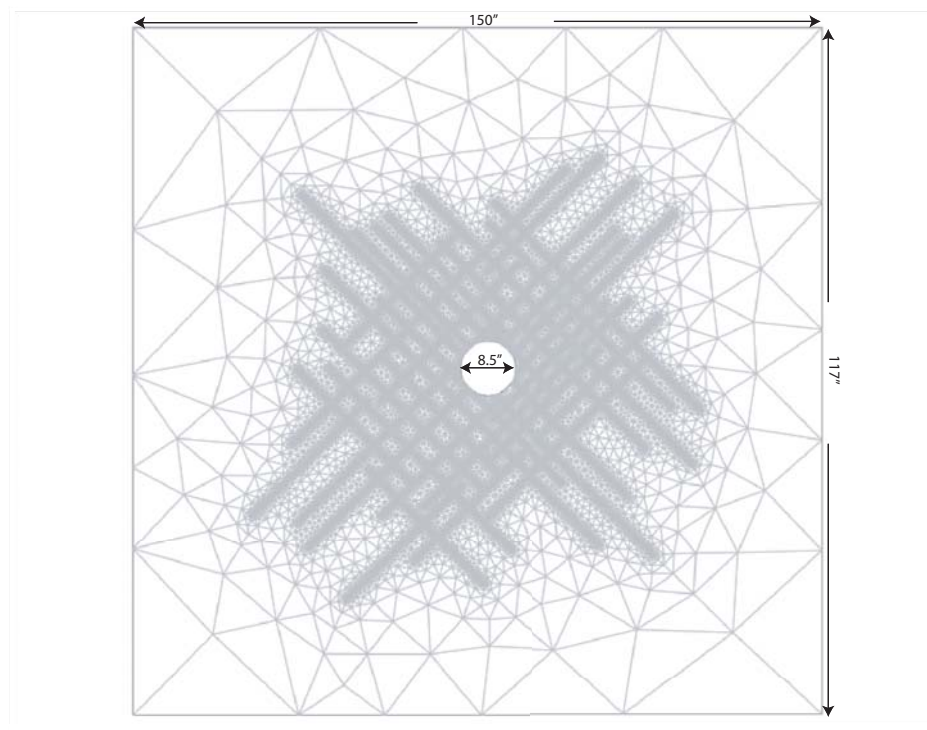


Fig. 2.20: A triangular mesh of the schematic model for the area around the borehole. Permeability values of  $1\text{mD}$  and  $0.004\text{mD}$  are used for fracture and matrix respectively. Mud pressure and pore pressure are kept at  $33\text{MPa}$  and  $29\text{MPa}$  respectively.

Modeling of the pressure diffusion process between the borehole into the formation indicates a slow penetration rate. Mud starts penetrating the relatively high permeable fractures and gradually spreading around the borehole with time. Hence, the initial shape of the diffusion front is dependent on the number of fractures and their intersecting locations with the borehole. However, the final shape of the diffusion front

is guided by the fracture pattern in the formation. Modeling shows first sign of pressure change around the borehole at  $\sim 3$ hrs (Fig. 2.21a). Fig. 2.21b, 2.21c, and 2.21d show pressure front after 2days, 2weeks, and 4weeks. It illustrates that diffusion process is slow and it takes at the order of 2-4weeks of time when pressure front spreads up to  $\sim 10$ -12 inches from the borehole wall, which is consistent with the rate of time dependent failure observed in the SAFOD borehole.

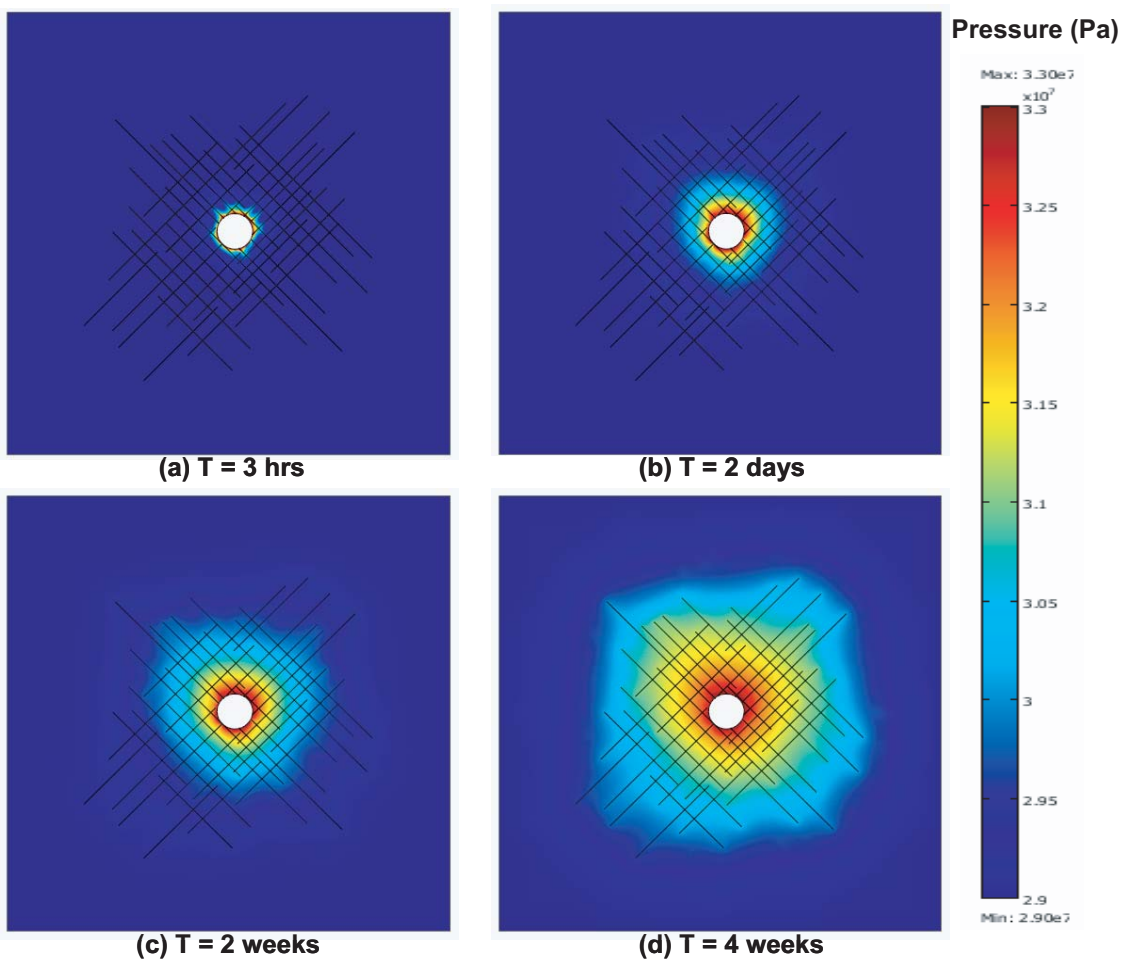


Fig. 2.21: Pressure front at (a) 3hours (b) 2 days (c) 2 weeks, and (d) 4 weeks show that it takes  $\sim 2$ -4 weeks for the front to spread up a mud wt. of  $\sim 33$ MPa to  $\sim 10$ -12 inches from the borehole wall by diffusion process.

At initial conditions, a formation pore pressure of  $\sim 29$ MPa is not sufficient to create any shear failure on fracture planes but as the pressure gradually rises with time and spreads over a larger area (reddish zone in Fig. 2.21) these planes are more likely to slip. For a symmetric distribution of fractures, the shape of the increased pore

pressure area where fracture planes may slip is symmetric around the borehole. Fracture sets around the SAFOD borehole strike sub-parallel to the SAF (Boness and Zoback, 2005). Fig 2.22 illustrates the zones (red colored) around the SAFOD borehole in a cross section view, where fracture sets may slip. However, observed failures are only from the top of the borehole (Fig. 2.18 insert). This is caused by the high deviation angle of the well, removable blocks from the top section of hole fall by gravity but there is no mechanism to remove the failing blocks from the bottom section if there is no mud circulation (Goodman, 1989; Goodman and Shi, 1985). Asymmetry of the hole shape is also enhanced by the accumulation of the failed blocks from the top sections in the bottom of hole and the artifact of the logging tool being near the bottom of the deviated well.

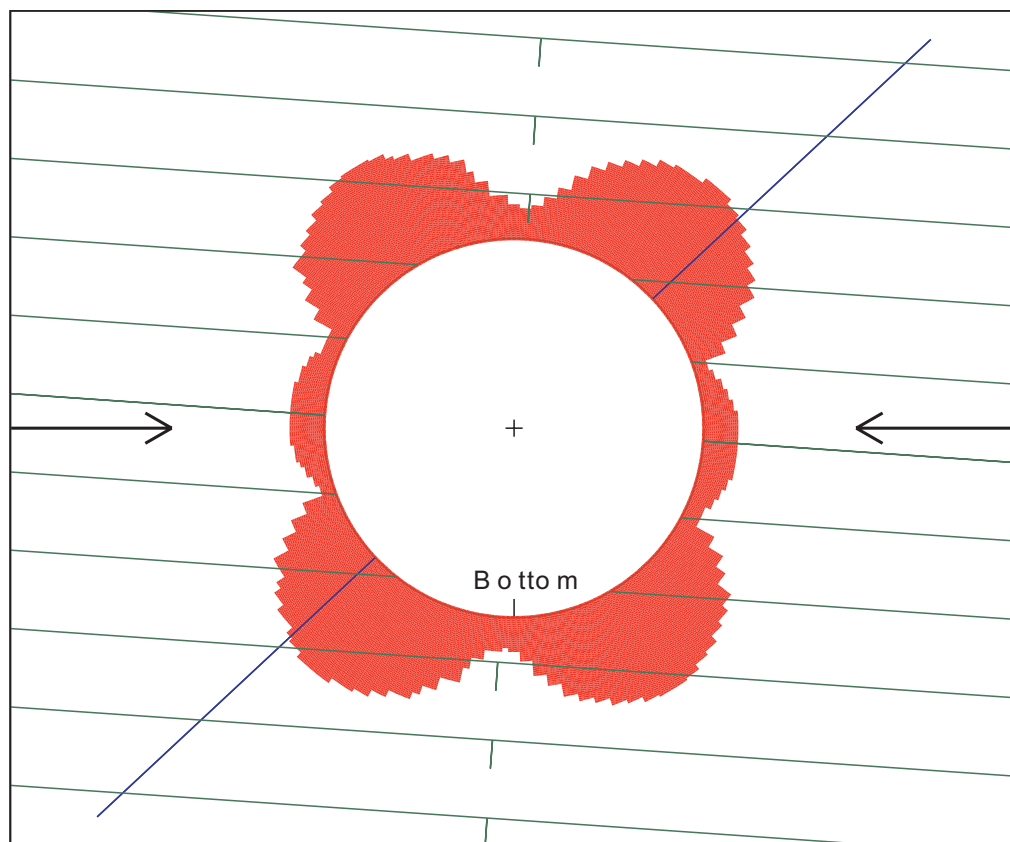


Fig. 2.22: Red color indicates the zone around the SAFOD borehole (cross section view) where fractures may slip due to mud penetration. Green lines indicate fracture planes intersecting the hole, which strike sub-parallel to the SAF.

## 2.14 Conclusions

This study defines a generalized workflow for a wellbore stability study for wells located in areas with complex stress environment and little information about the rock strength. Using the predicted mud weights of ~10.5-12.5 ppg, the SAFOD borehole was successfully drilled through the SAF with relatively little failure (as indicated by LWD caliper and hole volume data). Six-arm caliper data collected after drilling showed significant increases in the size of the borehole with time, which is most likely caused by mud penetration around the well. Mud penetration is indicated by the separation in the resistivity logs (run with six-arm caliper) with multiple depths of investigation. FEM modeling shows that penetration of the drilling mud into the rocks surrounding the wellbore is a slow process which explains the time dependency on the wellbore stability. Once the pore pressure in these bedded and fractured rocks cross the threshold for shearing the fracture planes, failure occurs. Asymmetry in the shape of the failed wellbore is mostly coming from the fact that the SAFOD borehole is highly deviated (~54°), so failed blocks at the bottom of the borehole can not be removed. This effect is enhanced by accumulation of debris falling from the top and an artifact introduced by the tool lying at the bottom of the hole.

We presented an explanation of the time dependent well bore stability and optimization of mud weight for drilling a well in a complex environment. Both of these processes have a wide range of applicability in drilling industry. However, supporting the above numerical and deterministic techniques by laboratory measurements on core samples may reduce the uncertainties in some of the stages of the workflow.

## References

- Annor, A. and Jackson, R., 1987, Mechanical, thermal and joint properties of rock samples from the Lac du Bonnet Batholith, Manitoba: Geotechnical Studies at Whiteshell Research Area (RA-3), CANMET Min. Res. Lab., Ottawa.
- Boness, N. and Zoback, M. D., 2006, A multi-scale study of the mechanism controlling shear velocity anisotropy in the San Andreas Fault Observatory at Depth", *Geophysics*, 71 (5), 131-146.

- Brown, E. T., 1970, Modes of failure in jointed rock masses, Proc. Second Cong Int. Soc. Rock Mech., 2, 3-42.
- Brune, J. N., Henyey, T. L., and Roy, R.F., 1969, Heat flow, stress, and rate of slip along the San Andreas Fault, California, J. Geophys. Res., 74, 3821-3827.
- Chang, C., Zoback, M. D. and Khakasar, A., 2004, Rock strength and physical property measurements in sedimentary rocks, paper presented at the 2004 SRB consortium, Stanford, June 21-23.
- Chappell, B. A., 1974, Load distribution and deformational response in discontinua, Geotechnique, 24, 641-654.
- Chery, J., Zoback, M. D. and Hickman, S., 2004, A mechanical model of the San Andreas fault and SAFOD Pilot Hole stress measurements, Geophys. Res. Lett., 31.
- Durrast, H., Rasolofosaon, P. N. J., and Siegesmund, S., 2002, P-wave velocity and permeability distributions of sandstones from a fractured tight gas reservoir, Geophysics, 67, 241-253.
- Donath, F. A., 1964, Strength variations and deformational behavior in anisotropic rock: State of Stress in the Earth's Crust, W. R. Judd, ed., American Elsevier Publishing Co., New York, N. Y., 281-248.
- Goodman, R. E., 1989, Introduction to Rock Mechanics, John Wiley and Sons, 257-280.
- Goodman, R. E., and Shi, G., 1985, Block theory and its application to Rock Engineering, Prentice-Hall Inc.
- Hickman, S. and Zoback, M. D., 2004, Stress orientations and magnitudes in the SAFOD Pilot Hole, Geophys. Res. Lett., 31.
- Hoek, E. and Brown, E. T.: "Practical estimates of rock mass strength", Int. J. Rock Mech. Min. Sci. (1997) 34, 1165-1186.
- Hoek, E. and Brown, E. T., 1980, Empirical strength criterion for rock masses, J. Geotech. Engg. Div., GT9, 1013-1035.
- Hongliang, H. and Ahrens, T. J., 1994, Mechanical properties of shock-damaged rocks, Int. J. Rock Mech. Min. Sci. & Geomech. Abstr., 31, 525-533.
- Hu, K. X. and Huang, Y., 1993, Estimation of the elastic properties of fractured rock masses", Int. J. Rock Mech. Min. Sci. & Geomech. Abstr., 30, 381-394.
- Jaeger, J. C., 1970, Behavior of closely jointed rock, Rock Mech. – Theory and Practice, Proceedings of the Eleventh Symposium on Rock Mechanics, 57-68.
- Jarosinski, M., 1998, Contemporary stress field distortion I the Polish part of the western outer Carpathians and their basement, Tectonophysics, 297, 91-119.
- Lachenbruch, A. H. and Sass, J. H., 1980, Heat flow and energetics of the San Andreas Fault zone, J. Geophys. Res., 85, 6185-6223.
- McLamore, R. and Gray, K. E., 1967, The mechanical behavior of anisotropic sedimentary rocks, J. Engg. for Ind. Trans., ASME, 89, 62-73.

- Moos, D., Peska, P., Finkbeiner, T., and Zoback, M. D., 2003, Comprehensive wellbore stability analysis using quantitative risk assessment, *Jour. Petrol. Sci. and Eng., Spec. Issue on Wellbore Stability*, 38, 97-109.
- Moos, D. and Zoback, M. D., 1999, Feasibility study of the stability of openhole multilaterals, cook inlet, Alaska, SPE Mid-continent Operations Symposium, Oklahoma City, OK, SPE.
- Mount, V. S. and Suppe, J., 1987, State of stress near the San Andreas Fault: Implications for wrench tectonics, *Geology*, 15, 1143-1146.
- Ottesen, S., Zheng, R. H., and McCann, R. C., 1999, Wellbore stability assessment using quantitative risk analysis, SPE/IADC 52864.
- Peska, P. and Zoback, M. D., 1995, Compressive and tensile failure of inclined wellbores and determination of in situ stress and rock strength, *J. Geophys. Res.*, 100(B7), 12791-12811.
- Provost, A. S. and Houston, H., 2003, Stress orientations in northern and central California: Evidence for the evolution of frictional strength along the San Andreas plate boundary system, *J. Geophys. Res.*, 108(B3), 2175.
- Rice, J. R., 1992, Fault stress states, pore pressure distributions, and the weakness of the San Andreas Fault, in *Fault Mechanics and Transport Properties of Rock*, Academic, San Diego, CA, 475-503.
- Thurber, C., Roecker, S., Zhang, H., Baher, S. and Ellsworth, W., 2004, Fine-scale structure of the San Andreas Fault zone and location of the SAFOD target earthquakes, *Geophys. Res. Lett.*, 31.
- Townend, J. and Zoback, M. D., 2004, Regional tectonic stress near the San Andreas fault in central and southern California”, *Geophys. Res. Lett.*, 31.
- Unsworth, M. and Bedrosian, P. A., 2004, Electrical resistivity structure at the SAFOD site from magnetotelluric exploration, *Geophys. Res. Lett.*, 31.
- Zoback, M. D., 2006, SAFOD penetrates the San Andreas Fault, *Scientific Drilling*, 2, 32-33.
- Zoback, M. D. et al., 1987, New evidence on the state of stress of the San Andreas fault system, *Science*, 238, 1105-1111.
- Zoback, M. D., Barton, C., Brudy, M., Castillo, D., Finkbeiner, T., Grollmund, B., Moos, D., Peska, P., Ward, C., and Wiprut, D., 1998, Determination of stress orientation and magnitude and magnitude in deep wells, *J. Rock Mech. Min. Sci. Geomech. Abstr.*, 40, 1049-1076.



## Chapter 3

# **GEOMECHANICAL MODELING, PETROPHYSICS, AND WELL SCALE ANALYSIS OF A FIELD IN THE TIMOR SEA**

*Part of this chapter was written as a paper with Mark Zoback and Peter Hennings, and has been accepted by SPE (SPE 110542)*

### **3.1 Abstract**

In this chapter we estimate stress orientations and magnitudes at several well locations and analyze fractures at the well scale for a field in the Timor Sea. In this field, production data does not match with the fluid flow simulation response from a classical reservoir model. Production history suggested that the mismatch between actual production and model prediction was due to fracture flow, which was not included in the model. The objective of the study is to find the role of fractures and stress heterogeneity at the well scale on fluid production from the field, which was initially considered as a matrix dominated reservoir. Image logs show that stress orientations are homogenous at the field scale with a maximum horizontal stress

orientation of NE-SW, which is consistent with regional stress orientations from the world stress map. The magnitude of principal stresses (minimum horizontal stress from leak off tests, overburden stress from density log, and maximum horizontal stress from frictional faulting theory) indicates a homogenous strike-slip/normal faulting stress regime in the reservoir. Observed fracture zones in wells are mostly associated with well scale fault and bed boundaries. These zones do not show any anomaly in production logs and well test data, because most of the fractures are not optimally oriented to the present day stress state, and matrix permeability is high enough to mask any small anomaly from the fracture zones. However, fracture density along the wells is inversely related to distance from the nearest reservoir scale fault, indicating high fracture density zones close to these faults, which is consistent with the preferred flow direction indicated by interference and tracer test done between the wells.

### **3.2 Introduction**

Fractures present both problems and opportunities for exploration and production from hydrocarbon reservoirs. The heterogeneity and complexity of fluid flow paths in fractured rocks always makes it difficult to predict how to optimally produce a fractured reservoir. It is usually not possible to define the geometry of the fractures and faults controlling flow and it is difficult to integrate data from markedly different scales associated with faults mapped in seismic surveys and those seen in wellbore image logs.

Several studies (Luthi and Souhaite, 1990; Luthi, 1990; Pezard and Luthi, 1988; Plumb and Luthi, 1986) show characterizations of fractures and wellbore features from wellbore images. Studies by Barton and Zoback (2003) and Barton et al. (1988) suggest that stress orientations in the present day stress field can be identified by analyzing features in wellbore images such as breakouts and tensile fractures. Additionally it is shown that fluid conductivity at the well scale from the temperature and the production logs indicates fluid flow from critically stressed fractures (Barton and Zoback, 1994; Barton et al., 1995; Townsend and Zoback, 2000), indicating the link

between geomechanics and fluid flow. A number of studies in hydrology and the petroleum industry deal with the modeling of fractured reservoirs by integrating multiscale data (Martel and Peterson, 1991; Lee et al, 2001; Long and Billaux, 1987; Gringarten, 1997; Srivastava, 2002). The work by Smart et al. (2001), Oda (1985, 1986), Maerten et al. (2002), Bourne and Willemse (2001), and Brown and Bruhn (1998) quantify the stress sensitivity of fractured reservoirs. Additional studies emphasize the importance and challenges of coupling geomechanics in reservoir fluid flow (Chen and Teufel, 2000; Couples et al., 2003; Bourne et al., 2000). These studies found that geomechanical effects may be very significant in some of the fractured reservoirs and well scale analysis may play an important role to create the link between fracture distribution, geomechanics and fluid flow in the reservoir.

In this chapter, we estimate stress orientation and magnitude at well locations and build a geomechanical framework of the study area in the Timor Sea. Also, we discuss the petrophysical model of the reservoir section and analyze fractures at the well scale to find their contribution in fluid production. To estimate stress orientation and fracture distribution, we analyzed image logs and calibrated log derived rock strength with lab measurements. Then we used density logs, leak-off tests, and frictional faulting theory to define the present day stress state in the reservoir. We analyzed production logs, core permeability measurements, and well test models to define the relationship between fluid flow and fracture units at well scale and then studied the fracture units under the present day stress field to project the role of geomechanics in fluid flow. We found that well scale fracture units do not show any production anomaly with respect to matrix section but fracture density increases towards the reservoir scale fault.

### **3.3 Regional tectonic setting around the study area**

The chosen field area (CS) is located in the Timor gap between Australia and Indonesia (Fig. 3.1). The field is located on a structural high, which separates regional scale synclinal features with a NNW trend. Regional scale extensional faulting created

many E-W oriented tilted fault blocks, horsts and half-grabens, including the high structure of the field.

Fig. 3.1 shows that the maximum horizontal stress ( $S_{Hmax}$ ) in the region is oriented NE-SW direction (Reinecker et al, 2004). The regional stress orientation appears to be guided by major strike slip-extensional faults striking in NE-SW direction. Thrust faulting locations (Blue dots) on the map represent the Timor trough, which is oriented in NE-SW direction.

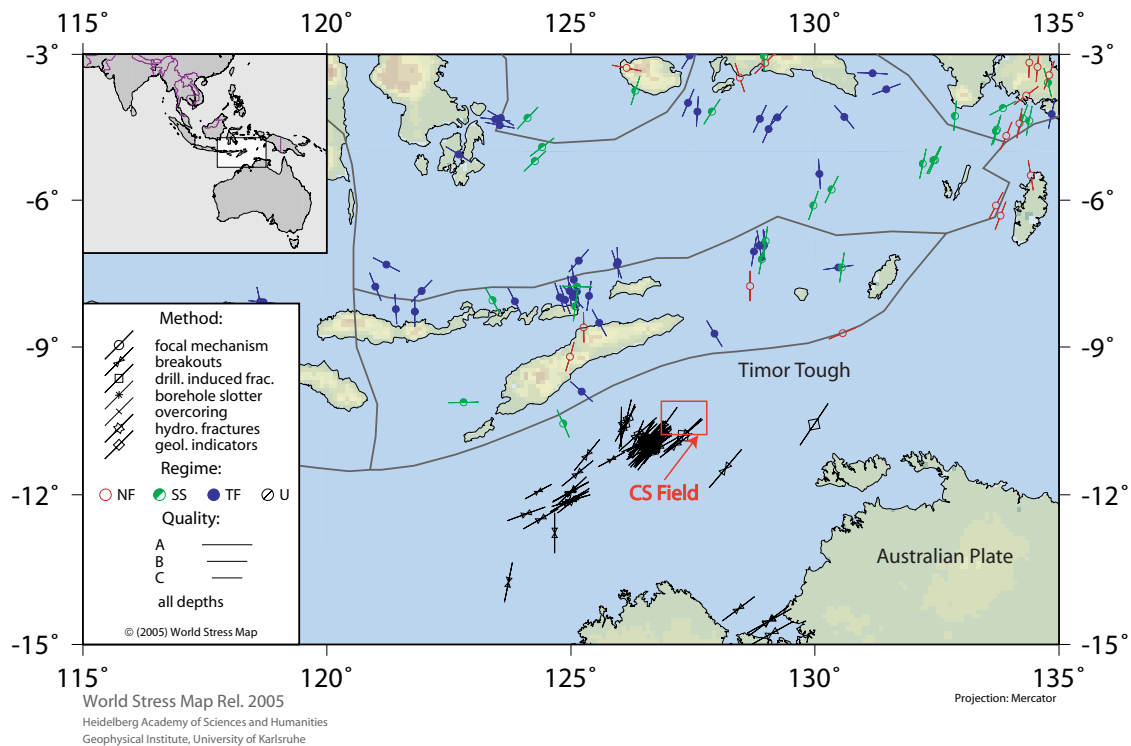


Fig. 3.1: Regional tectonic and location map of the study area (World Stress Map, Reinecker et al, 2004).

### 3.3.1 Stress variations within the study area

Fig. 3.2 shows a structural map of the CS field, which has a number of large, reservoir scale faults striking in E-W direction. Seismic data show normal slip amounts as large as ~300m on some of these faults, some of which extend up to surface as shown in seismic line A-B (Fig. 3.3). These faults form horsts and half-graben structures extending in N-S direction. Seismic data and the structural map (Fig. 3.2)

also show several small scale faults with N-S orientation. These faults have smaller slip and do not appear to extend to depths shallower than the reservoir. Regional tectonic studies indicate that the E-W oriented faults are strike-slip/normal faults. The reddish region in Fig. 3.2 indicates the main reservoir, which is a horst structure in between two half-grabens. This map also shows locations of the exploratory wells (CSB1, CSB2, CSB3, CSB4, CSU1, CSU2, CSU3, CSU4, CSF1, CST1 and CSH1), production wells (P1, P2, P3, P4, P5, P6, P7 and P8), and injection wells (I1, I2, I3 and I4) in the field. The exploration wells are all near vertical (the maximum deviation is ~5deg) while production and injection wells are deviated up to ~45deg.

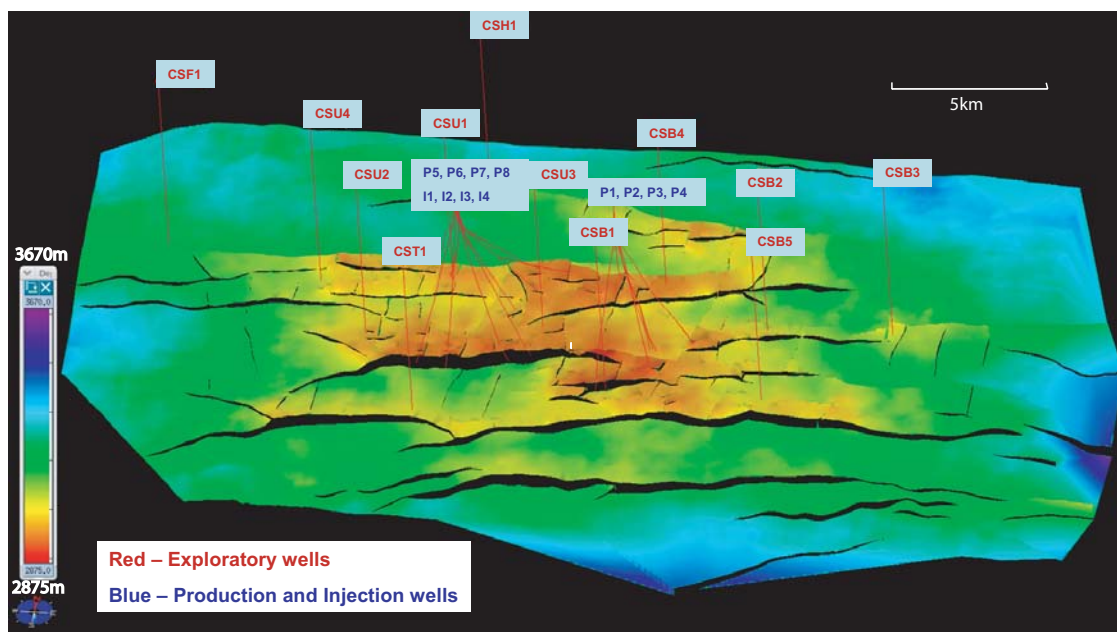


Fig. 3.2: Structural map of the CS field showing exploratory, production and injection well locations along with field scale faults. Red color indicates the shallowest points and blue color indicates the deepest points. Line AB indicates trace of seismic line shown in Fig. 3.3 (modified from a ConocoPhillips internal report, 2003).

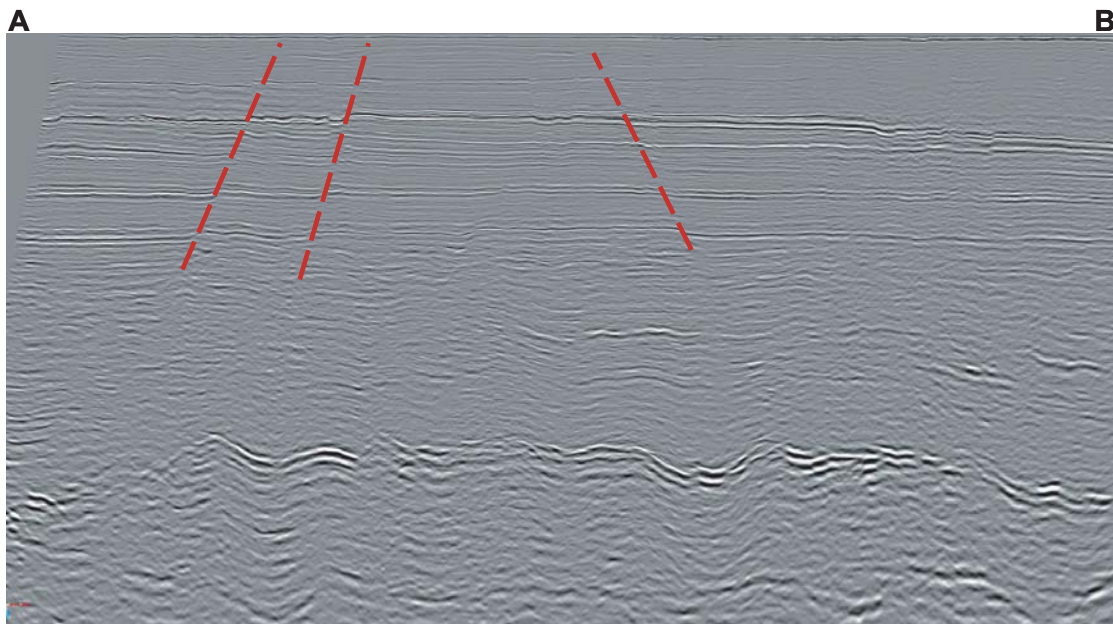


Fig. 3.3: Dip line section (AB) of the CS field shows that the large faults striking in ENE direction are extended up to surface (modified from a ConocoPhillips internal report, 2003).

Wellbore resistivity images and dual arm calipers from the CS field show drilling-induced tensile fractures and breakouts within the reservoir section. Fig. 3.4 shows a qualitative diagram of stress related features within a vertical borehole. Tensile fractures form when the hoop stresses equal the tensile strength of the rock and indicate the direction of the maximum horizontal compressive stress ( $S_{Hmax}$ ) (Brudy and Zoback, 1999; Zoback et al, 1985). Breakouts occur when the hoop stress exceeds the compressive strength of the rock and indicates the direction of the minimum horizontal compressive stress ( $S_{Hmin}$ ) (Bell and Gough, 1979). Four arm mechanical calipers tend to orient themselves in the direction of maximum and minimum hole size so unequal calipers often indicate breakout orientation.

Fig. 3.5 shows rose diagrams of the orientations of tensile cracks and breakouts within the reservoir section of the CS field. Analysis from all exploratory wells shows breakouts in an NW-SE orientation with  $\sim 30-70$ deg breakout widths and tensile fractures in an orthogonal (NE-SW) direction, thus giving the orientation of the present day  $S_{Hmax}$  (Fig. 3.5). This observation is consistent with the regional maximum horizontal stress orientation found by Castillo et al.(1999).  $S_{Hmax}$  orientation is quite

similar at all of the well locations around the field but varies with depth near some of the well-scale faults and bed boundaries.

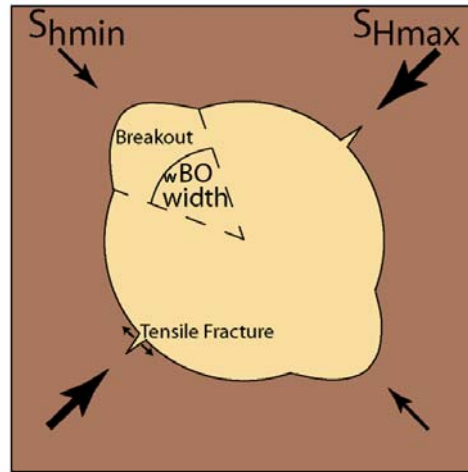


Fig. 3.4: In a vertical well, tensile fractures indicate the direction of  $S_{Hmax}$  and breakouts indicate direction of  $S_{Hmin}$ . The width of breakouts depends on stress magnitude and rock strength.

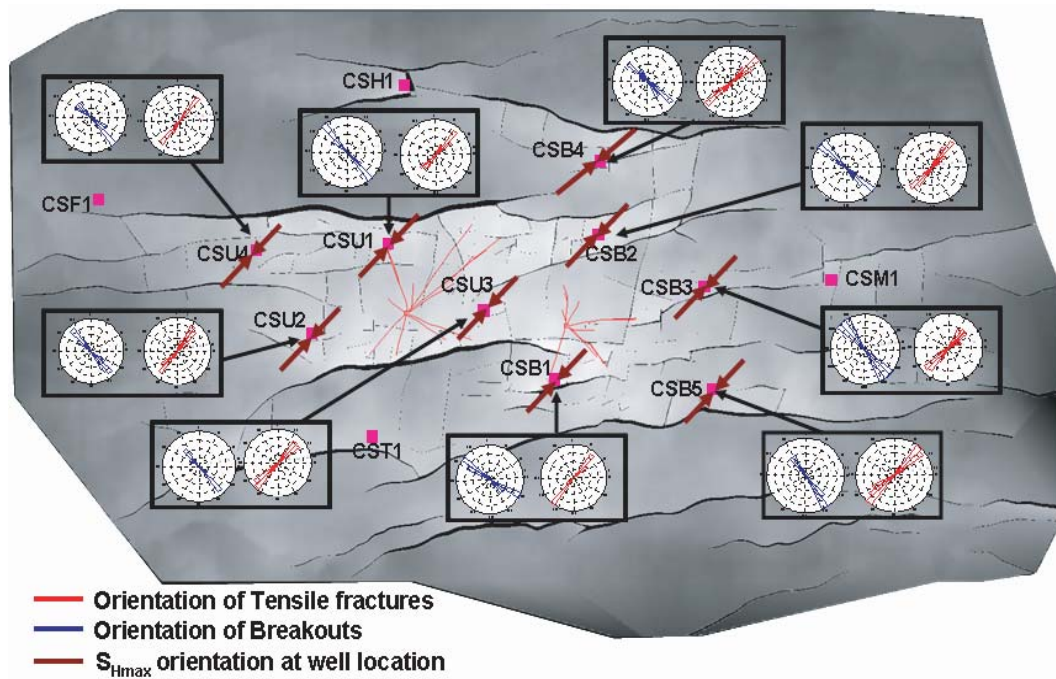


Fig. 3.5: Stress-induced wellbore breakouts and tensile wall fractures in the CS field consistently show a NE-SW direction of the maximum horizontal principal stress,  $S_{Hmax}$ . This direction is similar to the regional stress orientation as shown in the World Stress Map.

### 3.4 Rock strength and petrophysical properties of the reservoir

Logs from the well CSU2 (Fig. 3.6) show that the reservoir section is separated into two parts by an unconformity. The upper section, Formation-1, is comprised largely of sandstone with alternating mudstone and siltstone beds. Sandstone layers show a coarsening upward profile and are occasionally bio-turbated. Mudstones contain modular pyrite and siderite nodules and are occasionally laminated and bio-turbated. The lower section, Formation-2, is composed predominantly of sandstone with alternating mudstone layers. Log response indicates sandstones as high energy deposit with occasional to no bio-turbation. Both the formations are from a fluvial-deltaic dominated depositional environment and have porosity of ~10-15%. These formations also show cross-bedding, faulting and occasional natural fractures. Borehole images show low fracture density in the exploratory wells. The reservoirs have mostly matrix dominated porosity and permeability. Average reservoir permeability is ~100-200mD but core and log measurements show permeability up to ~1200mD in places, which correlates with production logs and well tests from those intervals. More about the nature of fractures and their role to guide fluid flow will be discussed in the fracture analysis section.

Dual caliper measurements (Fig. 3.6) and core samples from Formation-1 and 2 suggest that while the sandstones are fairly strong, fractures in the samples sometimes act as planes of weakness that decrease the strength. Triaxial and unconfined strength (UCS) measurements on the core samples from well, CSU2, at Formation-1 (Castillo et al., 1999) are used to calibrate a log derived rock strengths. Fig. 3.7 shows the results of laboratory tests from four different samples of Formation-1. It appears that both UCS and internal friction ( $\mu$ ) vary in these samples. Samples from MD 3065m and 3128m show an average UCS value of ~75MPa while samples from MD 3085m and 3092m, which are more shaly, show a relatively lower average value of ~65MPa.

We represent the continuous rock strength for the sandstone intervals of Formation-1 using the empirical UCS model proposed by McNally (1987) using the



core UCS values. Eq. 3.1 represents the normalized rock strength model for the sand intervals of Formation-1.

$$UCS = 1000 * \exp(-0.037\Delta t) \quad (3.1)$$

where UCS is in MPa and  $\Delta t$  is fluid-substituted compressional slowness in  $\mu\text{s}/\text{ft}$ . This model can be also used to represent rock strength for the sand intervals of Formation-2 because the two formations show similar wellbore failure in image and caliper logs, while drilling with similar mud weights.

Shale sections within Formation-1 and Formation-2 can be considered strong and compacted because we do not see major breakouts in the caliper data. We define the UCS of shaly intervals by the power law using the dynamic Young's modulus ( $E$ ) as proposed by Castillo et al. (1999). However, because most of the wells do not have S-wave measurements, we also define the shaly-sand UCS with only P-wave slowness, which is done by normalizing the power law model proposed by Horsrud (2001) with the core data from the shaly intervals. Eqs. 3.2 (using  $E$ ) and 3.3 (using  $\Delta t$ ) represent normalized rock strength models using lab rock strength measurements from shaly intervals.

$$UCS = 0.0011 * E^{0.712} \quad (3.2)$$

$$UCS = 1.55 * (304.8 / \Delta t)^{2.6} \quad (3.3)$$

where UCS and  $E$  are in MPa, and  $\Delta t$  is in  $\mu\text{s}/\text{ft}$ . Continuous UCS values for both sand and shaly intervals along with core UCS values are shown in the right most column of Fig. 3.6.

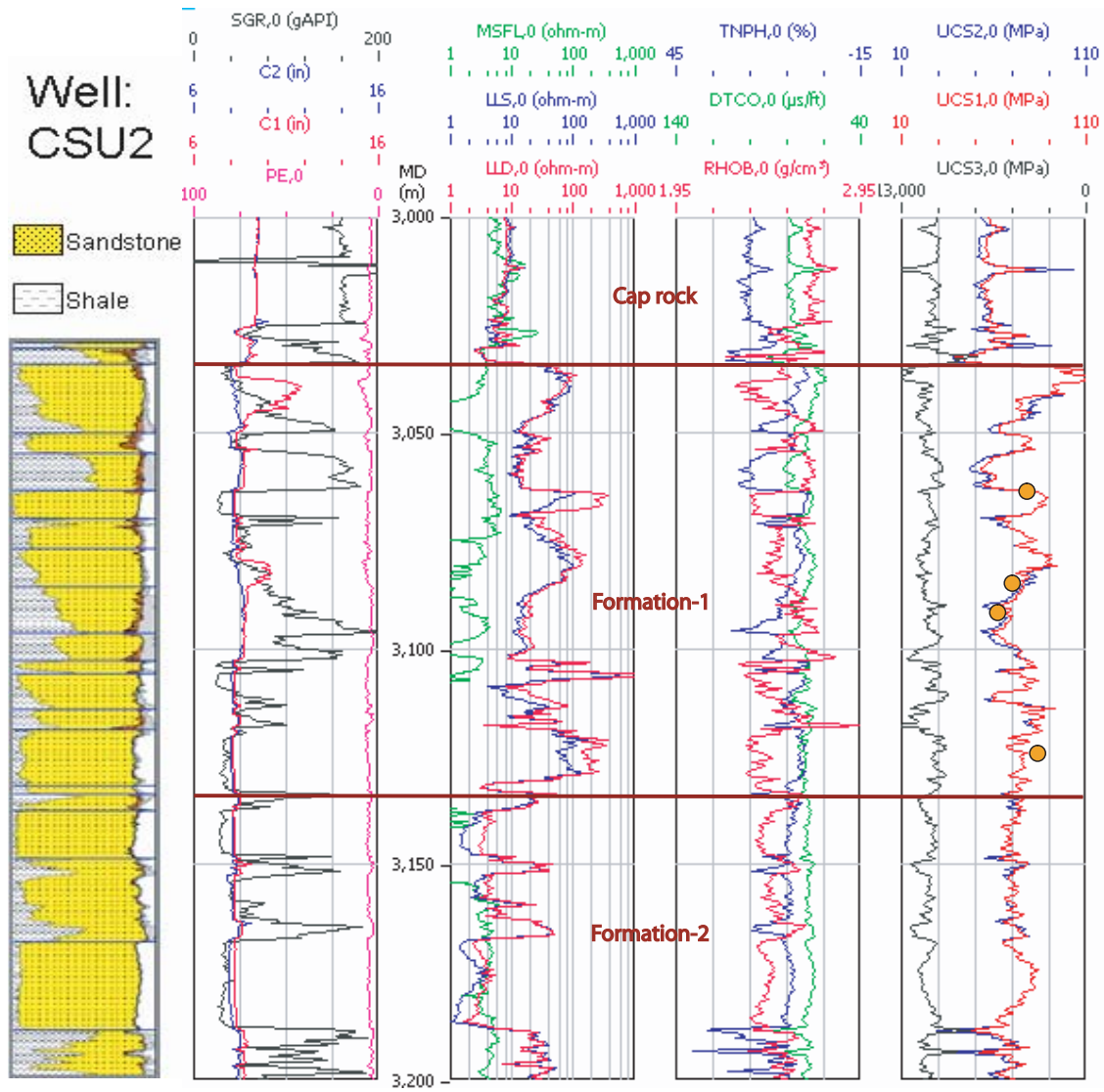


Fig. 3.6: Lithology of formation section for the well - CSU2: Column1; GR(Gamma Ray), C1(Caliper 1), C2 (caliper 2), PE Photoelectric Factor): Column 2; Measured depth: Column 3; LLD (Deep Resistivity), LLS (Shallow Resistivity), MSFL (Micro Shallow Resistivity): Column 4; RHO(Bulk Density), TNPH (Thermal Neutron Porosity), DTCO (Compressional Slowness): Column 5; Impedance, UCS1 (uses 'E' model-Equation 3 for shaly intervals), UCS2 (uses Δt model-Equation 4 for shaly intervals), Core UCS (dots): Column 6.

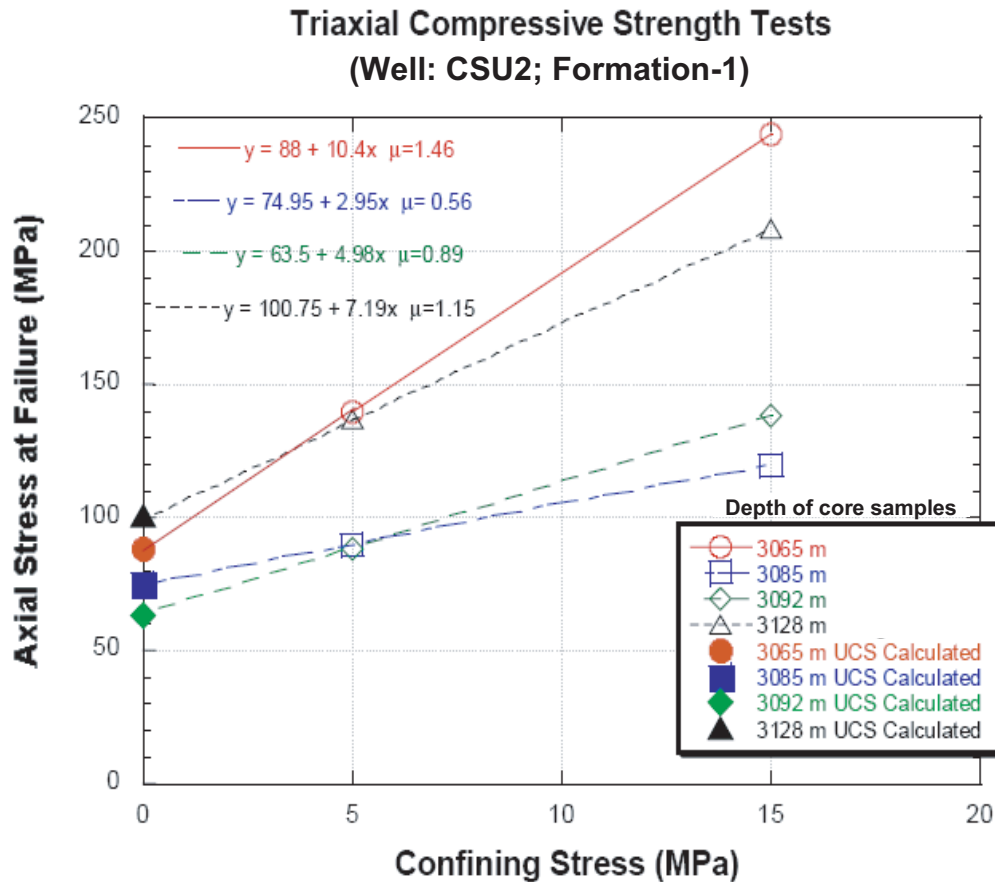


Fig. 3.7: Confining stress versus axial stress at failure for core samples from Formation-1 (modified from a ConocoPhillips internal report, 2003).

### 3.5 Stress magnitudes

Following Zoback et al. (2003) we use frictional faulting theory to constrain magnitudes of the horizontal principal stresses ( $S_{Hmax}$  and  $S_{Hmin}$ ) and the vertical stress ( $S_v$ ). The vertical stress ( $S_v$ ) is estimated by integrating bulk density log at well locations. Only well CSH1 has a density log going up to the surface. The missing density data above the reservoir section in other wells was approximated by an exponential function, which follows the trend of bulk density in the reservoir section and decreases steeply at sections above 304m. We find that in the reservoir section,  $S_v$  is  $\sim 72.2$ MPa at 3170m depth, and the overburden gradient is  $\sim 2.34SG$  (19.47ppg or 0.02277MPa/m).

Direct measurements of pore pressure in the reservoir section across the CS field indicate a hydrostatic pore pressure ( $P_p$ ) gradient of  $\sim 1.04SG$  (8.66ppg or 0.01013MPa/m). Sonic log and other measurements do not indicate any overpressure zones in the section above the reservoir, so we assume a hydrostatic pore pressure for the entire section.

In situ least principal stress ( $S_3$ ) was estimated using extended leak-off tests (XLOT), leak-off tests (LOT), and pressure while drilling (PWD) data. An XLOT gives the fluid pressure required to open and propagate a fracture. It also gives the fracture closure pressure. LOT indicates the initiation pressure for fracture, and hence can be used to approximate  $S_3$ . PWD data can be used to constrain  $S_3$  by measuring the equivalent circular density (ECD) at the time of fluid loss. Among the above measurements, XLOT gives the most reliable estimate of  $S_3$ . We analyze XLOTs measurements of well, CSP2, at true vertical depths  $\sim 1926m$  (MD $\sim 2078m$ ) and  $\sim 2971m$  (MD $\sim 3315m$ ) to estimate  $S_3$ . At  $\sim 1926m$  depth, second and third cycles of XLOT (Fig. 3.8) show a fracture closure pressure of  $\sim 785psi$  (5.41MPa), which gives a  $S_3$  gradient of  $\sim 1.65SG$  (13.7ppg or 0.01602MPa/m). At  $\sim 2971m$  depth, the fracture closure pressure from second and third cycles is approximately  $\sim 2018psi$  (13.91 MPa), which gives  $S_3$  gradient  $\sim 1.61SG$  (13.4ppg or 0.01567MPa/m) (Fig. 3.9). Pressure tests done on other parts of the field show similar  $S_3$  gradients as illustrated in Fig. 3.11.

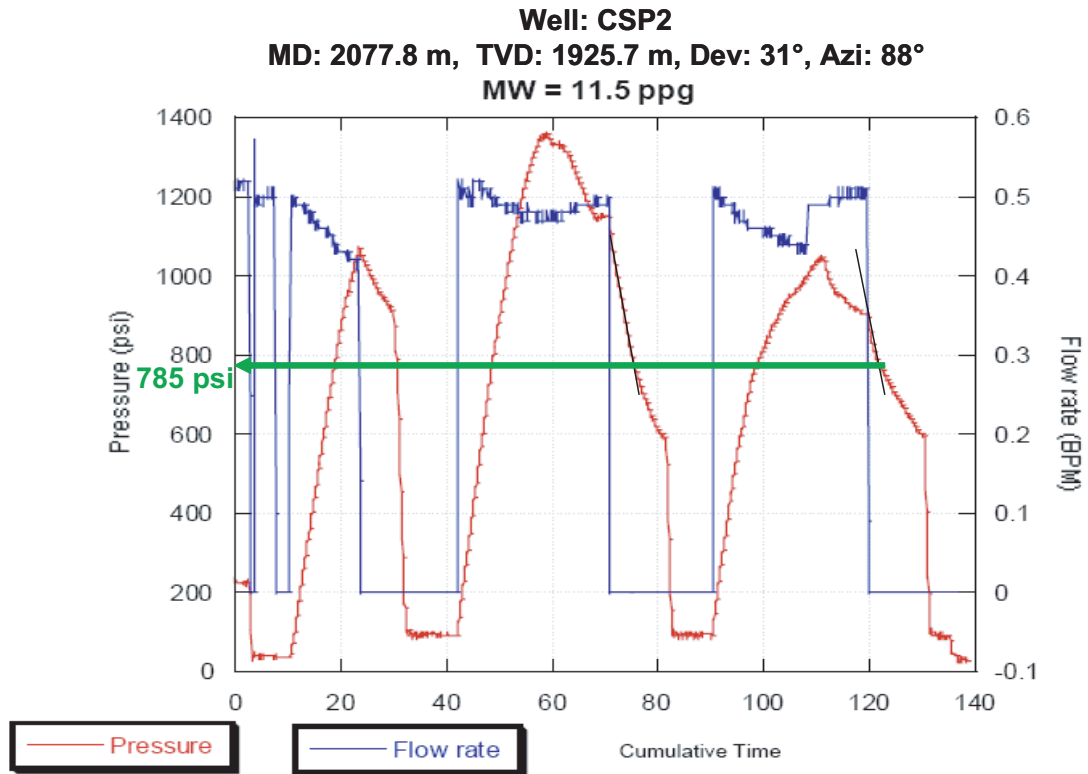


Fig. 3.8: In well CSP2, XLOT shows a fracture closure pressure of ~785 psi at 2078m MD, which gives  $S_3$  gradient of 1.65 SG (~ 13.7 ppg).

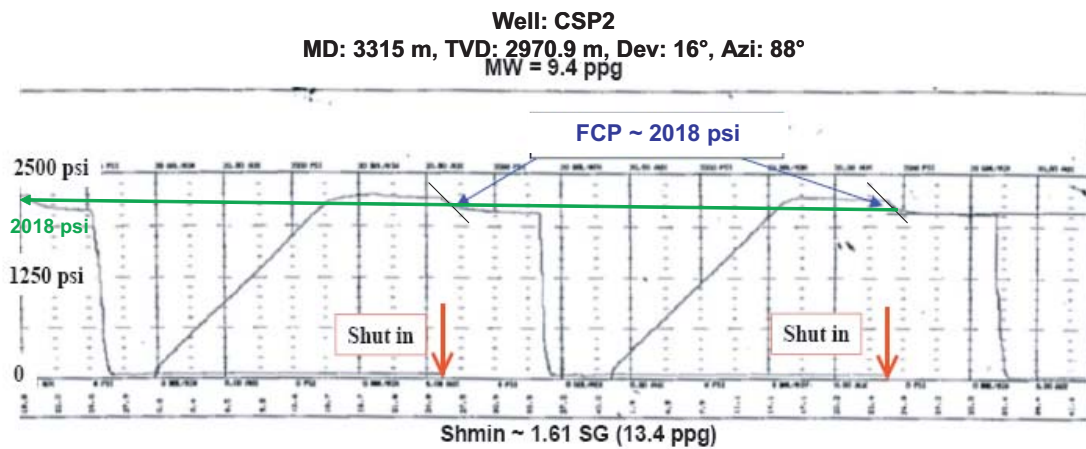


Fig. 3.9: XLOT shows a fracture closure pressure of ~2018 psi at 3315m MD in well CSP2.  $S_3$  gradient at this depth is ~ 1.61 SG (~ 13.4 ppg).

In the final step of the stress analysis, we estimate a magnitude of the maximum horizontal stress ( $S_{Hmax}$ ) using the stress polygon technique proposed by Moos and Zoback (1990), where each stress polygon indicates the range of permissible stress magnitudes based on Coulomb frictional faulting theory. The boundaries of the polygon constrain the conditions on which rock fails as a function of maximum ( $S_1$ ) and minimum ( $S_3$ ) principal stresses, pore pressure ( $P_p$ ), and coefficient of sliding friction,  $\mu$ . Eq. 3.4 represents the relationship between  $S_1$ ,  $S_3$ ,  $P_p$  and  $\mu$  (Jaeger and Cook, 1979).

$$\frac{\sigma_1}{\sigma_3} = \frac{S_1 - P_p}{S_3 - P_p} = (\sqrt{\mu^2 + 1} + \mu)^2 \quad (3.4)$$

Anderson's faulting theory classifies the combination of principal stresses ( $S_1$ ,  $S_2$ ,  $S_3$ ) as either Normal Faulting (NF):  $S_v < S_{Hmax} < S_{hmin}$ , Reverse Faulting (RF):  $S_{Hmax} < S_{hmin} < S_v$ , or Strike Slip (SS):  $S_{Hmax} < S_v < S_{hmin}$ . The width of breakouts depends on the stress magnitudes and rock strength (UCS). Hence, if the rock strength is known, then the breakout width indicates the magnitude of  $S_{Hmax}$  (Zoback et al, 2003). Other parameters required for the modeling are hole geometry, mud weight, sliding friction, Biot coefficient and Poisson's ratio. Breakout width, observed values of  $S_{Hmax}$  azimuth, and estimated UCS values give the range of  $S_{Hmax}$  magnitude.

Fig. 3.10 represents the stress polygon with full range of permissible  $S_{Hmax}$  gradient at TVD ~3063m in Formation-1. The presence of breakouts in Formation-1 indicates that  $S_{Hmax}$  is higher than the UCS, ~72MPa, which gives a lower bound of  $S_{Hmax}$  gradient of ~2.52SG (21ppg or 0.02456MPa/m) in the sand intervals. After including the effect of shaly sand intervals and also the previously estimated  $S_{hmin}$  magnitude, we define the range of  $S_{Hmax}$  gradient as ~21±2ppg. Formation-2 breakouts are similar in nature to Formation-1 breakouts, so a reasonable approximation is to assume similar stress gradient for both the formations.

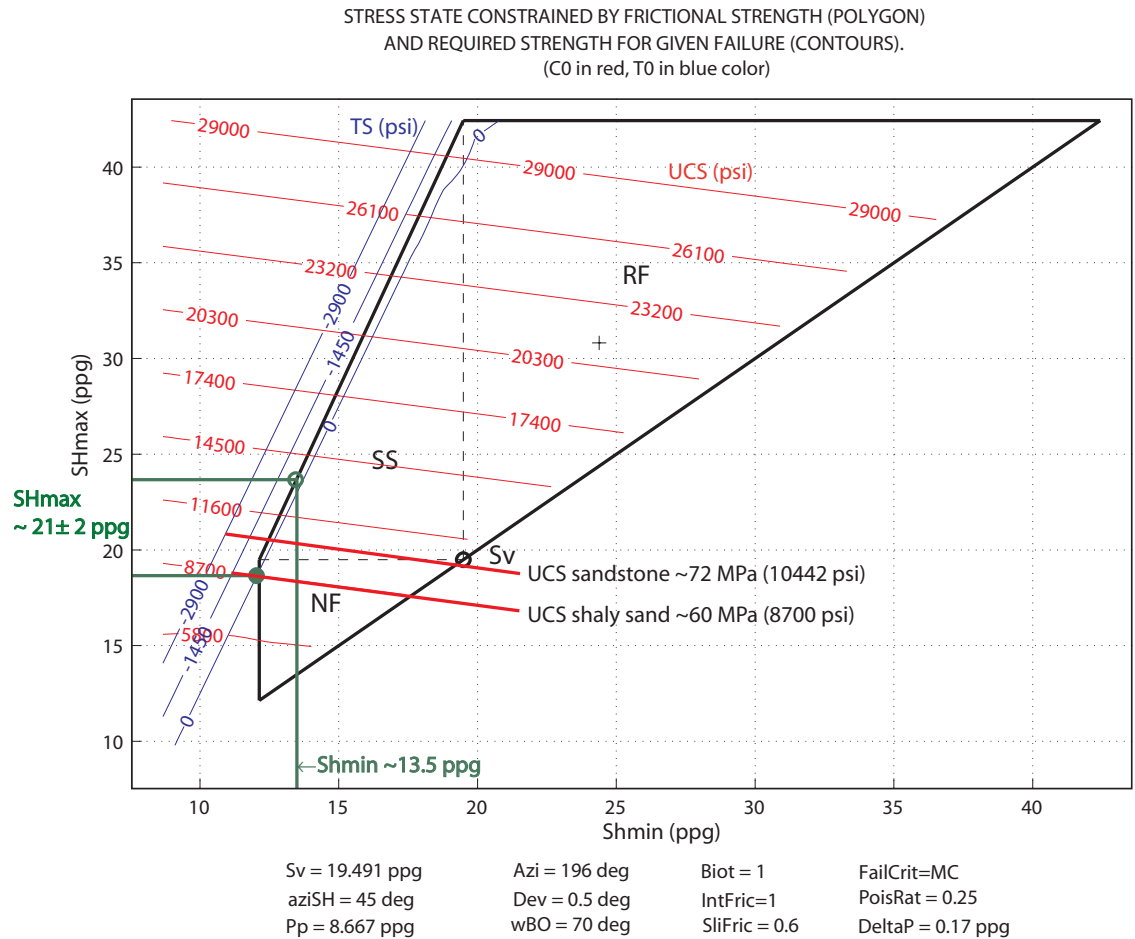


Fig. 3.10: Based on the estimates of  $S_{hmin}$  from XLOT,  $S_v$  from density log and estimated UCS for the Formation 1, the estimated  $S_{Hmax}$  gradient is  $\sim 21 \pm 2 \text{ ppg}$  for well CSU2.

Fig. 3.11 shows the principal stress magnitudes estimated from different parts of the field, indicating a strike-slip faulting regime. However, the stress state in shaly sections or weaker sections where  $S_v$  magnitude is close to the  $S_{Hmax}$  magnitude gives a strike-slip/normal faulting environment ( $S_{Hmax} \geq S_v > S_{hmin}$ ) at reservoir depths, which is consistent with the geological history of the field area.

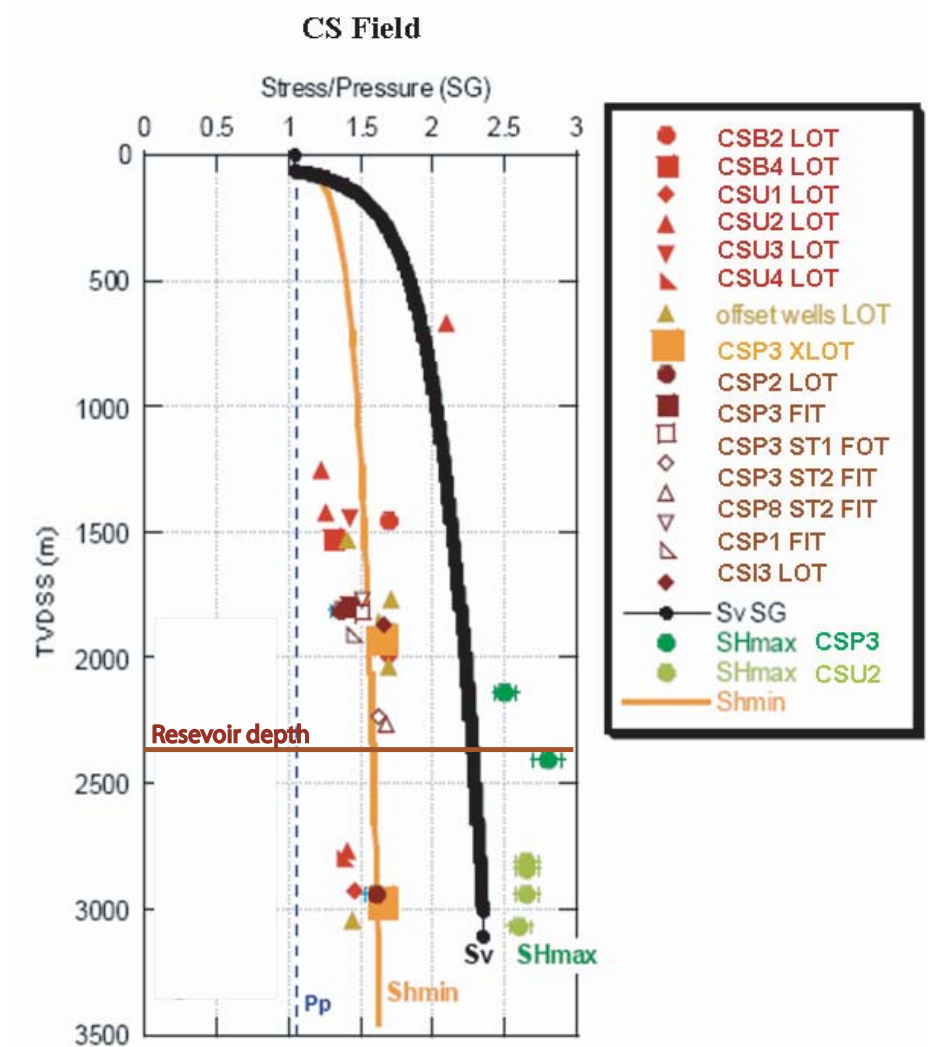


Fig. 3.11: Present day stress profiles ( $S_v$  gradient  $\sim 22.7$  kPa/m,  $S_{Hmax}$  gradient  $\sim 24.5$  kPa/m, and  $S_{Hmin} \sim 15.6$  kPa/m) and pore pressure profile ( $P_p \sim 10.1$  kPa/m) at reservoir depth of the CS field. Note that the data indicate a Strike-Slip faulting regime. (modified from a ConocoPhillips Internal Report, 2003).

### 3.6 Fracture analysis at well scale

In this section, we analyze the geometry of the fractures from the wellbore resistivity images and correlate their flow properties using production logs and well test data. Image logs show sets of bedding planes in the sandstone formations, and drilling enhanced fractures and laminations in the shaly layers. Fig. 3.12 shows a core photograph from well CSB2 with some bedding planes and high dip angle (near vertical) fractures. Natural fractures are not prominent in the image logs of any of the



eight exploratory wells of the field. The possible reasons for low fracture density in the image logs are: 1) actual fracture density is very low, 2) fractures have high dip angle (near vertical) and probability of mapping a high angle fracture using an image log of a vertical well is very low, and 3) the image quality in some wells is poor.

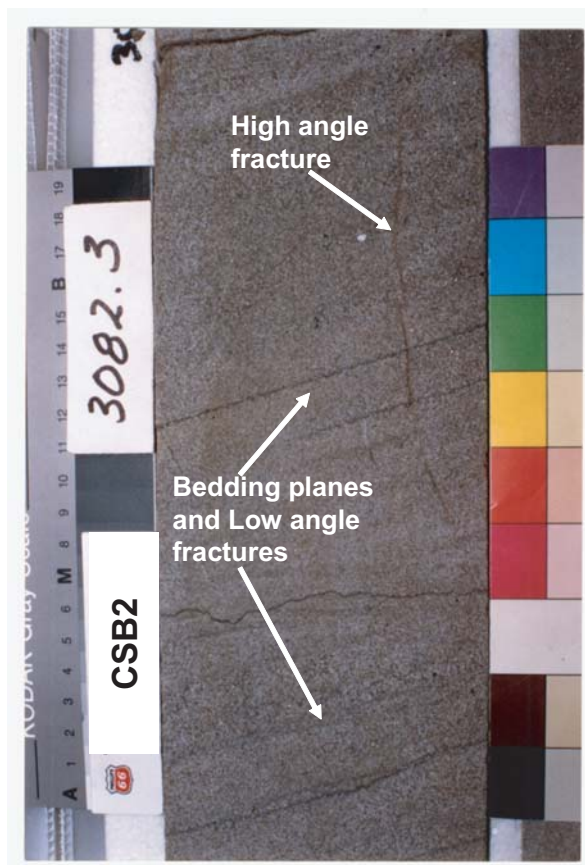


Fig. 3.12: Core image from well CSB2 shows high angle fractures, which are not visible in image logs.

The fractures that we do observe in the wells are associated with well scale faults and bed boundaries. Observed rotations of the stress field associated with these fractured zones indicate shearing of some faults in the current stress field. Among all the exploratory wells, well CSU2 shows a relatively large fractured/damage zone in the reservoir section, which may be considered as the best zone to effectively represent fluid flow properties through the well scale faults and fractures. Fig. 3.13 (right column) shows the wellbore resistivity image of the fracture zone from well CSU2. The red curve is a possible well scale fault, which separates high angle fractures from

low angle fractures. The left column of Fig. 3.13 indicates rotation in  $S_{Hmax}$  orientation just above the fractured zone. The stereographic plot in Fig. 3.14 shows that fractures and faults are generally south dipping in well CSU2.

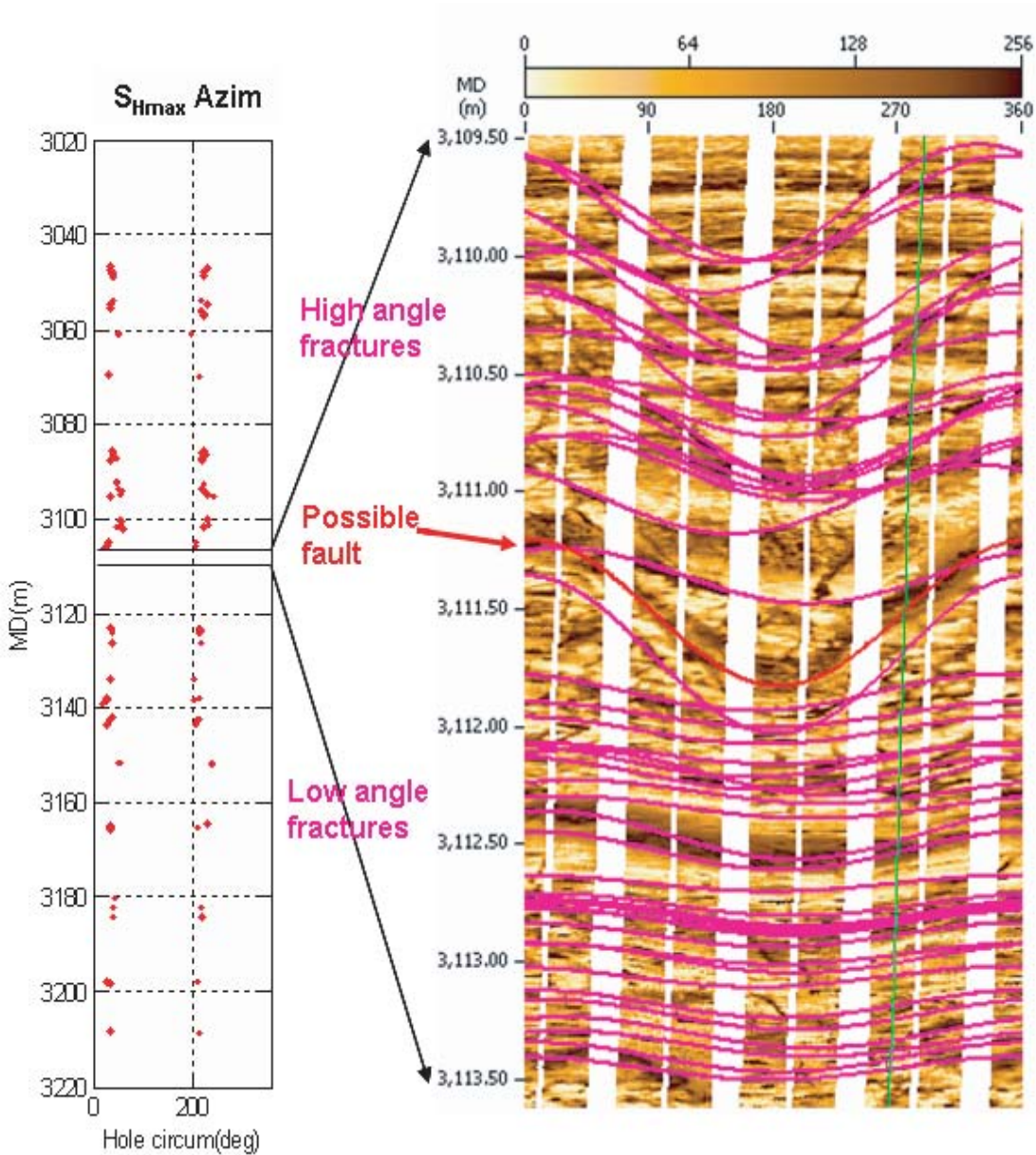


Fig. 3.13: The highest density fracture zone in well CSU2 shows that a small fault appears to separate high angle fractures from low angle fractures. A change in the observed  $S_{Hmax}$  orientation at the fault zone indicates that some of these fractures are active in the current stress field.

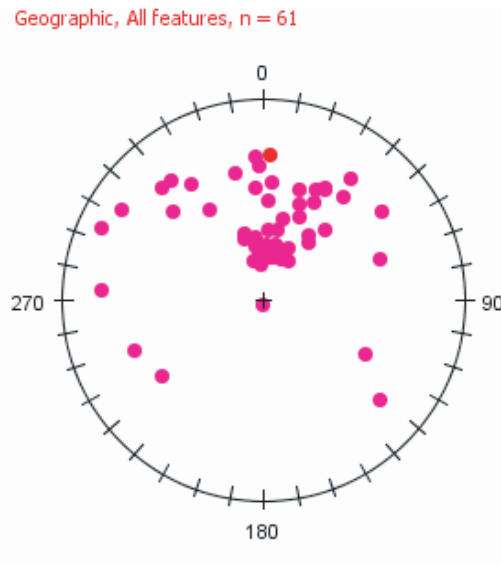


Fig. 3.14: In well CSU2, the stereographic plot shows a southerly dip direction from the fractures picked in the image log.

### 3.7 Fluid flow through the fractured zone

Having completed the stress and fracture analysis, we turn our attention to production and fluid flow in the reservoir. First, we analyze production logs from the reservoir section of the wells to estimate the contribution of the fractured zone in the fluid production. Next, we correlate well test analysis and core permeability to quantify the effect of fracture porosity and permeability in the reservoir flow model. Fig. 3.15 shows the production logs, spinner and gradiometer (column 3), and temperature logs (column 4) with the petrophysical model (column 1) and the fractures (column 2) from the zone shown in Fig. 3.13. In column 5 of Fig. 3.15, we can see core permeability of the fracture zone. Both spinner and temperature logs indicate that most of the fluid enters into the well through intervals 3103-3104.5m, 3105.5-3109m, and 3120-3124m. As predicted by the petrophysical model, these intervals are relatively clean sands with negligible clays. However, fractures are mainly concentrated at interval 3110-3114m, which is a relatively shaly section and do not show any significant contribution in the fluid production. Core measurements indicate a permeability on the order of  $\sim 800$ - $1200$ mD for high producing intervals and  $\sim 200$ mD from the fractured interval. The petrophysical explanations for the low fluid production from the fractured interval are

the presence of clay in the fractured zone and high matrix permeability in the adjacent zones, which may mask the effect of fractures within the entire test zone.

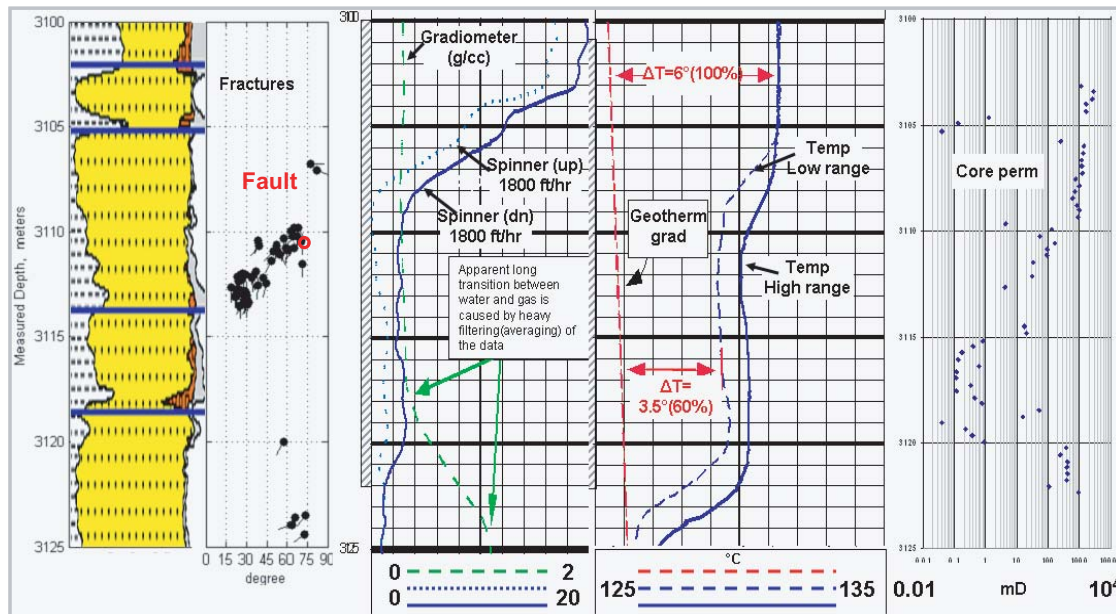


Fig. 3.15: In well CSU2, petrophysical model (column 1), fracture geometries as tadpoles (column 2), production logs, spinner and gradiometer (column 3), temperature logs (column 4), and core permeability (column 5) indicate that most of the fluid entering into the well through intervals 3103-3104.5m, 3105.5-3109m, and 3120-3124m. Fractures are mainly concentrated at interval 3110-3114m but this interval does not show any significant contribution in fluid production.

To determine if fractures are contributing in fluid flow away from the well or not, we also analyzed the well test data from the same interval. Pressure transient analysis of the well test data does not support dual porosity and dual permeability behavior in the reservoir, which again verifies relatively small effect of fractures on the fluid flow. Constraining the well test model with the  $kH$  (where  $k$  is the permeability from core measurements and  $H$  is the thickness of zones using the production logs) ratio of high producing intervals and the rest of the well test interval shows that a dual layered well test model fits the best with the observed pressure transient data (Fig. 3.16). In Fig. 3.16, we see first (green) and second (red) derivatives of observed pressure values with incremental time ( $x$ -axis). Continuous red and white curves on the top of first and second derivative points represent the predicted response of the best fit dual layer model, which has the skin of the higher permeability layer ( $s_1$ ) = -3.31, skin

of the low permeability layer ( $s_2$ ) = -3.06, kH ratio ( $\kappa$ ) = 0.88, storativity ratio ( $\omega$ ) = 0.21, and transmissivity ratio ( $\lambda$ ) =  $3.75 \times 10^{-7}$ . The estimated permeability from the well test model is close to the core permeability. Also, the thickness ratio between high and low production zones is reproduced as the storativity ratio by the well test model. Thus, the results from this exercise verify the inferences from production data analysis shown in Fig. 3.15 that the fluid flow pattern in the reservoir is stratigraphically controlled and the effect of fluid flow through fractures is possibly masked due to high matrix permeability of the reservoir.

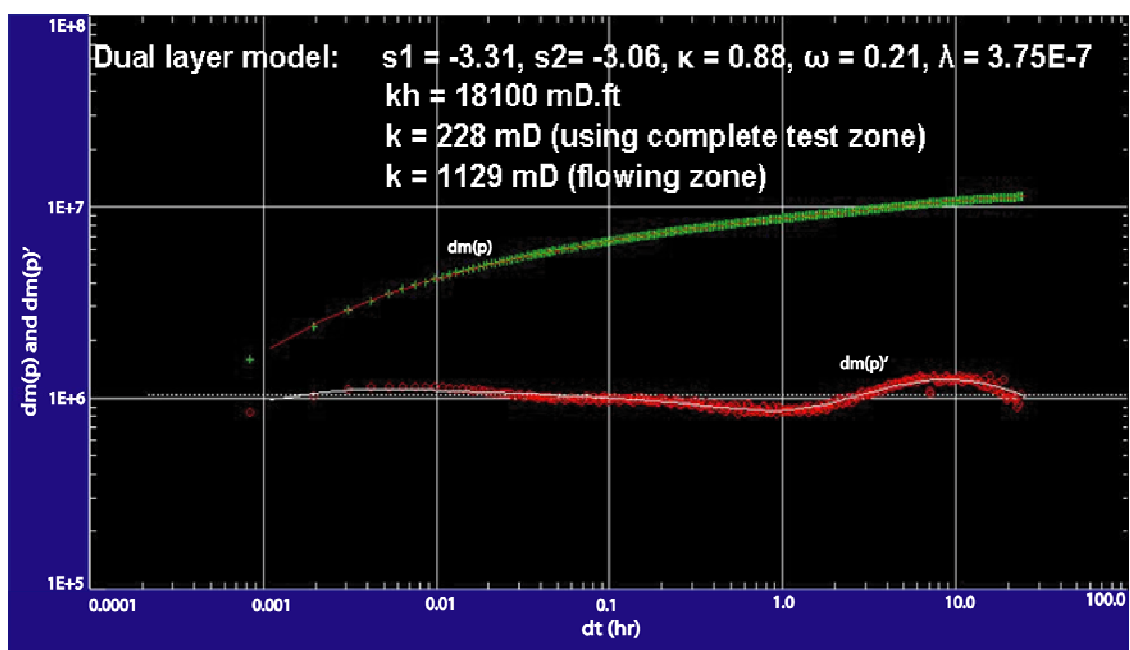


Fig. 3.16: In well CSU2, the dual layered well test model fits best with the observed pressure transient. The estimated permeability from the well test model is close to the core permeability and the thickness ratio between high and low production zones is reproduced as storativity ratio by a dual layer well test model but not by a dual porosity model, which again indicates relatively low production from the fracture system.  $S_1$  and  $S_2$  are the skin values of high and low permeable layers,  $\lambda$  = transmissivity ratio,  $\omega$  = storativity ratio, and  $\kappa$  = kH ratio between high and low permeability layers.

### 3.7.1 Effect of stress in fluid flow and critical stress hypothesis

The laboratory experiments done by Makurat et al. (1990) and Olsson et al. (2001) show changes in transmissivity due to shear dilation and normal closure on fractures. For a fracture system with a multitude of fractures with different orientations and geometries, the actual transmissivities or the changes in transmissivities of the



critically oriented fractures are much higher than the respective parameters of the other fractures (Barton et al., 1995, 1998; Hickman et al., 1998). Critical orientation is defined as the orientation of fractures/faults in which the shear-normal stress ratio on them is sufficient to produce a shear failure or they are above the frictional failure line (red colored fractures in Fig. 3.17a) in the given stress state. Further work by Townend and Zoback (2000) in Cajon Pass, Long Valley and the Nevada test sites confirms the hydraulic conductivity of critically stressed fractures and faults (Fig. 3.17b) in the field. Wiprut and Zoback (2000) find evidence in the Visund oil field, North Sea of gas leakage through critically stressed faults due to increases in pore pressure.

The above studies show that the concept of critically stressed faults and fractures is effective in identifying permeable fractures at well scale. To test if the relatively low fluid production from the fractures of the well CSU2 may also be related to its geometry in the current stress field, we analyze these fractures with respect to the estimated stress and pressure profiles. Fig. 3.18 illustrates the value of Coulomb Failure Function (CFF) on a stereonet (lower hemisphere projection) and classifies the fractures as critically and non-critically stressed fractures. Fracture and faults (shown as poles) in higher CFF range (red color area) are optimally oriented for shear failure in the given stress state. A 3D Mohr diagram indicates the fractures with respect to the frictional failure line. Fractures above the frictional failure line are critically stressed and should add extra permeability to the reservoir matrix permeability. However, we see that only a few fractures from the well CSU2 are optimally oriented for shear failure in the given stress field, which may be one of the explanations why these fractures do not show significant contribution in fluid production comparing to the high permeability matrix sections.

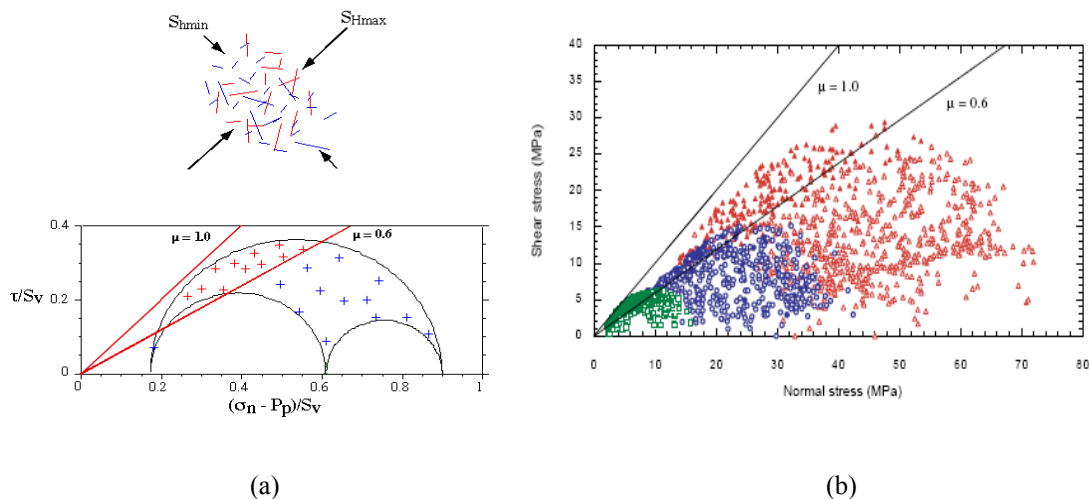


Fig. 3.17: (a) Red colored fractures exceed the frictional strength of the rock and are considered to be critically stressed for the given stress state. (b) Shear and normal stresses on fractures identified with borehole imaging techniques in Cajon Pass (triangles), Long Valley (circles), and Nevada Test site (squares) boreholes show hydraulically conductive fractures and faults (filled symbols) are also critically stressed. (Townend and Zoback, 2000).

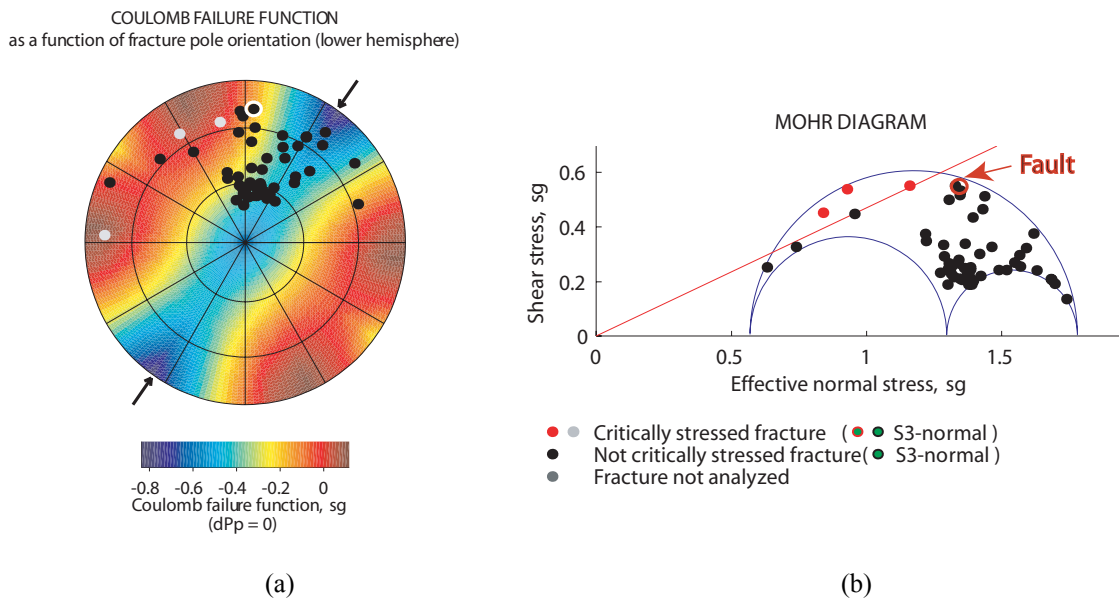


Fig. 3.18: In well CSU2, (a) the stereoplot showing CFF in a lower hemisphere projection indicates optimally oriented zones (dark red color). (b) A 3D Mohr diagram with frictional coefficient line of 0.5 indicates that only a few fractures are in a frictional failure state.

### 3.8 Well scale fracture density and distance from the reservoir scale faults

In the above sections, we argued that the well scale fractures/faults do not significantly contribute to fluid production in a reservoir with high matrix permeability. However, interference tests done between various production and injection wells in the field show preferential flow along the large reservoir scale faults. In this section, we will see the relationship between fracture densities at exploratory well locations versus their distance from the reservoir scale faults. Fig. 3.19 shows the number of fractures observed in the reservoir section of all exploratory wells with respect to the MD (~TVD-exploratory wells are almost vertical). We find that the fracture swarms are correlated with the well scale faults or bed boundaries, and for most of the cases they coincide with the observed rotation in stress orientation. Then, to find a relationship between fracture density and reservoir scale faults, we derive the best fit lines on a fracture versus depth distribution, ignoring the localized fracture swarms. After shifting the best fit lines at a common origin, we see an inverse relation between the slopes of the best fit lines to the distance of the wells from the reservoir scale faults (Fig. 3.20). The plot of the slopes of these lines with respect to the distance from the reservoir scale faults (Fig. 3.21) indicates that the fracture density decreases with the distance from the reservoir scale fault. A logarithmic best fit line gives the quantitative relationship (Eq. 3.5) between the parameters.

$$f_{md} = -0.294 \ln(d) + 2.3612 \quad (3.5)$$

where  $f_{md}$  is number of fractures/MD and  $d$  is distance from the reservoir scale fault in meters. Eq. 3.5 gives a fracture density value of approximately 2 fractures/m at a distance close to the reservoir scale faults, which is an order of magnitude higher than fracture density away (>1000 m) from the faults. However, most of the exploration wells are far from the reservoir scale faults. The closest exploration well (CSB1) is ~200m away from the fault, which makes it difficult to infer the fracture density at the damage zones very close to the fault. The small number of fractures in some wells and



the limited numbers of wells suggest using this relationship (Eq. 3.5) with extreme caution. Thus, to estimate the fracture density in the damage zones associated with the fault, we propose to use geomechanically-constrained models, which are discussed in the next chapter.

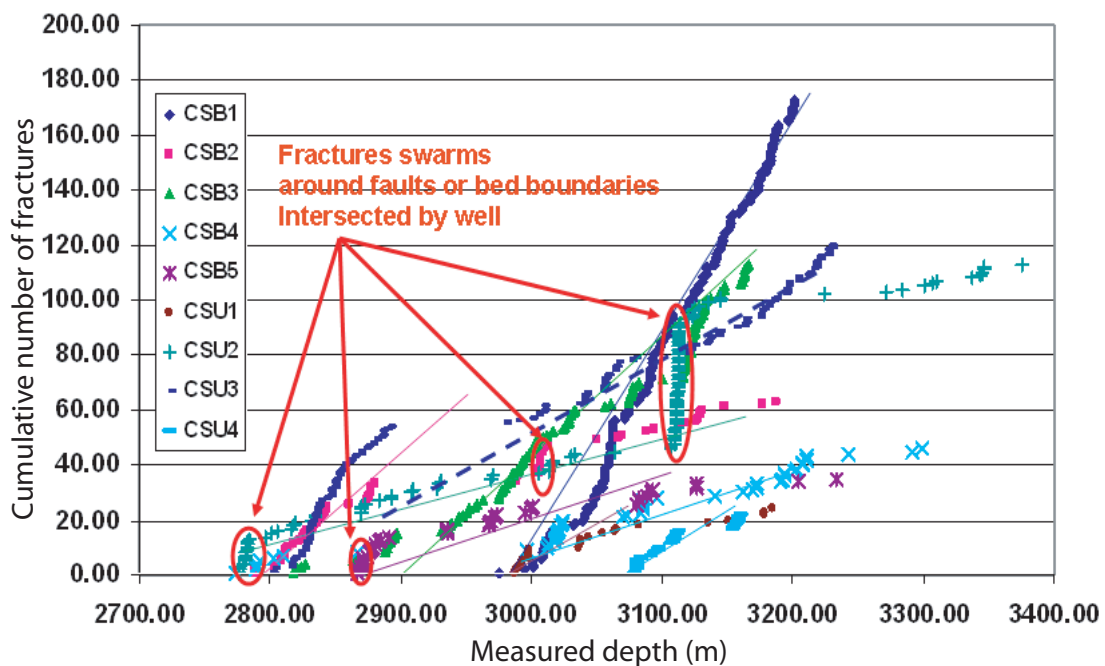


Fig. 3.19: Plot indicates well MD in the x axis and number of fractures intersected by the well in the y axis for all exploratory sections of the CS field. Fracture swarms are associated with local faults and bed boundaries. Lines are best fit line after removing the effect of local faults and bed boundaries.

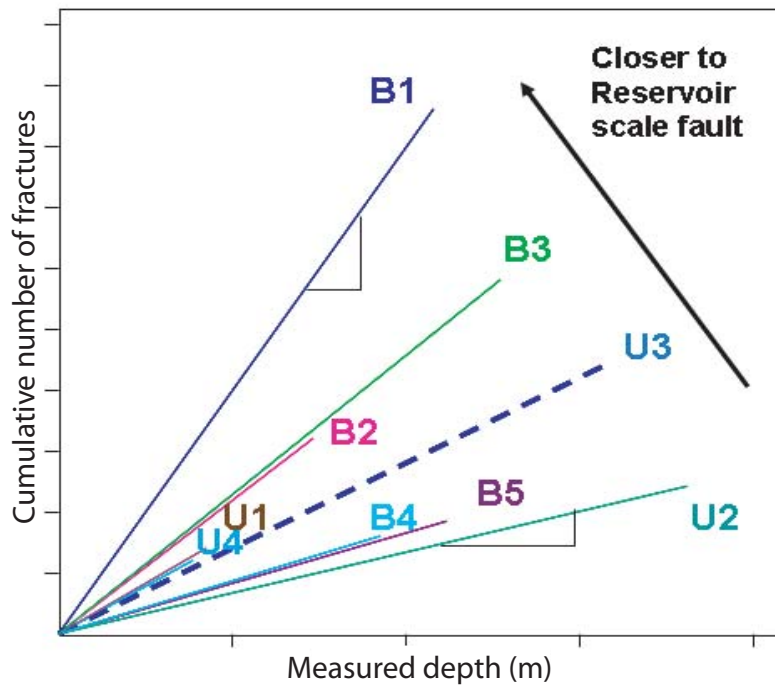


Fig. 3.20: After removing the effect of local faults and bed boundaries, the slop of MD vs. number of fractures lines increases as we get close to the reservoir scale faults.

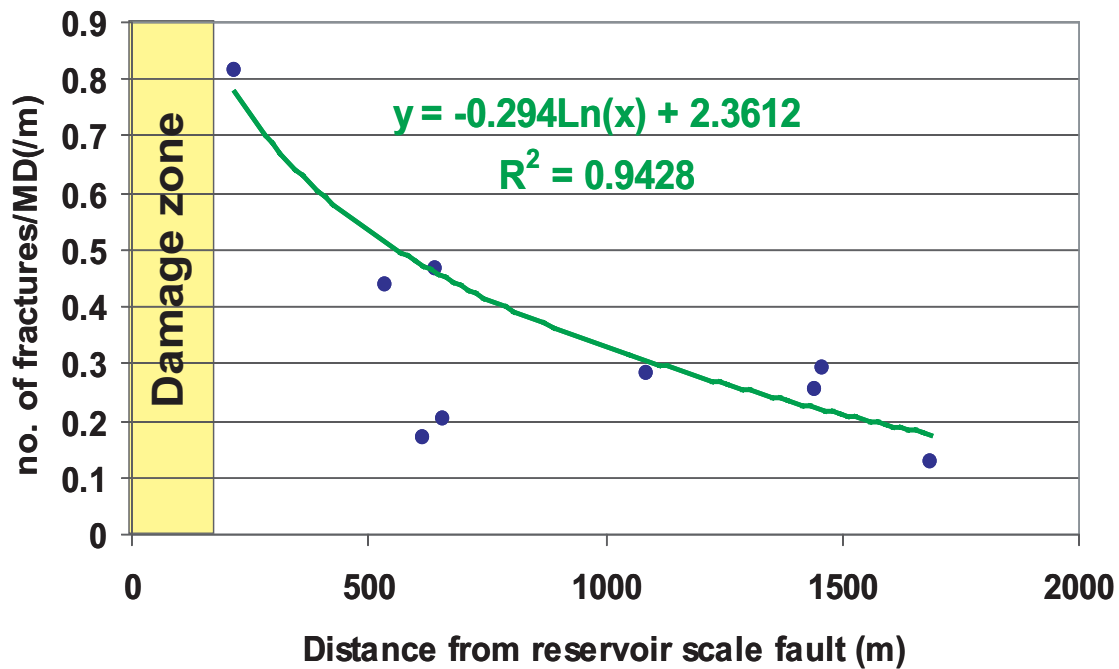


Fig. 3.21: Observed data at well locations indicate that fracture density decreases as a function of log of distance from the reservoir scale faults.

### 3.9 Conclusions

This chapter discusses the present day stress field, the petrophysical model and well scale fracture analysis in the CS field. Maximum horizontal stress is oriented towards  $\sim N45^{\circ}E$  and it is homogenous around the field. The estimated stress magnitudes indicate a Strike-Slip/Normal faulting stress state in the reservoir with gradient values  $S_{H_{max}} \sim 21$ ppg,  $S_v \sim 19.5$ ppg, and  $S_{H_{min}} \sim 13.4$ ppg. The reservoir section is mainly made of alternating sandstone and shaly layers with uniaxial rock strength  $\sim 72$ MPa to  $\sim 60$ MPa respectively. Fracture density at well locations, is very low and fractures are mainly concentrated around local faults and bedding planes. Production logs and well test models indicate relatively low production from the fractured zone in the well CSU2. High matrix permeability and a large number of non-optimally oriented fractures may be the possible explanation for why we do not see the effect of fractures in the fluid flow at well scale. However, interference tests between wells indicate preferential flow along the large reservoir scale faults. The fracture density model from the exploratory wells shows an increasing trend of fracture density towards the reservoir scale faults. However, none of the exploratory wells are close enough to the reservoir scale faults to support any concrete inference about the fracture density and fluid flow properties very close (in the fractured/damage zone) to these faults. Thus, in the next chapter, we discuss the geomechanical modeling of these fractured/damage zones using the properties of faults itself, which may give a better quantitative model to constrain the reservoir simulation model adjacent to the reservoir scale faults.

### References

- Barton, C. A., and Zoback, M. D., 2003, Wellbore imaging technologies applied to reservoir geomechanics and environmental engineering, Geological Applications of well logs, M. L. A. N. Parkinson.
- Barton, C.A., Zoback, M.D., and Moos, D., 1995, Fluid flow along potentially active faults in crystalline rock: *Geology*, v. 23, p. 683-686.
- Barton, C. A., and Zoback, M. D., 1994, Stress perturbations associated with active faults penetrated by boreholes: Possible evidence for near-complete stress drop and a new technique for stress magnitude measurements: *Journal of Geophys. Res.*, v. 99, p. 9373-9390.

- Barton, C.A., Hickman, S.H., Morin, R., Zoback, M.D., and Benoit, D., 1998, Reservoir-scale fracture permeability in the Dixie valley, Nevada, geothermal field: Proceedings of Society of Petroleum Engineers/International Society of Rock Mechanics and Mining Sciences Rock Mechanics in Petroleum Engineering, v. 2: Trondheim, Norway, SPE, p. 315-322.
- Barton, C. A., Zoback, M. D., et al., 1988, In-situ stress orientation and magnitude at the Fenton Geothermal site, New Mexico, determined by wellbore breakouts, *Geophy. Res. Lett.*, v. 15(5), 467-470.
- Bell, J. S., and Gough, D. J., 1979, Northeast-southwest compressive stress in Alberta: evidence from oil wells: *East Planet Sc. Letters*, v. 45, p. 475-482.
- Bourne, S.J., and Willemse, E.J.M., 2001, Elastic stress control on the pattern of tensile fracturing around a small fault network at Nash Point, UK: *Journal of Structural Geology*, v. 23, p. 1753-1770.
- Bourne, S.J., Brauckmann, F., Rijkels, L., Stephenson, B.J., Weber, A., and Willemse, E.J.M., 2000, Predictive modeling of naturally fractured reservoirs using geomechanics and flow simulation: ADIPEC0911.
- Brown, S.R., and Bruhn, R.L., 1998, Fluid permeability of deformable fracture networks: *Journal of Geophysical Research*, 103(B2), 2489-2500.
- Brudy, M., and Zoback, M. D., 1999, Drilling-induced tensile wall fractures: implications for the determination of in-situ stress orientation and magnitude: *Int. J. of Rock Mech. and Min.*, v. 36, p. 191-215.
- Castillo, D. A., Hills, R. R., Asquith, K., and Fischer, M., 1999, Frictional and wellbore failure constraints for estimating the in-situ stress tensor in deep boreholes: Application to the Timor sea and Fault-seal integrity: The Sedimentary basins of Western Australia, Proceedings of the Petroleum Exploration Society of Australia Symposium, Perth, p. 1-20.
- Chen, H., and Teufel, W., 2003, Coupling fluid-flow and Geomechanics in Dual-porosity modeling of naturally fractured reservoirs – Model description and comparison: SPE 59043
- Couples, G.D., Lewis, H., Reynolds, M.A., Pickup, G.E., and Ma, J., 2003, Upscaling fluid-flow and Geomechanical properties in coupled matrix+fracture+fluid systems: SPE 79696.
- Gringarten, E., 1997, Geometric modeling of fracture networks: Ph. D. thesis, Petroleum Engg. Department, Stanford University.
- Hickman, S.H., Zoback, M.D., and Benoit, D., 1998, Tectonic control on fault-zone permeability in a geothermal reservoir at Dixie valley, Nevada: Proceedings of Society of Petroleum Engineers/International Society of Rock Mechanics and Mining Sciences Rock Mechanics in Petroleum Engineering, v. 1: Trondheim, Norway, SPE, p. 79-86.
- Horsrud, P., 2001, Estimating mechanical properties of shale from empirical correlations, *SPE Drilling and Completion*, v. 16(2), 68-73.
- Jaeger, J. C., and Cook, N. G. W., 1979, *Fundamentals of rock mechanics*: 3<sup>rd</sup> edition, Chapman and Hill, New York, p. 593.
- Lee, S.H., Lough, M. F., and Jensen, C.L., 2001, Hierarchical modeling of flow in naturally fractured formations with multiple length scales: *Water Resources Research*, v. 37, p. 443-455.

- Long, J. C. S., and Billaux, D. M., 1987, From field data to Fracture Network modeling: An example incorporating spatial structure: *Water Resources Research*, v. 23, p. 1201-1216.
- Luthi, S. M., and Souhaite, P., 1990, Fracture apertures from electrical borehole scans, *Geophysics*, V. 55, 821-833.
- Luthi, S. M., 1990, Sedimentary structures of clastic rocks identified from electrical borehole images, Geological applications of wireline logs: *Geol. Soc. London Special Publication*.
- Maerten, L., Gillespie, P., and Pollard, D.D., 2002, Effects of local stress perturbation on secondary fault development: *Journal of structural Geology*, v. 24, p. 145-153.
- Makurat, A., Barton, N., Rad, N.S., and Bandis, S., 1990, Joint conductivity variation due to normal and shear deformation: *Proc. Int. Symp. Rock Joints*, p. 535-540.
- Martel, S.J., and Peterson, J., 1991, Interdisciplinary characterization of fracture systems at the US/BK site, Grimesl Laboratory, Switzerland: *Int. J. of Rock Mech. and Min. Sc. Abstracts*, v. 28, p. 259-323.
- McNally, G. H., 1987, Estimation of core measures rock strength using sonic and neutron logs: *Geoexploration*, v.24, p. 381-395.
- Moos, D. and Zoback, M D., 1990, Utilization of observations of well bore failure to constrain the orientation and magnitude of crustal stresses: Application to continental deep sea drilling project and ocean drilling program boreholes, *J. Geophy. Res.*, 95, 9305-9325.
- Oda, M., 1985, Permeability tensor for discontinuous rock masses: *Geotechnique*, v. 35, p. 483-495.
- Oda, M., 1986, An equivalent continuum model for coupled stress and fluid flow analysis in joined rock masses: *Water Resour. Res.*, v. 22, p. 1845-1856.
- Olsson, R., and Barton, N., 2001, An improved model for hydro mechanical coupling during shearing of rock joints: *Int. J Rock Mech Min Sci*, v. 38(3), p. 317-329.
- Pezard, P. A., and Luthi, S. M., 1988, Borehole electrical images in the basement of the Cajon Pass scientific drillhole; fracture identification and tectonic implications: *Geophys. Res. Lett.*, v. 15, 1017-1020.
- Plumb, R. A., and Luthi, S. M., 1986, Application of borehole images to geologic modeling of an eolian reservoir, *SPE* 15487.
- Reinecker, J., Heidbach, O., Tingay, M., Connolly, P., and Muller, B., 2004, The 2004 release of the world stress map: [www.world-stress-map.org](http://www.world-stress-map.org).
- Smart, B.G.D., Somerville, J.M., Edlman, K., and Jones, C., 2001, Stress sensitivity of fractured reservoirs: *Journal of Petroleum Science and Engineering*, v. 29, p. 29-37.
- Srivastava, R. M., 2002, Probabilistic discrete fracture network models for the Whiteshell Research area: Internal report, FSS Canada Consultants Inc.
- Townend, J., and Zoback, M.D., 2000, How faulting keeps the crust strong: *Geology*, v. 28, p. 399-402.
- Wiprut, D., and Zoback, M.D., 2000, Fault reactivation and fluid flow along a previously dormant normal fault in the northern North Sea: *Geology*, v. 28, p. 595-598.

Zoback, M. D., Barton, C. A., Brudy, M., Castillo, D. A., Finkbeiner, T., Grollmund, B. R., Moos, D. B., Peska, P., Ward, C. D., and Wiprut, D. J., 2003, Determination of stress orientation and magnitude in deep wells: *Int. J. of Rock Mech. and Min.*, v. 40, p. 1049-1076.

Zoback, M. D., Moos, D. et al., 1985, Well bore breakouts and In situ stress, *Journal of Geophy. Res.*, 90(B7), 5523-5530.

## Chapter 4

# **MODELING FAULT DAMAGE ZONES USING A DYNAMIC RUPTURE PROPAGATION METHOD**

*Part of this chapter was written as a paper with Mark Zoback and Peter Hennings, and has been accepted by SPE (SPE 110542)*

### **4.1 Abstract**

Secondary fractures and faults associated with reservoir-scale faults affect both permeability and permeability anisotropy and hence may play an important role in controlling the production behavior of a faulted reservoir. It is well known from geologic studies that there is a concentration of secondary fractures and faults in a damage zone adjacent to larger faults, as documented in chapter 3. Because there is usually inadequate data to fully incorporate damage zone fractures and faults into reservoir simulation models, in this study we utilize the principles of dynamic rupture propagation from earthquake seismology to predict the nature of fractured/damage zones associated with reservoir scale faults. We include geomechanical constraints in

our reservoir model and propose a workflow to more routinely incorporate damage zones into reservoir simulation models.

The model we propose calculates the extent of the damage zone along the fault plane by estimating the stress perturbation associated with dynamic rupture propagation. We apply this methodology to the reservoir discussed in chapter 3 utilizing both field and well scale observations. At the rupture front, damage intensity gradually decreases as we get away from the rupture front or fault plane. In the studied reservoir, the secondary features in the damage zone are high angle normal faults striking sub-parallel to parent fault. Because these secondary features are optimally oriented for shear failure in the present day stress state they affect the permeability of the reservoir in both the horizontal and vertical directions. We calibrate our modeling with both field (outcrop) scale and well scale observations from a number of studies and show that dynamic rupture propagation gives a reasonable first order approximation of damage zones in terms of permeability and permeability anisotropy in order to be incorporated into reservoir simulators.

## 4.2 Introduction

Fracture mechanisms in the earth's crust often involve shear faults because compressive lithostatic pressure and tectonic stresses prevents tensile failure on a large scale. These shear faults may contain damage zones (also called fractured zones), which are created during the three stages of faulting: prior to faulting, during fault growth, and during slip along the existing fault.

Pre-faulting deformations are likely to be quasi-uniformly distributed in the region and under favorable conditions of the stress-strain field; they may lead to failure localization and faulting (Aydin and Johnson, 1978; Lyakhovsky et al., 1997; Nanjo et al., 2005). Deformation during dynamic fault growth is mostly concentrated at the fault-tip of the growing fault and is caused by localized stress concentration (Chinnery, 1966; Cowie and Scholz, 1992; Anders and Wiltchko, 1994; Vermilye and Scholz,



1998; Pollard and Segall, 1987; Reches and Lockner, 1994). Deformation related to slip along an existing fault is caused by stress perturbations due to slip, which are related to the geometry and geomechanical properties of the fault and associated rock (Freund, 1974; Suppe, 1985; Chester and Logan, 1986). A mature fault damage zone results from the cumulative effects of the pre-faulting stage, the fault growth stages, and the slip along existing faults (Fig. 4.1).

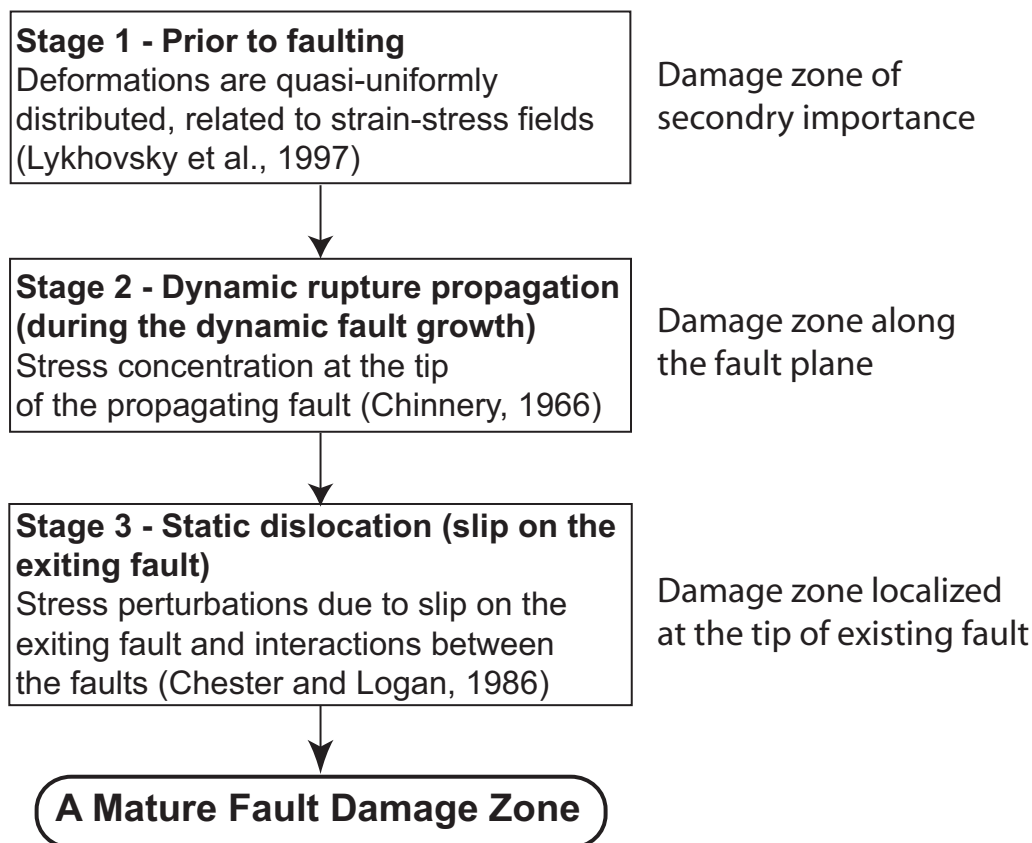


Fig. 4.1: A mature fault damage zone is the cumulative effect of pre-faulting stage, fault growth stages, and the slip along existing faults.

Estimating the physical properties of rocks during each step of faulting is a challenge modeling the damage zones in a reservoir model. When we numerically model them at a reservoir scale, non-linearity between the parameters and complex fault geometries further complicate the problem. So it is important to optimize the workflow to include the feasible size and complexity of the problem. Lockner et al. (1992) and Vermilye and Scholz (1998) show that the damage zones from the pre-

faulting stage are very narrow and can be ignored for reservoir scale faults. We can approximate the damage zone during fault growth using the dynamic rupture propagation along a fault plane. When a rupture travels along a pre-existing fault, it concentrates stresses at the rupture front, which creates fractured or damage zones associated with the fault (Madariaga, 1976; Kostov, 1964; Virieux and Madariaga, 1982; Harris, 2004).

Damage zones due to slip on existing faults are important, especially when faults are active in present day stress conditions, because slip creates splay fractures at the tips of the fault. In a reservoir with a developed fault network, fault-slip extends the damage zone created during the fault growth stage. We can use established numerical techniques to estimate the stress perturbation due to slip on the faults. The current general trend is to model the effects of damage zones using only this stage. However, this stage alone can only demonstrate the damage effects at the tips of the fault in its present form and misses the damage effects during the dynamic growth of the fault.

In this chapter, we discuss the concept of dynamic rupture propagation to model the damage zone associated with the reservoir scale faults. We also discuss the methodology and associated constraints for estimating the damage zone using this technique. We ignore the effect of damage zone for the stage prior to the faulting for the study area. Studies indicate that faults of the study are not active in present day stress state in the reservoir depth so the effect of slip along the existing fault may not be very important and there are established numerical algorithms to solve this stage. Thus, we do not include details of faulting stages 1 and 3 in this study. However, in the appendix of this chapter we summarize the concepts and methodology related to these two stages.

### **4.3 The formation, growth, and development of faults**

The previous section introduced a three stage model for a mature fault damage zone. The question is, how do the faults grow to such a great dimension and what are

the traces they leave behind during their growth? In field observations and laboratory measurements, we see that the displacement on the fault plane is maximum near the center and tapers off to zero at the edges. When slip accumulates in the interior of faults, stress concentrations at the fault tip also increase (Fig. 4.2). The stress concentration can not go higher than the strength of the medium so the fault has to grow in its dimension to relax the stresses at the tip. So the fault may be considered as having originated at a point and growing with progressive slip. During this process, faults develop a highly cracked zone around the tip, which is called a process zone. These are a dominant part of the damage zone when the fault becomes mature with time.

From the field observations, as shown in Fig. 4.3, we see that the width of the process zone increases linearly with the fault length. For an elastic, purely plastic material, Atkinson (1987) describes the zone of yielding at the crack tip as Eq. 4.1.

$$r_y = \frac{L}{8} \left( \frac{\sigma_a}{\sigma_y} \right)^2, \quad (4.1)$$

where  $r_y$  is the radius of the yielding zone,  $L$  is the length of the fault,  $\sigma_a$  is the applied stress, and  $\sigma_y$  is the yield strength.

If we interpret the process zone as a dominant part of the damage zone, then the damage zone formed due to stress concentrations of the propagating fault tip should show a similar scaling law. However, Eq. 4.1 fails to include the effects of other dimensions of the fault. And, if we use the full elastic crack model to predict the effects of the damage zone then the parameters required are virtually impossible to estimate for all events during fault growth. Hence, we use the propagation of a dynamic rupture front along the fault plane to model the dimension of the damage zone.

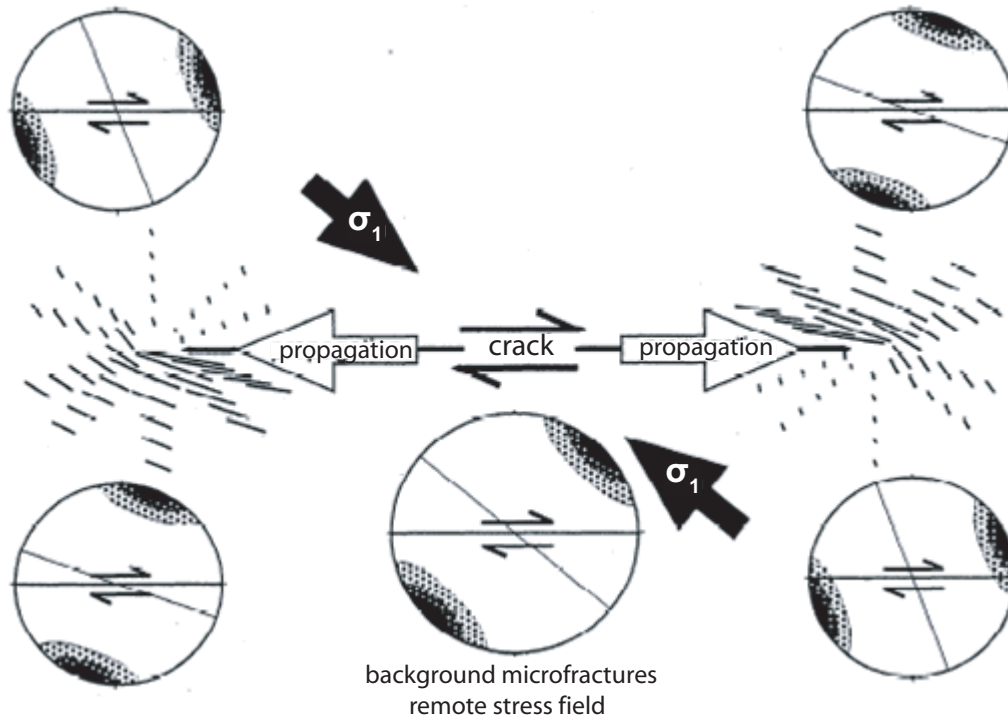


Fig. 4.2: Plot of calculated maximum compressive stress,  $\sigma_1$ , surrounding the tips of mode II type fracture growth. Plot indicates fractures rotate to lower angle in compressive quadrants. Stereonets indicate idealized plots of expected poles of fractures. (Scholz et al., 1993)

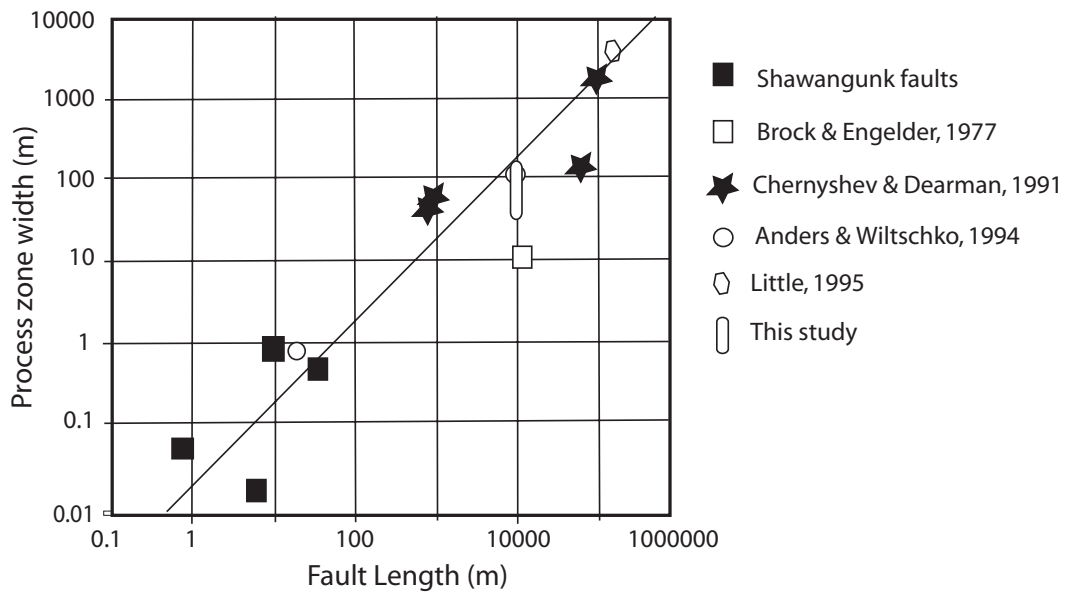


Fig. 4.3: The width of the process zone linearly scales to the length of the fault (modified from Vermilye and Scholz et al., 1998).

## **4.4 Modeling of the damage zone during the fault growth using a dynamic rupture propagation technique**

As mentioned in the previous section, scaling relations from the field observations omit the other dimensions of the fault such as the dip angle and the length along the dip. Estimating the dimensions of the damage zone using the crack mechanics concept requires parameters that may vary as the fault grows so it is virtually impossible to estimate these for all events during fault growth. However, we can approximate the dimension of the damage zone during the fault growth using the dynamic rupture front movement along the fault plane. During an earthquake, the rupture starts on a small patch and propagates along the fault plane with time. Stress concentrations at the tip of the rupture front give a process zone dimension, which may be scaled to the damage zone that is created during the fault growth. Rupture events originating in different orientations and from different patches may explain the multiple fracture patterns associated with the damage zones. In the next chapter we will see that these fracture patterns control the permeability anisotropy of the damage zone. The geometry and size of the damage zone controls the large scale permeability anisotropy in the reservoir. In the next sections, we discuss the analytical solutions (Freund, 1979; Madariaga, 1976) of the dynamic rupture propagation, which can be used to explain the creation of the damage zone due to the stress perturbations at the rupture front. We also discuss the similarity between the crack mechanics and dynamic rupture propagation concepts to support that the latter can be used as an alternative of fault/crack growth mechanisms.

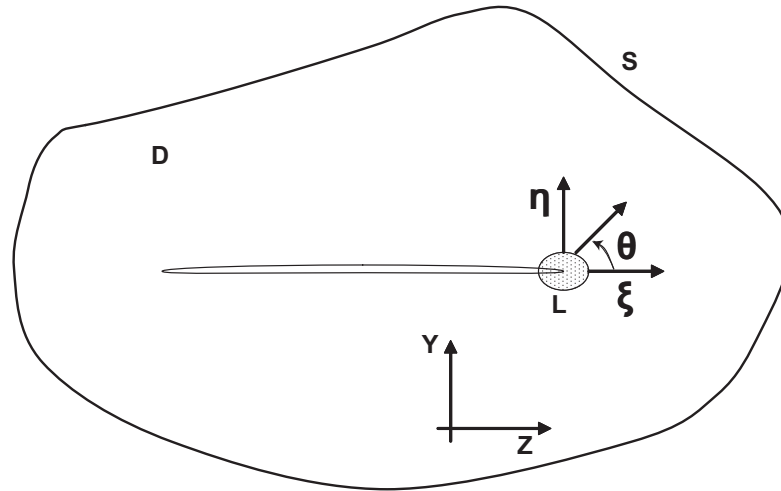
### **4.4.1 The mechanics of dynamic rupture propagation (Freund, 1979)**

In the dynamic rupture propagation technique, the source which creates the earthquake is assumed to be a dynamically extending planar crack. The pre-existing fault provides a weak path for the growth of the crack. Because confining pressure reduces the effects of tensile stresses near the crack tip, the crack extends along the fault plane, which might otherwise lead to an oblique crack growth. The medium is considered to be an isotropic elastic material. The elastodynamic stress and

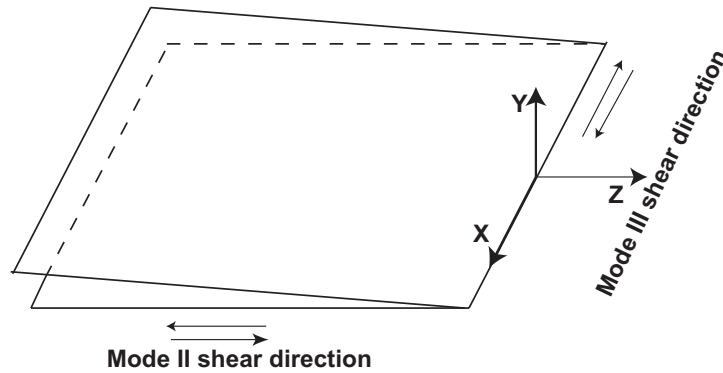
deformation fields define the dynamic stress intensity factor and the dynamic energy release for the crack propagation.

For a dynamic crack, the speed of crack propagation, or rupture velocity, guides the spatial distribution of the crack. When the rupture velocity becomes zero, the expression solves for a stationary crack. This solution for spatial distribution of a dynamic crack is independent of the configuration of the body and the details of how the system has been loaded, but it depends on the spatial position of the crack tip with time.

To define the stress perturbations due to a dynamic crack, we focus on the particle velocity near the crack tip. Fig. 4.4a shows the y-z plane (D) of a body with the particle displacement along the plane. Fig. 4.4b illustrates a 3D configuration of the coordinate system with respect to the crack and the directions for mode II and III shearing. The inner boundaries on the plane, D, are crack faces and the outer boundary is S, which can have either a traction boundary condition or a displacement boundary condition or a combination of the two.



(a)



(b)

Fig. 4.4: (a) Plane view (y-z) of a body containing a crack at a fixed instant of time (Freund, 1979). (b) A 3D configuration of the coordinate system with respect to the crack and the directions for Mode II and III shearing.

Fig. 4.4a shows a loop  $L$  at the crack tip with a local Cartesian coordinate system  $(\xi, \eta)$  and a polar coordinate system  $(r = \sqrt{\xi^2 + \eta^2}, \theta = \tan^{-1}(\eta/\xi))$ , which vary with time. If the crack extends in its plane with rupture velocity,  $v$ , which continuously varies with time, then the following equations define the stress components for all plane elastodynamic solution for mode II (Eq. 4.2) and III (Eq. 4.3) cracks using the asymptotic method (Freund and Clifton, 1974). These equations are only valid in the subsonic range of rupture velocity (less than S-wave velocity), which is the range observed during most of the earthquake events (Xia et al., 2004, 2005; Harris and Day, 1997).

$$\sigma_{zz} = -\frac{2\kappa_2(t)c_\beta}{(2\pi)^{1/2}R(\nu)} \left\{ (1+2c_\alpha^2-c_\beta^2) \frac{\sin(\theta_\alpha/2)}{r_\alpha^{1/2}} - (1+c_\beta^2) \frac{\sin(\theta_\beta/2)}{r_\beta^{1/2}} \right\} \quad (4.2a)$$

$$\sigma_{zy} = \frac{\kappa_2(t)}{(2\pi)^{1/2}R(\nu)} \left\{ 4c_\beta c_\alpha \frac{\cos(\theta_\alpha/2)}{r_\alpha^{1/2}} - (1+c_\beta^2) \frac{\cos(\theta_\beta/2)}{r_\beta^{1/2}} \right\} \quad (4.2b)$$

$$\sigma_{yy} = \frac{2\kappa_2(t)c_\beta(1+c_\beta^2)}{(2\pi)^{1/2}R(\nu)} \left\{ \frac{\sin(\theta_\alpha/2)}{r_\alpha^{1/2}} - \frac{\sin(\theta_\beta/2)}{r_\beta^{1/2}} \right\} \quad (4.2c)$$

$$\sigma_{yx} = \frac{\kappa_3(t)}{(2\pi)^{1/2}r_\beta^{1/2}} \cos(\theta_\beta/2) \quad (4.3a)$$

$$\sigma_{xz} = -\frac{\kappa_3(t)}{(2\pi)^{1/2}c_\beta r_\beta^{1/2}} \sin(\theta_\beta/2) \quad (4.3b)$$

$$\begin{aligned} \sigma_{xx} &= 0, \text{ for plane stress condition} \\ &= \nu(\sigma_{zz} + \sigma_{yy}), \text{ for plane strain condition} \end{aligned} \quad (4.3c)$$

In the above equations,  $\theta$  is the angle from the fracture propagation direction,  $\xi$ , in a local coordinate system at the crack tip,  $\nu$  is the Poisson's ratio, and  $\nu$ ,  $\alpha$ , and  $\beta$  are rupture, P-wave, and S-wave velocity respectively.  $R(\nu)$  is the Rayleigh function defined in Eq. 4.4.  $c_\alpha$ , and  $c_\beta$  are the constants related to P-wave and S-wave velocity and can be denoted as Eq. 4.5a and 4.5b, and  $(r_\alpha, \theta_\alpha)$  and  $(r_\beta, \theta_\beta)$  are the coordinates of P-wave and S-wave related to local coordinate  $(r, \theta)$  by Eq. 4.6a and 4.6b.

$$R(\nu) = 4c_\alpha c_\beta - (1+c_\beta^2)^2 \quad (4.4)$$

$$c_\alpha = \sqrt{1-\nu^2/\alpha^2} \quad (4.5a)$$

$$c_\beta = \sqrt{1-\nu^2/\beta^2} \quad (4.5b)$$

$$r_\alpha = \delta c_\alpha \text{ and } \tan \theta_\alpha = c_\alpha \tan \theta \quad (4.6a)$$



$$r_\beta = \delta c_\beta \text{ and } \tan \theta_\beta = c_\beta \tan \theta, \quad (4.6b)$$

where  $\delta$  defines the distance from the instantaneous position of the crack tip to a point around the crack tip where we calculate the stress perturbation due to the rupture propagation.  $\kappa_2$  and  $\kappa_3$  in Eq. 4.2 and 4.3 are the instantaneous rupture intensity factors for mode II and III, which can be defined by Eq. 4.7a and 4.7b.

$$\kappa_2(t) = \lim_{r \rightarrow 0} (2\pi\delta)^{1/2} \sigma_{zy}(r, \theta = 0, t) \quad (4.7a)$$

$$\kappa_3(t) = \lim_{r \rightarrow 0} (2\pi\delta)^{1/2} \sigma_{yx}(r, \theta = 0, t) \quad (4.7b)$$

To estimate the stress components at the tip of the rupture front using Eq. 4.2 and 4.3, we need to estimate  $\kappa_2$  and  $\kappa_3$  at each instant of time using Eq. 4.7a and 4.7b. But, Eq. 4.7a and 4.7b need on-plane solutions for mode II and III shearing to calculate the dynamic stress intensities. In the next section, we discuss on-plane solutions for mode II and III shearing for a dynamic circular crack (Madariaga, 1976). By combining those with Freund's solutions we can obtain all the components of the stress tensor and explain the stress perturbation around the rupture front.

#### 4.4.2 The dynamic circular-shear-crack model (Madariaga, 1976)

Analytical solutions for a dynamic circular shear crack of finite radius are complex and difficult to obtain. However, the analytical solution may be found for a circular shear crack with a self-similar assumption. A self-similar shear crack starts from a point and then grows symmetrically with a constant rupture velocity without stopping. For a self-similar circular crack, the rupture nucleates at the center and proceeds at constant subsonic velocity,  $v$ , until it suddenly stops at an arbitrary time  $t = a_r/v$ , leaving a final rupture front radius of  $a_r$ . Fig. 4.5 shows the geometry of the problem, where the fault is contained in the x-z plane and the nucleation point is at the origin of the coordinates. The medium is infinite, homogeneous, isotropic, and elastic so that displacement,  $u$ , satisfies the equation of motion. Normal and shear stresses on

the fault before the rupture initiates are  $\sigma_{yy}^0$ , and  $\sigma_{xz}^0$  respectively, where shear stress is assumed to be sufficient to initiate rupture at the fault.

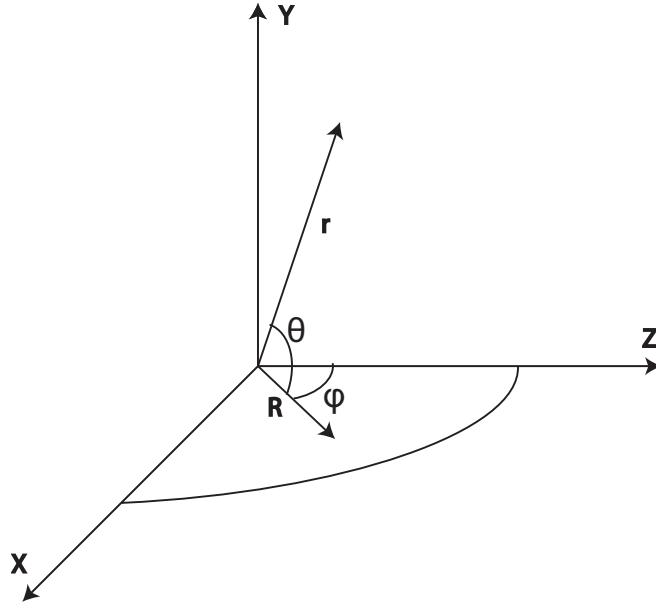


Fig. 4.5: The geometry of the problem where the fault is contained in the x-z plane and the nucleation point is at the origin of the coordinates (modified from Madariaga, 1976).

The solution of a dynamic self-similar crack can be calculated by Cagniard's method (Kostov, 1964). The slip is driven by a drop in the shear stress. Assuming the slip is parallel to fault plane ( $\Delta u_y=0$ ) and the shear drop is only in the  $\sigma_{xz}$  component, the amount of slip parallel to z-axis can be described by Eq. 4.8,

$$\Delta u_z(r,t) = \frac{\Delta\sigma}{G} C(v)(v^2 t^2 - r^2)^{1/2} \text{ for } r < vt, \quad (4.8)$$

where  $C(v)$  is an almost constant function of rupture velocity,  $v$ , in a subsonic velocity range.  $G$  is the shear modulus of the elastic medium, and  $\Delta\sigma$  is the shear drop from initial stress load,  $\sigma_{xz}^0$ , to the shear resistance,  $\sigma_{xz}^f$ .

If  $\delta$  is the distance along the fault plane ( $r \approx R$ ) measured from the instantaneous position of the rupture front then the radial distance from the center of the circular crack on the x-z plane is given by Eq. 4.9.

$$r = vt \pm \delta \quad (4.9)$$

Around the edge of the crack the total stress concentrations due to mode II and mode III shearing can be defined by Eq. 4.10.

$$\sigma_{xz}(r) = (K_{II} \cos \varphi + K_{III} \sin \varphi) \delta^{\frac{1}{2}}, \quad (4.10)$$

where  $\varphi$  is the azimuth on the fault plane measured from the z-axis.  $K_{II}$  and  $K_{III}$  are stress intensity factors for mode II and mode III fractures and can be defined by Eq. 4.11a and 4.11b respectively.

$$K_{II} = \Delta\sigma\sqrt{v}k_2(v) \quad (4.11a)$$

$$K_{III} = \Delta\sigma\sqrt{v}k_3(v), \quad (4.11b)$$

where  $k_2(v)$  and  $k_3(v)$  are velocity dependent functions and defined by Eq. 4.12a and 4.12b respectively.

$$k_2(v) = \frac{C(v)}{2\sqrt{2}} \frac{\beta^2}{v^2} \frac{R(v)}{\sqrt{1-v^2/\beta^2}} \quad (4.12a)$$

$$k_3(v) = \frac{C(v)}{2\sqrt{2}} \sqrt{1-v^2/\beta^2} \quad (4.12b)$$

As rupture velocity,  $v$ , tends to zero,  $k_2 \approx 0.515$  and  $k_3 \approx 0.385$ . At higher rupture velocities,  $k_2(v)$  and  $k_3(v)$  decrease monotonically and become zero at the Rayleigh-wave velocity and the shear wave velocity respectively. For a realistic seismic source, the self-similar shear crack stops suddenly at some radius,  $a_r$ , which generates strong healing waves that propagate inward from the edge of the crack. High friction along the plane is assumed to cause freezing of the slip.

As shown in Eq. 4.10, the shear stress along the crack plane at the edges of a dynamic circular crack is a combination of mode II (on-plane shear) and III (anti-plane shear) shearing. The stress intensities of these shearing modes at any instant of time depend on the rupture velocity and the stress drop. For identical conditions of rupture

velocity and stress drop, the rupture front moves faster along the direction of on-plane shear, because stress intensity for on-plane shear ( $K_{II}$ ) is greater than stress intensity for anti-plane shear ( $K_{III}$ ). This effect rapidly transforms a circular crack to an elliptical crack with its major axis along the on-plane shear direction. This phenomenon explains why a dip slip fault extends more along the dip direction and a strike slip fault extends more along the strike direction. However, an accurate model of this phenomenon needs numerical modeling rather than a pure analytical solution as shown in Fig. 4.6 (Virieux and Madariaga, 1982). In this study, we approximate the effects of on-plane and anti-plane shearing at the rupture front using Eq. 4.10.

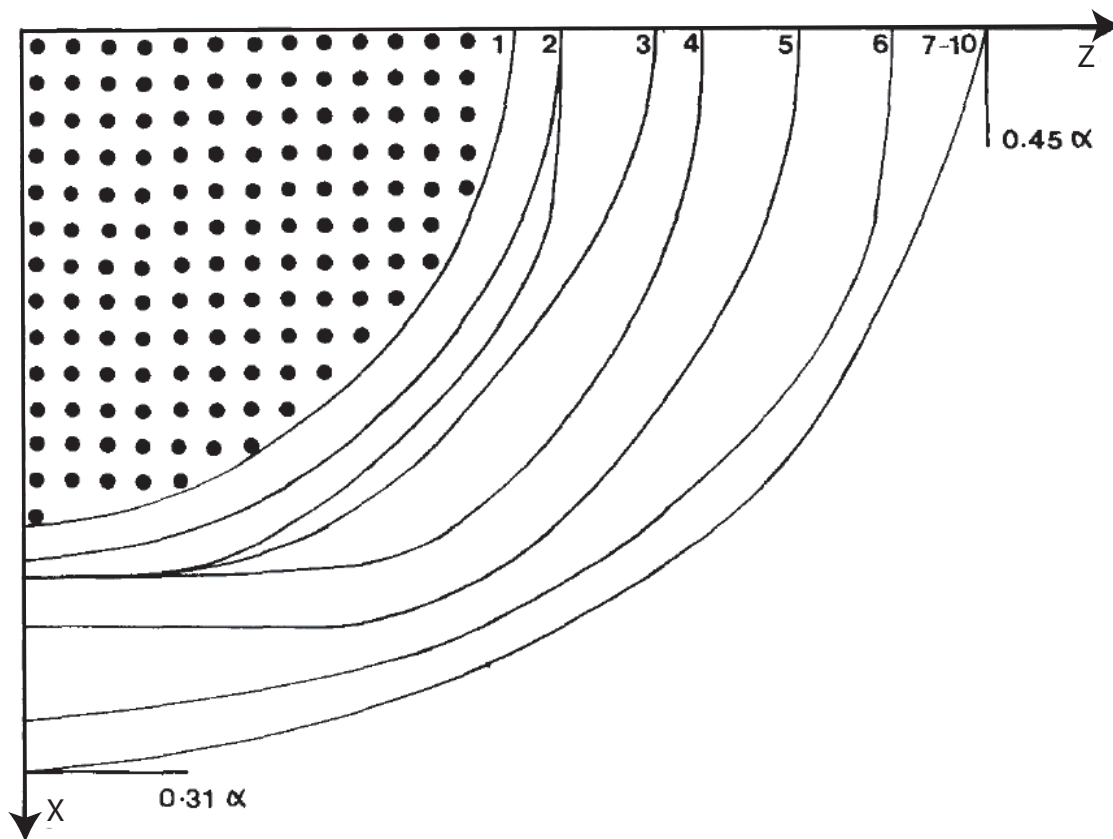


Fig. 4.6: Rupture front motion for a spontaneous initially circular crack under static pre-stress loading. The dotted part is the pre-existing circular crack and the lines are the rupture front at 10 different times. The rupture front velocity in the  $z$  direction is greater than  $x$  direction, which transforms the circular crack to an elliptical crack with the major axis parallel to the  $z$  direction. (modified from Virieux and Madariaga, 1982)

#### 4.4.3 Combining the dynamic circular-shear-crack solution (Madariaga, 1976) with the dynamic rupture propagation solution (Freund, 1979)

In the above sections, we have seen that the dynamic rupture propagation solution (Freund, 1979) needs an on-plane solution of shear stresses at the rupture front (Eq. 4.7). We have also seen that the dynamic circular-shear-crack solution (Madariaga, 1976) gives an on-plane solution of shear stress for a dynamic circular crack (Eq. 4.10). By combining both solutions we can obtain the complete stress tensor (Eq. 4.2 and 4.3) around the rupture front.

In Eq. 4.7a,  $\sigma_{zy}(r,0,t)$  indicates a solution of mode II shear at  $\theta = 0^\circ$  i.e. a slip along the z direction on the x-z plane, which is indicated by the mode II part of Eq. 4.10. Similarly,  $\sigma_{yx}(r,0,t)$  in Eq. 4.7b indicates a solution of mode III shear at  $\theta = 90^\circ$  i.e. a slip along the x direction on the x-z plane, which is indicated by the mode III part of Eq. 4.10. The solutions of  $\sigma_{zy}(r,0,t)$  and  $\sigma_{yx}(r,0,t)$  are defined in Eq. 4.13a and 4.13b respectively.

$$\sigma_{zy}(r,0,t) = \sigma_{xz}^{II}(r, \varphi = 0, t) = K_{II}(r)\delta^{-1/2} \quad (4.13a)$$

$$\sigma_{yx}(r,0,t) = \sigma_{xz}^{III}(r, \varphi = 90, t) = K_{III}(r)\delta^{-1/2}, \quad (4.13b)$$

where  $\delta$  is the distance from the rupture front to the point of stress calculation and  $K_{II}$  and  $K_{III}$  can be defined by Eq. 4.11 and 4.12.

As we see above, by combining the on-plane solution of a dynamic circular crack to Freund's (1979) solution we can estimate stress tensors around the rupture front. When this propagating stress concentration exceeds the strength of the rock, this solution gives a reasonable first order estimation of the damage or fractured zone, which may capture the effects of fractures associated with the damage zone in a reservoir simulation model. However, to estimate higher order variations of the damage zone width, we have to numerically simulate the rupture front propagation of a dynamic crack initiating as an arbitrarily shaped crack.

## 4.5 The mechanism of the growth of elastic-brittle fractures

The modeling of a dynamic rupture front can give insight into deformation zones associated to fault planes. Now, we compare the mechanism of growing elastic-brittle-fractures or faults to the rupture propagation technique. Similarities between the two may give us more confidence in using the rupture front technique as an alternative to the actual fault growth mechanism. However, as mentioned before, fracture mechanics need estimates of required parameters at each step of fracture/fault growth, which is not feasible for a realistic scenario where reservoir scale faults grow through a several steps over a geological time period.

There are two basic concepts for the growth of elastic-brittle-cracks. The first is based on the stress intensity factor,  $K_i$  (Irwin, 1960), where  $i=I, II, \text{ and } III$ , representing the three different modes of fracture growth. When  $K_i$  reaches the critical stress intensity,  $K_{ic}$ , also known as fracture toughness, a fracture can grow and keep growing while  $K_i$  remains greater than  $K_{ic}$ . The second approach is based on the balance between available energy to drive the crack and the energy absorbed by the inelastic breakdown process at the tip of the crack. Here, we discuss only the first approach because it is similar to the rupture propagation concept.

Near a sharp crack tip as shown in Fig. 4.7, the stress field based on linear elastic fracture mechanics can be expressed with the following equations (Rice, 1968):

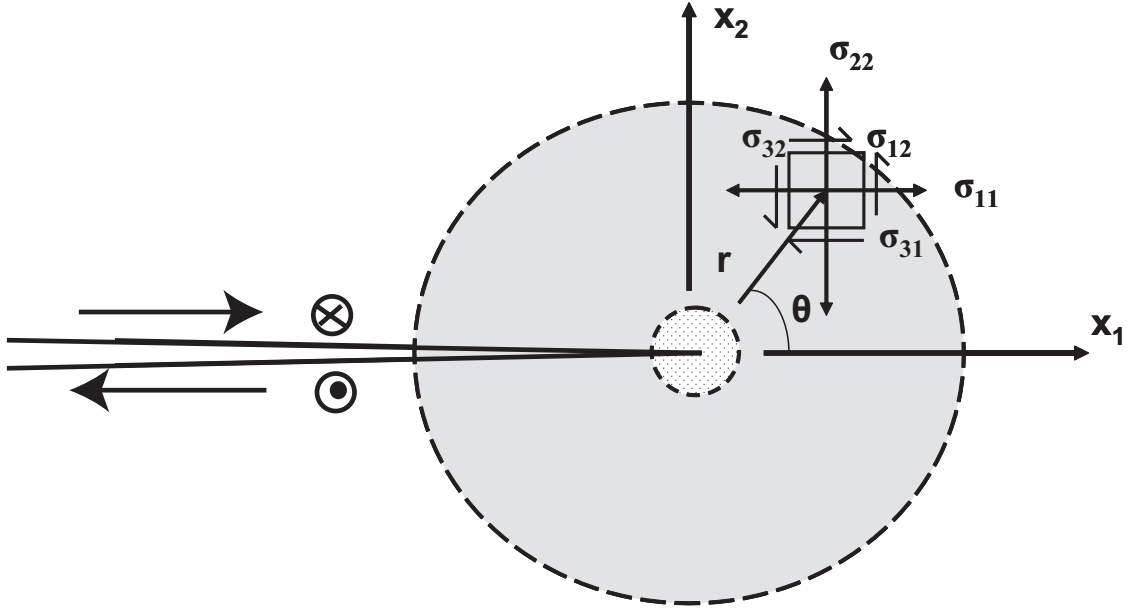


Fig. 4.7: Tip of a shear crack in mode II and mode III deformation. The darker shade denotes an annular region in which the asymptotic crack tip stress fields given by Eq. 4.14 and 4.16 are valid. (modified from Li, 1987)

For Mode II deformation, stresses and shear slip (plain strain) can be described with Eq. 4.14 and 4.15 respectively.

$$\sigma_{12} = K_{II} (2\pi r)^{-1/2} \cos(\theta/2) [1 - \sin(\theta/2) \sin(3\theta/2)] + \sigma^f + o(r^{1/2}) \quad (4.14a)$$

$$\sigma_{22} = K_{II} (2\pi r)^{-1/2} \sin(\theta/2) \cos(3\theta/2) + \sigma_n + o(r^{1/2}) \quad (4.14b)$$

$$\sigma_{11} = K_{II} (2\pi r)^{-1/2} \sin(\theta/2) [2 + \cos(\theta/2) \cos(3\theta/2)] + o(1) \quad (4.14c)$$

$$\Delta u_1 = u_1^+ - u_1^- = \frac{1-\nu}{\mu} K_{II} (8r/\pi)^{1/2} + o(r^{3/2}) \quad (4.15)$$

For Mode III deformation, stresses and shear slip can be described with 4.16 and 4.17 respectively.

$$\sigma_{13} = -K_{III} (2\pi r)^{-1/2} \sin(\theta/2) + o(1) \quad (4.16a)$$

$$\sigma_{23} = K_{III} (2\pi r)^{-1/2} \cos(\theta/2) \cos(3\theta/2) + \sigma^f + o(r^{1/2}) \quad (4.16b)$$

$$\Delta u_3 = u_3^+ - u_3^- = K_{III} (8r / \pi)^{1/2} + o(r^{3/2}) \quad (4.17)$$

where  $u_1$  is the displacements in the  $x_1$  direction,  $u_3$  is the displacement in a direction perpendicular to the plane of the crack,  $r$  is the distance from the tip of the crack,  $\theta$  is the angle from the  $x_1$  direction,  $\sigma^f$  is the shear resistance,  $\sigma_n$  is the normal stress, and  $\mu$  and  $\nu$  are the shear modulus and Poisson's ratio respectively. A general form of the stress intensity factor,  $K$ , is defined in Eq. 4.18. For a rectangular block, the stress intensity factors,  $K_{II}$  and  $K_{III}$  are defined in Eq. 4.19a and 4.19b (Tse et. al., 1985).

$$K = \sigma \sqrt{LF}(\text{geometry, loading}) \quad (4.18)$$

$$K_{II} = (\sigma^0 - \sigma^f) \sqrt{l} \sqrt{\pi} \quad (4.19a)$$

$$K_{III} = \sigma \sqrt{H} [2 \sin(\pi b / H) / (1 + \cos(\pi b / H))]^{1/2}, \quad (4.19b)$$

where  $L$  is the characteristic length in the geometry of the crack,  $l$  is the half length of the crack,  $\sigma^0$  is the remote load,  $H$  is the thickness of the slab/zone in shear, and  $b$  is the anti-plane (mode III) displacement.

Eq. 4.14-4.17 are valid only at a particular area around the crack tip, shown by the darker shaded area in Fig. 4.7. At the crack tip, the first term of the stress expressions are singular, but no material can withstand infinite stresses so a possible explanation is an inelastic behavior of the material close to the tip. Far from the crack tips, outside the dark shaded area, the last term of the stress expressions can be too significant to be ignored so in those regions equations are not valid without a full definition of the last term. These equations describe the spatial distribution of the near-tip stress and the crack face displacement.

In the stress tensor expressions of the fracture growth mechanism, the shear stresses in Eq. 4.14 and 4.16 are similar to Eq. 4.2 and 4.3, which define the shear stresses around the rupture front. Also, the stress intensity expressions (Eq. 4.18 and 4.19) for fracture growth are similar to the stress intensity expression (Eq. 4.11) for



rupture propagation. So the fracture growth mechanism and the rupture propagation are similar mechanisms and therefore we proceed to model the effect of fracture growth by the rupture propagation physics.

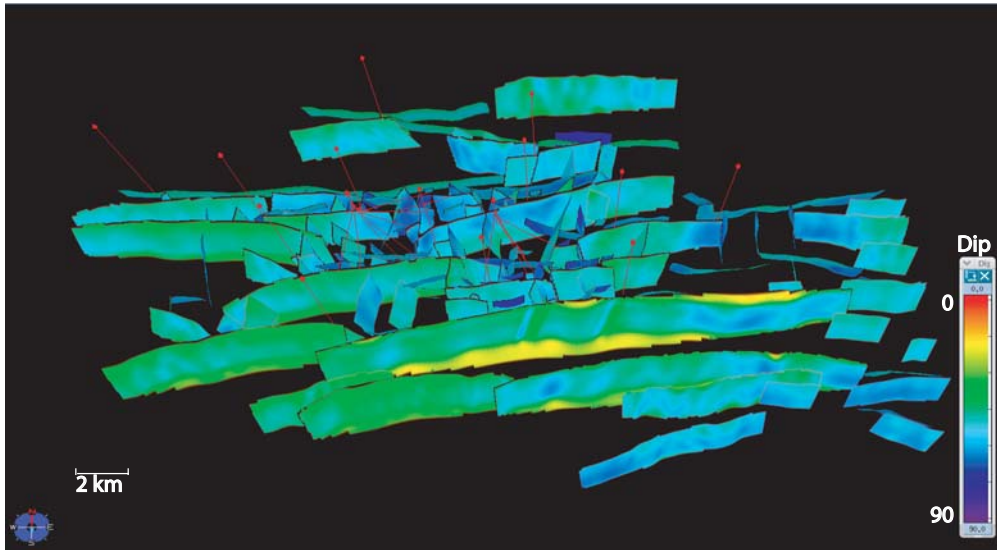
## **4.6 Methodology to estimate damage zone width using dynamic rupture propagation**

In previous sections, we have seen the concepts and analytical solutions related to the rupture propagation technique. In this section, we discuss the methodology of the rupture propagation technique to estimate damage zone properties. We also discuss the assumptions and uncertainties related to the input parameters, which are required to estimate the damage zone using this technique. The objectives of this chapter is to get a first order approximation of the damage zone width and in the next chapter we will see the nature of permeability anisotropy within the damage zone for the reservoir scale faults of the CS field. First, the structural model of the reservoir is discussed. Then, we discuss how to estimate and use the input parameters to achieve our objectives using the rupture propagation technique.

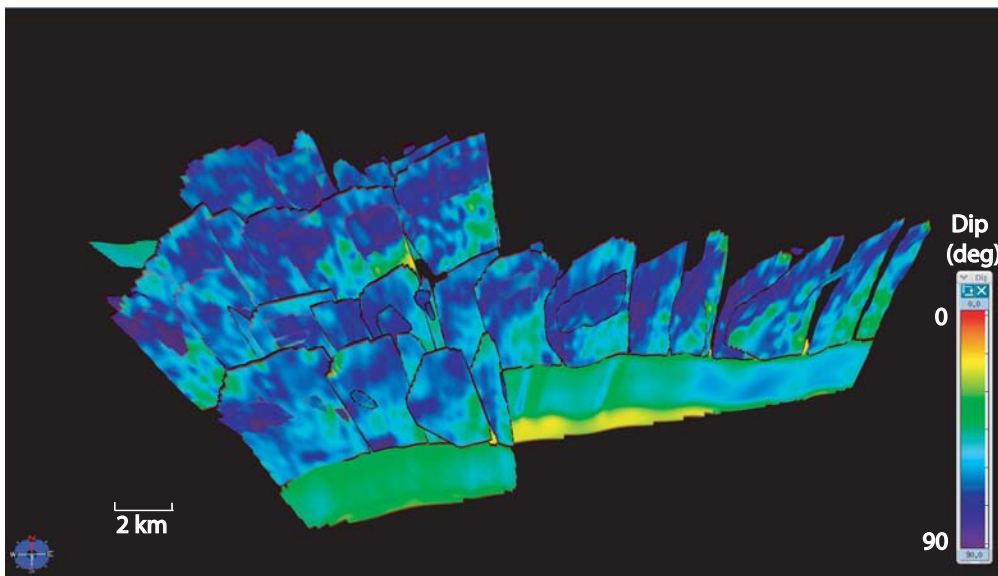
### **4.6.1 The structural model of the CS field**

The structural model of the CS field indicates that the major faults in the reservoir strike approximately EW. They form horsts and half-graben structures that developed sub-parallel to the NS direction in the geological past in a normal faulting environment. The structural model also indicates smaller faults striking sub-parallel to the NS direction, which may have formed in a different geological period. Fig. 4.8a indicates the dip of the reservoir scale faults. The average dip of the EW striking faults at reservoir depth is  $\sim 45^\circ$  with a maximum value of  $\sim 60^\circ$ . The NS striking faults have an average dip of  $\sim 60^\circ$  and the maximum dip is  $\sim 78^\circ$ . As shown in Fig. 4.8b, larger EW striking faults are extended up to shallow level ( $\sim 300\text{m}$  from surface) with higher average dip angle ( $\sim 65^\circ$ ) from reservoir level and a maximum dip angle of  $\sim 80^\circ$ . Fig. 4.9 illustrates the throw observed in the seismic surveys at reservoir depth. The average

value of throw is  $\sim 60\text{m}$  and maximum value is  $\sim 300\text{m}$  for the EW striking faults, while the average and maximum throw values for the NS striking faults are  $\sim 10\text{m}$  and  $\sim 60\text{m}$  respectively.



(a)



(b)

Fig. 4.8: Dip angle of the reservoir scale faults from seismic data (a) at reservoir depth and (b) above reservoir depth. At shallow level, faults are split and bluish color indicates a relatively high dip angle from reservoir level (greenish-yellowish color).

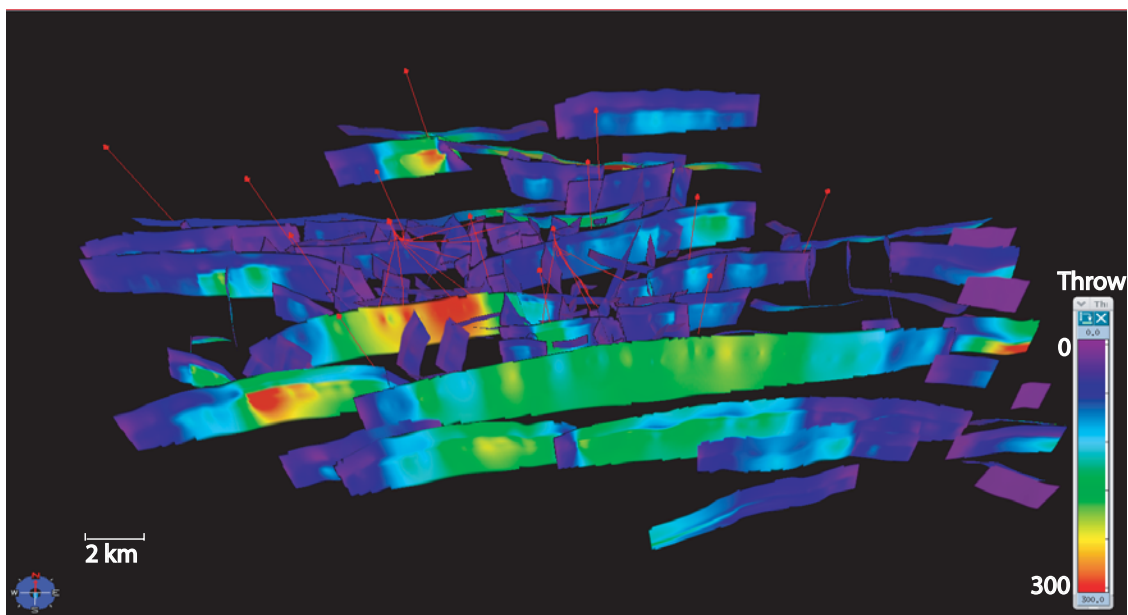


Fig. 4.9: Archaic time dip slip movement on the reservoir scale faults at reservoir depth. Red lines indicate well locations in the reservoir.

To determine whether the throw observed in the seismic data may have occurred under the present day stress conditions or in the geological past, we study the reservoir scale faults with respect to the present day stress field. Fig. 4.9 illustrates the Coulomb Failure Function (CFF) on a stereonet (lower hemisphere projection) where the red zones indicate the favorable geometries (strike  $\sim$ EW or  $\sim$ NS, and dip greater than  $60^\circ$ ), which may slip in the present day stress condition. This suggests that even though the E-W striking faults have favorable strike direction they may not slip at reservoir depth in the present day stress condition because their dip angle is too shallow ( $<60^\circ$ ). Hence, slip movement at reservoir depth on these faults must have occurred in a historical stress regime. However, some of the N-S striking faults at reservoir depth have strike and dip both optimally oriented for a shear failure. Shallow extension of large E-W striking faults may be active in present day stress state because of their higher dip angles, which also explains the split nature of these faults above reservoir level. Because the E-W striking faults show larger throw at reservoir depth than the N-S striking faults, they produce larger damage zones and dominate in reservoir fluid flow behavior (next chapter). In the next section, we estimate the historical stress regimes when these faults may have slipped and created most of the dynamic ruptures. We also

discuss other required parameters to estimate the damage zone width using dynamic rupture propagation.

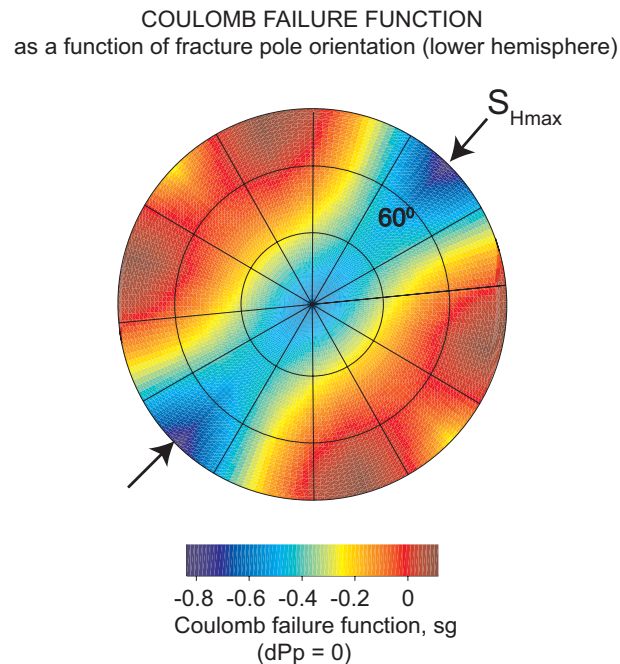


Fig. 4.10: Stereonet in a lower hemisphere projection shows the Coulomb Failure Function (CFF) values for all possible fault geometries. Dark red (positive CFF) indicates the favorable geometries (strike ~EW or NS and dip > 60°) of the faults which may slip in the present day stress condition.

#### 4.6.2 The historical stress regimes and the input parameters to estimate the damage zone width

To estimate the historical stress state when the EW reservoir scale faults may have slipped, first, we find all possible stress states which could result in slip on the faults with the given geometries and then constrain the magnitude and orientation of the stresses using the stratigraphic/geological history of the area. The geological history and the nature of slip observed through the seismic interpretations indicate a normal faulting or a dominant dip-slip regime when the EW striking faults might have slipped in the past. Hence, we assume a normal faulting stress regime ( $S_v > S_{Hmax} > S_{hmin}$ ) with maximum horizontal stress,  $S_{Hmax}$ , striking ~EW. Stratigraphic studies indicate that the reservoirs were at a shallow depth (~2/3 of the current reservoir depth of ~3500m) when most of the slip occurred in the EW striking faults. To pretend the

reservoir is at its historic shallower depth, we reduce the lithostatic gradient to  $\sim 2/3$  of the current lithostatic gradient ( $\sim 13$ ppg or  $0.0152$ MPa/m), which defines the vertical stress,  $S_v$ . The minimum horizontal stress,  $S_{hmin}$ , can be defined as  $\sim 2/3$  of the current minimum horizontal stress gradient i.e.  $\sim 8.8$ ppg or  $0.0104$ MPa/m.  $S_{Hmax}$  is assumed to be around the mean of  $S_v$  and  $S_{hmin}$   $\sim 10.52$ ppg or  $0.0123$ MPa/m. The historical stress regime of the NS striking fault is also a normal faulting environment, but the slip in this case is  $\sim$ EW. Hence, we assume a normal faulting stress regime with  $S_{Hmax}$  striking  $\sim$ NS. These faults may have been activated if  $S_{Hmax}$  at the time of the slip on the EW striking faults is relaxed to a level lower than the  $S_{hmin}$  of that time such that the horizontal stresses switched orientations. The magnitudes of the stresses when the NS faults slipped are estimated to be:  $S_v$   $\sim 13$ ppg or  $0.0152$ MPa/m,  $S_{Hmax}$   $\sim 8.8$ ppg or  $0.0104$ MPa/m, and  $S_{hmin}$   $\sim 8.7$ ppg or  $0.0106$ MPa/m. For both EW and NS striking faults, the pore pressure,  $P_p$ , is estimated as  $\sim 2/3$ rd of the current pore pressure gradient  $\sim 5.8$ ppg or  $0.0068$ MPa/m. These estimations are based on stratigraphic evidence, but they are a major source of uncertainty in determining the final objectives. In a later section we incorporate the effect of these uncertainties in estimating damage zone width.

The other input parameters that are required to estimate damage zone width in the dynamic rupture propagation technique are the velocity profiles (P-wave, S-wave, and rupture velocities), the rock strength, and the stress drop during slip. First, we define the P-wave velocity using a power law of the confining pressure (Eq. 4.20). The P-wave velocity is calibrated against the P-wave velocity from the sonic logs at the present day reservoir depth  $\sim 4500$  m/s at  $\sim 3500$ m.

$$\alpha = 55(P_{conf})^{1/4}, \quad (4.20)$$

where  $\alpha$  is the P-wave velocity in m/s.  $P_{conf}$  is the confining pressure at depth, defined by the mean of the principal stresses in the present day condition (Eq. 4.21). Stress gradients in the present day condition are estimated in the previous chapter using wellbore measurements and frictional faulting theory.

$$P_{conf} = z * (S_v\_grad + S_{h_{min}}\_grad + S_{H_{max}}\_grad) / 3, \quad (4.21)$$

where depth,  $z$ , is in meters and the principal stress gradients,  $S_v\_grad$ ,  $S_{h_{min}}\_grad$ , and  $S_{H_{max}}\_grad$  are in Pa/m.

Then all other parameters except stress drop are correlated to the P-wave velocity. The S-wave velocity,  $\beta$ , is correlated to the P-wave velocity by Eq. 4.22, which is calibrated from the S-wave measurements available in well CSU2. Rupture velocity,  $v$ , is related to the S-wave velocity as a gradient from the deepest point on the faults to the shallowest point on the faults of the study area (Eq. 4.23).

$$\beta = 0.55\alpha \quad (4.22)$$

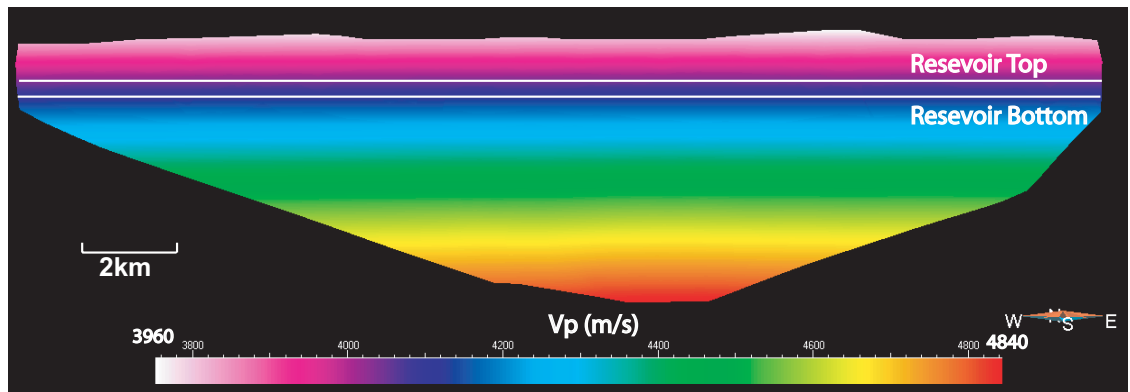
$$\begin{aligned} v &= 0.9\beta \text{ at the deepest point in all faults} \\ &= 0.67\beta \text{ at the shallowest point in all faults} \end{aligned} \quad (4.23)$$

The Uniaxial Compressive strength, UCS, is related to the P-wave slowness,  $\Delta t$ , by Eq. 4.24, where  $\Delta t$  is in  $\mu\text{s}/\text{ft}$  and UCS is in MPa. This relation is derived by calibrating the log measurements and the core measurements from the sandy intervals at reservoir depths. Rock strength is related to the UCS, which is based on the triaxial measurements (discussed in chapter 3; ConocoPhillips internal report, 2003) done on the core samples at reservoir depth (Eq. 4.25).

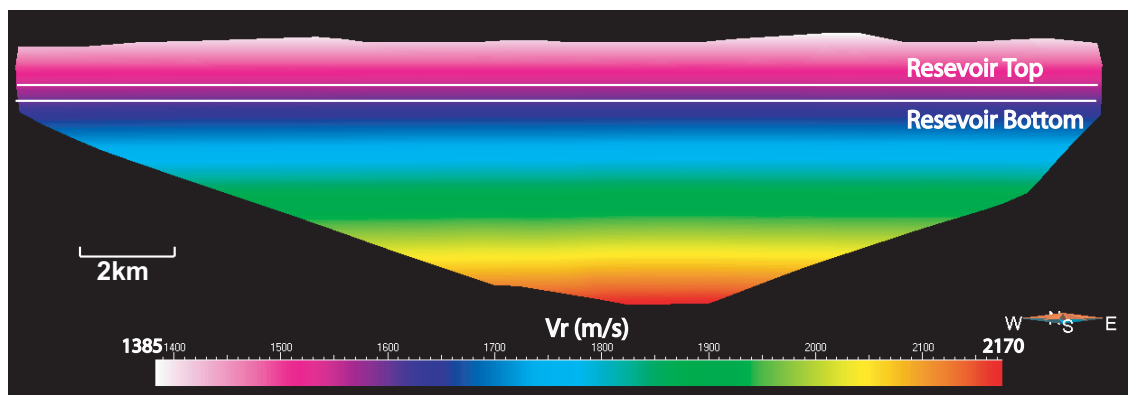
$$UCS = 1000 * \exp(-0.037\Delta t) \quad (4.24)$$

$$rock\_strength = UCS + 0.5P_{conf} \quad (4.25)$$

In all the above calculations, the parameters are estimated using  $P_{conf}$  at  $\sim(2/3)$  of the current depth to pretend the reservoir depth at the time of slip. Stress drop is assumed to be  $\sim 1\text{MPa}$  which is a typical value observed from the earthquake data on the faults of this size. Fig. 4.11a and 4.11b show the P-wave velocity and the rupture velocity profiles respectively. Fig. 4.12 shows the rock strength profile for a reservoir scale fault.



(a)



(b)

Fig. 4.11: (a) P-wave velocity and (b) Rupture velocity profiles along a reservoir scale fault. These velocity profiles are calculated using confining pressure at a depth  $\sim 2/3$  of the current depth to model the stress environment where we postulate that fault slip occurred.

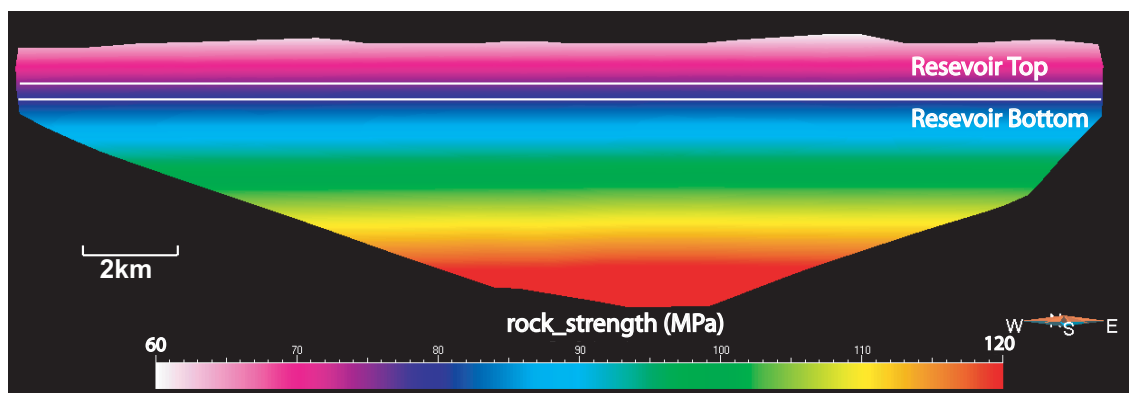


Fig. 4.12: Rock strength profile along a reservoir scale fault. This rock strength profile is calculated using confining pressure at a depth  $\sim 2/3$  of the current depth to model the stress environment where we postulate that fault slip occurred.

### 4.6.3 Rupture source and propagation along a fault plane

We want to model the damage zone associated with the growth of a fault; using the dynamic rupture technique, we want to replicate the same effect. This section discusses the rupture source to model the effect of rupture propagation along a fault plane. For a reservoir that does not have any recorded earthquake data such as this study area, we can not identify the actual source points of the rupture initiation. So we need to assume something about where the source point is located. A reasonable choice for the rupture source is the bottom center part of the fault, which simulates a fault growing from bottom to top (Fig. 4.13). The dynamic rupture starts from a source with a simple circular shape but gradually becomes elliptical because the dynamic stress intensity for an on-plane shear is larger than an anti-plane shear (Fig. 4.13). So for a dip-slip fault, the rupture prefers to travel along the dip rather than along the dip direction.

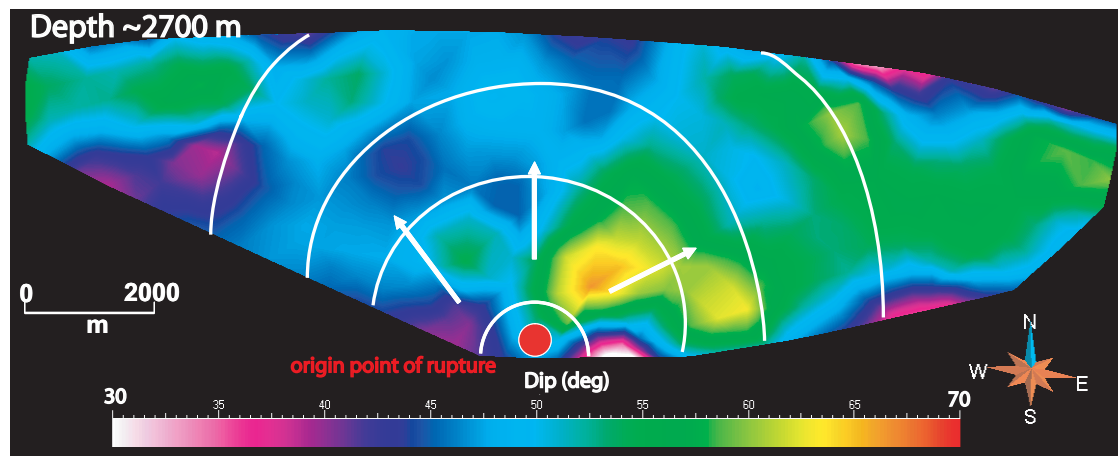


Fig. 4.13: Rupture is assumed to originate at the bottom-center of the fault. The rupture zone initially has a circular pattern but gradually becomes elliptical. Color in the figure indicates dip on the fault plane.

For the simplicity of calculation, we also assume that the global coordinate system at the source point is parallel to a local coordinate system at the rupture front i.e. x-axis parallel to the average strike direction, z-axis parallel to the dip of the fault, y-axis perpendicular to the fault plane (Fig. 4.14). This is a valid assumption because reservoir scale faults are generally planer on a first order approximation, and the rupture prefers to propagate along the weakest path, i.e. the fault plane.



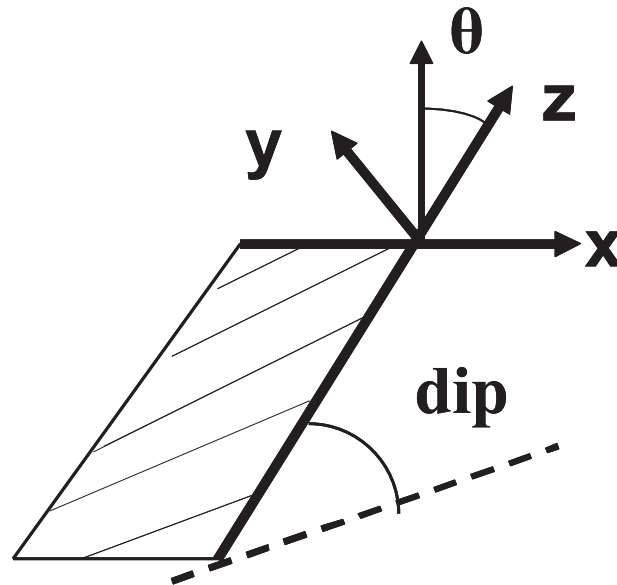


Fig. 4.14: The coordinate system at the rupture front i.e. x-axis parallel to average strike direction, z-axis parallel to dip of the fault, y-axis perpendicular to the fault plane.

#### 4.6.4 Fracture density and failure plane directions within the damage zone

Once we know the source point of the dynamic rupture and the input parameters to model its effects, we can use the combined solution of Freund (1979) and Madariaga (1976) to estimate the stress perturbations around the reservoir scale faults. Fig. 4.15a, 4.15b and 4.15c illustrate the components of the stress tensor at the rupture front in the directions  $0^\circ$ ,  $45^\circ$ , and  $90^\circ$  from the fault plane. Stress values are calculated at the reservoir depth ( $\sim 3500\text{m}$ ) of the same fault shown in the Fig. 4.11-4.13. We see that the shear component,  $s_{zy}$ , is the dominant component (larger than normal components) in all three cases, which creates high angle features in the damage zone. In the case along the fault ( $0^\circ$  from z axis),  $s_{zy}$  is the largest component, and the  $s_{zz}$  and  $s_{zx}$  components are almost zero, which creates large failure features that strike sub-parallel to the parent fault. These large fault parallel features ahead of the rupture front help to propagate the rupture along the fault plane, or in an actual growing fault case, some of these failure planes coalesce and support growing the fault. In a direction perpendicular to the fault plane, the  $s_{zx}$  and  $s_{zz}$  components are larger in comparison to the  $0^\circ$  case, which reduces the size of the features. These features also strike at a slight angle to the strike of the parent fault. In the  $0^\circ$  case, the principal stresses are almost sub-parallel to

the coordinate system, with maximum compression sub-parallel to the parent fault and minimum compression perpendicular to the fault. For the  $90^\circ$  case, the principal components are at an angle from the coordinate system, which orients the failure features closer to vertical than the  $0^\circ$  case, but they are smaller in size.

In Fig. 4.15, we can see that without the rupture propagation effect, the far-field octahedral shear is lower than the rock strength so failures do not occur. During rupture propagation, the rupture front octahedral shear combines with the far-field octahedral shear stress and the total exceeds the rock strength, which creates damage around the rupture front. The dimension of the damage zone is largest in the  $0^\circ$  case ( $\sim 78\text{m}$ ) and gradually decreases to  $\sim 42\text{m}$  in a direction perpendicular to the faults. This gives an elliptical shape to the damage zone with the major axis parallel to the fault.

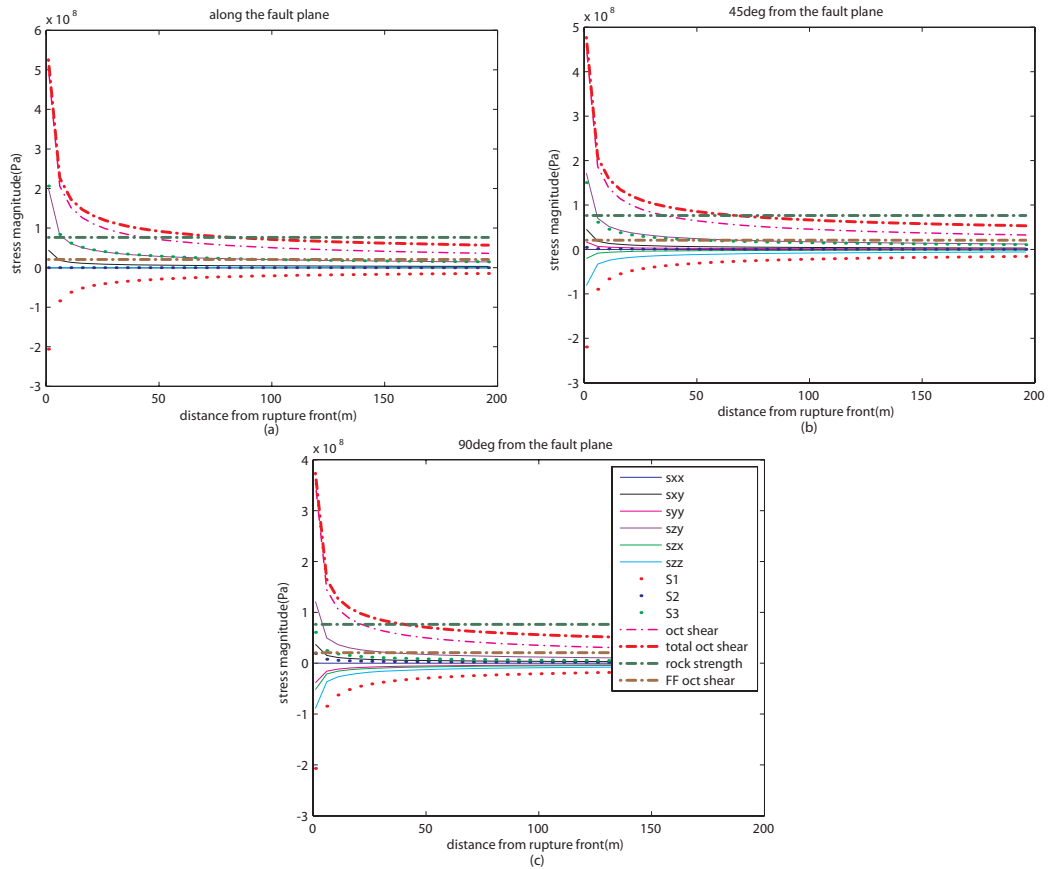


Fig. 4.15: Stress tensor, principal stresses, octahedral shear stress due to dynamic rupture propagation, far-field octahedral shear stress, total octahedral shear stress, and rock strength at (a)  $0^\circ$  (b)  $45^\circ$  (c)  $90^\circ$  from the fault plane. The damage zone is created when total octahedral shear stress is greater than rock strength.

Fig. 4.16a and 4.16b show the schematic of the damage zone dimension and the nature of failure planes in cross section and map view respectively. In the damage zone of the studied fault, which is a normal fault by origin, the dynamic rupture hypothesis predicts a normal faulting pattern for the secondary failure features. In the direction perpendicular to the fault plane ( $90^\circ$  case) they are closer to vertical, and ahead of the rupture front ( $0^\circ$  case) they are parallel to the parent fault. The strikes of the failure planes are at an angle to the strike of the parent fault for the  $90^\circ$  case (high angle case), while they are parallel to the strike of the parent fault in the  $0^\circ$  case. This is consistent with the field observations where we see secondary normal fault adjacent to a large normal faults. Stress intensity increases towards the rupture front, which results in a higher fracture intensity. In our study area, the dynamic rupture technique predicts

damage zone features trending sub-parallel to parent faults and dipping at high angle ( $>60^\circ$ ) so they are optimally oriented in the present day stress state as shown in Fig. 4.10. And they give a preferential flow parallel to the strike of the parent fault. High angle failure planes increase the permeability in the vertical direction, but the effect will be less or negligible along the dip of the parent fault, particularly for a reservoir with high matrix permeability such as our study area. This is due to the limited damage zone width and the strike of the secondary failure planes being sub-parallel to the strike of parent fault. In the next chapter, we discuss a fine scale simulation study to show the effects of permeability anisotropy on a grid block of the upscaled model (simulation model) due to the presence of the damage zone.

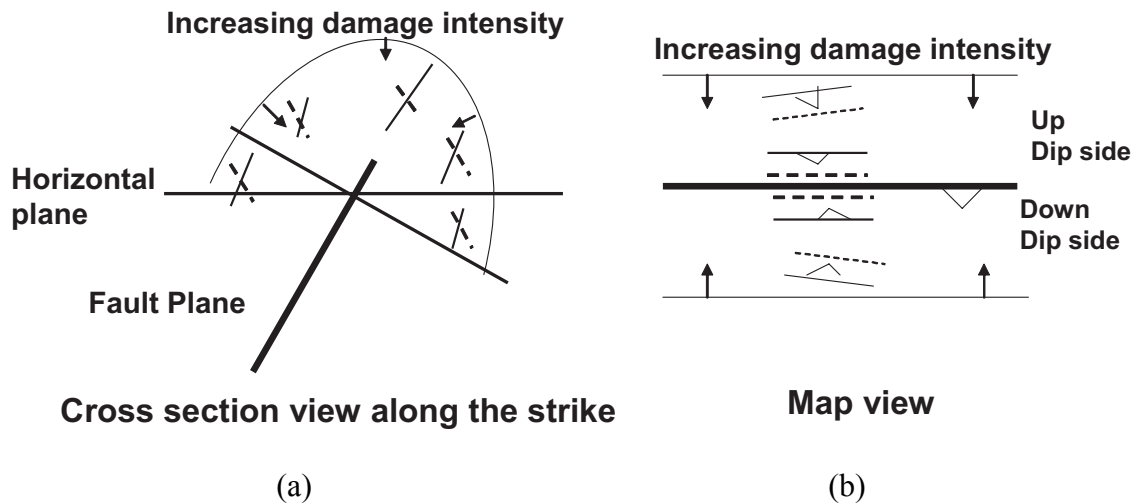


Fig. 4.16: (a) Cross section view of the damage zone along the strike, and (b) Map view of the damage zone. Away from the fault plane ( $90^\circ$ ) failure planes are at higher angle than along the fault plane ( $0^\circ$ ) and damage intensity increases as we get close to the fault.

#### 4.6.5 Monte Carlo Simulation of the input parameters

As discussed before, the input parameters and the stress values used to model the damage zone may include a lot of uncertainties. This section discusses how to incorporate the effects of those uncertainties in estimating the properties of the damage zone. This is done with Monte Carlo Simulation of each parameter at every estimation point. The Monte Carlo method uses pseudo-random numbers to incorporate the

uncertainty around the best possible value of a parameter. In this study, the pseudo-random numbers are generated by a Gaussian algorithm, in which we assume the best possible value as the mean value and define a standard deviation around it to incorporate the range of uncertainty in the parameter.

We have already discussed the workflow to estimate mean values of the parameters in the previous sections. Table 4.1 lists the mean and uncertainty range of input parameters used in Monte Carlo Simulation at reservoir depth  $\sim 3500\text{m}$ . Along the faults, uncertainty range of stresses, pore pressure, P-wave velocity ( $\alpha$ ), S-wave velocity ( $\beta$ ), and rupture velocity ( $v$ ) increases with the depth.

Table 4.1: Mean and range of the input parameters (at  $\sim 3500\text{m}$  depth) used in Monte Carlo Simulation

Parameters	Mean (units)	Range (units)
$S_v$	53.20 MPa	45.5 – 61.5 MPa
$S_{H\max}$	43.05 MPa	35 – 51 MPa
$S_{H\min}$	36.40 MPa	28 – 45.5 MPa
Pore pressure	23.8 MPa	20 – 25 MPa
Stress drop	1 MPa	0.4 – 1.6 MPa
P-wave velocity ( $\alpha$ )	4050 m/s	3800 – 4300 m/s
S-wave velocity ( $\beta$ )	2225 m/s	2050 – 2400 m/s
Rupture velocity ( $v$ )	1575 m/s	1450 – 1700 m/s
UCS	62 MPa	50 – 75 MPa
Rock strength	78 MPa	65 – 90 MPa

Fig. 4.17 illustrates the uncertainty ranges and the corresponding effects on the damage zone width using cross plots at the reservoir depth ( $\sim 3500\text{m}$ ) of the same fault shown in Fig. 4.11. The analysis of 100 simulations indicates that stress drop is the most sensitive parameter in determining the width of the damage zone using the dynamic rupture technique. The histogram of the damage zone width shows a dominant uncertainty range of the damage zone width is between 20m to 60m with an average of  $\sim 45\text{m}$ ; however, if we include outliers this may go up to 120m.

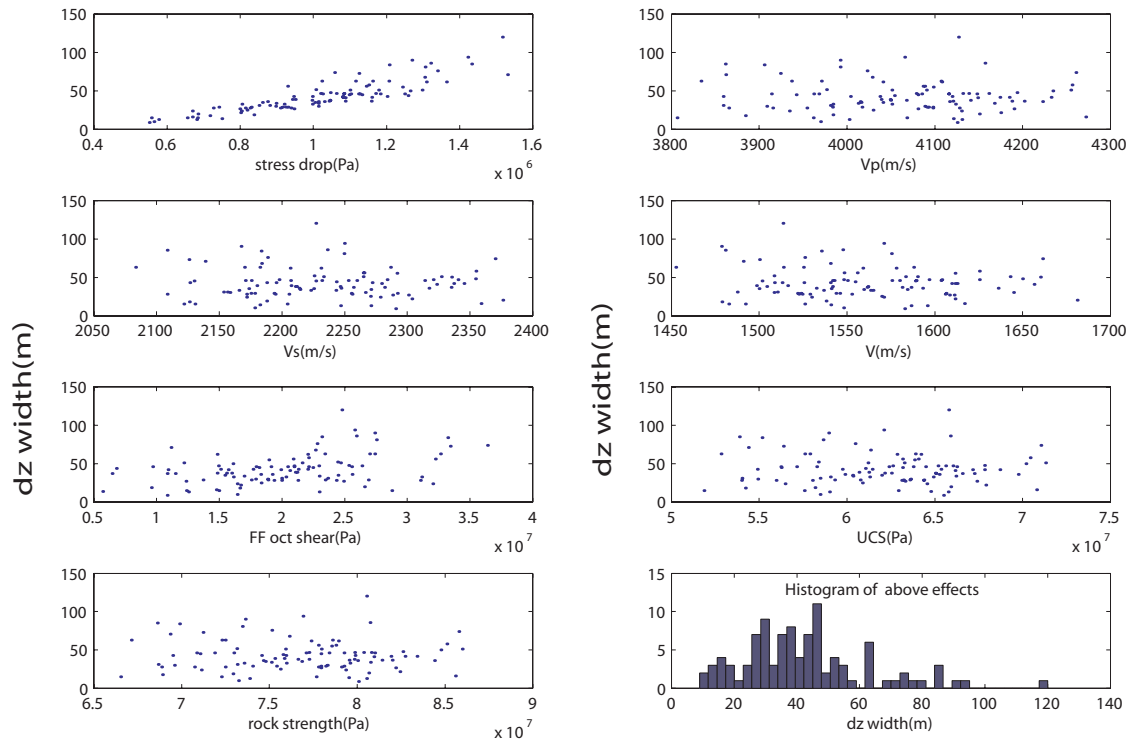


Fig. 4.17: Variation in the damage zone width with respect to the uncertainty in the input parameters stress drop, P-wave velocity, S-wave velocity, rupture velocity, far-field octahedral shear stress, uniaxial compressive strength, and the rock strength. The damage zone modeling is most sensitive to the stress drop among all the input parameters. The histogram of damage zone width shows the dominant uncertainty range is between 20m to 60m with an average  $\sim 45$ m.

Fig. 4.18 shows four out of the 100 simulations included in the Fig. 4.17 over the entire fault. Fig. 4.19 shows the mean and standard deviations of damage zone width from all 100 simulations. At reservoir depths, the damage zone width is  $\sim 40$ -60m at the center of the fault and  $\sim 70$ -100m at the edges of the faults, which is consistent with the field observation of the damage zone width for the faults of this length (Fig. 4.3). The standard deviation or uncertainty range of the damage zone width is on the order of  $\sim 5$  m to 20m at the reservoir depth but higher in places where the estimated damage zone width is larger, i.e. the size of the uncertainty scales with the size of the damage zone.

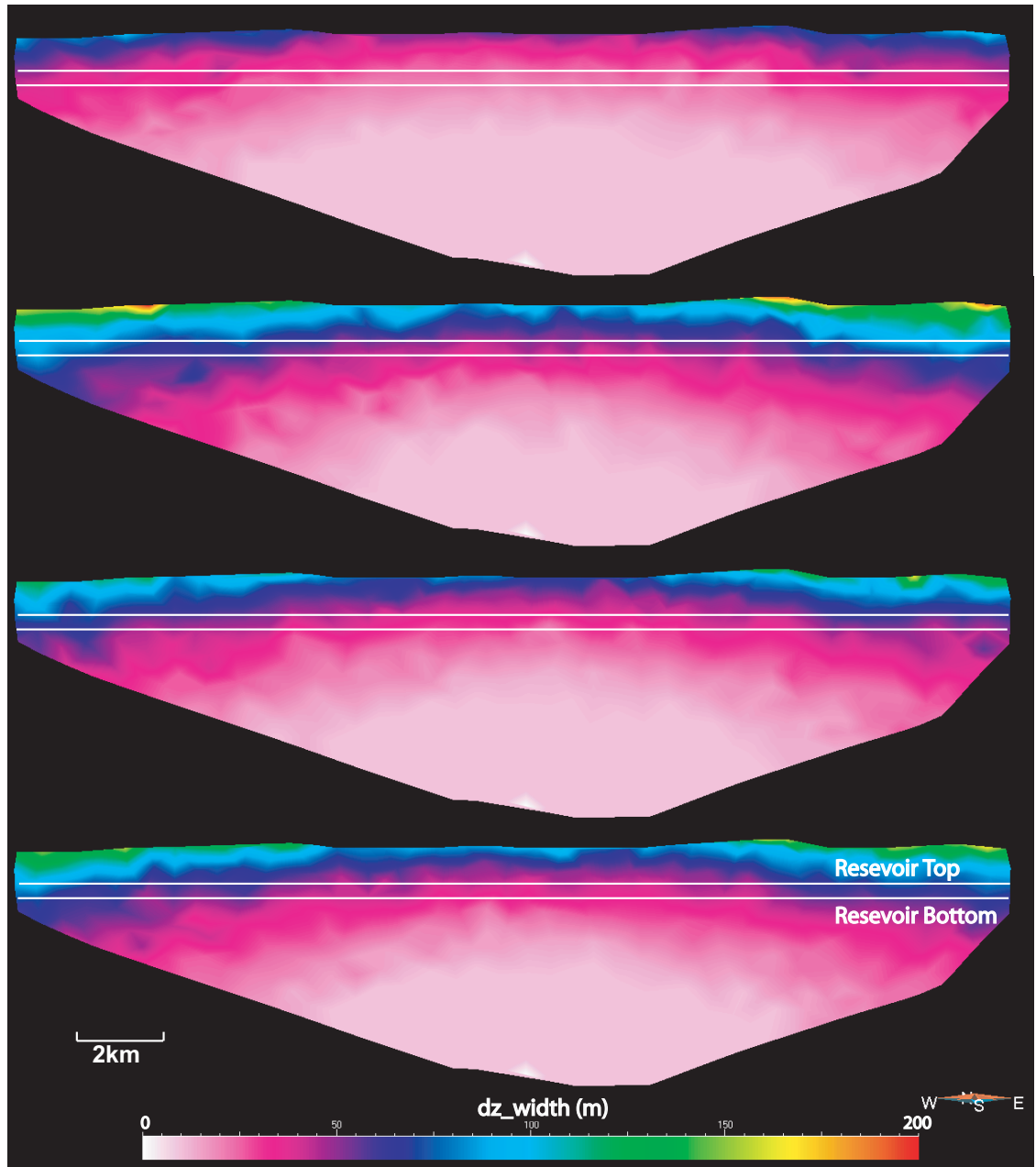
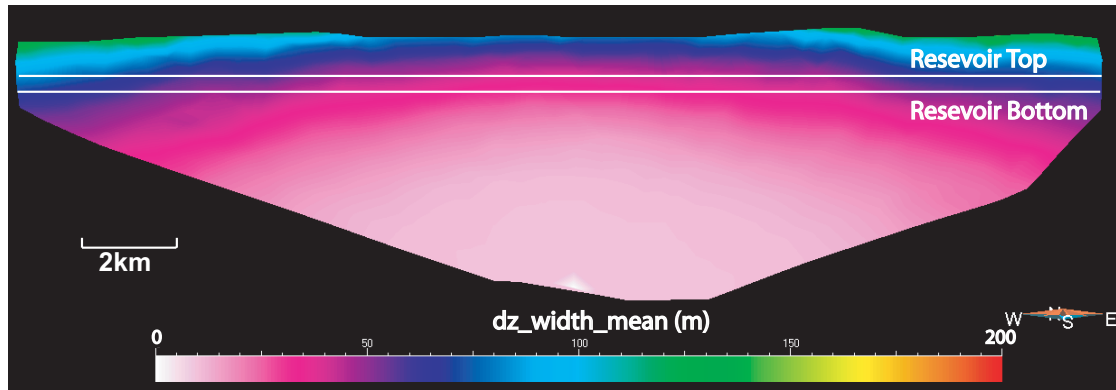
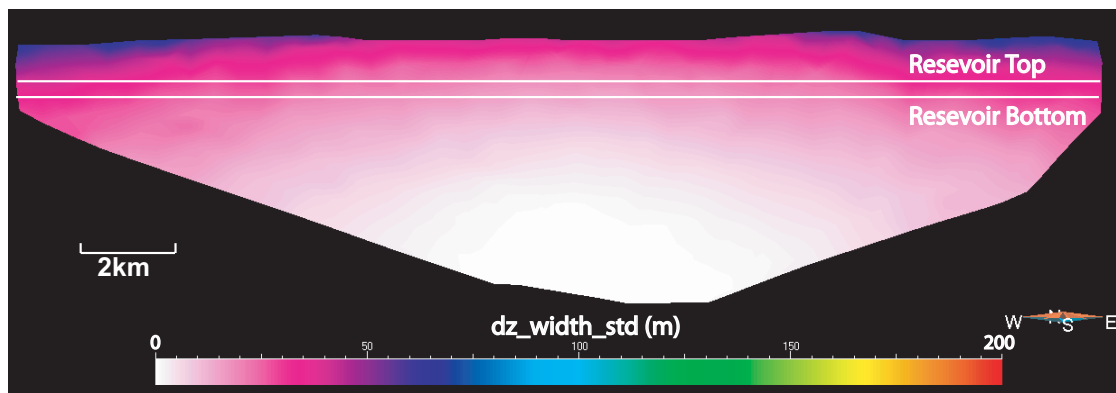


Fig. 4.18: Four simulations of the damage zone width. Reservoir depth lies between the white lines where damage zone width varies between  $\sim 40\text{-}60\text{m}$  at the center of the fault and  $\sim 70\text{-}100\text{ m}$  close to the edges of the fault.



(a)



(b)

Fig. 4.19: (a) The mean and (b) the standard deviation of the damage zone width (m) from 100 simulations. The average damage zone at the reservoir depth varies from  $\sim 40$ m at the center to  $\sim 80$ m at edges. Standard deviation increases with the increase in the damage zone width.

## 4.7 Damage zone modeling of the Nojima Fault: well scale calibration of the rupture propagation technique

In the previous section, we have seen that the dynamic rupture technique gives reasonable values for the damage zone width in one of the reservoir scale fault in the CS field. However, there is no way to calibrate the technique at smaller scale because the faults in the study area are subsurface faults and none of the wells drill through any of the reservoir scale faults. To calibrate the technique at well scale, we model the damage zone of the Nojima fault and compare this with the observations of the damage zone in the scientific boreholes drilled through it.



#### 4.7.1 Location of the Nojima Fault and the scientific boreholes

The Nojima fault runs along the northwestern margin of the Awaji Island of Japan for ~8km and extends beneath the Osaka Bay for ~12km (Fig. 4.20). This fault is a right-lateral active fault with a minor reverse component. It trends in NE-SW direction (average strike ~N40°E) and dips in SE direction at a high angle (~80°). It juxtaposes granitic and grano-diorite rocks and partly overlain by the sediments of different geological ages (Ando, 2001; Tanaka et al., 2001).

The 1995 Hyogo-ken Nanbu (Kobe) earthquake,  $M = 7.2$ , ruptured the Nojima fault and resulted ~6500 fatalities. The surface rupture was generated along the Nojima fault but extended farther southwest with a total length of ~10-18km (Awata et al., 1996; Lin and Uda, 1996). The hypocenter of the earthquake was located ~10km beneath the Akashi Strait and the rupture propagated bilaterally towards Kobe and Awaji Island (Ide et al., 1996; Hashimoto et al., 1996). After the earthquake several scientific institutions drilled boreholes close to the hypocenter to reveal the mechanism of healing and recovery process of the fault zone. GSJ (Geological Survey of Japan) and NIED (National Research Institute for Earth Sciences and Disaster Prevention) selected the Hirabayashi site and DPRI (Disaster Prevention Research Institute, Kyoto University) selected the Toshima site, 5km south of the Hirabayashi site, to drill the boreholes (Fig. 4.20). The drilling site consists of granite and partly covered with sediments. This location was selected because it is located near a branching of the Nojima fault and there was a chance of hitting multiple faults with deep drilling, enabling a comparison of properties of the fault zones with depth (Fig. 4.21). In this study, we compare the damage zone width observed in the boreholes drilled by GSJ and NIED with the damage zone estimated using the rupture propagation technique.

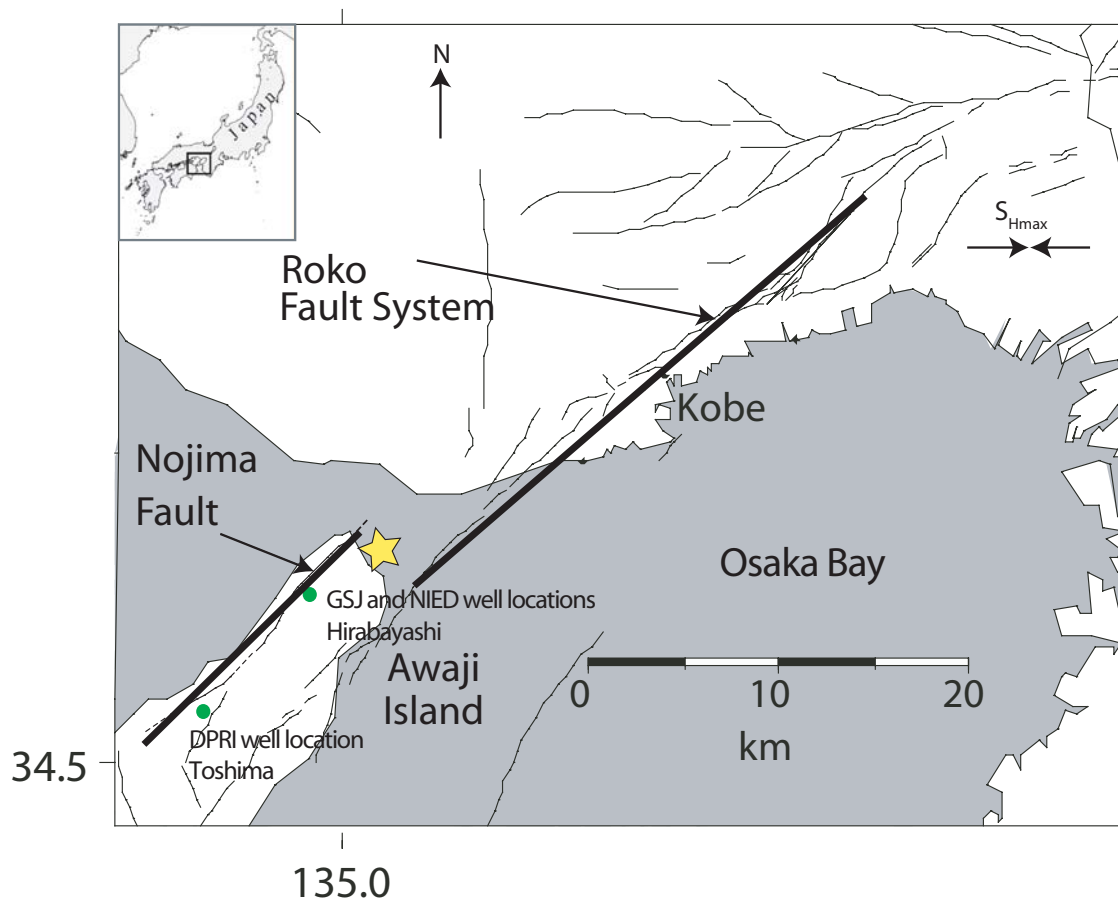


Fig. 4.20: Map showing the Nojima Fault – source of the M 6.9 1995 Kobe earthquake. It is an NE trending fault with dip angle  $\sim 80^\circ$  oriented in SE direction. Green dots are the locations of the DPRI, GSJ, and NIED boreholes drilled into the Nojima Fault.

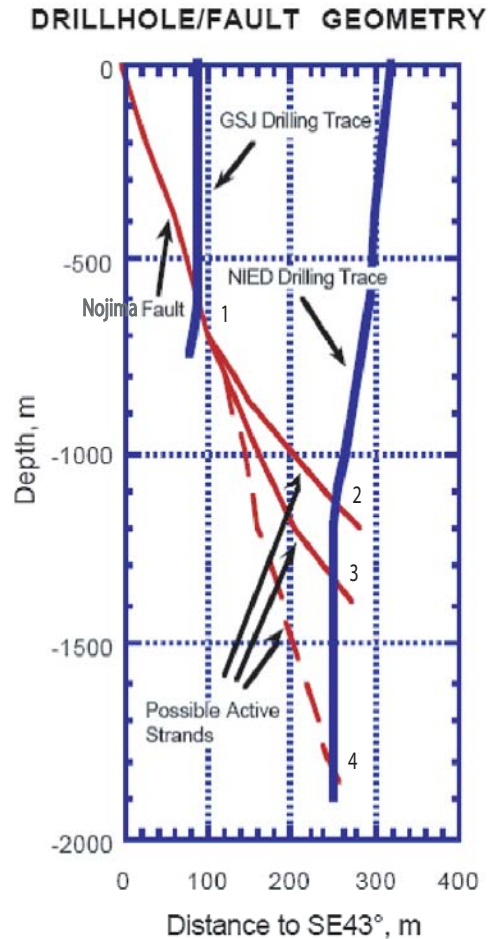


Fig. 4.21: Schematic diagram of the Nojima fault in the vicinity of GSJ and NIED boreholes, showing the depths at which shear zones were intersected (Lockner et al., 2003).

#### 4.7.2 Input parameter and model of the Nojima fault

The dimension and properties of the Nojima fault for this study is based on the study done by Wald (1995). Wald (1995) used near-source ground motions, teleseismic body waveforms, and geodetic displacements produced by the 1995 Kobe, Japan, earthquake to determine the spatial and temporal dislocation pattern on the faulting surfaces. He used a two-fault model, with rupture planes beneath Kobe and Awaji Island. He found that the ground motions recorded within the severely damaged region of Kobe originated from the part beneath Kobe, which is relatively deep ( $\sim 10$ km) and has relatively low slip ( $\sim 1$ m) in comparison to shallower ( $\sim 5$ km) part beneath Awaji Island with  $\sim 3$ m of slip. Fig. 4.22 shows a schematic of the slip distribution found by Wald (1995) and the location of the rupture source. As discussed in previous sections,

the rupture front tends to be elliptical in shape. In this case, the major axis of the ellipse is sub-parallel to the fault plane in the dip direction because the Nojima fault is a strike slip fault and rupture front prefers to travel in the anti-plane direction (along the dip) rather than the on-plane direction (along the strike). Table 4.2 illustrates the parameters to define the dimensions and properties of the Nojima fault and the rupture source used in this study.

Table 4.2: Parameters used to define dimension and properties of the Nojima Fault

Fault length	20 km
Fault width	20 km
Average dip	80°
Average strike	N40°E
Depth of the rupture source point (Hypocenter)	16.5 km (below the epicenter)
P-wave velocity range at 0-20km depth	2.5 -7.1 km/s
S-wave velocity range at 0-20km depth	1.2 -3.8 km/s
Rupture velocity range from surface to source	0.67 - 0.9 of S-wave velocity
$S_{Hmax}$ gradient	0.0283 MPa/m
$S_v$ gradient	0.0226 MPa/m
$S_{hmin}$ gradient	0.0214 MPa/m
$P_p$ gradient	0.0100 MPa/m
Stress drop	1 MPa

The uniaxial compressive strength, UCS, around the Nojima fault is defined using the P-wave velocity,  $\alpha$ , by Eq. 4.26, which is the modified form of UCS model proposed by Hickman and Zoback (2004) for the granites around the San Andreas Fault. To calculate rock strength from the UCS, we use Eq. 4.25 with a coefficient of 0.75, which incorporates the higher frictional strength of the granite.

$$UCS = 60 + 0.0145\alpha \quad (4.26)$$

where UCS is in MPa, and  $\alpha$  is in m/s. Fig. 4.23a and 4.23b illustrates P-wave and rupture velocity profiles, and Fig. 4.24 indicates rock strength along the fault. Uncertainty in the input parameters are incorporated using the Monte Carlo Simulation with the standard deviations mentioned in the Table 4.1.

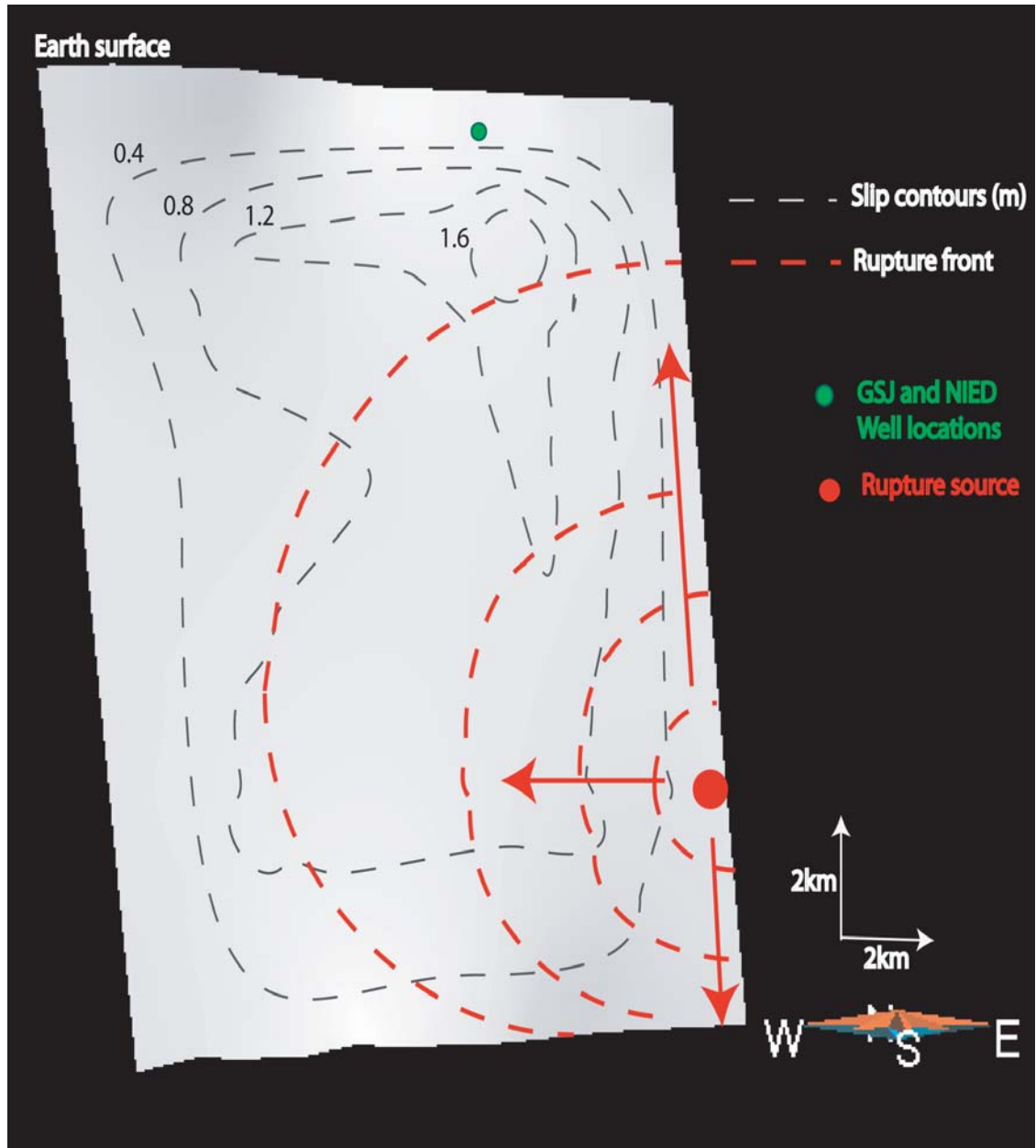
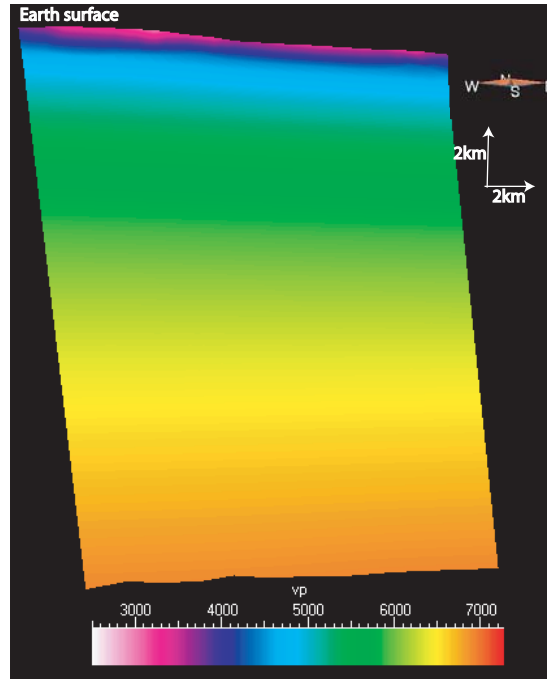
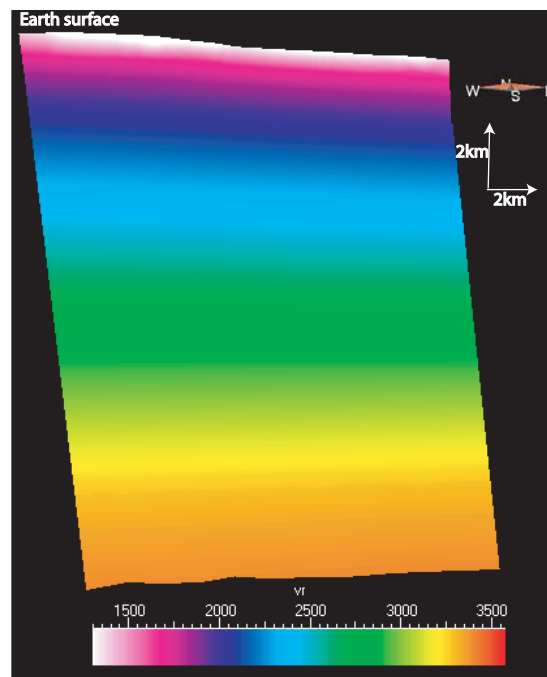


Fig. 4.22: A cross sectional view of the Nojima fault from the south. Gray dashed lines indicate slip on the fault due to Kobe 1995 earthquake, estimated by combined source inversion technique (Wald, 1995). Red dot is the hypocenter or rupture source point of the earthquake, which is located  $\sim 17$ km beneath the surface at the edge of the fault. Rupture front (red dashed line) starts as a circular pattern but gradually becomes elliptical with major axis sub-parallel along the strike direction because dynamic stress intensity for an on-plane shear (along the strike) is larger than an anti-plane shear (along the dip).



(a)



(b)

Fig. 4.23: (a) P-wave velocity and (b) Rupture velocity profiles along the Nojima fault. P-wave velocity profile is based on the model used by Wald (1995).

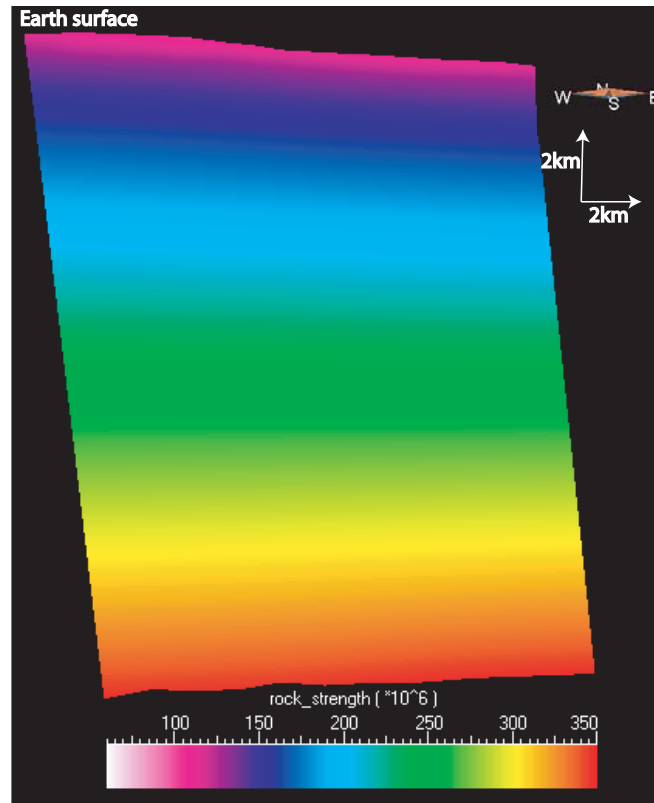
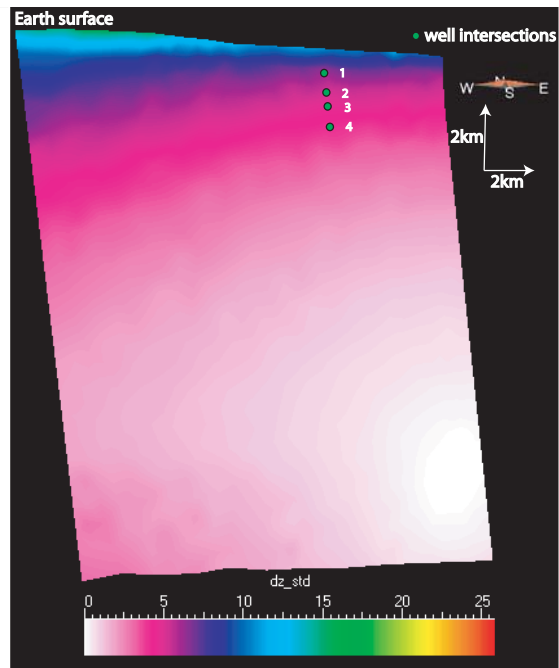


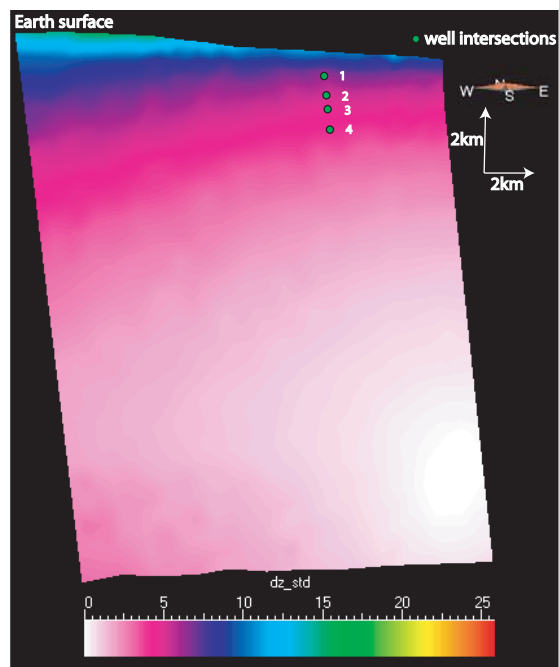
Fig. 4.24: Rock strength profile along the Nojima fault.

### 4.7.3 Modeling results and comparison with the observed data

Using the above input parameters within their uncertainty range, the damage zone width for 100 equally-likely cases is estimated by the dynamic rupture technique. Fig. 4.25a and 4.25b illustrate the mean and standard deviation of the damage zone width of 100 simulations. The mean values of the damage zone width decrease with the increase in depth. At the GSJ ( $\sim 625$  m) and NIED ( $\sim 1150$  m,  $\sim 1320$  m,  $\sim 1800$  m) intersection points with the Nojima fault, the estimated damage zone widths are  $\sim 44$  m,  $\sim 37$  m,  $\sim 33$  m, and  $\sim 23$  m respectively. At these intervals, the standard deviation values of the damage zone width from all simulations indicate a range of 3.5-7.0 m with higher range towards the shallower sections. Estimated damage zone widths are consistent with the damage zone width observed in the core samples from the boreholes (Fig. 4.26). Permeability measurements done in the core samples from these intersecting zones indicate a 4-5 higher order magnitude with respect to the intact rock.



(a)



(b)

Fig. 4.25: (a) Mean damage zone width and (b) standard deviation of the width in meters along the Nojima fault. Well intersections points are shown as 1,2,3, and 4. The damage zone width decreases with increase in depth.



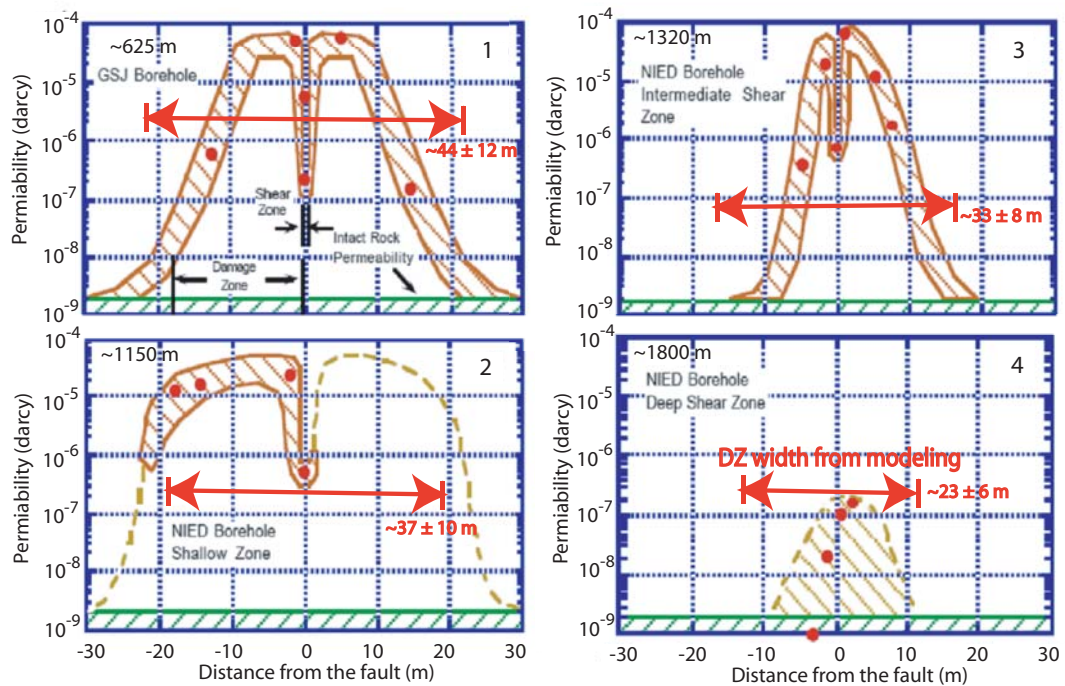


Fig. 4.26: The damage zone widths estimated using the rupture propagation technique (shown in red lines) are consistent with the damage zone width observed in GSJ and NIED boreholes. Matrix permeability measured at 50 MPa effective confining pressure indicate 4-5 order magnitude higher permeability in comparison to the intact rock permeability. (modified from Lockener et al., 1999)

## 4.8 Damage zone width for the faults from the CS field

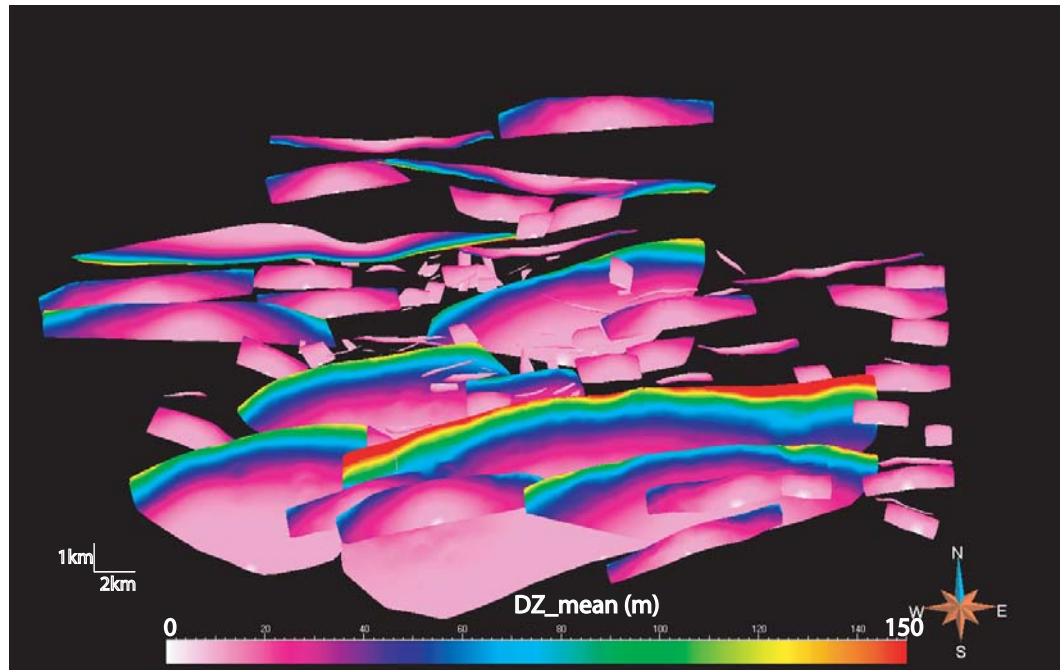
In this section, we discuss the damage zone modeling results for all the faults of the CS field using the dynamic rupture propagation technique. The input parameters are already discussed in a previous section. We use same input parameters for both E-W and N-S trending faults, except that they require different stress regimes to generate rupture on them.

Fig. 4.27a and 4.27b show the mean and standard deviation from the 100 simulations for all the E-W trending faults. At the reservoir depth, the average damage zone width from all faults varies from ~60m (center of the fault) to ~140m (edges of the fault). However, we can see that most of the contributions in this average value come from the few large faults and smaller faults have relatively narrow damage

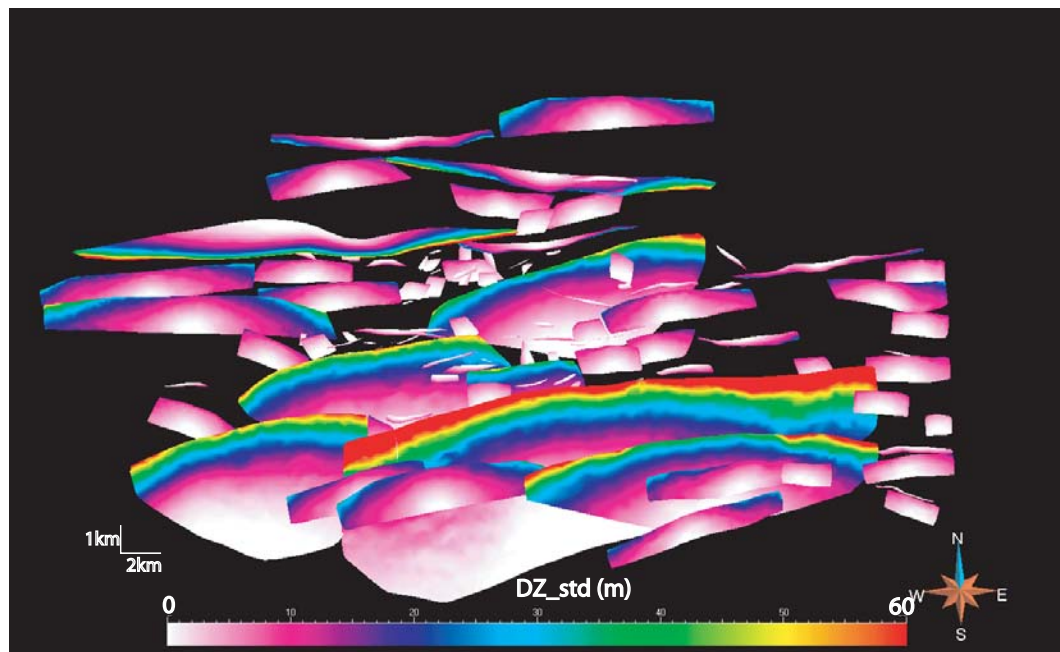
zones. Standard deviation for those 100 simulations varies from ~15-40m with higher values corresponding to higher damage zone width.

Fig. 4.28a and 4.28b illustrate the mean and standard deviation from 100 simulations using a west side view for all N-S striking faults. In this case, the average damage zone width at reservoir depth is ~20m at the center and ~60m at the edges, which is much smaller than the EW striking fault. This is because N-S striking faults are much smaller in size in comparison to E-W trending faults. The standard deviation in this case varies from ~7-18m.

As discussed before, interference and tracer tests between production and injection wells show high permeability anisotropy along the EW trending faults, which are consistent with the modeling results because larger damage zones width along E-W faults give better fluid flow path in comparison to smaller N-S trending faults. In the next section, we discuss a fine-scale simulation study through a damage zone to quantify the relative nature of permeability anisotropy in the reservoir due to the presence of damage zones.

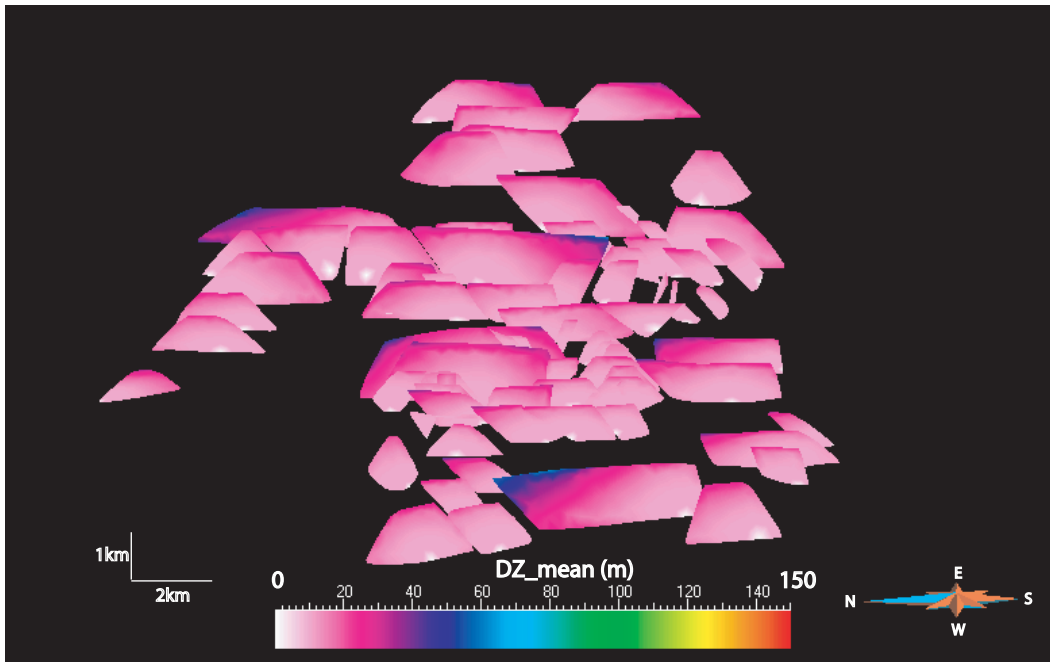


(a)

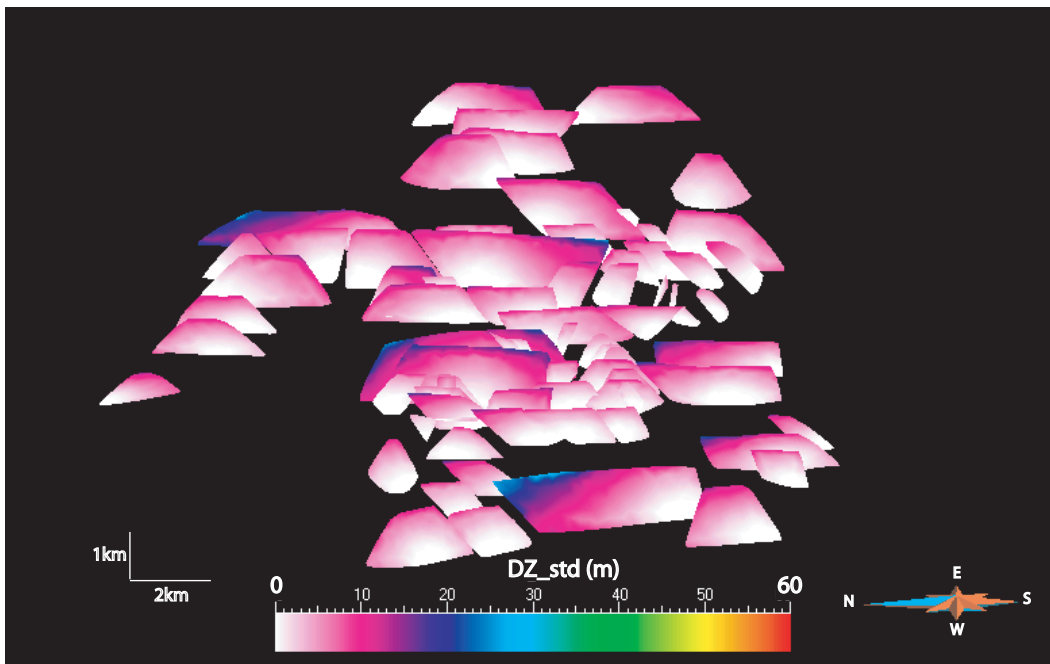


(b)

Fig. 4.27: (a) Mean damage zone width and (b) standard deviation of the width in meters along the EW trending fault of the CS field (south view).



(a)



(b)

Fig. 4.28: (a) Mean damage zone width and (b) standard deviation of the width in meters along the NS trending fault of the CS field (west view).

## 4.9 Conclusions

In this chapter, we presented a workflow to estimate the damage zone associated with reservoir scale faults using dynamic rupture propagation. We found that the damage zone width gradually increases with the increase of the distance from the rupture source because of the increasing dynamic rupture intensity factors. At the reservoir depth of the CS field, we found a damage zone width of ~50-140m for the E-W trending faults and ~20-60m for the N-S trending faults, which are reasonable values and consistent with the field observations. In this reservoir, secondary features in the damage zone are normal faults trending sub-parallel to the parent fault. These secondary features are optimally oriented for shear failure in the present day stress regime, which may provide high permeability along the reservoir faults. We also calibrated the damage zone width at well scale by the Nojima Fault study and find that results from dynamic rupture propagation technique are consistent with the core observations from the borehole drilled through the fault.

By implementing the effects of fractures associated with the reservoir scale faults to a simulation model, we can quantify the permeability anisotropy in the reservoir due to damage zones and can improve production predictability. In this study, we use analytical solutions to model damage zones, which gives a reasonable first order approximation. However, numerical modeling techniques using the same concepts will be needed for accurate results in a complex and dynamic environment.

In the next chapter, we present fine scale simulation studies to quantify the effect of damage zones in terms of permeability anisotropy. We also discuss the workflow to implement this permeability anisotropy in a reservoir simulation model and verify their effects with history matching of the production data in the CS field.

## 4.10 Appendix

### 4.10.1 Damage zone prior to faulting

Before a macroscopic failure, fracturing processes control the mechanical response of the rock mass. Evolving micro-cracks reduce the elastic moduli and strength of the rock and lead to a macroscopic failure. So a macroscopic failure may contain pre-failure micro-crack zones/damage zones around it. Laboratory studies indicate that the pre-failure fracturing processes can not be described using linear elastic fracture mechanics concepts alone. The theory of continuum damage mechanics explains the degradation of the elastic moduli and strength of the material in terms of an increase in the density of cracks (Kachanov, 1986). It is assumed that there are no cracks in the rock below the yield point. Deformations start when stress-strain is above the yield point, which can be modeled as a power law for viscous fluid (Turcotte and Glasscoe, 2004).

Experimental studies have demonstrated that the micro-cracks induced during loading are predominantly tensile cracks oriented parallel to the maximum compressive stress (Wong, 1982; Kranz, 1979). Most of the experiments done on the damage rheology describe the temporal evolution of the damage zone prior to a macroscopic failure, which is related to increase in micro-crack intensity in the rock. However, very few studies discuss on the spatial evolution of the micro-crack zones. Laboratory experiments by Lockner et al. (1992) (Fig. 4.29) and numerical modeling by Hamiel et. al. (2004) shows the spatial distribution of evolving damage zones. For a homogenous medium, damage is not localized in the early stages of micro-crack evolution. Latter stages localize the damage and in the final stage localized damage creates the macroscopic failure. However, in a heterogeneous medium, damage is concentrated around heterogeneities since the early stages and failure takes place along the maximum shear plane. Below, we discuss an analytical solution of the temporal evolution of the damage zone prior to faulting. We also discuss the spatial distribution of micro-fractures based on a field data set collected by Vermilye and Scholz (1998).

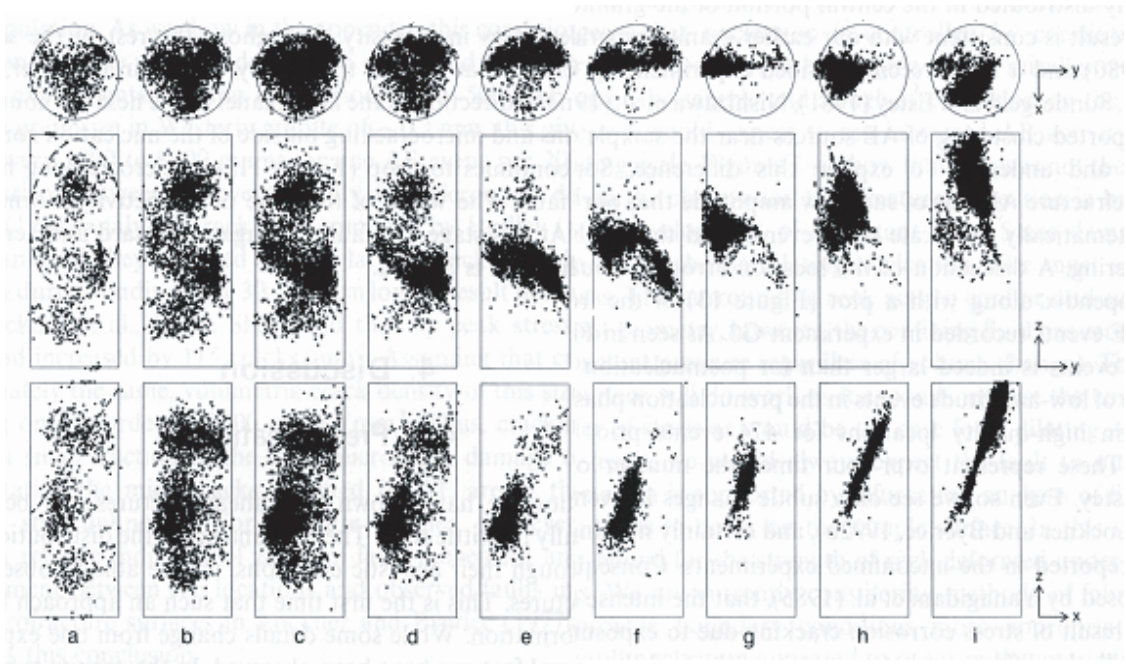


Fig. 4.29: Plots of Acoustic Emission (AE) locations for a Berea Sandstone sample under confining stress of 50 MPa. The axial stress increases from a to i with time. AE activity is not localized in the early loading stage of experiment but become localized along the failure plane in latter stages. (Lockner et al., 1992)

In order to simulate the damage evolution from an undamaged state, material has to cross yield stress,  $\sigma_y$ , and yield strain,  $\epsilon_y$ . If the stress,  $\sigma$ , is below yield stress, material behaves like a linear elastic material. However, if  $\sigma > \sigma_y$ , the damage occurs, which can be quantified using a non-dimensional damage variable,  $\alpha$ , which depends on the density of micro-cracks (Fig. 4.30).



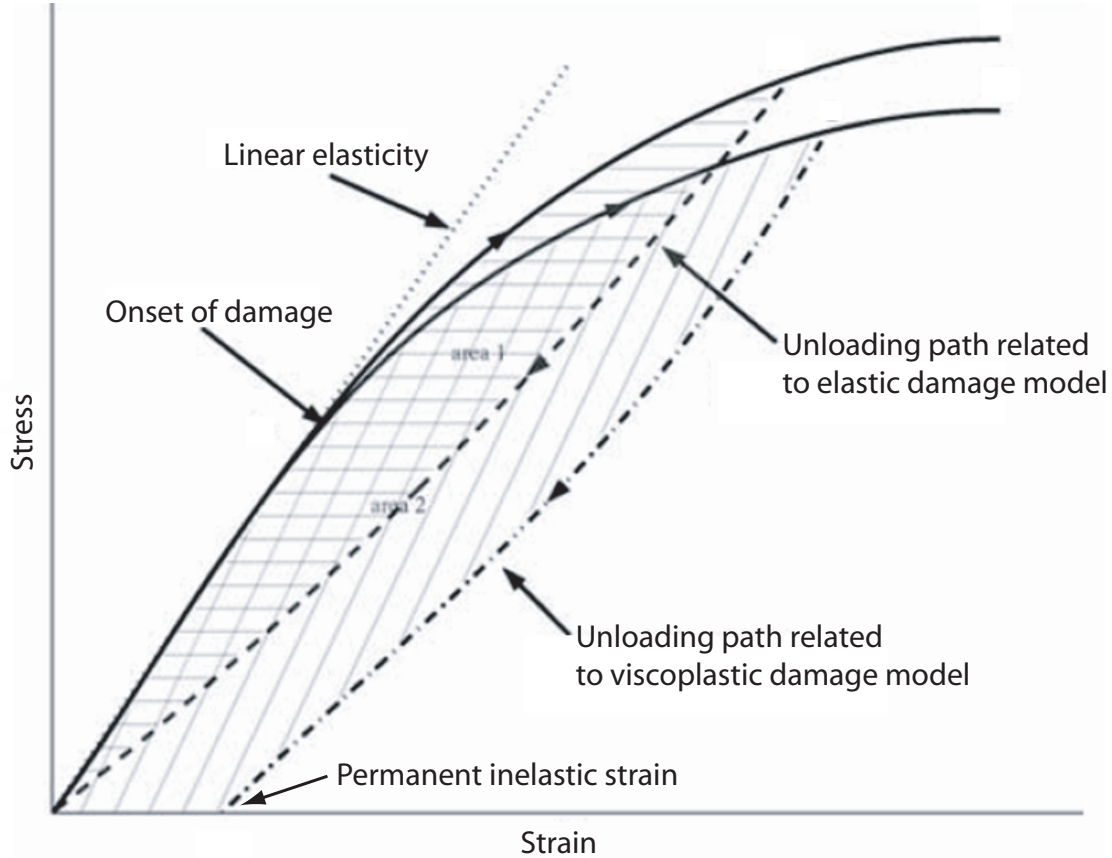


Fig. 4.30: Stress-Strain relations for pure elastic and viscoelastic damage models. The shaded areas indicate dissipation of strain energy in terms of microcracks in elastic and viscoelastic models. (Hamiel et. al., 2004)

Shcherbakov et. al (2005) introduced the damage variable,  $\chi$ , into the Hook's law to define a simplified constitutive law beyond yield stress,  $\sigma_y$  (Eq. 4.26).

$$\varepsilon - \varepsilon_y = \frac{\sigma - \sigma_y}{E_0(1 - \chi)} \quad (4.26)$$

where  $0 < \chi < 1$  defines deviation from the linear elasticity ( $\chi=0$ ) and also the distribution of micro-cracks in the material. A failure occurs at  $\chi=1$ , when the above law is undefined. The damage variable,  $\chi(t)$ , evolves with time but it can be an instantaneous process. If a constant stress  $\sigma > \sigma_y$ , is applied instantaneously then micro-cracks will develop until  $\chi$  becomes 1 then failure takes place and stress is relaxed. If a constant strain  $\varepsilon > \varepsilon_y$ , is applied, material will relax until  $\sigma = \sigma_y$ , then micro-cracks will develop.



The damage variable,  $\chi$ , depends on stress,  $\sigma$ , and strain,  $\varepsilon$ . Eq. 4.27 shows the modified form of the thermodynamic basis of defining time dependency of  $\chi$  (Shcherbakov and Turcotte, 2003, 2004; Shcherbakov et. al., 2005).

$$\frac{d\chi}{dt} = A(\sigma) \left( \frac{\varepsilon}{\varepsilon_y} - 1 \right)^2 \quad (4.27)$$

where

$$A(\sigma) = 0, \text{ if } 0 \leq \sigma \leq \sigma_y \quad (4.28)$$

$$A(\sigma) = \frac{1}{t_d} \left( \frac{\varepsilon}{\varepsilon_y} - 1 \right)^\rho, \text{ if } \sigma > \sigma_y \quad (4.29)$$

where  $t_d$  is the characteristic time for the damage, and  $\rho$  is a power law exponent to be determined from experiments.

If we assume that stress increases linearly with time from the initial condition,  $\sigma_0 = \sigma_y$  at  $t=0$ , the stress,  $\sigma$ , is defined in Eq. 4.30.

$$\sigma = \sigma_y + E_0 \dot{\varepsilon} t \quad (4.30)$$

Solving Eq. 4.27 using Eq. 4.28-4.30, we can define the damage variable,  $\alpha$ , in Eq. 4.31.

$$\chi = 1 - \left\{ 1 - \frac{3}{t_d} \left( \frac{\dot{\varepsilon}}{\varepsilon_y} \right)^{\rho+2} \frac{t^{\rho+2}}{\rho+3} \right\}^{1/3} \quad (4.31)$$

Failure occurs at  $\chi=1$ , which gives failure time,  $t_f$ , in Eq. 4.32.

$$t_f = \left\{ \frac{(\rho+3)t_d}{3} \right\}^{\frac{1}{\rho+3}} \left( \frac{\varepsilon_y}{\dot{\varepsilon}} \right)^{\frac{\rho+2}{\rho+3}} \quad (4.32)$$

The failure stress or static frictional stress and the mean stress during the run-up to failure are given by Eq. 4.33 and 4.34.

$$\sigma_f = \sigma_y + E_0 \dot{\epsilon} t_f \quad (4.33)$$

$$\bar{\sigma} = \sigma_y + \frac{1}{2} E_0 \dot{\epsilon} t_f \quad (4.34)$$

Once the failure takes place, stress is released and it goes back to a new yield stress i.e. yield stress of the failed or fractured rock.

Laboratory experiments and numerical techniques indicate a narrow localized zone of micro-cracks associated to the pre-faulting stage. Laboratory studies on the collected samples from faults along the Shawangunk ridge, Ulster County, NY, confirm a narrow localized zone of microcracks (Vermilye and Scholz, 1998). The damage zones are mostly concentrated within 1000 mm from the faults and the density of microcracks is linearly related to the log of the distance from the fault in millimeters. In absence of any analytical formulation of spatial distribution, we can use these field correlations to model the damage zone dimensions prior to the faulting. For a more rigorous solution of the damage zone prior to the faulting, we can use the finite element technique with damage rheology. However, for the reservoir scale faults the effect of pre-faulting microcracks is negligible in comparison to the damage evolution during the fracture growth and the fault slip stages, so we may ignore their effect in a simulation model.

#### **4.10.2 Damage zone during slip along existing faults**

The deformation zone during slip events along fault planes is related to the stress perturbations and interactions among the faults. These effects depend on the geometry and geomechanical properties of faults and associated host rock. A slip along the fault leads to the formation of splay fractures at the tips of the fault. Subsequently, slip on those splay faults may generate a new set of splay fractures and so on. In a favorable stress environment, the process of slip and interaction between the parent faults and the

splays may expand the damage zone into the surrounding host rock, which produces the fault damage zones much wider in respect to their fault offsets (Davatzes and Aydin, 2002; Myers and Aydin, 2004). However, estimating the stress history for different steps of splay generation is a challenge, especially for the subsurface reservoirs, which limits any rigorous mathematical modeling of the deformation zone.

We can use boundary element modeling with the stress states causing slip along the fault to model the effects of this stage. The static solutions using the present day stress state may indicate the stress perturbations due to slip on the currently active faults.

The boundary element modeling of a geological structure is done using Cauchy's formulation, which relates tractions at the boundaries of the model to the stress components on an element adjacent to the boundary (Eq. 4.35). The normal and shear components of the traction vector can be determined by Eq. 4.36.

$$t_i(n) = \sigma_{ji}n_j \quad (4.35)$$

$$t = t_n + t_s = (t \cdot n)n + n \times (t \times n) \quad (4.36)$$

where  $t$  is the traction vector on a surface defined by normal vector,  $n$ .  $\sigma$  is the stress tensor on a given reference, and  $t_n$  and  $t_s$  are the normal and the shear components of the traction.

Some of the commercial boundary element codes to estimate displacements and stress perturbations due to fault slip use the triangular boundary elements or the Cauchy tetrahedrons to define faults. Fig. 4.31 shows relationships among the traction and stress components on a Cauchy's tetrahedron. To model the slip or frictional sliding on a fault plane, we calculate the shear and normal components of the traction vector due to the stresses from the rock mass adjacent to the fault plane. For a set of fault elements with same frictional strength, those who carry the relatively high shear traction and low normal traction show slip along the fault, which is based on some failure criteria. The Coulomb criteria for shear failure for the material with cohesive

strength, UCS, and coefficient of internal friction,  $\mu$ , is shown in Eq. 4.37. The amount of slip would be determined by the balance in body force and traction components such that the shear traction is smaller than normal component. On an arbitrary plane, the normal stress,  $\sigma_{nn}$ , is related to traction components by Eq. 4.38.

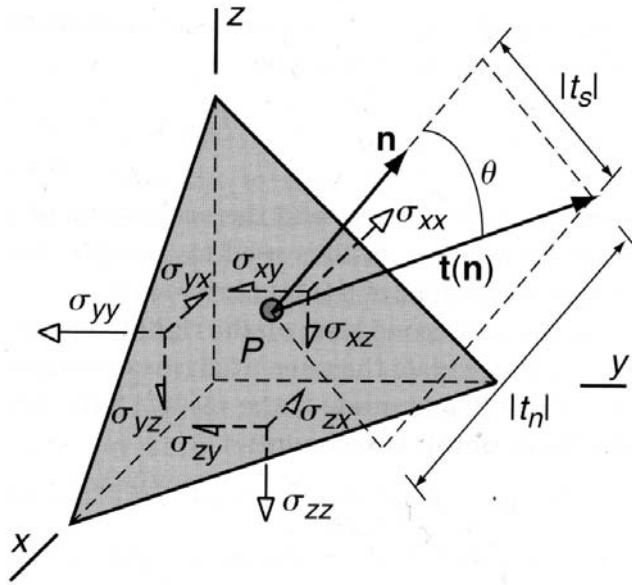


Fig. 4.31: Cauchy's tetrahedron with traction vector  $t(n)$ . Traction vector is decomposed in normal and shear components. (Pollard and Fletcher, 2005)

$$t_s = UCS + \mu t_n \quad (4.37)$$

$$t_i(n) = \sigma_{ni} n_i \quad (4.38)$$

$$\begin{vmatrix} \sigma_{xx} - \sigma_{nn} & \sigma_{yx} & \sigma_{zx} \\ \sigma_{xy} & \sigma_{yy} - \sigma_{nn} & \sigma_{zy} \\ \sigma_{xz} & \sigma_{yz} & \sigma_{zz} - \sigma_{nn} \end{vmatrix} = 0 \quad (4.39)$$

Solving Eq. 4.35 and 4.38 in a 3D space gives three real roots for  $\sigma_{nn}$ , which are three principal stresses (Eq. 4.39). These principal stresses can be transformed to any reference axis and subsequently we can calculate perturbation in the shear traction magnitude around the fault due to slip along the fault. If the system consists of multiple

faults, then the resultant stress perturbation at a location depends on the cumulative effect due to slip in all faults within the effective range.

Collettini and Sibson (2001) suggest that sets of normal faults with parallel dip may show lower frictional strength and remain shearing, if they are initially in an optimal orientation for the shear failure and then rotate (domino rotation) to a lower dip with the regional extension and no longer in a favorable direction of shear failure.

Lockner and Byerlee (1993) and Faulkner et. al. (2006) suggest that the mature fault zone may act as a local traction boundary, which allows the maximum principal stresses to rotate at  $\sim 45^\circ$  (a much lower angle than actual remote principal stress orientation) within the gouge/damage zone, resulting in an apparent lower normal stress and a higher shear stress. This produces Riedel shear planes within the gouge zone and gives an apparent lower frictional coefficient to the fault plane, which keeps the faults shearing even with an unfavorable direction of shear failure.

In a field where some of the faults show the evidence of domino rotation or Riedel shearing, we should use a lower coefficient of friction for those faults while calculating the stress perturbations using the above boundary element approach.

## References

- Anders, M. H., and Wiltschko, D. V., 1994, Microfracturing, paleostress and the growth of faults. *Journal of Structural Geology*, 16, 795-815.
- Ando, M.: Geological and geophysical studies of the Nojima fault from drilling”, An outline of the Nojima fault zone probe, the Island arc (2001) 10, 206-214.
- Atkinson, B. K., 1987, Introduction to fracture mechanics and its geophysical applications. *Fracture Mechanics of Rock*, Academic Press, London, 1-26.
- Aydin, A., Johnson, A.M., 1978, Development of faults as zones of deformation bands and as slip surfaces in sandstone. *Pure and Applied Geophysics*, 116, 931-942.
- Chinnery, M. A., 1966, Secondary faulting; Part 1. Theoretical aspects; Part 2, Geological aspects. *Canadian Journal of Earth Sciences*, 3, 163-190.
- Chester, F. M., and Logan, J. M., 1986, Implications from mechanical properties of brittle faults from observations of the Punchbowl fault zone, California, *Pure and Applied Geophysics*, 124, 79-106.

- Ciliberto, S. A., Guarino, A., and Scorretti, R., 2001, The effect of disorder on the fracture nucleation process, *Physica D*, 158, 83-104.
- Collettini, C., and Sibson, R. H., 2001, Normal faults, normal friction?, *Geology*, 29, 927-930.
- ConocoPhillips, Ltd., 2003, Stress state and wellbore stability for the CS field, ConocoPhillips Internal report
- Cowie, P. A., and Scholz, C. H., 1992, Physical explanation for the displacement-length relationship of faults using a post-yield fracture mechanics model. *Journal of Structural Geology*, 14, 1133-1148.
- Davatzes, N. C., and Aydin, A., 2003, The formation of conjugate normal fault systems in folded sandstone by sequential jointing and shearing, Waterpocket monocline, Utah, *Journal of Geophysical Research*, 108, 2478-2493.
- Faulkner, D. R., Mitchell, T. M., Healy, D., and Heap, M. J., 2006, Slip on weak faults by the rotation of regional stress in the fracture damage zone, *Nature*, doi:10.1038/nature05353.
- Freund, L. B., 1979, The Mechanics of dynamic shear crack propagation, *Journal of Geophysical Research*, 84, 2199-2209.
- Freund, L. B., and Clifton, R. J., 1974, On the uniqueness of plane elastodynamic solutions for running cracks, *J. of Elasticity*, 4, 293-299.
- Freund, R., 1974, Kinematics of transform and transcurrent faults. *Tectonophysics*, 21, 93-134.
- Freund, L. B., 1990, *Dynamic fracture mechanics*, Cambridge University Press, New York, pp 563.
- Griffith, A. A., 1920, *Phil. Trans. R. Soc. London*, A.221, 163-198.
- Irwin, G.R., 1960, In *Structural Mechanics: Proc, 1<sup>st</sup> Sym./Naval Structural Mech.*, Pergamon, New York, 557-591.
- Kachanov, L. M., 1986, *Introduction of Continuum Damage Mechanics*, Martinus Nijhoff, Zoetermeer, Netherlands, pp 135.
- Kostov, B. V., 1964, Selfsimilar problems of propagation of shear cracks, *J. Appl. Math. Mech.*, 28, 1077-1087.
- Hamiel, Y., Liu, Y., Lyakhovskiy, V., Ben-Zion, Y., and Lockner, D.A., 2004, A Viscoelastic damage model with applications to stable and unstable fracturing, *Geophysics Jour. Inter.*, 159, 1155-1165.
- Harris, R. A., and Day, S. M., 1997, Effects of a low-velocity zone in a dynamic rupture, *Bull. Seismol. Soc. Am.*, 87, 167-1280.
- Hickman, S. and Zoback, M. D.: "Stress orientations and magnitudes in the SAFOD pilot hole", *Geophys. Res. Lett.* (2004) 31, L15S12, doi:10.1029/2004GL020043.
- Li, V. C., 1987, *Mechanics of shear rupture applied to earthquake zones*, Fracture Mechanics of Rock, Academic Press, London, 351-428.

- Lockner, D.A., and Byerlee, J. D., 1993, How geometrical constraints contribute to the weakness of mature faults, *Nature*, 363, 250-252.
- Lockner, D.A., Byerlee, J.D., Kuksenko, V., Ponomarev, A., and Sidorin, A., 1992, Observations of quasi-static fault growth from acoustic emissions, *Fault mechanics and transport properties of rocks*, international Geophysics Series, 51, p-3-31, Academic Press, san Diego, CA.
- Lockner, D., Naka, H., Tanaka, H., Ito, H., and Ikeda, R.: "Permeability and Strength of Core samples from the Nojima Fault of the 1995 Kobe Earthquake", *Proc. of the Inter. workshop on the Nojima Fault Core and Borehole Data Analysis (1999)*, 147-152.
- Lyakhovsky, V., Ben-Zion, Y., Agnon, A., 1997, Distributed damage, faulting and friction. *Journal of Geophysical Research*, 102, 27635-27649.
- Madariaga, R., 1976, Dynamics of an expanding circular fault, *Bulletin of Seismological Society of America*, 66, 639-666.
- Myers, R., and Aydin, A., 2004, The evolution of faults by shearing across joint zones in sandstone, *Journal of Structural Geology*, 26, 947-966.
- Nanjo, K. Z., Turcotte, D. L., and Shcherbakov, R., 2005, A model of damage mechanics for the deformation of the continental crust, *Journal of Geophysical Research*, 110, B07403, doi:10.1029/2004JB003438.
- Pollard, D. and Fletcher, F., 2005, *Fundamentals of Structural Geology*, Cambridge University Press.
- Pollard, D. D., and Segall, P., 1987, Theoretical displacements and stresses near fractures in rock; with applications to faults, joints, veins, dikes, and solution surfaces. In: Atkinson, B. K., (Ed.), *Fracture Mechanics of Rock*, Academic Press, London, pp. 277-349.
- Reches, Z., and Lockner, D. A., 1994, The nucleation and growth of faults in brittle rocks. *Journal of Geophysical Research*, 99, 18159-18174.
- Rice, J. R., 1968, *Fracture and advance treatise*, 2, Academic Press, NY, 191-331.
- Rundle J. B., Klein, W., and Gross, S., 1999, A physical basis for statistical patterns in complex earthquake populations: Models, predictions and tests, *Pure and Applied Geophysics*, 155, 575-607.
- Rundle J. B., Klein, W., Turcotte D. L., and Malamud, B. D., 2000, Precursory seismic activation and critical-point phenomenon, *Pure and Applied Geophysics*, 157, 2165-2182.
- Schlische, R. W., Young, S. S., Ackermann, R. V., and Gupta, A., 1996, Geometry and scaling relations of a population of very small rift-related normal faults, *Geology*, 24, 683-686.
- Scholz, C. H., Dawers, N. H., Yu, J. Z., Anders, M. H., and Cowie, P. A., 1993, Fault growth and scaling laws: Preliminary results, *J. Geophys. Res.*, 98, 21951-21961.
- Scorretti, R. S., Ciliberto, S. A., and Guarino, A., 2001, Disorder enhances the effects of thermal noise in the fiber bundle model, *Europhysics Letter*, 55, 626-632.
- Selinger, R. L. B., Wang, Z. G., Gelbart, W. M., and Ben-Shaul, A., 1991, Statistical-thermodynamic approach to fracture, *Physics Review A*, 43, 4396-4400.

- Shcherbakov, R., and Turcotte, D. L., 2003, Damage and self-similarity in fracture, *Theoretical and Applied Fracture Mechanics*, 39, 245-258.
- Shcherbakov, R., and Turcotte, D. L., 2004, A damage mechanics model for aftershocks, *Pure and Applied Geophysics*, 161, 2379-2391.
- Shcherbakov, R., Turcotte, D. L., and Rundle, J. B., 2005, Aftershocks statistics, *Pure and Applied Geophysics*, 161, 1051-1076.
- Suppe, J., 1985, *Principles of Structural Geology*, Prentice-Hall, New Jersey, pp 537.
- Tanaka, H., Fujimoto, K., Ohtani, T., and Ito, H.: "Structural and chemical characterization of shear zones in the freshly activated Nojima fault, Awaji Island, southwest Japan", *Journal of Geophysical Research* (2001) 106, 8789-8810.
- Tse, S. T., Dmowska, R., and Rice, J. R., 1985, *Bull. Seism. Soc. Am.*, 75, 709-736.
- Turcotte, D. L., and Glasscoe, M. T., 2004, damage model for the continuum rheology of the upper continental crust, *Tectonophysics*, 283, 71-80.
- Vermilye, J. M., and Scholz, C. H., 1998, The process zone; a microstructural view of fault growth. *Journal of Geophysical Research*, 103, 12223-12237.
- Virieux, J., and Madariaga, R., 1982, Dynamic faulting studied by finite difference method, *Bull. of the Seis. So. of America*, 72, 345-369.
- Wald, D. J.: "Slip history of the 1995 Kobe, Japan, earthquake determined from strong motion, teleseismic, and geodetic data", *Journal of Physics of the earth* (1996) 44, 489-503.
- Xia, K., Rosakis, A. J., and Kanamori, H., 2004, Laboratory Earthquakes: The Sub-Rayleigh-to-Supershear rupture Transition, *Science*, 303, 1859-1861.
- Xia, K., Rosakis, A. J., Kanamori, H., and Rice, J. R., 2005, Laboratory earthquakes along inhomogeneous faults: Directionality and Supershear, *Science*, 308, 681-684.
- Zapperi S., Ray, P., Stanley, H. E., and Vespignani, A., 1997, First-order transition in the breakdown of disordered media, *Physics Review Letter*, 78, 1408-1411.



## Chapter 5

# **IMPLEMENTATION OF PERMEABILITY ANISOTROPY ASSOCIATED WITH DAMAGE ZONES IN RESERVOIR SIMULATION**

*Part of this chapter was written as a paper with Mark Zoback and Peter Hennings, and has been accepted by SPE (SPE 110542)*

### **5.1 Abstract**

Damage zones are associated with reservoir scale faults and the permeability anisotropy due to these zones is related to the orientation and size of the faults in the reservoir. Faults are generally oriented in several directions in a reservoir, and therefore are often not aligned with the simulation grid. Based on the complexity of fault shape, a simulation grid may have complex cell geometry adjacent to the faults. In this study we present a methodology to implement the effects of damage zones in the simulation grid which are generally located in fault-adjacent grid blocks. Using fluid simulation in a fine scale model with discrete secondary features of damage zones

we demonstrate that the permeability anisotropy due to damage zones exists due to increased permeability along the strike of the fault and in the vertical direction. However, there is no significant change in the permeability perpendicular of the faults for the studied reservoir. To incorporate the effect of permeability anisotropy in the simulation grid that is directly related to fault orientation, we use the strike and dip of faults with reference to the grid axes. The relative effect of the dimension of the damage zone is incorporated using the normalized damage zone width with respect to cell volume and surface area. The absolute value of permeability anisotropy corresponding to is then defined by several steps of history matching with the observed production data of the CS field. History matching of the simulation model with the damage zone shows a significant improvement with respect to the base reservoir simulation model (petrophysical model with no damage zones). We analyze the uncertainty of the damage zone modeling in the reservoir simulation by simulating multiple equiprobable models. Response from these equiprobable models shows an improvement from the base model, indicating the robustness of the modeling and implementation techniques and the improved model should better predict the production behavior.

## 5.2 Introduction

Fluid flow through secondary fractures associated with damage zones can be significant in many reservoirs. These effects can be represented in reservoir simulation by adding them either in the fine scale geological model or in the coarse scale reservoir simulation model. Damage zones may contain several thousands of secondary fractures so including each one of them as a discrete feature in the simulation model is limited by the computational power and time of the reservoir simulator (Durlafsky, 2003). However, there has been considerable progress made in upscaling the flow effects of small-scale geological heterogeneities (Flodin et al., 2001; Jourde et al., 2002; Ahmadov et al., 2007; Pickup and Stephan, 2000; Pickup et al., 2000; Corbett et al., 1992; Ringrose et al., 1993). An efficient upscaling technique transforms the geological models to a simulator model, but maintains the required properties to get an

average flow behavior of the reservoir. Reservoirs with complex heterogeneities such as fractures, and faults may pose an additional challenge to this process. In addition, to assess the uncertainty of these scenarios, we simulate a number of geological realizations, which need fast time-efficient algorithms for both upscaling and simulation steps.

Fractured porous media are typically simulated using dual-porosity models, but these models are not suited for reservoirs with only a few fractures or localized fracture zones with dominant flow. Faults are defined as discrete features in an upscaled model. To maintain their complex geometries, we may have to use a special discretization scheme and multipoint flux approximation adjacent to the faults (Verma and Aziz, 1997; Rodriguez et al., 2004). Localized features such as fractures associated with the fault damage zone can be modeled as discrete features but due to limited computational power it is not suggested to model lots of them in a full reservoir simulation model. Also, upscaling and history matching of a number of geological scenarios with fault damage zone fractures can be a very lengthy process. One of the alternatives is the multi-laminate model (Pande, 1980; Koutsableoulis et al., 1994), in which we first construct a base upscaled model of the geological model with reservoir scale faults and stratigraphical heterogeneities. Then we include different scenarios of the effects of the localized fractures on the base upscaled model. So instead of discrete features, fractures are treated as an effective medium changing the base model properties in localized areas. There are various techniques to define localized fine-scaled heterogeneities on an upscaled grid such as Local Grid Refinement-LGR (Ciment and Sweet, 1973; Nacul, 1991; Pedrosa and Aziz, 1985) or windowing technique (Mlacnik and Heinemann, 2003). However, the effectiveness of these techniques depends on the type of upscaled grid, the type and scale of localized heterogeneity, and the ability of the reservoir simulator to handle these treatments.

In this chapter, we discuss a fine scale upscaling experiment to show the effects of the damage zone in the upscaled block permeability. Then we use the nature of the permeability anisotropy of the upscaled block to incorporate the effect of the damage

zones in the upscaled reservoir model (simulation model), which is a non-orthogonal grid with corner point geometries. Adjacent to the fault, grid blocks are truncated to keep the actual shape of the faults. We discuss a workflow to implement the effects of permeability anisotropy due to damage zones in the base simulation model and quantify the effects using history matching of the production data.

### 5.3 Field pressure behavior and project motivation

In the CS field, interference and tracer tests between the wells show preferential flow along the reservoir scale faults trending in E-W direction (Fig. 5.1). Well P3 shows a clear indication of pressure interference with the wells P1 (~2.5 km), P2 (~1.5 km), P4 (~3 km) and injectors (~5.5 km) within 24 hrs. Well P4 also sees pressure support from injectors (~4.4 km) but the response is delayed relative to well P3 even though the injectors are closer, which may be explained as fluid flow around the fault rather than across the fault. Well P7 shows pressure communication with well P6 (~3 km) after 30 hrs and P5 (~1.5 km) after 12 hrs, which are much delayed relative to the response of well P3. Injector pressure support in the well P7 is observed after 48 hrs, which is again a delayed response relative to pressure support from injectors to wells to the east. The colored lines connecting wells in Fig. 5.1 indicate the connectivity of the flow paths in a relative scale. Red lines indicate the highest connectivity paths and white and yellow lines indicate the lowest connectivity paths. We can see that lines sub-parallel to the large E-W trending fault colors are mostly red and pink, which indicate a relatively high permeability parallel to the faults. However, these same faults appear to be barriers to cross-fault flow and thus inhibit north-south flow within the reservoir.

In the CS field, production is constrained by the hydrocarbon production rate at well locations; hence we compare the bottom hole pressure (BHP) and water production response of the model and actual field observations to assess the quality of the model. Response from the base simulation model (porosity and permeability models from classical geostatistical techniques, discussed in detail later in this chapter)

shows a poor match with actual production and injection data from the wells. Fig. 5.2 shows the well location map and mismatch between the BHP response of three representative wells using the base model and their actual field response. Also, we found that water production match between the model response and field observations is poor. However, when we increase the permeability of blocks adjacent to the reservoir scale faults in the base simulation model, it shows an improvement in the production history match, suggesting a possibility of high permeability zone associated with these faults. We hypothesize that the enhanced flow parallel to the E-W trending faults but relatively low flow normal to them suggests that enhanced flow is occurring in the damage zones adjacent to these fault planes. Below, we show fine scale simulation studies to quantify the effect of a damage zone in terms of permeability anisotropy in a single simulation grid block. Then we propose a workflow for incorporating the damage zones into reservoir simulation models in terms of their effect on localized permeability variations and large scale permeability anisotropy in the reservoir.

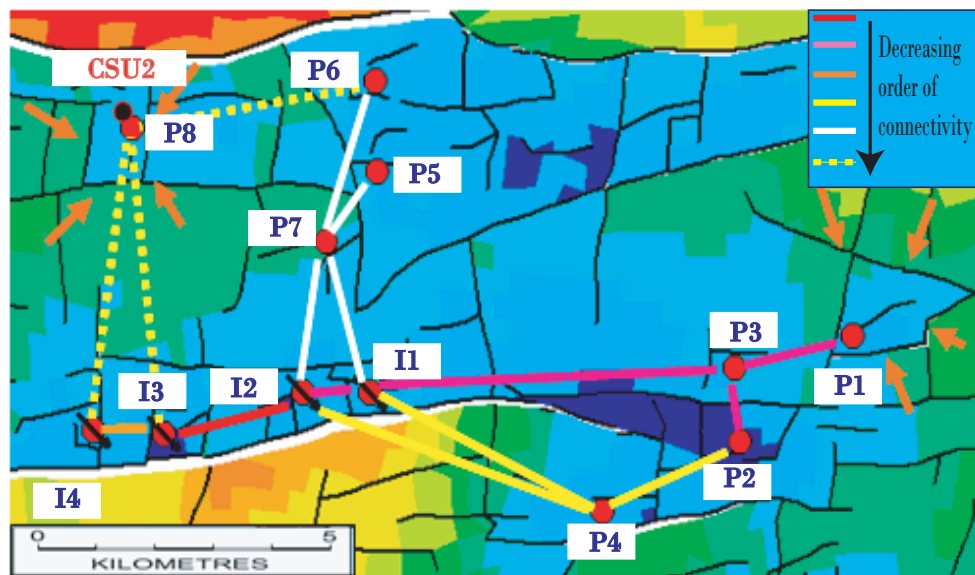


Fig. 5.1: Interference and tracer tests between the wells show a high order of connectivity along the reservoir scale faults trending in EW direction. The lines connecting wells show permeability between the wells in a relative scale. The lines in red indicate the highest permeability paths and white and yellow lines indicate the lowest permeability paths.

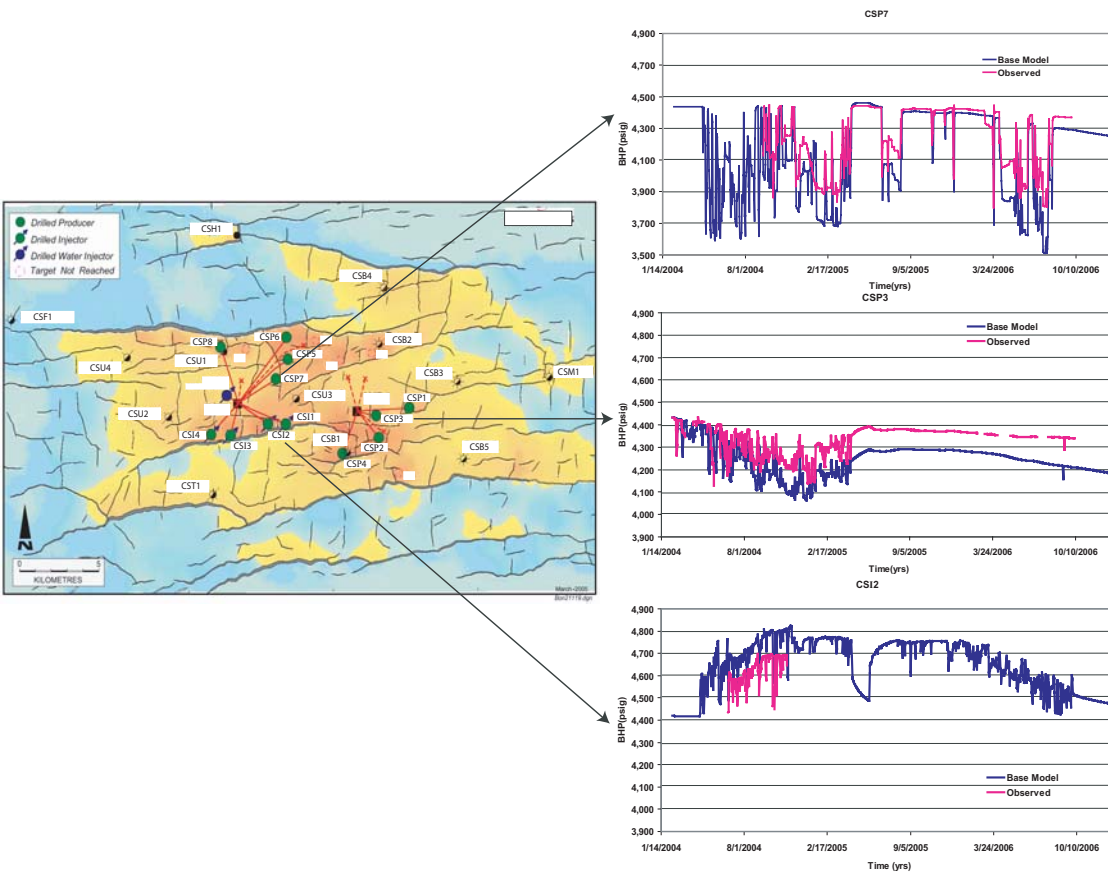


Fig. 5.2: Well description map and simulation response of three wells using the base model. Base model response shows a poor match for wells close to the large faults but shows a better match with the well far from the fault. Blue curves represent the responses from the base model and magenta shows the actual observations.

## 5.4 Permeability anisotropy due to the damage zones

In this section, we quantify the permeability anisotropy effect due to a damage zone using fine scale simulation studies. First, we define the trend of the permeability anisotropy using a 3D model and then use 2D models to quantify its magnitude in terms of fracture density.

### 5.4.1 3D study

The objective of the 3D study was to define the permeability anisotropy trend in a reservoir grid block due to damage zones. Hence, the model is sized to optimize the computational time and also to honor the effect of anisotropy in X-Y plane for an

average block size ( $360 \times 380 \times 14 \text{m}^3$ ) of the reservoir simulation model of the CS field. The model dimension perpendicular to fault is kept  $\sim 380 \text{m}$  but the fault-parallel dimension is reduced  $\sim 100 \text{m}$  because for a constant damage zone width, anisotropy trend parallel to fault is same for any given length of grid block in that direction (Fig. 5.3). The height of model is increased to  $\sim 80 \text{m}$  to optimize the computational time and numerical error due to high aspect ratio in the real grid. The failure planes in the damage zone are created using the dynamic rupture technique as discussed in chapter 4 and combined with Monte Carlo Simulation to incorporate the uncertainty in their locations, and geometry. They are defined as discrete features in the model. As shown in Fig. 5.3, failure planes are mostly striking parallel to the south face of the block, which is the fault face in the simulation model. Fracture density in the model decreases away from this fault face and becomes zero beyond the limit of the damage zone ( $\sim 60 \text{m}$ ), which is defined as the average damage zone width associated with the moderate size reservoir scale faults in the CS field. Faults of moderate size and fracture density of  $\sim 0.3$  fracture/m are used to optimize the computational time of the study.

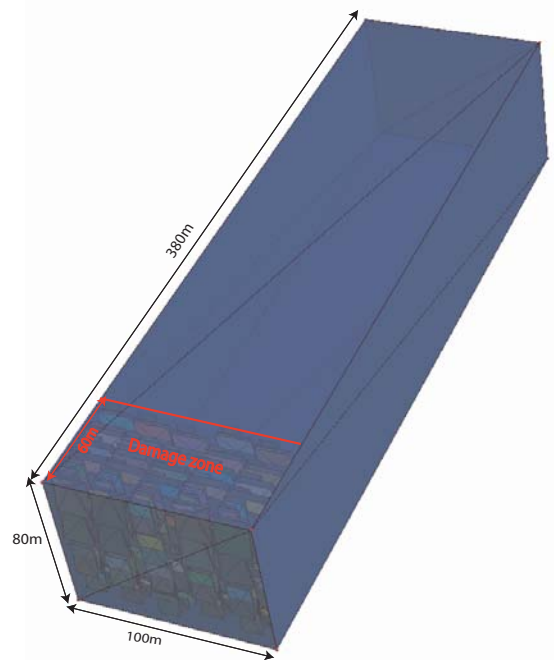


Fig. 5.3: Discrete fractures associated with the fault damage zone within the model.

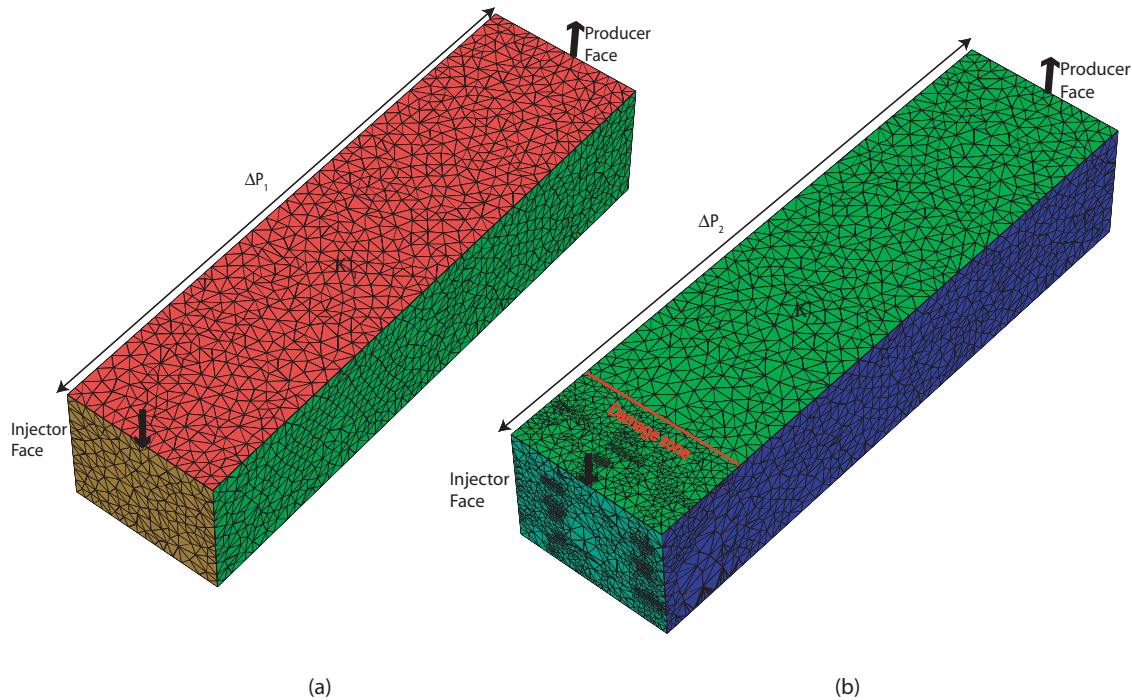


Fig. 5.4: The fine scale unstructured grid (a) without damage zone and (b) with damage zone (damage zone is represented as very fine grid cells). In a steady state with similar injection and production constraints, the ratio of pressure difference between injection and production face gives the change in permeability along the flow direction.

Using the discrete fracture model we generate a fine scale unstructured grid with total cells  $\sim 600,000$ . Fig. 5.4b represents the simulation grid, where we can see smaller tetrahedrons in the damage zone defining the discrete fractures. Fig. 5.4a shows a model of the same size but without damage zone fractures. The matrix porosity and permeability ( $k_m$ ) of the reservoir are 0.13 and 150 mD, which are based on petrophysical analysis of the CS field. Fracture permeability is defined as  $10^6$  times larger than  $k_m$  and fracture width is 1mm, which are values observed in field and lab studies (Brown and Bruhn, 1998; Luthi and Souhaite, 1990). These are converted to the cell volumes and the transmissibilities between the connected volumes using the algorithm proposed by Karimi-Fard et al. (2004). One face of the model along the flow is defined as injector with 1500 bbl/day of water injection and opposite face is defined as a producer with production at pressure constraint equivalent to reservoir pressure, 4000 psi. Running the simulation for a single phase flow until steady state is reached gives the pressure difference ( $\Delta P$ ) between injector and producer faces of the model. As shown in the Fig. 5.5, at steady state the simulation shows a somewhat linear



pressure profile between the two faces. By comparing the pressure difference ( $\Delta P$ ) for the cases with and without fractures using the same fluid we can estimate the change in the permeability along the flow due to the presence of fractures (Eq. 5.1),

$$\frac{k_2^*}{k_1^*} = \frac{\Delta P_1}{\Delta P_2}, \quad (5.1)$$

where  $k_1^*$  and  $k_2^*$  are the equivalent or upscaled permeability, and  $\Delta P_1$  and  $\Delta P_2$  represent the pressure difference of steady state solution along the flow for the models without and with fractures.

To define the permeability anisotropy due to the fractures in the damage zone, we repeat the experiment for flow along all three possible coordinate directions. In our experiment, we find that the permeability sub-parallel to the reservoir scale fault increases by  $\sim 1.36$  times due to the presence of the damage zone. In the vertical direction, permeability increment is  $\sim 1.39$  times but across the damage zone there is a no change in permeability,  $\sim 1$  times the matrix permeability. These experiments define the permeability anisotropy trend in a grid block but the magnitude of anisotropy is small because of low fracture density ( $\sim 0.3$  fracture/m) in the model, which can be large with higher fracture density. By comparing the simulation results for different cases ( $k_m$  value of 150 mD vs. 10 mD) we conclude that the anisotropy effect increases only with increasing contrast between the matrix and fracture permeability and there is no absolute effect for matrix permeability. In Table 5.1 we can see that the effect of anisotropy due to a permeability ratio of  $10^6$  between fractures and matrix is the same for both  $k_m$  values of 150 mD and 10 mD. A permeability ratio of  $10^9$  between  $k_f$  and  $k_m$  shows a similar effect but slightly enhances the anisotropy. These experiments represent an accurate model of the reservoir, except that the number of fractures is limited by computational time and resources, hence the values of permeability enhancement can be only used as a trend of permeability anisotropy due to the damage zone. The anisotropy trend shows a same order of increased permeability parallel to the reservoir scale faults and in the vertical direction but there is no change in the permeability in the direction perpendicular to the faults. In the next section we present

a study with 2D model (X-Y:parallel-perpendicular to fault) in actual grid block size and calibrate the permeability anisotropy on a horizontal plane with respect to fracture density in the damage zone. We can calibrate vertical (Z) direction permeability by X direction results of the 2D model because 3D study indicates same order of permeability anisotropy in X and Z directions.

Table 5.1:  $\Delta P$  and  $k^*$  for the different cases of fracture-matrix permeability ratio and matrix permeability.

Models	Along the fault		Vertical		Across the fault	
	$\Delta P$	$k^*$	$\Delta P$	$k^*$	$\Delta P$	$k^*$
$k_m=150$ , no fracture	28.2	161.46	16.62	162.1	386.33	157.35
$k_m=150$ , $k_f=10^6 k_m$	20.89	217.97	11.9	226.41	366.68	165.78
$k_m=150$ , $k_f=10^9 k_m$	20.68	220.18	11.84	227.56	365.85	166.16
$k_m=10$ , no fracture	423.02	10.76	249.3	10.81	5794.98	10.49
$k_m=10$ , $k_f=10^6 k_m$	313.34	14.53	178.43	15.1	5500.19	11.05
$k_m=10$ , $k_f=10^9 k_m$	310.16	14.68	177.52	15.2	5487.71	11.08

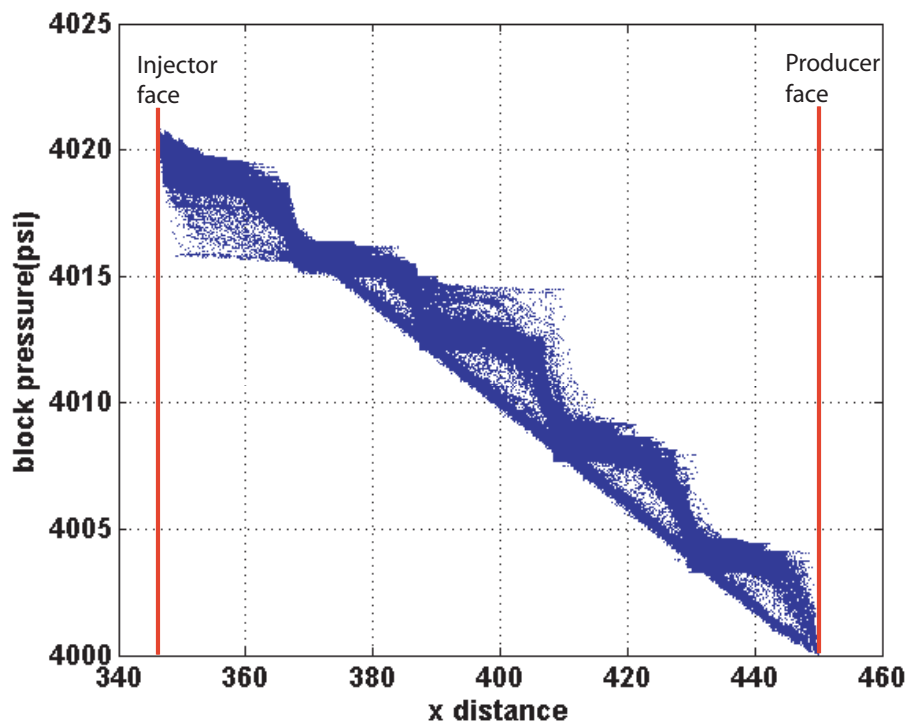


Fig 5.5: At steady state, simulation shows a linear flow between the Injector and Producer with a pressure difference of 20.89 psi. Blue dots are the pressure at cells relative to the faces. This example is for the model with fractures and  $k_m = 150$  mD,  $k_f = 10^6 k_m$  and flow is along the fault.

### 5.4.2 2D study

The models used for the 2D study represent the average grid block size ( $\sim 360 \times 380 \text{m}^2$ ) of the reservoir simulation model. Fig. 5.6 illustrates the 2D model with average fracture density of  $\sim 0.8$  fractures/m in the damage zone of  $\sim 60\text{m}$  wide. The fracture and matrix properties are the same as 3D model i.e.  $k_m = 150 \text{ mD}$ ,  $\phi_m = 0.13$ ,  $k_f = 10^6 k_m$ , and fracture aperture of 1 mm. Fracture density decreases going away from the fault. The size and orientation of the fractures are determined by the Monte-Carlo simulation using the parameters estimated by the geomechanical modeling in chapter 4.

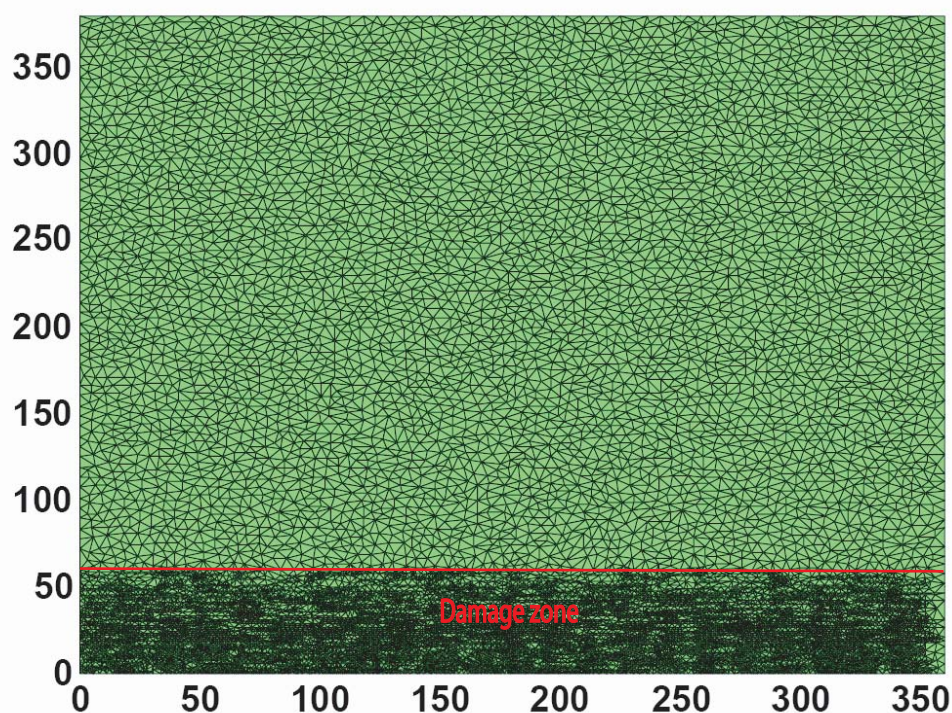


Fig 5.6: A 2D unstructured grid with damage zone width of  $\sim 60\text{m}$  and an average fracture density of  $\sim 0.8$  fractures/m.

Similar to 3D study, we define the opposite sides as injector and producer, and measure the pressure difference between the sides at steady state. Injection flow rate is 1500 bbl/day and production is at 4000 psi. We repeat the experiment in both coordinate directions and compare the homogenous (no fracture) model response with the response from the models with increasing fracture density within the defined  $\sim 60\text{m}$

damage zone. In Fig. 5.7, fluid simulations indicate a linear increase in permeability of the grid block in the direction parallel to fault with increasing average fracture density, but there is almost no change in permeability in the direction perpendicular to the fault. Permeability parallel to fault increases  $\sim 1.5$  times for fracture density  $\sim 0.3$  fracture/m, which is consistent with the 3D model results. We see an increase in the permeability parallel to faults  $\sim 4$  times for fracture density  $\sim 1$  fracture/m and  $\sim 7$  times for fracture density  $\sim 2$  fractures/m. In chapter 3, well scale analysis indicates a fracture density model with distance from the fault (Eq. 3.5), which suggests fracture density of  $\sim 2$  fracture/m in the damage zone. Assuming fracture density model is correct, a damage zone of width  $\sim 60$ m should increase the permeability  $\sim 7$  times for a grid of  $360 \times 380 \text{m}^2$  in the CS field and it should show a much higher increment for wider damage zones. Within the damage zone, permeability increment is  $\sim 40$  times from the matrix permeability, which is estimated using the concept of arithmetic averaging between the matrix part and damage zone from the permeability increment ( $\sim 7$  times) of the entire grid block. In the next section, we implement the damage zones in the reservoir simulation grid of the CS field and calculate the permeability multipliers by history matching, which may verify the correlation between fracture density model and fine scale simulations.

To define the uncertainty due to geometry (length, orientation, and intersections) of the fractures in the damage zone, we repeat the 2D experiments for several equiprobable model with same fracture density and damage zone width. In this study, we limit the uncertainty analysis only for the model with fracture density of  $\sim 1.3$  fractures/m because of longer computational time with high fracture density models. Running fluid flow simulations for five equiprobable fracture models suggests an uncertainty range (spread of red triangles in Fig. 5.7) of  $\sim 0.5$  permeability multiplier parallel to the fault but there is almost zero uncertainty range from the flow in the direction perpendicular to the fault.

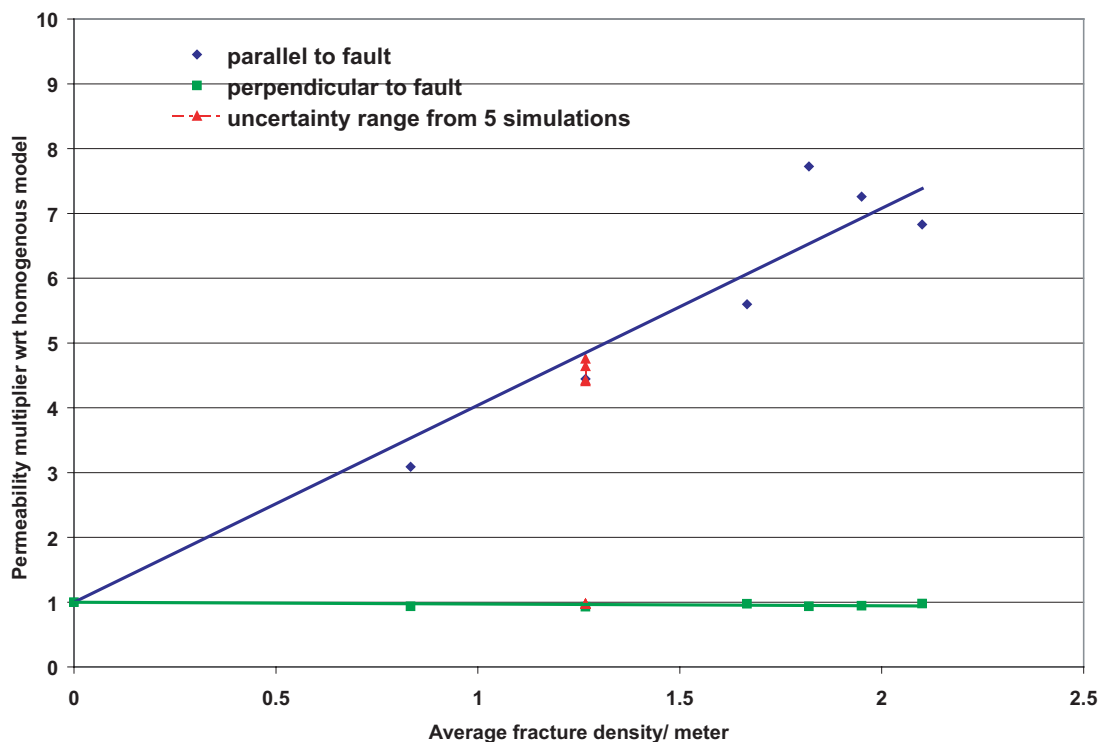


Fig 5.7: Permeability parallel to fault increases linearly with the increase of fracture density in the damage zone of  $\sim 60\text{m}$  but no change in permeability in the direction perpendicular to fault. Red points indicate uncertainty range from five simulations for a fracture density of  $\sim 1.3$  fracture/m in parallel and perpendicular directions to the fault.

## 5.5 Description of Geocellular model

The geocellular model of the CS field reservoir (Fig. 5.8) is a non-orthogonal grid with total cell  $300 \times 160 \times 265$  in the X, Y, and Z directions respectively. It has 183 modeled faults. The CS field closure is on the peak of a structural high. The reservoir is a broad E-W trending horst with closure at 2930m sub-sea to the gas-water contact at 3108 m sub-sea. Structure is gently dipping in both east and west directions with a number of internal peaks at E-W and N-S trending faults. A fault seal study of this field suggests that faults with throws greater than 20m would form potential seals (Lozada et al., 2005). A semi-regional critical stress study indicates that the critically-stressed faults would override any sealing potential but most of the faults, especially large E-W trending faults, are not critically-stressed and are assumed to be inactive. A study including fluid samples collected from drill stem tests (DST) supports that the

reservoir acts as a single compartment with common gas water contact (Lozada et al., 2005).

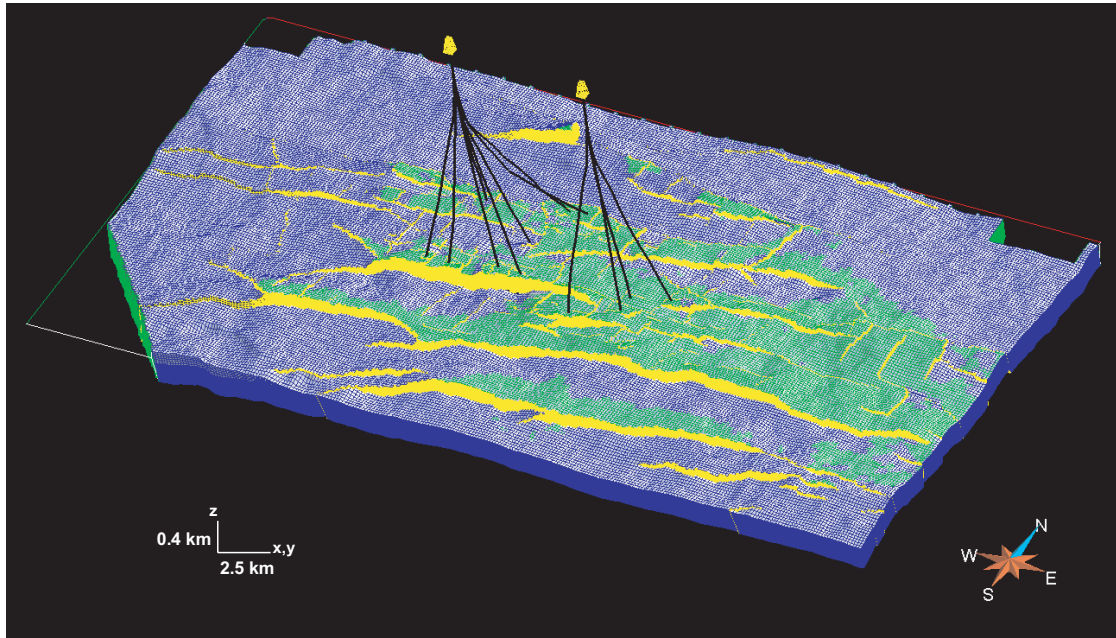


Fig. 5.8: Geocellular model of the CS field. It is a non-orthogonal grid with total cell 300x160x265 in the X, Y, and Z directions respectively.

Stratigraphically, the CS field reservoir has 19 units, which are represented as 265 layers in the geological models. These layers are medium to coarse grained sandstone to very fine to fine grained shale, which are based on detailed core description, log characterization, sequence stratigraphy, facies identification for fluvial zones, and paleo-current transport patterns from borehole image data. At least two of the shale layers run across the entire field. Well isopach data is used to convert depth maps for each reservoir layer. Isochores are established using proportional thickness relationships between the well data and the seismically interpreted reservoir tops.

Porosity and permeability in the model are defined based on the reservoir quality. Reservoir quality is strongly facies dependent, which is guided by grain size, sorting and lithofacies. The high energy fluvial, distributary/tidal channels and upper shore face facies have the highest reservoir quality. The interbedded sand and shale successions belonging to the crevasse splay, flood plain, estuarine and middle delta-



front facies form intermediate reservoir category. The low energy facies in the flood plane, swamp, distal delta-front/prodelta and interdistributary bays form the poorest quality reservoirs. These facies distributions are modeled using the paleo-current transport models from seismic and image logs. Then they are converted to a porosity model by the facies correlation of log data and core data. Thus, it is a deterministic geomodel, which best fits within a probabilistic range determined using petrophysical and structural data. Porosity in the model varies from 2-20% with an average value of 8.6%. Permeability (k) values are related to the porosity by an exponential function (Eq. 5.2) and also depend on the reservoir facies qualities (Lozada et al., 2005).

$$k = a \exp(b\phi) \quad (5.2)$$

where  $\phi$  is the porosity of the facies, and a and b are the coefficients for seven reservoir facies ranging from best quality to non-reservoir quality, listed in Table 5.2. Fig. 5.9 illustrates the porosity and permeability distributions of the facies for the entire reservoir section of the model. In the geocellular model, permeability is populated by a neural net technique, where the network is trained by core measurements and then log data is used to estimate the values. Estimated values are also calibrated with the production data.

Table 5.2: coefficients a and b for reservoir facies ranging from best quality reservoir to non-reservoirs.

Facies type	a	b
Facies 1 (best reservoir quality)	0.4989	54.375
Facies 2	0.2482	48.699
Facies 3	0.0045	85.845
Facies 4	0.0013	76.643
Facies 5	0.0008	77.002
Facies 6	0.0042	42.853
Facies 7 (non-reservoir quality)	0.0016	23.924

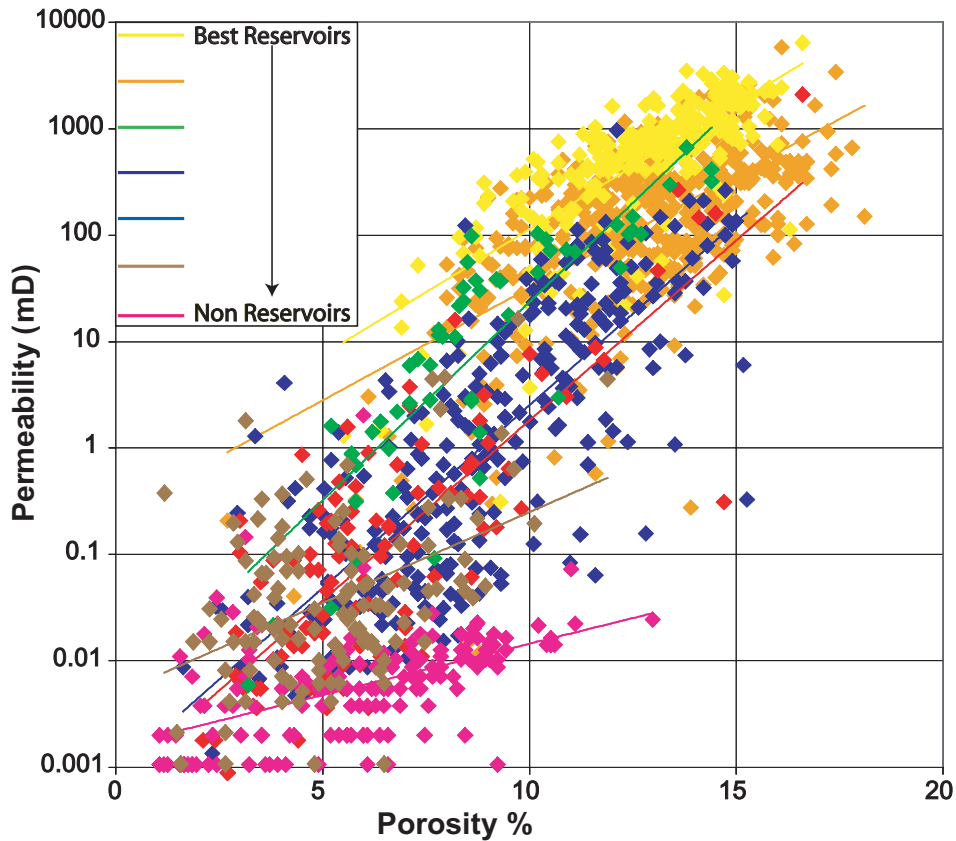


Fig. 5.9: Porosity and permeability distribution of the reservoir quality facies from best reservoir sand (yellow) to non-reservoir formations (magenta). (modified from Lozada et al., 2005)

Horizontal ( $k_h$ ) and vertical ( $k_v$ ) permeability of layers are correlated using horizontal and vertical core plug measurements from wells CSB2, CSB3, CSB4, CSB5, CSU1, CSU2, CSU3, and CSU4. Fig. 5.11 illustrates all the horizontal/vertical data point pairs. We can see that  $k_v$  and  $k_h$  are linearly related (Eq. 5.3) but values are very scattered at low permeability data points because of measurement errors and micro scale heterogeneities,

$$k_v = ck_h, \quad (5.3)$$

where variable,  $c$ , in Eq. 5.3 gradually decreases with the increase of  $k_h$  values but confidence of the best fit line increases as data become less scattered in high  $k_h$  values. Best fit lines on core measurements show the value of  $c$  as 4.3897, 1.6295, 0.9814, 0.7873, and 0.6901 for  $k_h$  ranges of <1 mD, 1-10 mD, 10-50 mD, 50-250 mD, and >250 mD respectively.  $k_h$  and  $k_v$  in the model lie in range 0.001-2200 mD and 0.001-



1350 mD with average values of 130.4 mD and 71.2 mD respectively. Fig. 5.11, 5.12, and 5.13 show porosity,  $k_h$ , and  $k_v$  distribution in a layer of the geocellular grid.

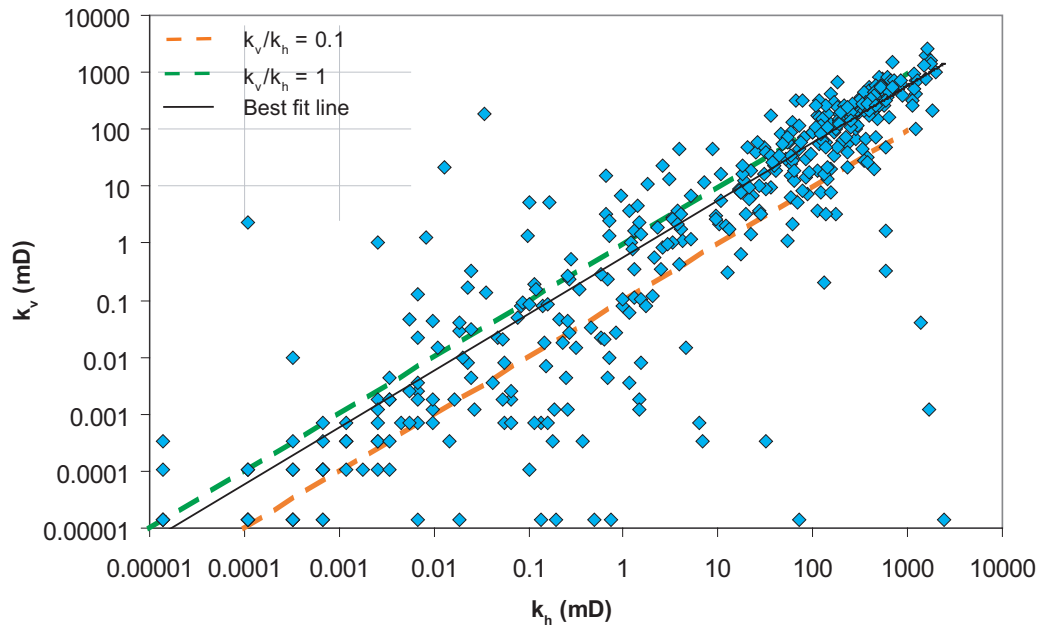


Fig. 5.10:  $k_v$  vs.  $k_h$  measurements showing all data point pairs. Values are scattered for low permeability values. (modified from Lozada et al., 2005)

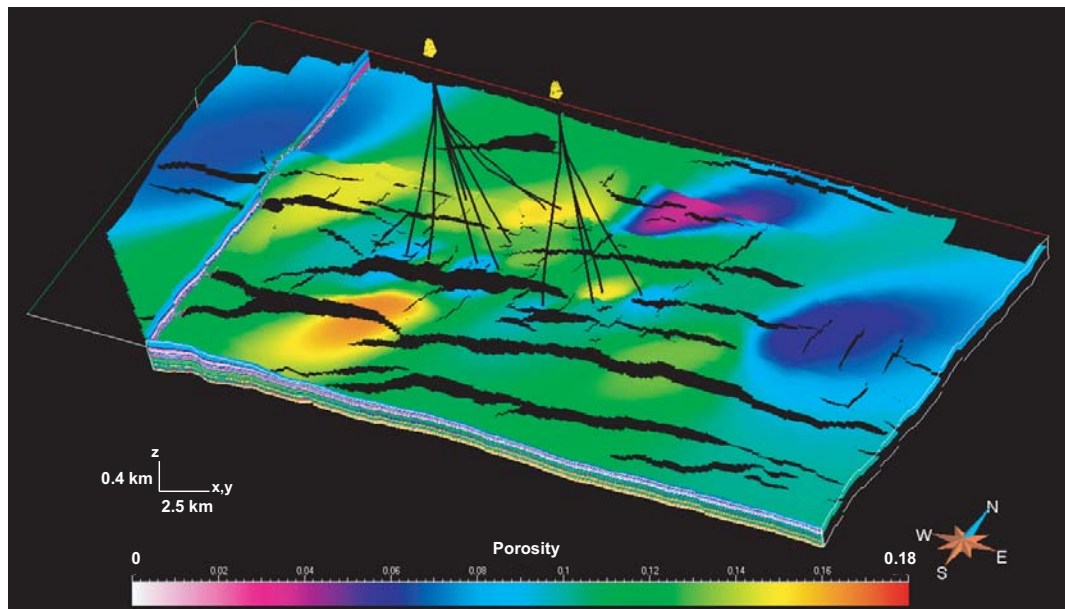


Fig. 5.11: Porosity distribution on a reservoir layer of geocellular model. Average porosity is  $\sim 8.6\%$  in the reservoir.

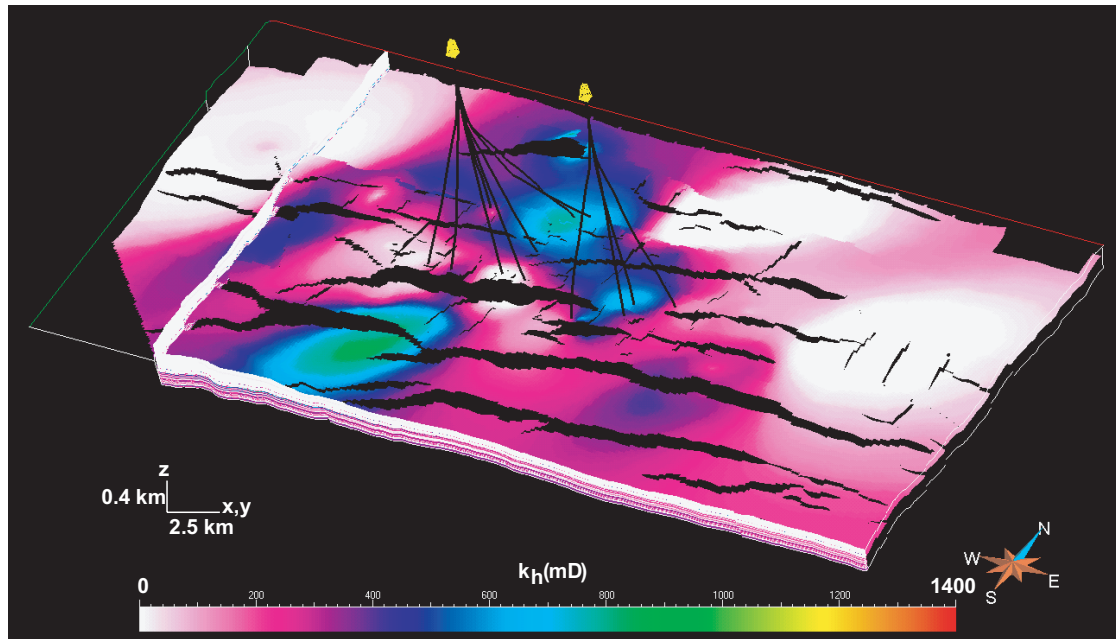


Fig. 5.12:  $k_h$  distribution on a reservoir layer of the geocellular model. Average  $k_h$  in the reservoir is  $\sim 200$  mD.

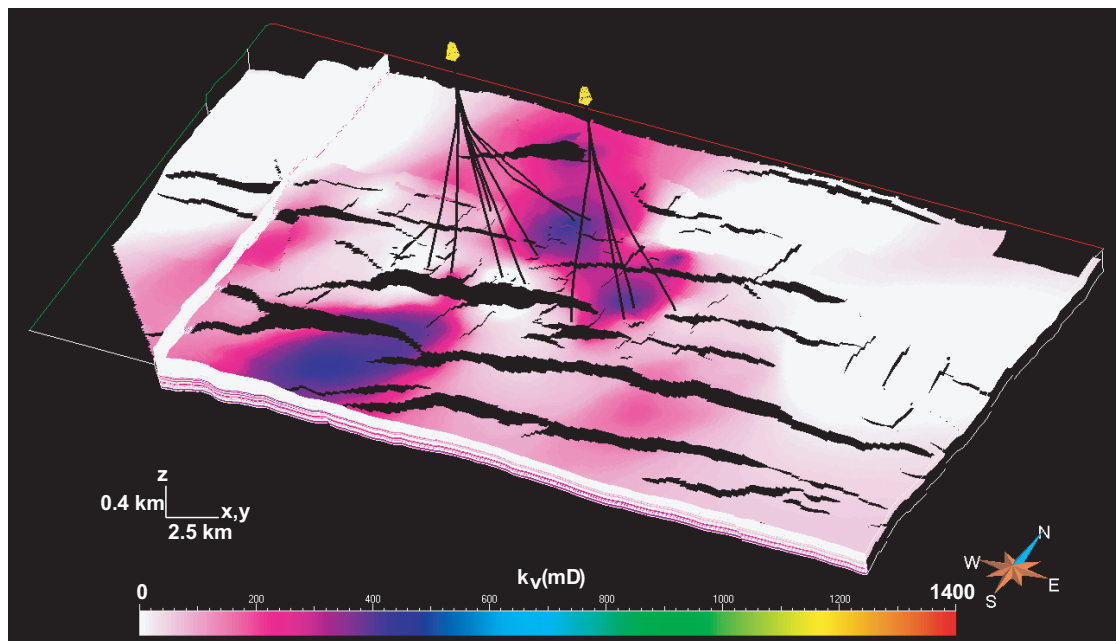


Fig. 5.13:  $k_v$  distribution on a reservoir layer of the geocellular model. Average  $k_v$  in the reservoir is  $\sim 60$  mD.

Regional geology is uncertain about the size and the properties of the aquifer volume connected to the CS field. The reservoir is normally pressured by the aquifer,

so it has a significant impact on overall recovery. In the model, aquifer volume is considered at least 100 times greater than the pore volume.

## 5.6 Initial conditions and fluid properties for reservoir simulation

Initial formation pressure obtained from downhole testers (MDT and RFT) shows initial reservoir pressure of  $\sim 4486$  psi at the gas water contact at  $\sim 3109$  m ss (sub-sea), which is common in all the appraisal wells. Pressure gradient analysis with the tests shows a normal water gradient of  $1.37$  psi/m and a gas gradient of  $0.35$  psi/m (Fig. 5.14).

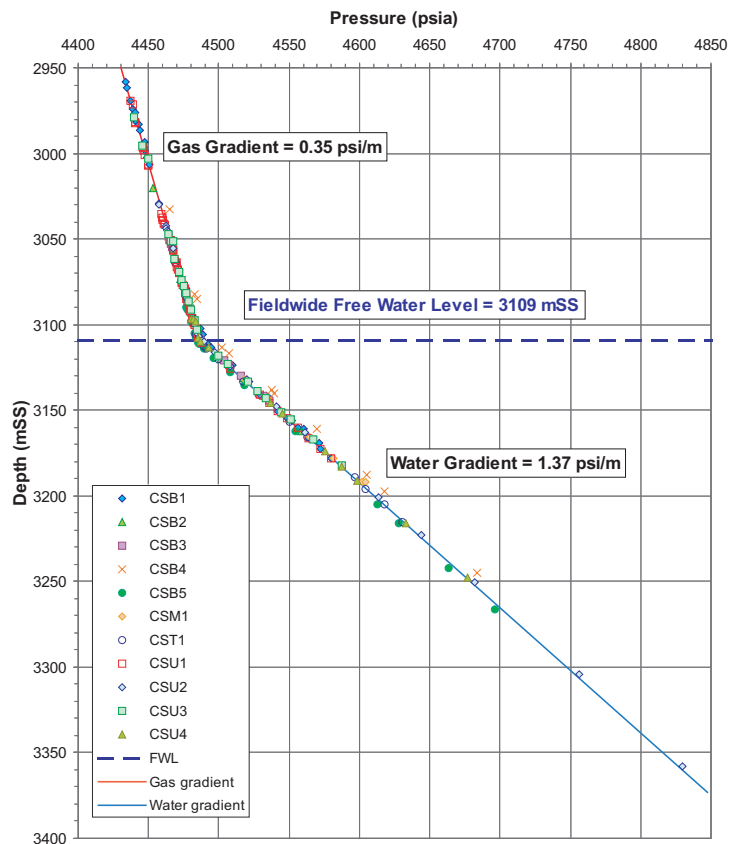


Fig. 5.14: Field wide gas and water gradient from the pressure tests in the exploration wells of the CS field. (modified from Lozada et al., 2005)

Compressibility of the rock matrix is obtained by uniaxial compressive testing on the core samples from CSB2, which suggest a very stiff and strong reservoir rock with a range of compressibility from  $1.2 \times 10^{-6} \text{ psi}^{-1}$  to  $3.8 \times 10^{-6} \text{ psi}^{-1}$  and an average compressibility of  $2.1 \times 10^{-6} \text{ psi}^{-1}$ .

Initial water saturation is defined as a function of porosity and permeability and height above the free-water-level (to include the effect of capillary pressure in transition zones). Initial water saturation ( $S_{w_i}$ ) and Flow Zone Indicator (FZI) are calibrated using core measurements and log data. Fig. 5.15 illustrates the relationship between the Klinkenberg corrected permeability ( $k$ ) versus irreducible water saturation ( $S_{w_{irr}}$ ) observed through core measurements. The best fit line of the data is shown in Eq. 5.4 (Lozada et al., 2005).

$$S_{w_{irr}} = -0.0615 \ln(k) + 0.4384 \quad (5.4)$$

FZI is defined using porosity and permeability values as in Eq. 5.5. Water saturation is then estimated using  $S_{w_{irr}}$ , FZI and height in meters above the free-water-level (Eq. 5.6). Fig. 5.16 shows initial water saturation distribution in the reservoir section, indicating an average value of  $S_{w_i} \sim 10\%$ .

$$FZI = 0.0314 \left\{ \frac{\sqrt{k/\phi}}{\phi(1-\phi)} \right\} \quad (5.5)$$

$$S_{w_i} = S\hat{w}(1 - S_{w_{irr}}) + S_{w_{irr}} \quad (5.6)$$

where  $S\hat{w}$  is defined in Eq. 5.7.

$$S\hat{w} = 1 - \left\{ \frac{0.1504.FZI^{1.1973}.h^{1.0529}}{(0.1483.FZI^{1.1973}.h^{1.0529}) + 0.9087} \right\} \quad (5.7)$$

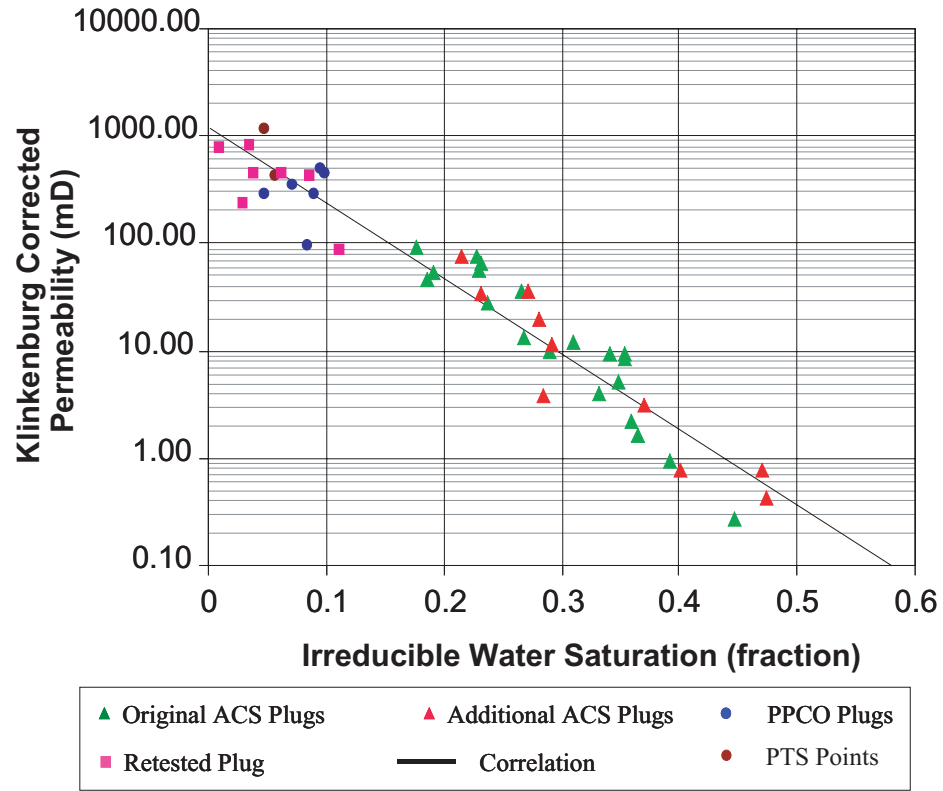


Fig. 5.15: Irreducible water saturation versus Klinkenberg corrected permeability data from core analysis. (modified from Lozada et al., 2005)

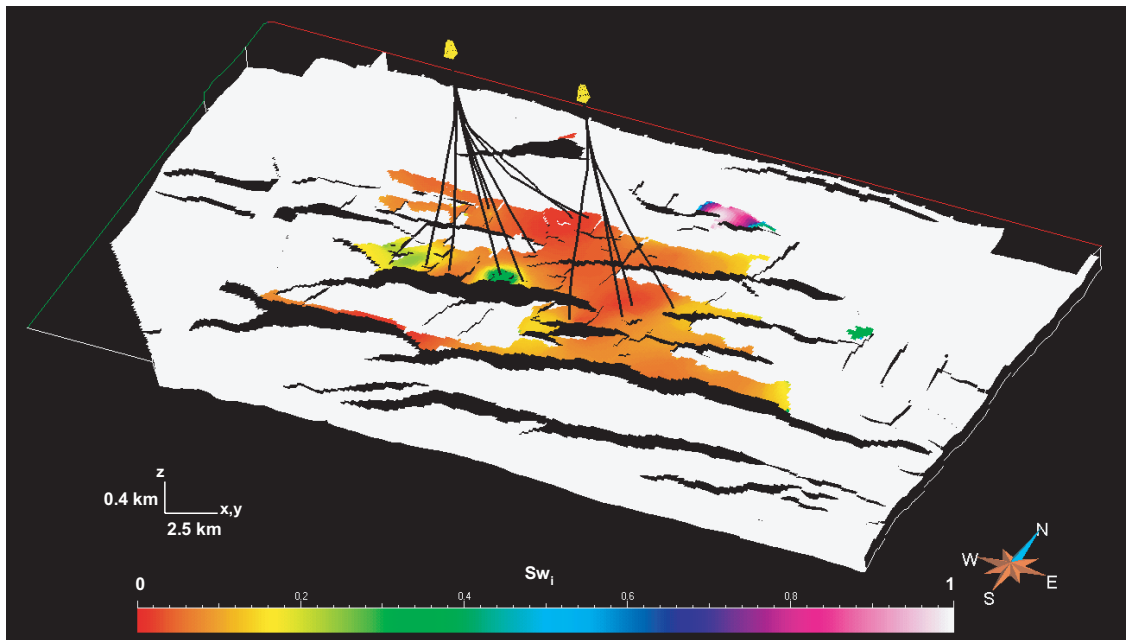


Fig. 5.16: Initial water saturation at reservoir depth of the CS field.

Residual gas saturation ( $S_{g_r}$ ) is obtained from core measurements using a brine immersion imbibition technique, which gives a range of 20-30% with an average value of 26.6%. Fig. 5.17 shows the observed values and the best fit line between  $S_{g_r}$  and the Klinkenberg corrected permeability ( $k$ )-porosity ( $\phi$ ) ratio (Eq. 5.8).

$$S_{g_r} = 35 - 0.131\sqrt{k/\phi} \quad (5.8)$$

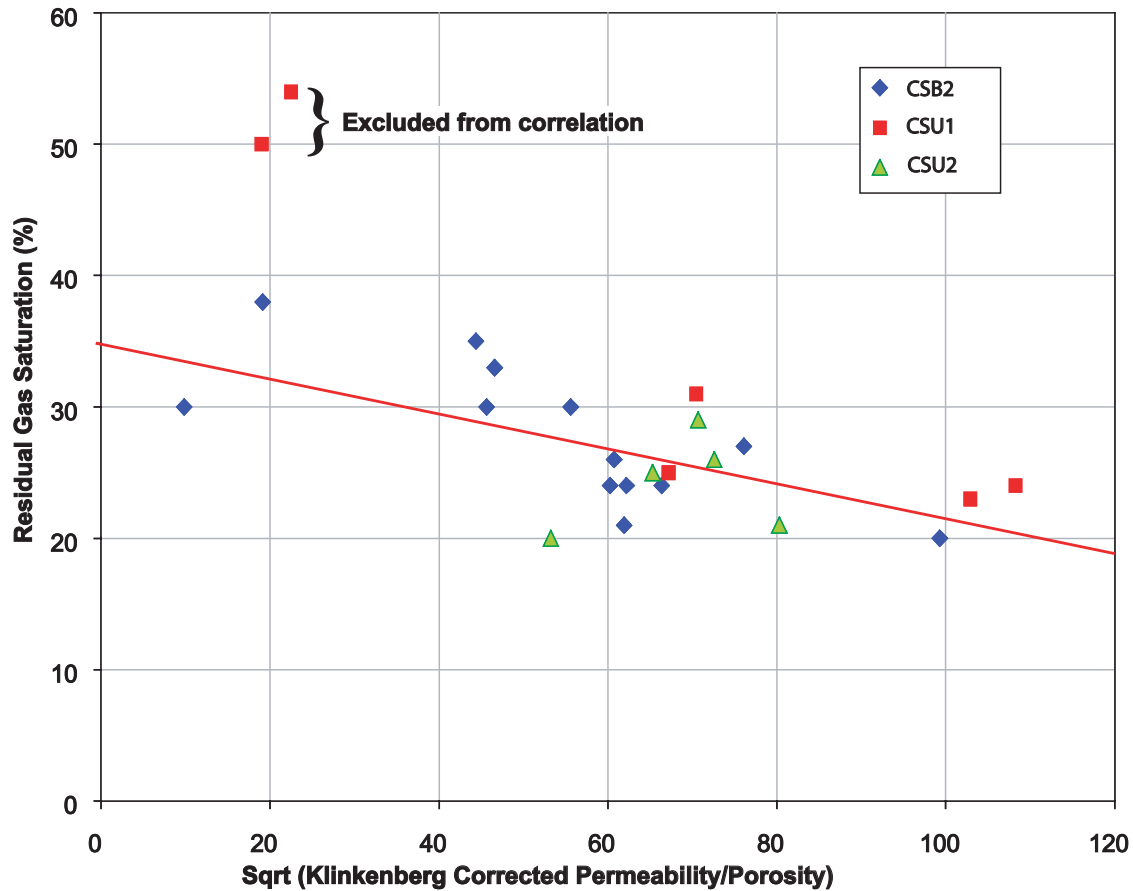


Fig. 5.17:  $S_{g_r}$  vs. permeability-porosity ratio indicates residual gas saturation above 30% in low permeability-porosity rocks. (modified from Lozada et al., 2005)

The relative permeability of the water at residual gas saturation is measured on core samples from the appraisal wells. Fig. 5.18 shows that the average relative permeability is 0.24 at residual gas saturation. This value is used to calibrate the water relative permeability curves from a similar sandstone reservoir. Fig. 5.19 shows the relative oil-water and oil-gas relative permeability curves used for reservoir simulation.

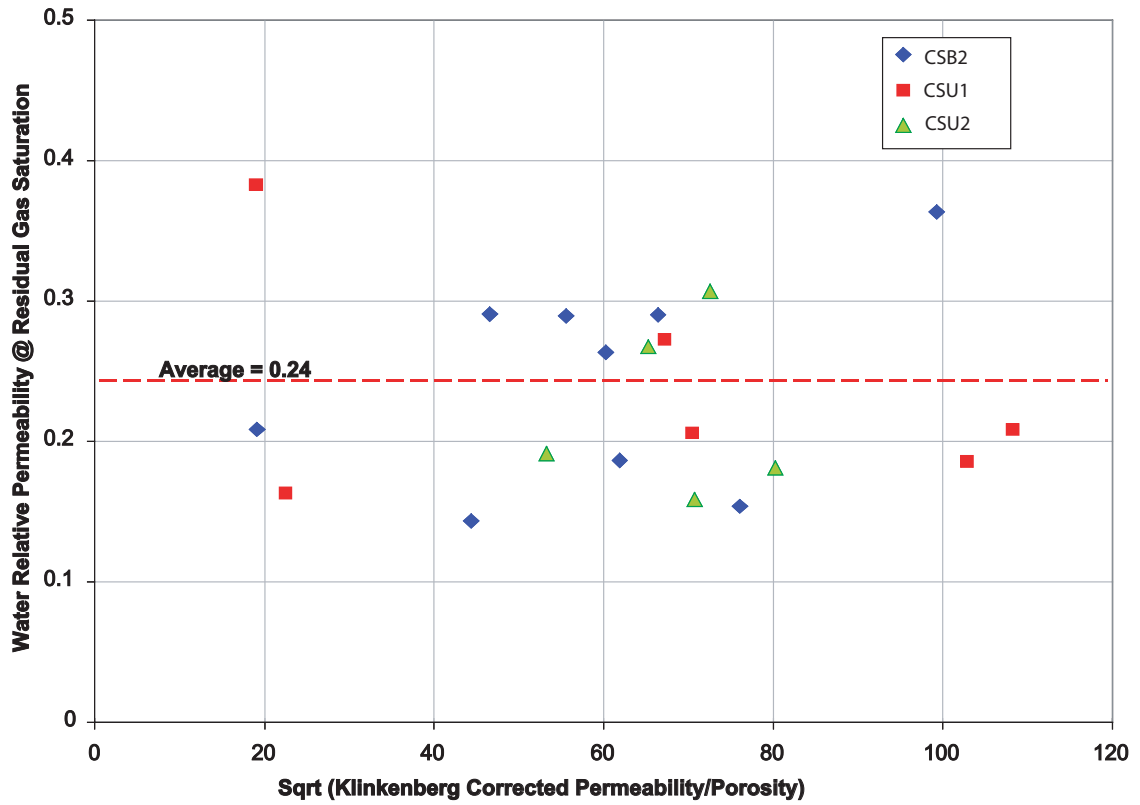


Fig. 5.18: Core measurements show an average water relative permeability of  $\sim 0.24$  at residual gas saturation. (modified from Lozada et al., 2005)

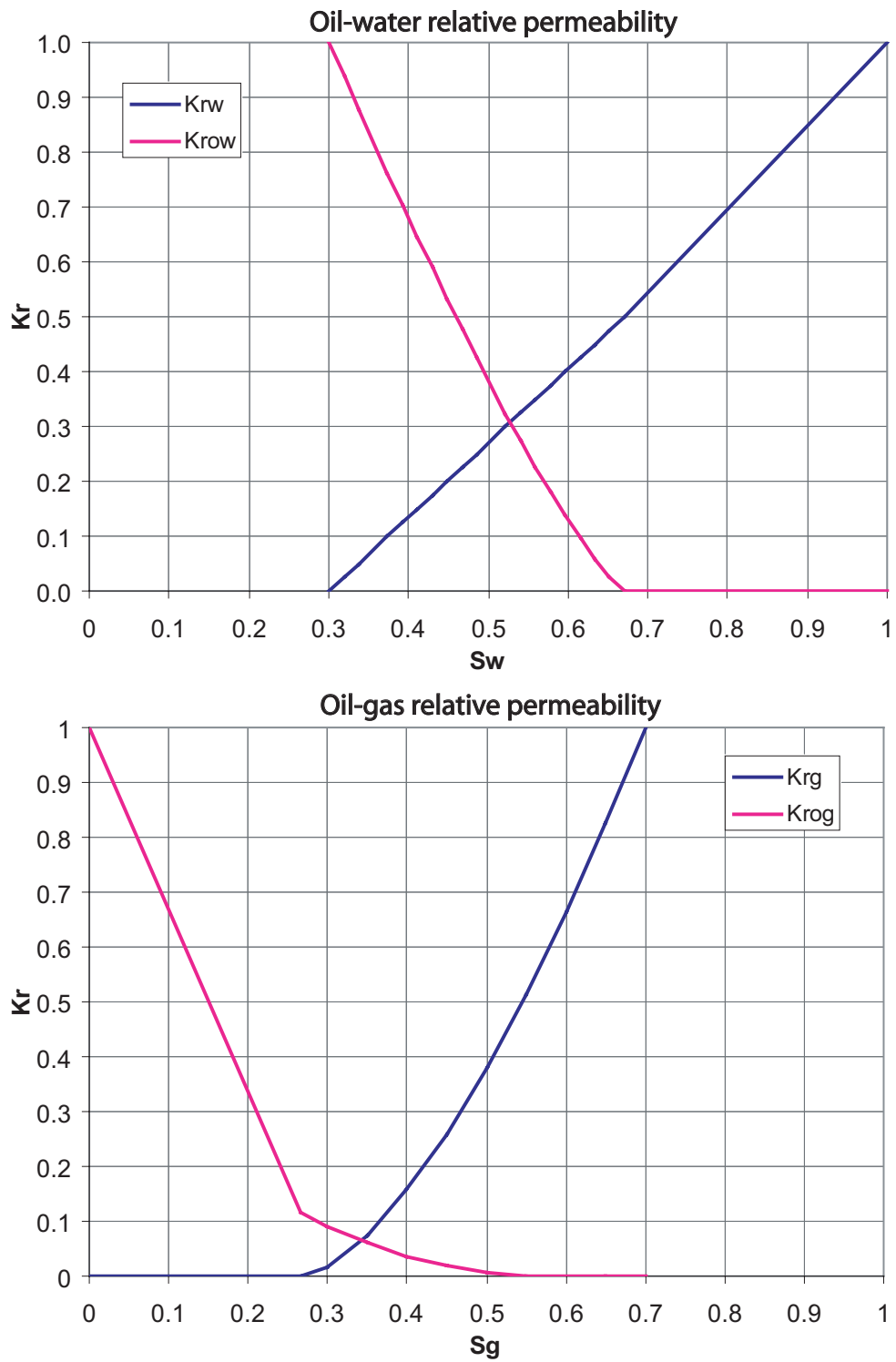


Fig. 5.19: Oil-water and Oil-gas relative permeability used during the simulation.



The simulation model of the CS field is a compositional model with 8 hydrocarbon components and 3 fluid phases. Properties of the water phase (Table 5.3) used during the simulation are measured from the samples collected during the drill stem testing in the well CSU2.

Table 5.3: Water properties used during the simulation

Reference pressure ( $P_{ref}$ )	4486 psia
Reservoir temperature ( $T_{res}$ )	264° F
Stock tank conditions	14.7 psia, 60° F
Formation volume factor ( $B_{wi}$ )	1.06 rb/stb, rb@ $P_{ref}$ and $T_{res}$
Compressibility ( $c_w$ )	$3.753 \times 10^{-6}$ psi <sup>-1</sup> @all pressure and $T_{res}$
Density ( $\rho_w$ )	63.7 lb/ft <sup>3</sup> @ stock tank condition
Viscosity ( $\mu_w$ )	0.232 cp@all pressure and $T_{res}$

Hydrocarbon fluid in the CS field reservoir is a retrograde gas condensate with a measured dew point of 4320 psia, which is lower than initial reservoir pressure of 4486 psia. Gas formation volume factor is 0.7921 rb/Mscf and viscosity is 0.0304 cp. Samples collected during drill stem tests (DST) in wells CSB1, CSB2, CSU1, and CSU2 show similar and uniform hydrocarbon fluid composition across the field. The average initial fluid composition used during the simulation is shown in Table 5.4.

Table 5.4: Initial hydrocarbon fluid composition in mol% used during the simulation

N2	CO2	C1	C2	C3	C4	C5	C6	C7-11	C12-19	C20+
3.42	5	71	7.35	4.63	1.2	2.5	1.51	2.7	0.53	0.01

Despite the similarities in the composition condensate yield in the wells located in the east of the field vary between 63-65 bbls/MMscf while the wells in west side show a value between 69-70 bbls/MMscf, so these zones are defined as two separate initial composition regions during the simulation. Constant volume experiments indicate that the maximum liquid phase volume is ~2.4% of total saturation volume at 1300 psi, which shows that most of the hydrocarbon volume is mobile and recoverable from the reservoir.

The properties of hydrocarbon fluids within the reservoir are defined using Peng-Robinson equation of state (Soereide and Whitson, 1992) for the reservoir simulation. The above list of 11 components is reduced to 8 components as C1/N2, C2/CO2, C3, C4, C5/C6, C7-C11, C12-C19 and C20+, and all the parameters for each of the 8 components for Peng-Robinson EOS are calibrated with the fluid samples observed in the appraisal wells.

## **5.7 Description of upscaled model and implementation of permeability changes due to damage zone**

The geocellular model is upscaled to a simulation model using an irregular non-orthogonal grid with grid size 80x46x45 cells in X, Y, and Z directions respectively. 45 layers in Z direction represent the 19 stratigraphic units or 265 layers of the geocellular model. The field is divided into six parts (Fig. 5.20) with different upscaling ratios to honor the heterogeneity of the reservoir. We can see in Fig. 5.20 that in the main gas bearing section, the simulation model is relatively fine (number of cells 60x40x45 in X, Y and Z directions for a 300m x 300m area) with respect to other parts of the reservoir. Average layer thickness varies from 3m to 20m. Fig. 5.21 shows depth of layer 18 of the upscaled grid where regions with pink to white color are structurally high areas with potential reservoirs.

The simulation model has 162 faults. Adjacent to the faults, the grid is truncated to honor the actual orientation and shape of the faults. In Fig. 5.21 we can see that the grid cells close to the faults are highly non-orthogonal and some of them are triangle shaped. Also, in most of the cases faults are not aligned to the grid axes. Due to these complexities a reservoir simulator with a two-point flux calculation (simulator used for this project) can only do an approximate calculation for this part of the grid. In the next section, we discuss how to implement the effects of damage zone in the grid blocks adjacent to the faults honoring the above complexities.

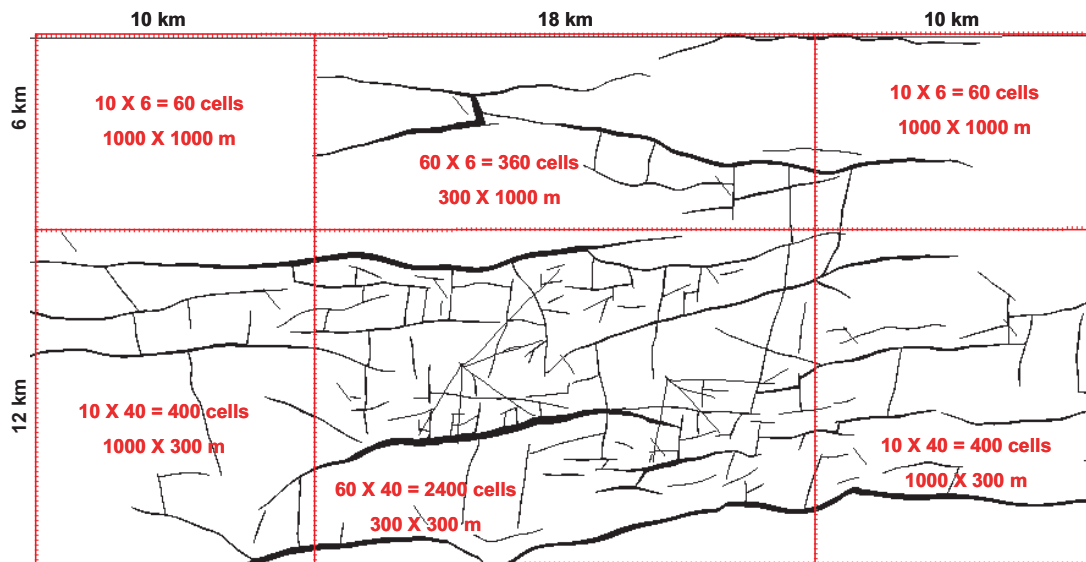


Fig. 5.20: In the reservoir part of the upscaled grid, number of cells is kept relatively high to honor the heterogeneity. (modified from Lozada et al., 2005)

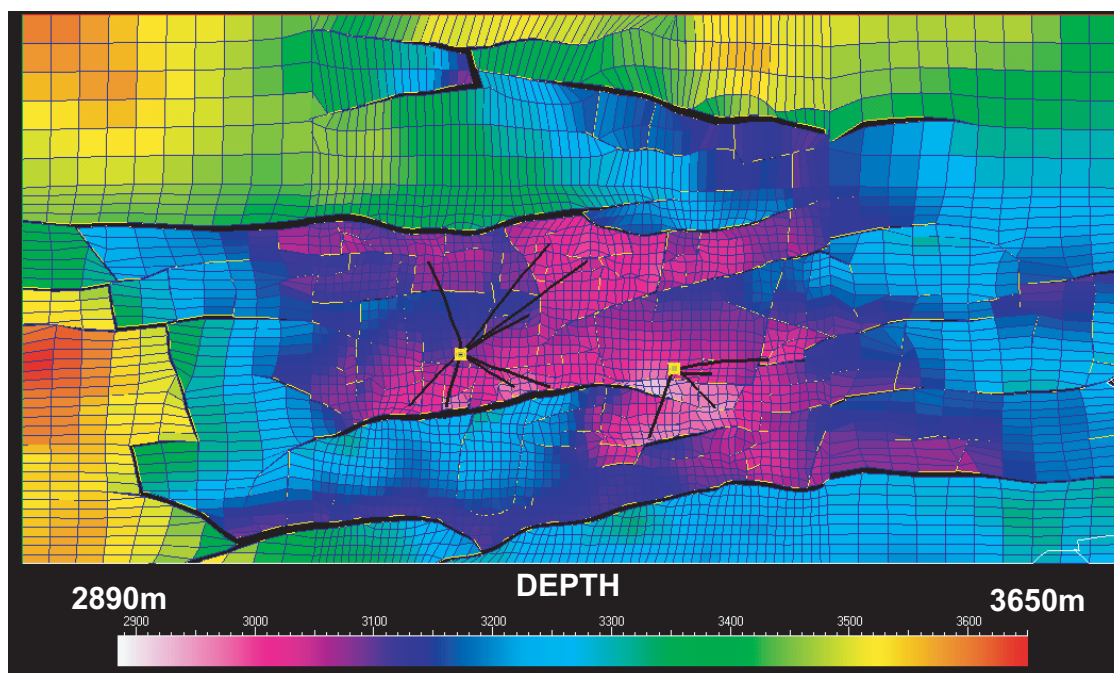


Fig. 5.21: Depth of layer-18 of the upscaled model. Main reservoir is located at the shallowest areas indicated by pink color on the map. Black lines with yellow head (platforms) indicate injector and producing wells.

Porosity is upscaled using arithmetic averaging. Horizontal permeability ( $k_h$ ) for fluvial layers is upscaled using a hybrid arithmetic-harmonic algorithm, while marine

layers are upscaled using a hybrid harmonic-arithmetic algorithm to capture the lateral reservoir heterogeneity. Vertical permeability ( $k_v$ ) is upscaled using harmonic-arithmetic averaging and in the grid blocks for shale layers with  $k_v < 0.1$  mD,  $k_v$  is set to zero to define them as a barrier to flow in the vertical direction. Water saturation is upscaled using a porosity weighted averaging algorithm. Fig. 5.22, 5.23, and 5.24 illustrate the porosity,  $k_h$  and  $k_v$  distribution of one of the reservoir layers (layer 18) of the base simulation model. Production in the CS field is constrained by hydrocarbon production rate and as we discussed before in this chapter that the response from the base simulation model shows a poor match for injection and production wells with actual field observations (Fig. 5.2).

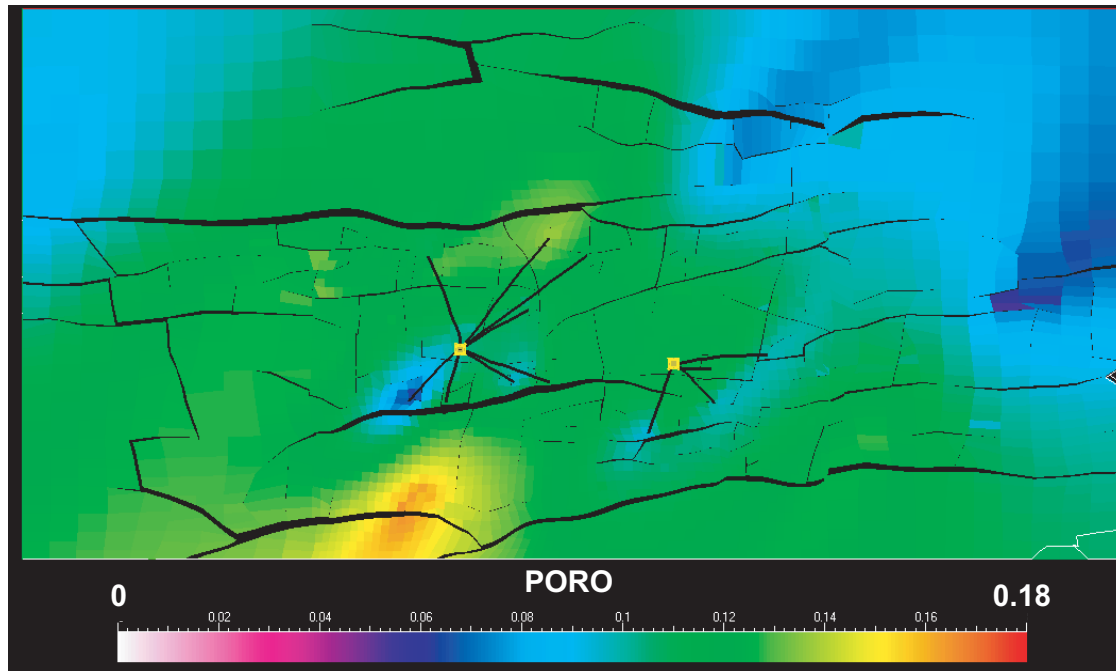


Fig. 5.21: Porosity of the main reservoir section (layer-18) of the upscaled model. Average porosity is 13%.

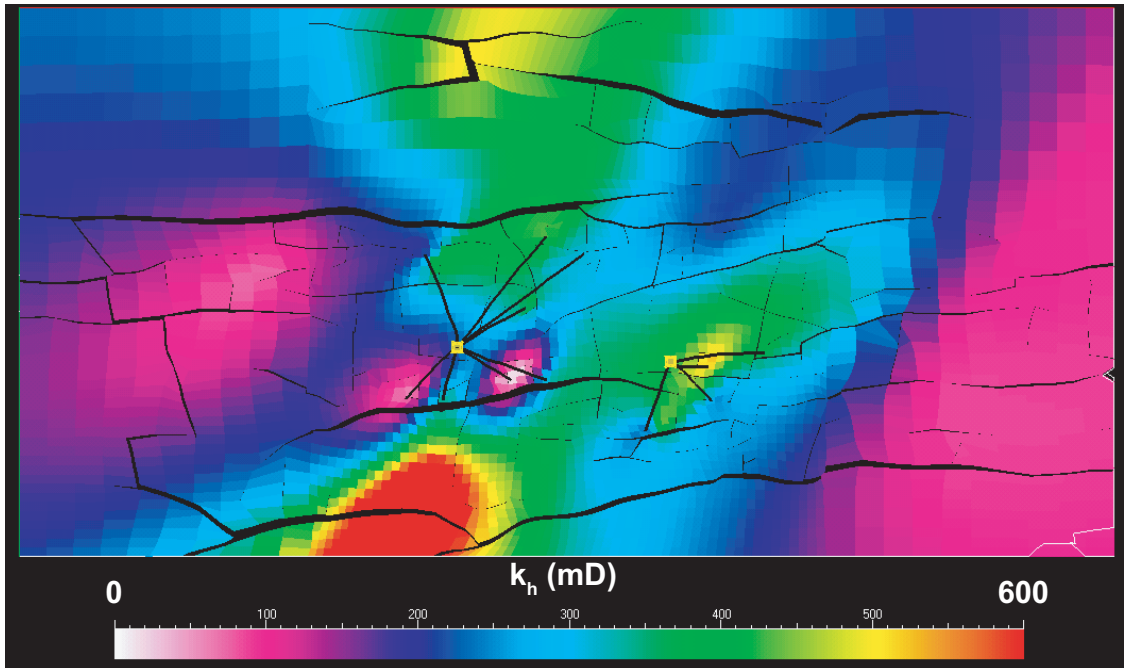


Fig. 5.22: Horizontal permeability ( $k_h$ ) of the main reservoir section (layer-18) of the upscaled model.  $k_h$  varies from 1 mD to 800 mD in the layer.

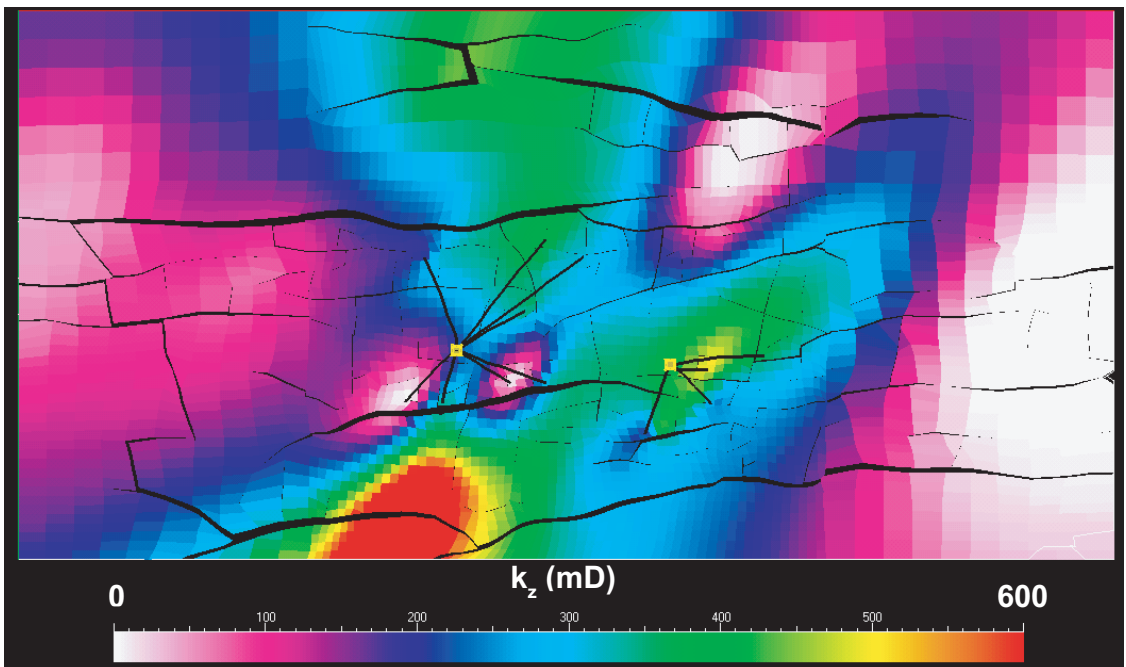


Fig. 5.23: Vertical permeability ( $k_v$ ) of the main reservoir section (layer-18) of the upscaled model.  $k_v$  varies from 0.6 mD to 600 mD in the layer.

### 5.7.1 Implementation of the damage zone in the upscaled grid

In chapter 4, we have estimated the extension of damage zones from the fault plane. Also from the fine scale simulations we have seen that these reservoir damage zones enhance permeability along the strike of the parent faults and in the vertical direction and there is negligible change perpendicular to the parent faults. Because permeability anisotropy caused by the damage zones is related to dip and strike of the parent faults, we need to project those directions on the upscaled grid. Fig 5.24 shows a generalized grid cell adjacent to the fault. In the damage zone, fault parallel permeability,  $k_1$ , is several tens of times higher than grid cell permeability,  $k_h$ , but fault perpendicular permeability,  $k_2$  is  $\sim k_h$ . This is a complex anisotropy problem, and ideally a full permeability tensor and/or local grid refinement (LGR) is used in the fault adjacent grid block to implement damage zone effect into the simulation model. However, the reservoir simulator we used could not handle either of the cases, so we approximate the anisotropy effect due to damage zones in X, Y, and Z direction permeabilities of the grid block. From the damage zone modeling in chapter 4 and well scale analysis in chapter 3, we know the relative distribution of fracture density (decreasing away from the fault) but we do not know the absolute effect of fracture density in each grid block adjacent to faults.

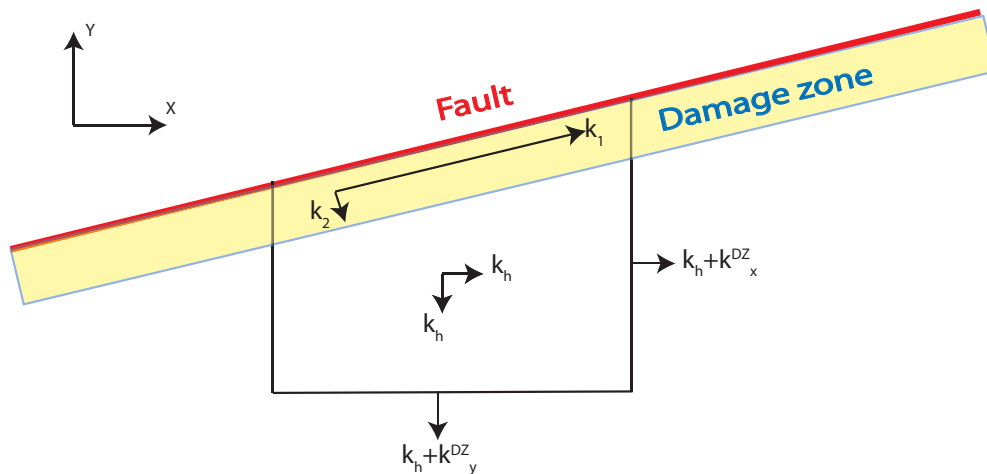


Fig. 5.24: Anisotropy in a generalized grid cell adjacent to a fault in the reservoir simulation model.

We assume that porosity change in the fault adjacent grid blocks is negligible because damage zone width and fracture volume are relatively low in comparison to the grid block size and the total pore volume of the grid block respectively. Following are the three steps we use to incorporate the effects of damage zones in the simulation grid.

1. Normalize the effect of damage zones in grid cells of different sizes.
2. Project the anisotropy effect associated with the damage zone on the fault adjacent grid blocks.
3. Estimate the effect of fracture density using history matching.

Fig. 5.26a and 5.26b illustrate the projected values of strike and dip at layer-18 of the model. Values are directly (no intra/extrapolation) projected from the fault plane to the nearest grid cell, which shows EW and NS trending faults are dipping with an average value of  $\sim 50^\circ$ - $60^\circ$ . Fig. 5.27a and 5.27b show the projected values of the mean,  $DZ\_mean$ , and standard deviation,  $DZ\_std$ , of the damage zone width from 100 simulations of the damage zone modeling discussed in chapter 4. Directly projected values of the damage zone mean onto the nearest grid cell indicates an average damage zone width of  $\sim 40$ - $50$ m with the maximum value ranging from  $\sim 90$ - $120$ m along the large faults. The standard deviation of 100 simulations is  $\sim 10$ - $15$ m at the average damage zone width but increases to  $\sim 60$ m in blocks with wide damage zones.

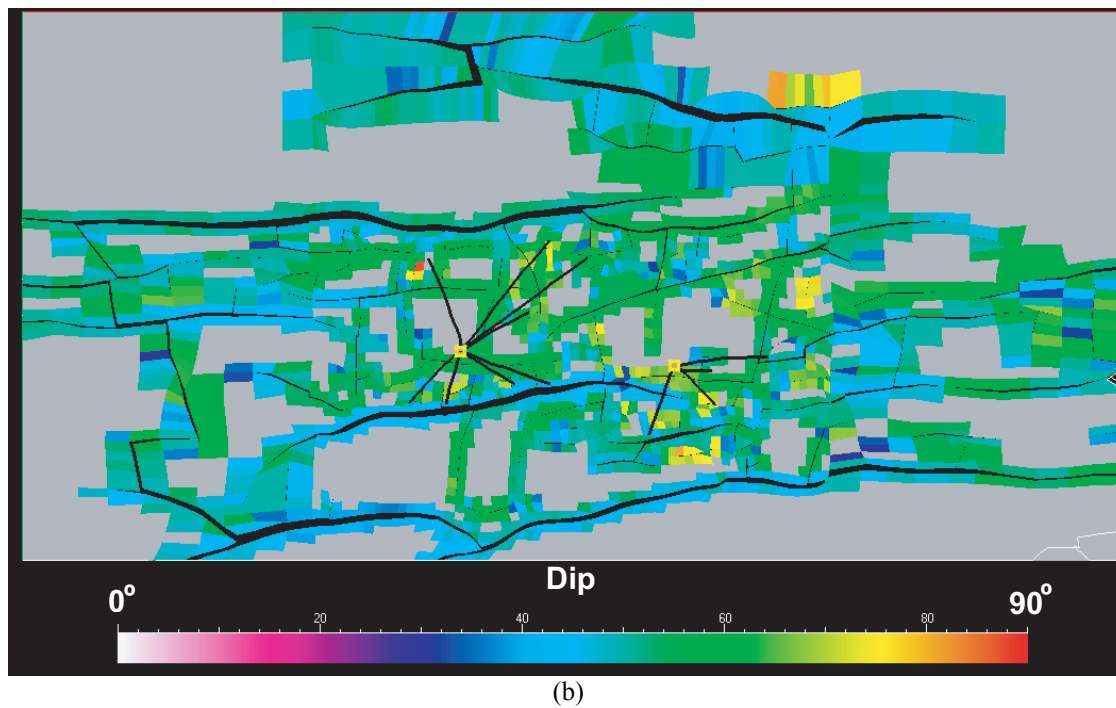
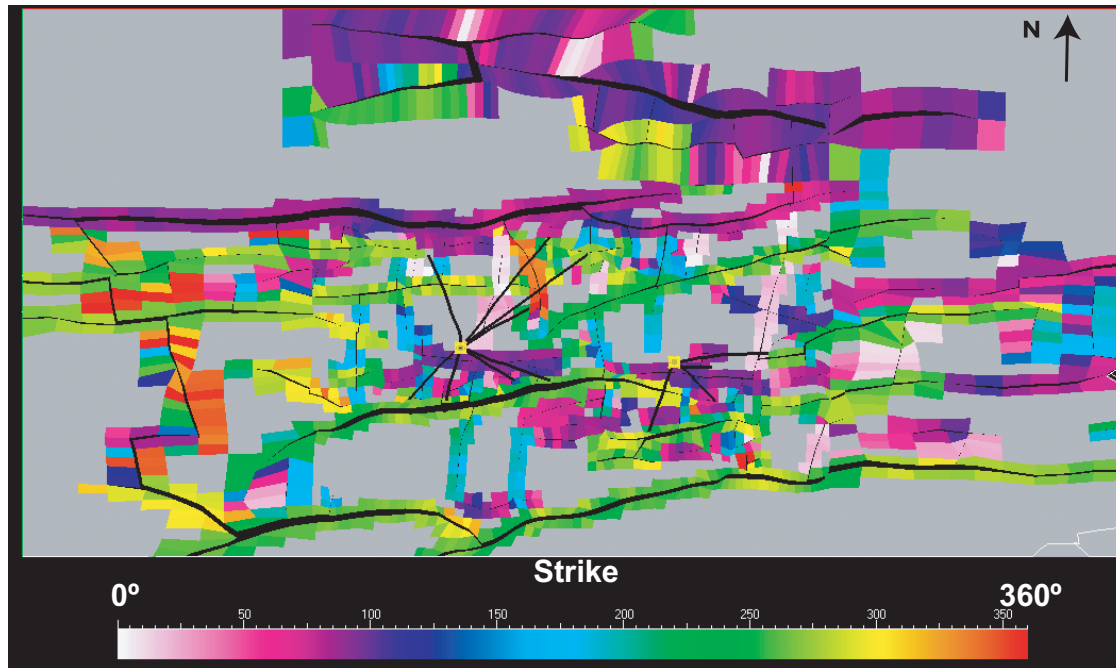


Fig. 5.26: Projected values of (a) strike and (b) dip of the reservoir scale faults shown on the layer-18 of the upscaled grid.



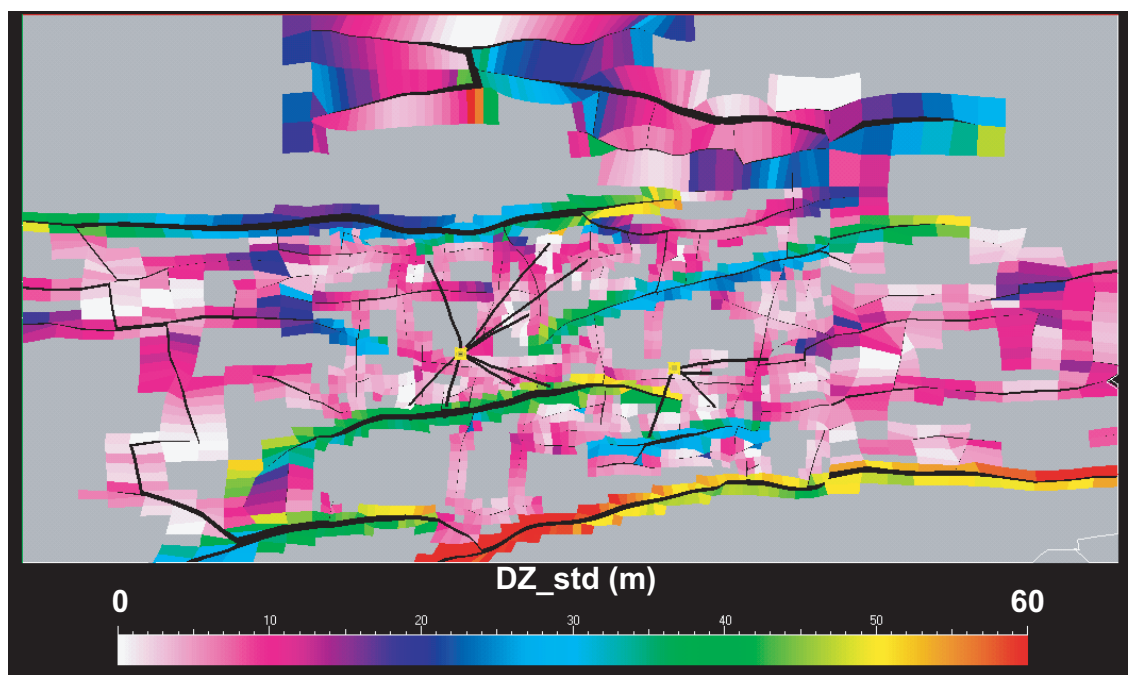
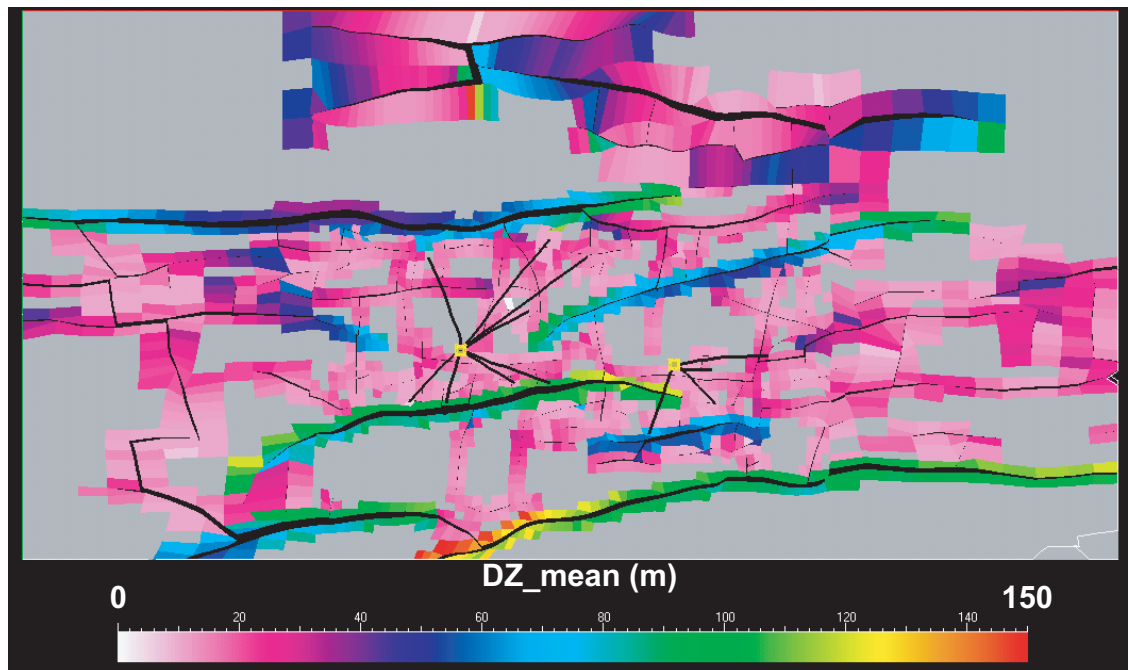


Fig. 5.27: Projected values of (a) mean and (b) standard deviation of the damage zone width on the layer-18 of the upscaled grid. Mean and standard deviation are estimated from 100 equiprobable simulations of the damage zone estimation using the rupture propagation technique.

In a simulation model grid blocks associated with reservoir scale faults may have different shapes and sizes, which is required to retain the actual shape of the faults. The effect of a damage zone on those grid blocks depends on the size of the blocks. Thus it is important to bring the estimated damage zone width into the simulator on a normalized scale and we call it the normalized damage zone intensity (NDZI). Damage zones run sub-parallel to reservoir faults but their width extends toward the dip so to normalize the damage zone width we divide it by bulk cell volume (CV) and the dimensions in vertical (DZ) and strike (DX or DY) directions of the associated fault, which is shown in Eq. 5.9a and 5.9b for faults trending in EW and NS directions respectively. Fig. 5.28 shows the NDZI values for layer-18 of the simulation grid. We can see that smaller cells associated with the same faults have higher NDZI and larger faults have higher NDZI because they have large damage zones.

$$NDZI_x = \frac{(DZ\_mean)(DX)(DZ)}{CV} \quad (5.9a)$$

$$NDZI_y = \frac{(DZ\_mean)(DY)(DZ)}{CV}, \quad (5.9b)$$

where  $DZ\_mean$  (Fig. 5.27a) is the mean of 100 simulations of damage zone models using rupture propagation technique discussed in chapter 4.

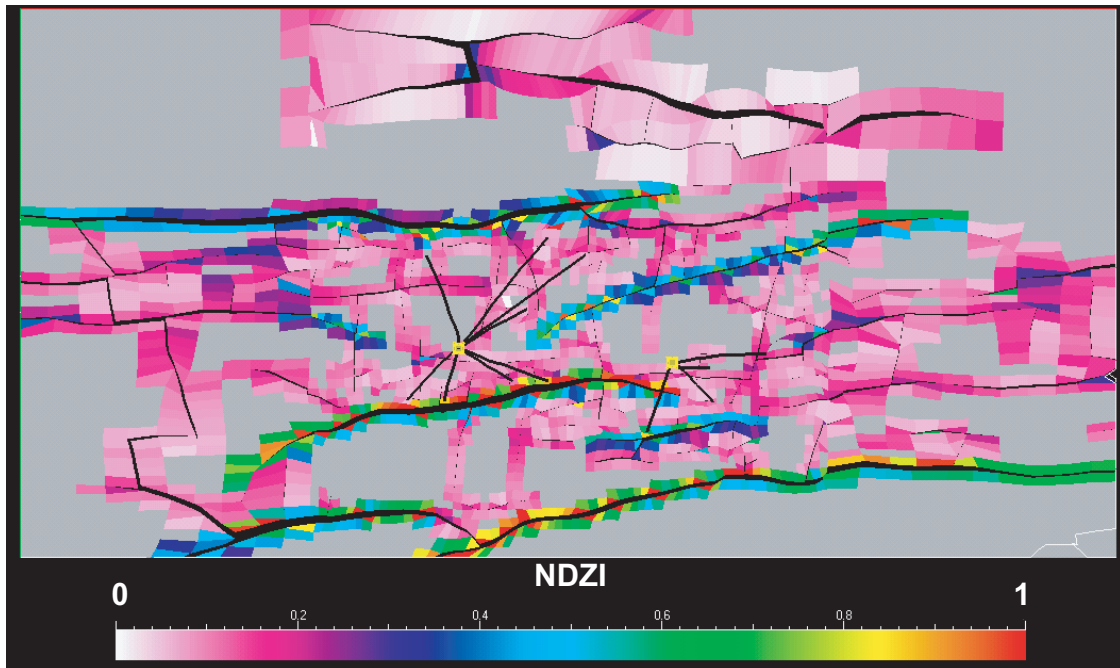


Fig. 5.28: Estimated values of normalized damage zone intensity (NDZI) on the layer-18 of the upscaled grid. Smaller grid cells adjacent to same fault show high NDZI value.

The fluid simulation study on a fine scale grid shows that the secondary features in the damage zone trend sub-parallel to strike of the parent faults so the maximum permeability enhancement is along the faults and in the vertical direction. Because most of the faults are not aligned to the grid axes, the effects are distributed in both the X and Y directions. The major component goes in the direction that is more aligned with the fault. The horizontal (X and Y) and vertical (Z) components of the permeability multiplier are related to the strike and dip of the fault respectively. Because the used reservoir simulator can not handle full permeability tensor, here we approximate the anisotropy effect using the magnitude of the dot product of full permeability tensor and normal vector of the grid faces for the damage zone. This is a reasonable approach because the permeability anisotropy effect is relatively high in the direction parallel to faults compared to perpendicular to faults, and most of the faults are either aligned to EW (X-direction) or NS (Y-direction). Eq. 5.10 represents the anisotropy coefficients in X, Y and Z directions, and in this study we call these components as normalized permeability factor (NPF). Fig. 5.29, 5.30, and 5.31 illustrate the NPF values for layer-18 on the simulator grids in the X, Y, and Z

directions respectively. We can see that faults aligned in EW direction have high NPF in the X-direction while the faults aligned in NS direction have a higher Y component. Also the NS trending faults have higher Z component because they have comparatively higher dip angle than the EW faults.

$$NPF_x = |\sin(\text{strike})| \quad (5.10a)$$

$$NPF_y = |\cos(\text{strike})| \quad (5.10b)$$

$$NPF_z = |\sin(\text{dip})| \quad , \quad (5.10c)$$

where strike and dip of the faults are in degrees.

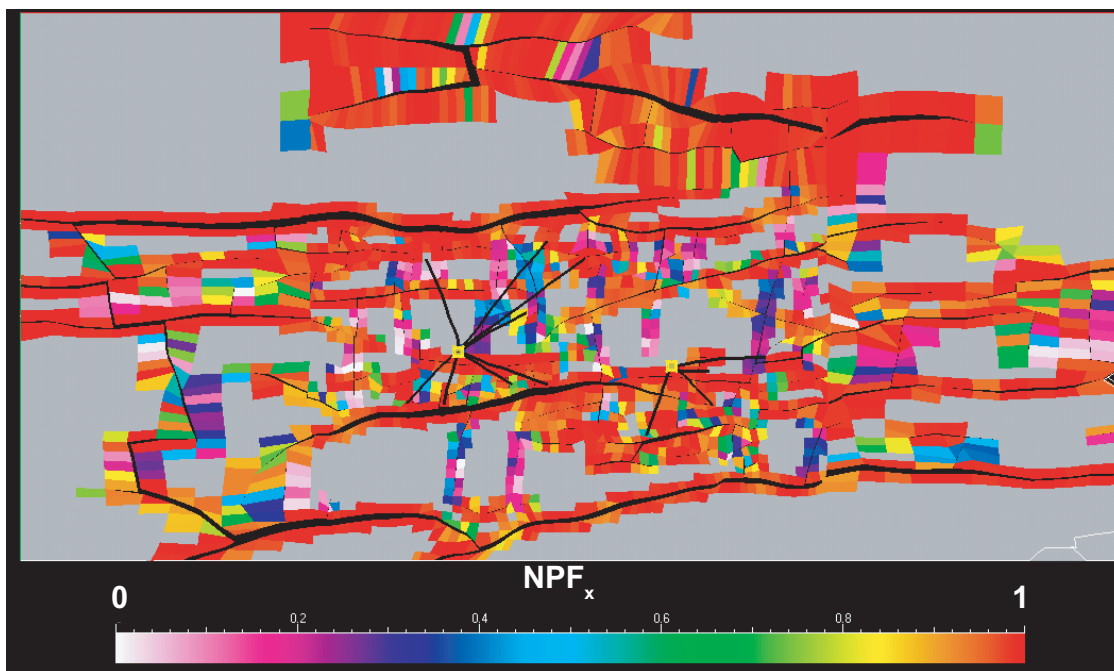


Fig. 5.29: Estimated values of normalized permeability factor (NPF) in X-direction on the layer-18 of the upscaled grid. It shows high connectivity in X-direction along the large reservoir scale faults trending in EW direction.

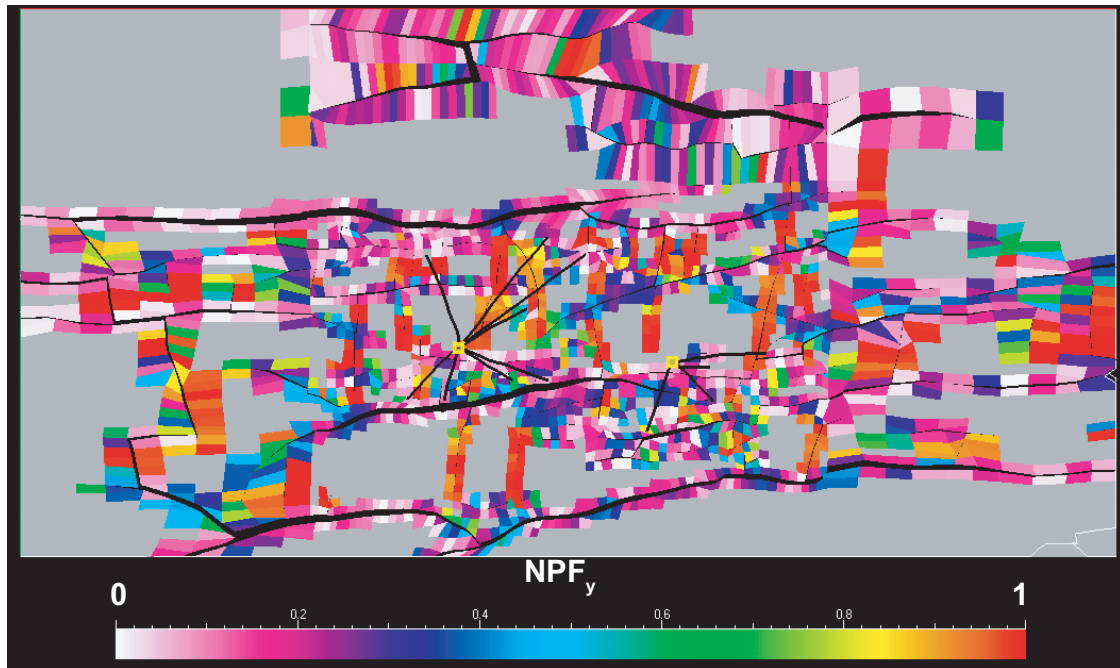


Fig. 5.30: Estimated values of normalized permeability factor (NPF) in Y-direction on the layer-18 of the upscaled grid.

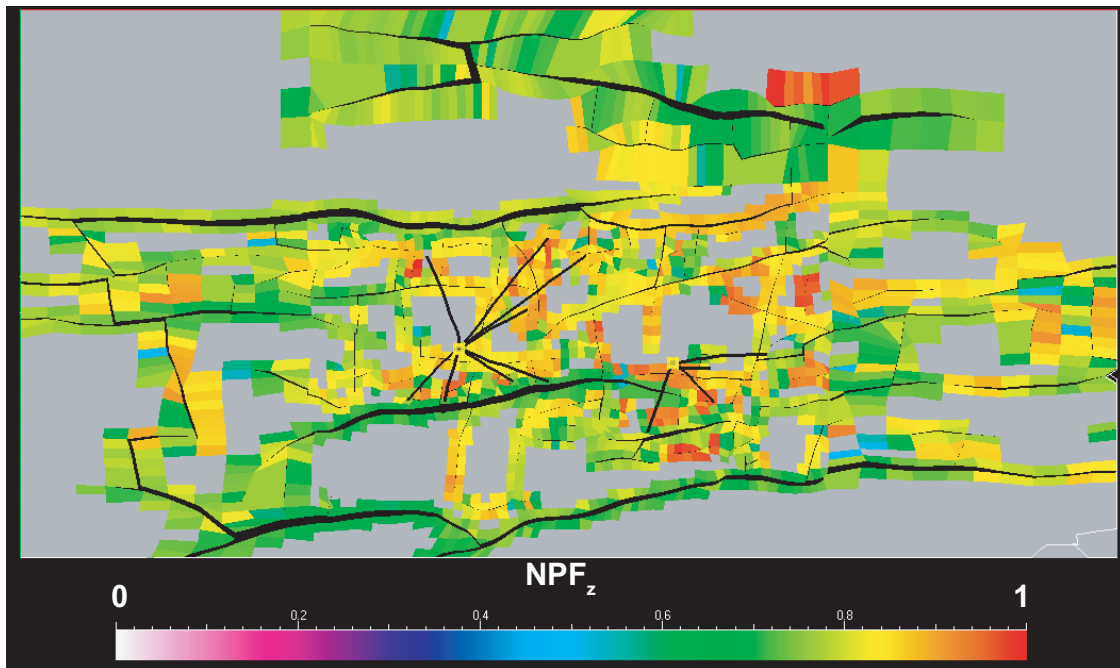


Fig. 5.31: Estimated values of normalized permeability factor (NPF) in Z-direction on the layer-18 of the upscaled grid. It shows relatively high vertical connectivity adjacent to the NS trending faults.

The next step is to include the effect of fracture density in each grid cell adjacent to the faults and then define a multiplier function using normalized damage zone intensity (NDZI), permeability anisotropy factors (NPF) and fracture density associated with damage zones to modify the permeability models in X, Y, and Z directions. Because absolute fracture density is an unknown factor, to define the multiplier function we use two parameters, m and n, for horizontal and vertical permeabilities respectively, which scale the fracture density among the grid blocks based on NDZI. Eq. 5.11a, 5.11b, and 5.11c define the actual permeability multipliers (APM) in X, Y, and Z directions.

$$APM_x = 1 + (NDZI)(NPF_x)(m) \quad (5.11a)$$

$$APM_y = 1 + (NDZI)(NPF_y)(m) \quad (5.11b)$$

$$APM_z = 1 + (NDZI)(NPF_z)(n), \quad (5.11c)$$

where NDZI and NPF are defined in Eq. 5.9 and 5.10 respectively. In this study, the values of m and n are defined by iterative history matching of the bottom hole pressure data from all producers and injectors. During the iterations we change the m and n values for fixed NDZI and NPF to modify the effect of fracture density associated with the faults, which modifies the permeability of the grid blocks adjacent to the faults by Eq. 5.12. The final values of m and n are values which produce the model giving the best history match in all the wells of the field. Fig. 5.32, 5.33, and 5.34 illustrate the APM values in the X, Y, and Z directions using m=20 and n=20 for layer-18 on the simulation grids, which gives the best history match. Figures show X (EW) and Z (vertical) direction APM values as high as ~15 and ~12 respectively and a maximum value of ~6 in Y (NS) direction. We see permeability enhancements of same order in X and Z directions, which is consistent with the 3D fine scale fluid simulation study discussed earlier in this chapter. For a grid block of 360x380m<sup>2</sup> with damage zone width ~60m and fracture density ~2 fracture/m (from well scale analysis in chapter 3), the 2D fine scale fluid simulation study suggests an enhance in fault-parallel permeability by ~6-7 times, which is consistent with the APM values of the

grid blocks of same size and damage zone width. The consistency of three independent technique validates the damage zone modeling and implementation techniques in this study and suggests that  $m = 20$  and  $n = 20$  indicates a fracture density  $\sim 2$  fractures/m.

If core permeability measurements are available in the damage zone (as described in the Nojima fault case study in chapter 4) we can calibrate  $m$  and  $n$  values in Eq. 5.11 by comparing those measurements with the permeability values in undamaged areas (far from the fault in a similar lithology).

$$k_{x\_mod} = (k_h)(APM_x) \quad (5.12a)$$

$$k_{y\_mod} = (k_h)(APM_y) \quad (5.12b)$$

$$k_{z\_mod} = (k_h)(APM_z) \quad (5.12c)$$

where  $k_h$  and  $k_v$  are horizontal and vertical permeability in the base simulator model (petrophysical model without damage zone effects).

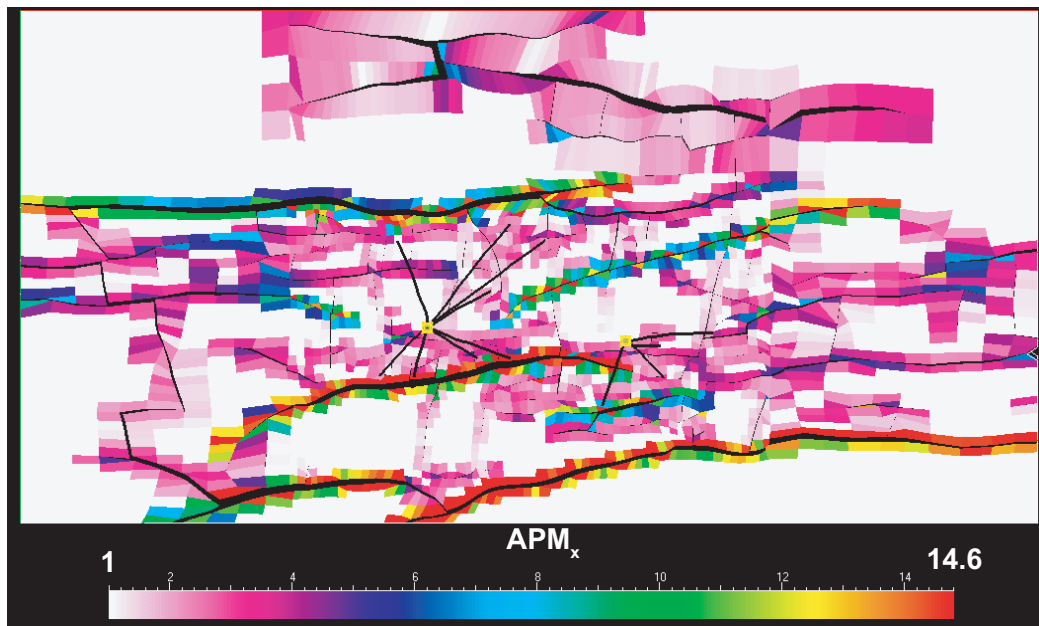


Fig. 5.32: Actual permeability multiplier (APM) in X-direction on layer-18 shows multiplier values up to  $\sim 15$  adjacent to the EW trending faults.



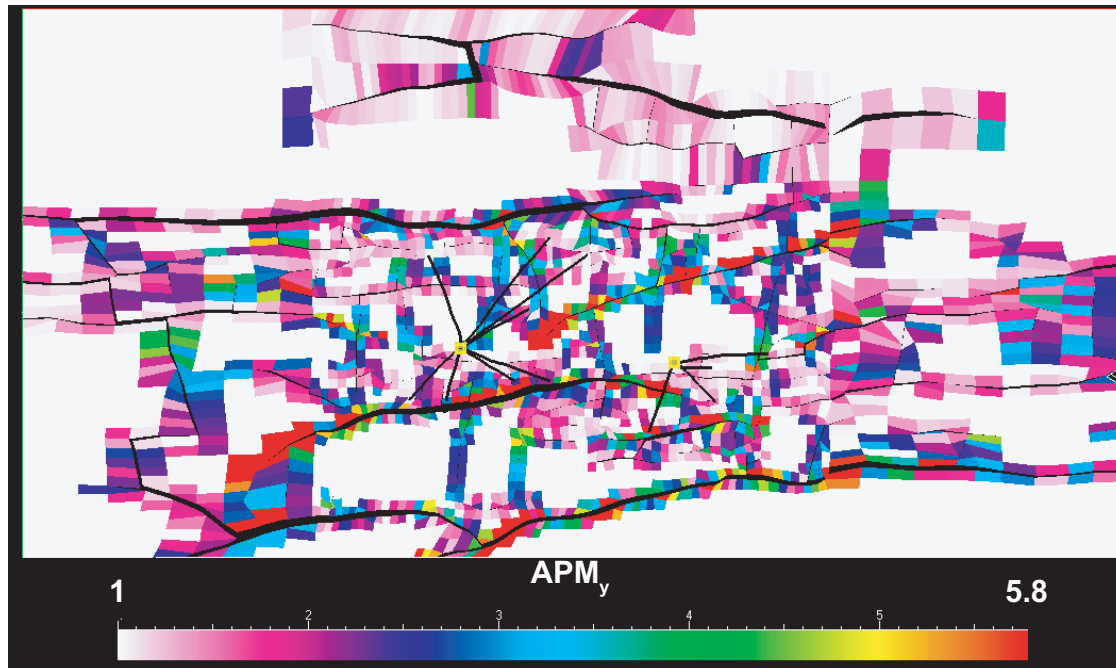


Fig. 5.33: Actual permeability multiplier (APM) in Y-direction on layer-18 shows relatively low values for multiplier. High values associated with some of the EW trending faults are related to the high inclination of those faults with respect to reservoir grid.

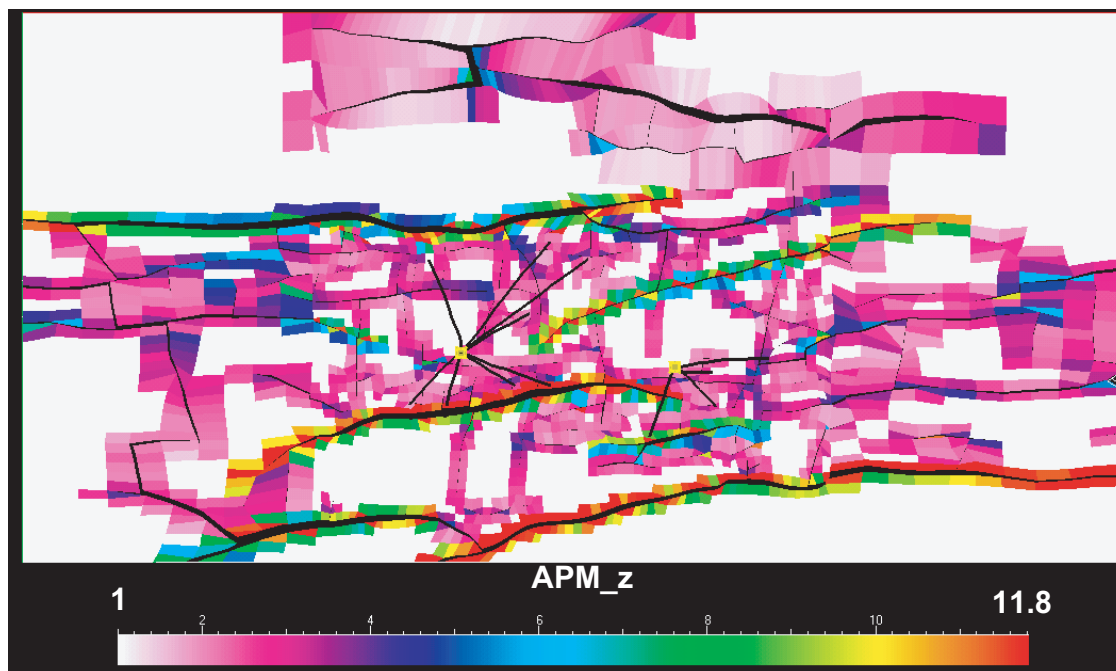


Fig. 5.34: Actual permeability multiplier (APM) in Z-direction on layer-18 shows that high multiplier are associated with the larger faults.



Fig. 5.35, 5.36 and 5.37 illustrate the modified permeability in the X, Y, and Z directions. The X-direction (EW) permeability ranges from 400-3200 mD in the grid blocks adjacent to the faults. Higher values are associated with the larger faults which are the major paths to give a preferential flow in EW direction and also observed in interference and tracer tests. The average value for the modified  $k_y$  is much lower than  $k_x$  values, which is consistent with the low connectivity in NS direction by the tests. Some of the high  $k_y$  values are associated with the inclined part of the EW trending fault, giving a high Y-component. The  $k_z$  values are relatively higher (1000-3000 mD) in the blocks associated with the larger faults, which may explain observations of good pressure support and also some of the water production from the aquifer. However, interbedded shale layers with very low permeabilities are still the barrier for overall vertical flow. Transmissibilities in the X, Y, and Z directions are estimated from the permeability models to use in the reservoir simulation.

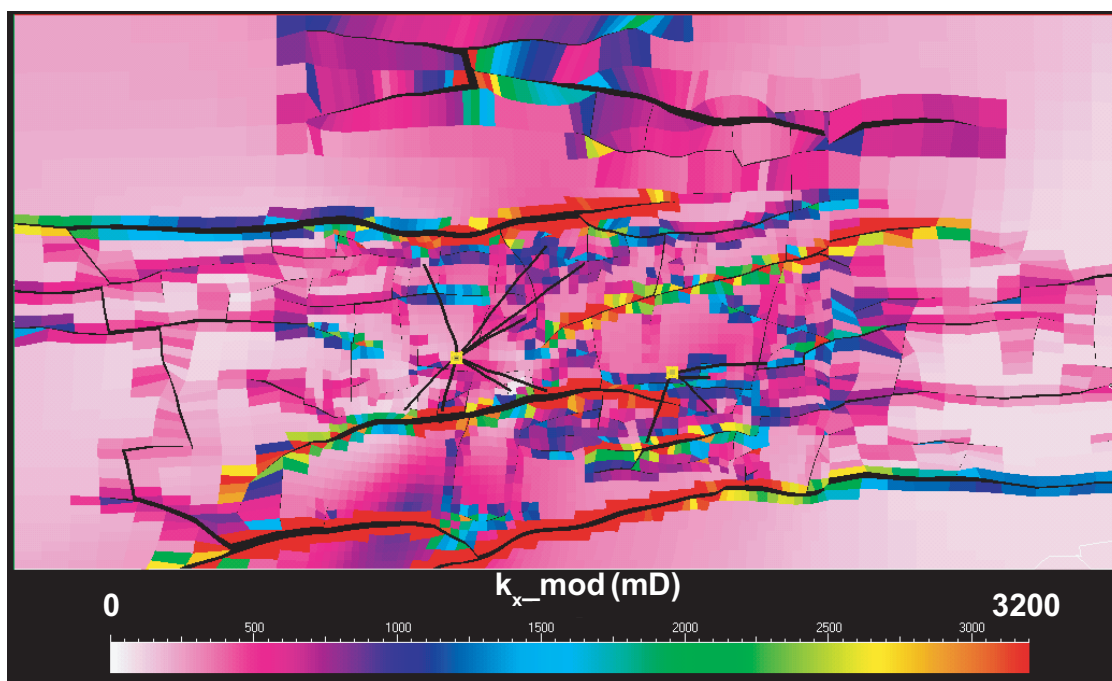


Fig. 5.35: Modified permeability in the X-direction ( $k_x$ ) on layer-18 of the simulation model. Large EW trending faults show high permeability anisotropy along the fault.

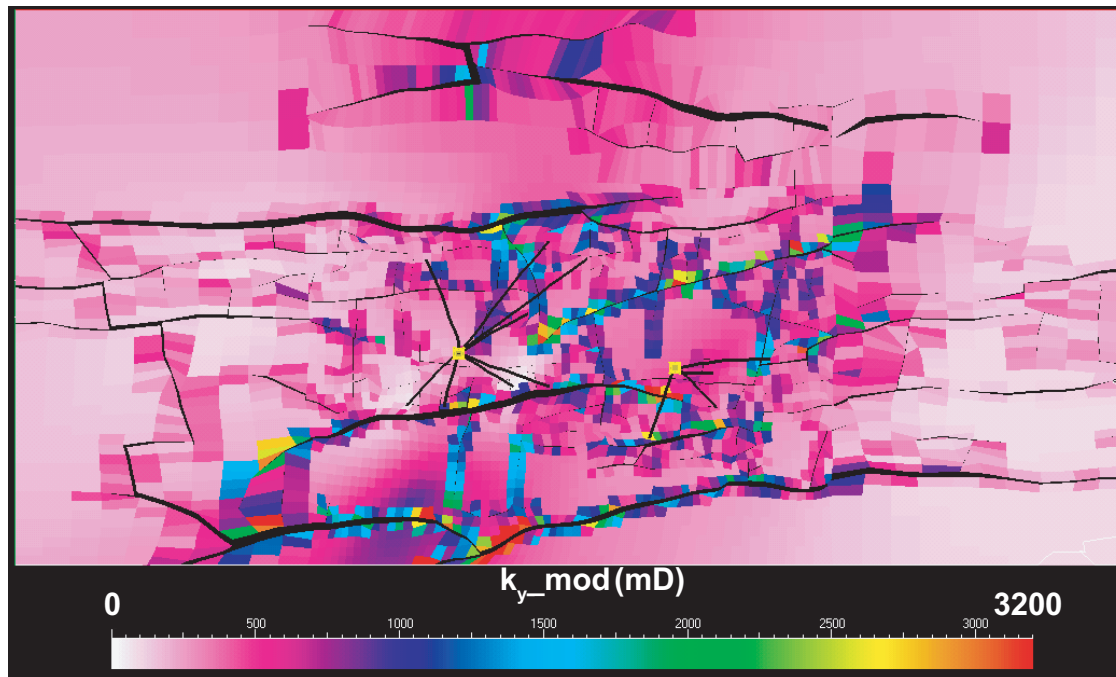


Fig. 5.36: Modified permeability in the Y-direction ( $k_y$ ) on layer-18 of the simulation model. Anisotropy in Y-direction is relatively low because of smaller faults in the NS direction.

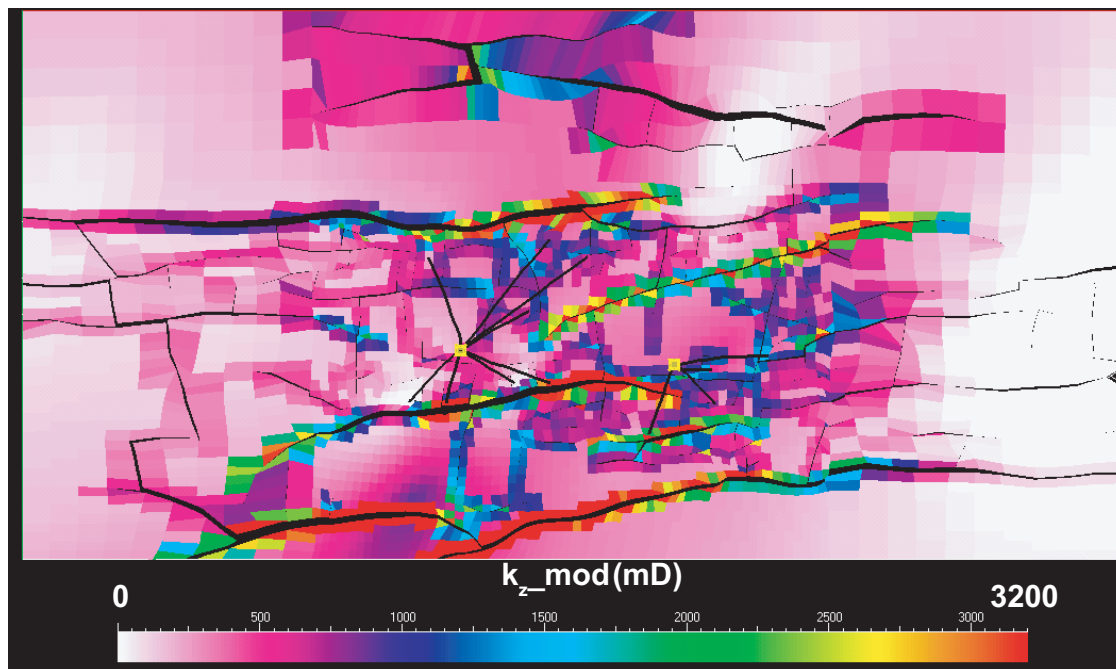


Fig. 5.37: Modified permeability in the Z-direction ( $k_z$ ) on layer-18 of the simulation model. Anisotropy in Z-direction is high for larger faults.

## 5.8 History matching

In this section we discuss history matching of the base reservoir simulation model and compare that with the history matching of the reservoir simulation model with the damage zones. We estimate the transmissibilities in X, Y, and Z directions and non-neighbor connections (NNC) from the permeability models discussed in the last section and use those in the reservoir simulation. Fig. 5.38 shows the locations of production (CSP1-CSP8) and injection (CSI1-CSI4) wells in the CS field. The CS field is a condensate reservoir and production and injection from the field are constrained by gas production and gas injection rates respectively, and bottom hole pressure (BHP) and water production from model response and field observation are compared qualitatively to do history matching. However, the gas rate constraint can not be implemented strictly in the model because of the condensate nature of the fluid. In most of wells the gas rate constraint and simulated gas rate are same but in some wells they are slightly different at the high gas production rates, which may affect the history matching of the water production. Because to apply the mass-conservation of the fluid for a given relative permeability distribution, the saturation of other phases has to change with the change of gas saturation.

Table 5.5 illustrates the listing of qualitative history matching for cases with m and n values of (= 10, 20, 30). All three cases show improvement from the base case and for m = 20 and n = 20 case, BHP and water production rate (WPR) both are improved from the cases with m and n values of (=10, 30). Blank boxes in the table indicate unavailability of the field data. Also, in some wells field data (magenta curve in Fig. 5.39 to 5.67) is available only for a limited production/injection period.

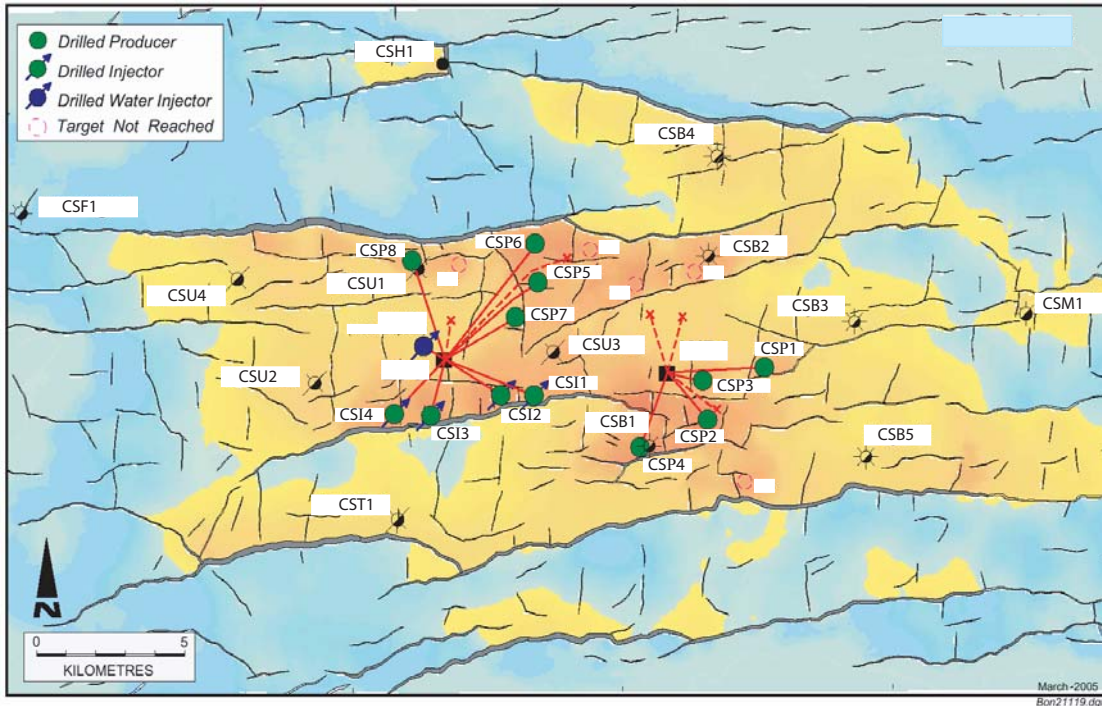


Fig. 5.38: Production and Gas Injection wells of the CS field. Wells are produced and injected using the rate constraint. (modified from Lozada et al., 2005)

Table 5.5: Qualitative history matching with BHP and water production rate (WPR) for cases with m and n values of (=10, 20, 30). Blank boxes indicate unavailability of field data.

Wells	m = 10, n=10		m = 20, n=20		m = 30, n=30	
	BHP	WPR	BHP	WPR	BHP	WPR
I - Injector	(psig)	(bbl/day)	(psig)	(bbl/day)	(psig)	(bbl/day)
P - Producer						
CSI1						
CSI2	> obs		≈ obs		< obs	
CSI3	> obs		≈ obs		< obs	
CSI4						
CSP1	≈ obs in BU << obs in DD	≤ obs	≈ obs in BU < obs in DD	≤ obs	≈ obs in BU < obs in DD	≤ obs
CSP2		>> obs		> obs		> obs
CSP3	< obs in both BU and DD	< obs	≈ obs in BU ≤ obs in DD	< obs	> obs in BU ≥ obs in DD	<< obs
CSP4	< obs in both BU and DD	≈ obs	≤ obs in BU ≥ obs in DD	≈ obs	≈ obs in BU >> obs in DD	≈ obs
CSP5		≈ obs		≈ obs		≈ obs
CSP6		≥ obs		≥ obs		≥ obs
CSP7	≤ obs in BU << obs in DD	> obs	≤ obs in BU < obs in DD	≈ obs	≤ obs in BU < obs in DD	≤ obs
CSP8	> obs in BU	>> obs	≈ obs in BU	≈ obs	< obs in BU	> obs

BU – Build up or no flow from the well  
 DD – Draw down or flow from the well  
 obs – observed field data

### 5.8.1 Reservoir pressure

In this field, reservoir pressure is supported by both aquifer and injected gas, so understanding fluid communication in both vertical and horizontal directions is important for the reservoir production behavior. In the base simulation model, the vertical communication is controlled by vertical permeability and the juxta-position of faults, and the horizontal communication is controlled by spatial lateral reservoir heterogeneity. Permeability anisotropy due to damage zones supports both horizontal and vertical communication. Thus, defining them into the reservoir simulation model may improve the pressure history match of the reservoir. Fig. 5.39 compares the simulated BHP response from the base model and the history matched BHP from the model with damage zone with observed BHP data for the wells shown in Fig. 5.2. We can see a significant improvement in the history matching. History matching of each well is discussed below in more details.

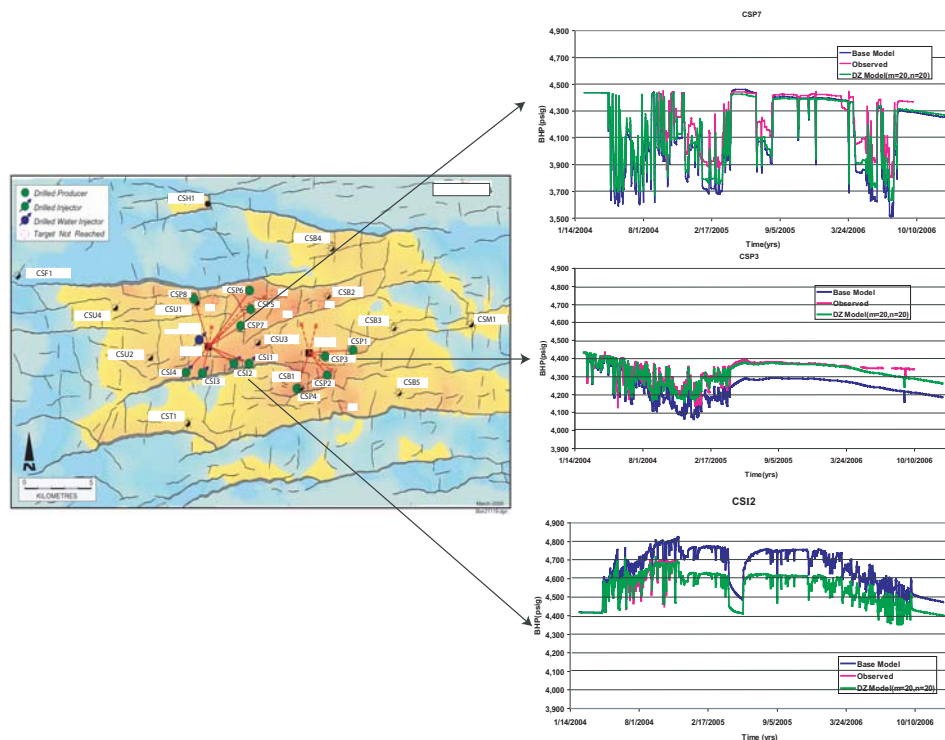


Fig. 5.39: Comparison of observed BHP (magenta), simulated BHP from the base model (blue), and history matched BHP from the damage zone model (green) for the wells shown in Fig. 5.2.



Figs. 5.40 and 5.41 compare the simulated bottom hole pressure (BHP) of the base reservoir model and damage zone reservoir model with the observed bottom hole pressure for two injector wells CSI2 and CSI3. The injection rate for well CSI3 is  $\sim 25000$  Mcf/day higher than well CSI2. However, the reservoir pressure adjacent to well CSI3 shows an increase of  $\sim 80$ psi from the initial static reservoir pressure of  $\sim 4486$ psi, which is less than the pressure increase around well CSI2 ( $\sim 150$ psi), indicating that injector CSI3 has better connectivity to the rest of the reservoir. In both the wells we can see that the base model is overestimating the reservoir pressure because of the lack of connectivity, which does not allow the dissipation of the pressure due to injected gas. The pressure match for the model with the damage zone is significantly improved because of increased permeability in the EW and vertical direction (along the larger faults), which dissipates the injected pressure.

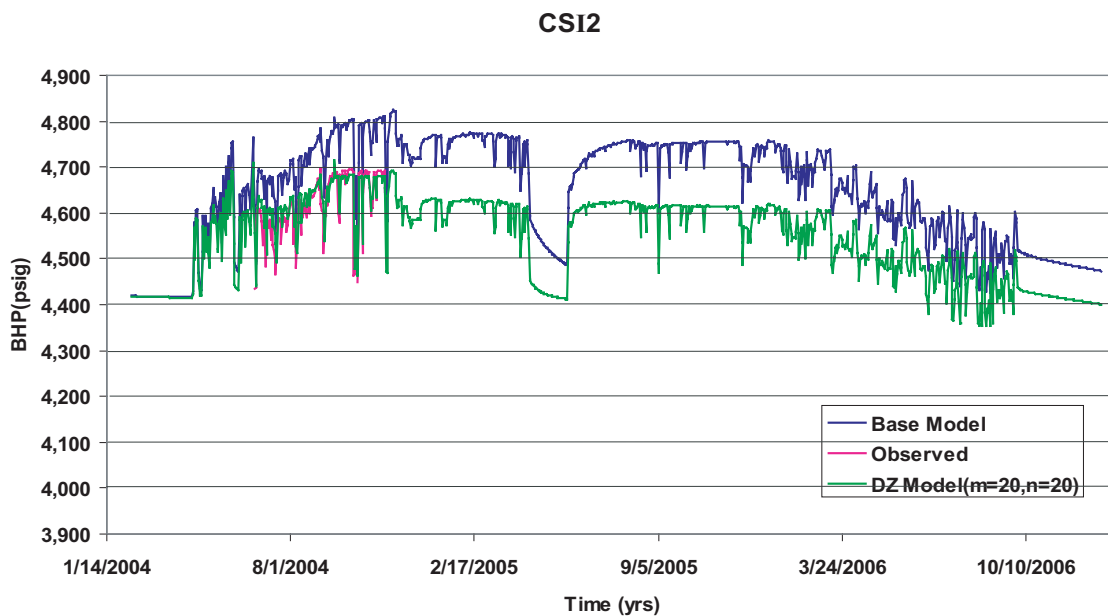


Fig. 5.39: Bottom Hole Pressure (BHP) history match of the injector well CSI2 shows a significant improvement in the damage zone model in comparison to the base simulation model.

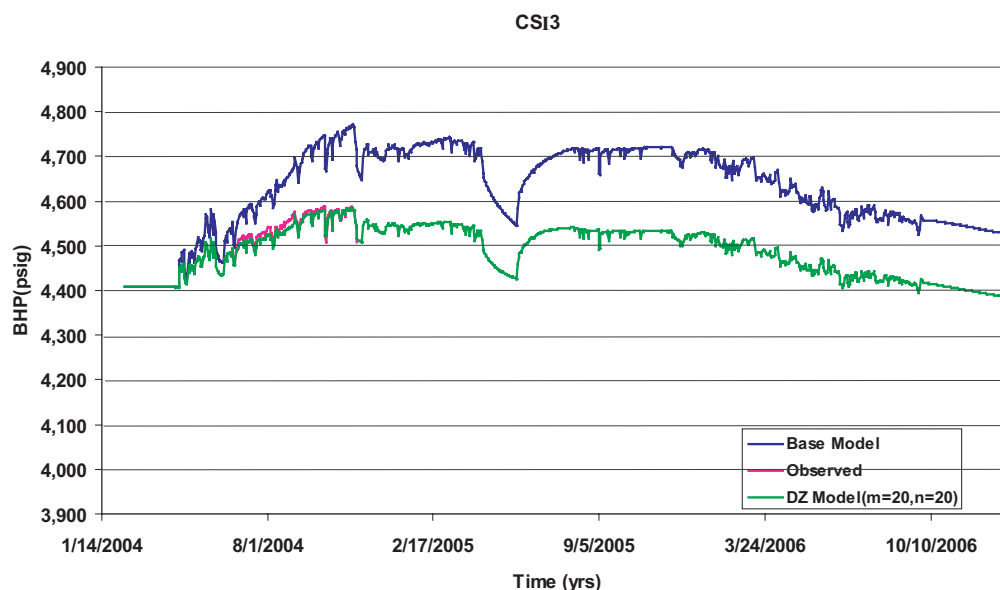


Fig. 5.41: Bottom Hole Pressure (BHP) history match of injector CSI3 shows a significant improvement in the damage zone model. Lower static pressure indicates better connectivity of this well with other parts of the reservoir.

In the well CSP3, which is located to the east of the injectors (Fig. 5.38) we see significant improvement in BHP match from the damage zone model comparing to the base model (Fig. 5.42). Because the base model does not have direct communication between well CSP3 and the injectors it predicts reservoir pressure  $\sim 90$ psi less than the observed pressure. The damage zone model provides high permeability paths along the EW trending paths which gives the pressure support from the injectors and is consistent with the observed pressure response. After one and half years of production  $\sim$ Jun 2005, pressure depletion is  $\sim 50$  psi. Also, at a later period, after Apr 2006, BHP from both the models (base model and damage zone model) have a sharper declining trend comparing to the observed values, which may be explained by the uncertainty in the aquifer size. During the early period of production aquifer support is not so effective because of high pressure in the reservoir section but after a period of production when the actual reservoir is depleted, pressure support from the aquifer has an important role in maintaining the average reservoir pressure. In this case, a sharp decline in BHP from the models indicates a need of higher pressure support from the aquifer, which may come from a larger aquifer. In this study we do not change the size

of the aquifer in the models because the objective of the study is to see the effect due to damage zones in the reservoir.

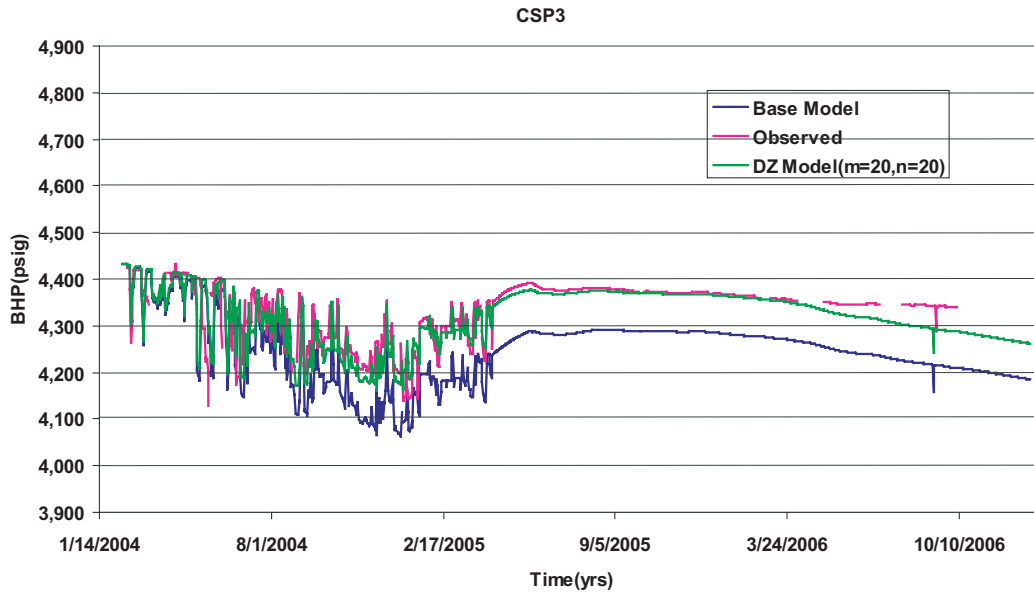


Fig. 5.42: Bottom Hole Pressure (BHP) history match of production well CSP3 shows a significant improvement in the damage zone model in comparison to the base simulation model. High decline trend in the late period indicates insufficient aquifer size to maintain the observed pressure.

In the well CSP4 which is in the same structure as well CSP3 (Fig. 5.38), the damage zone model shows a much improved BHP matching with the observed values in comparison to the base model (Fig. 5.43). However, for well CSP1 (Fig. 5.44), which is further east from wells CSP3 and CSP4 and at larger distance from the injectors (Fig. 5.38), the damage zone model shows a relatively poor history match of BHP after six months of production. Because this well is at the flank of the structure, aquifer effects may be visible even in an earlier period of the production and a sharp BHP decline from the models indicates the same.



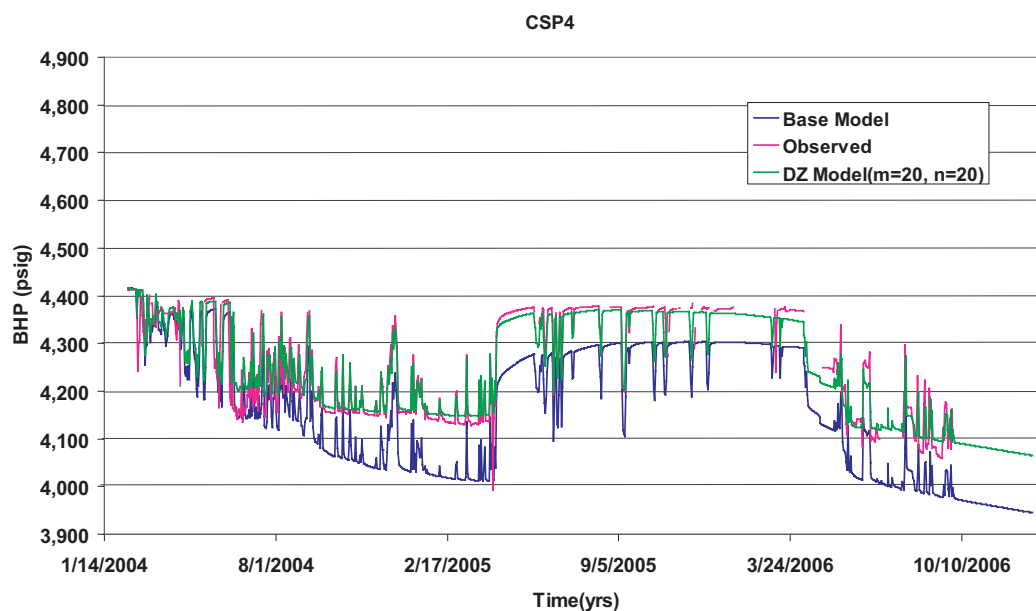


Fig. 5.43: Bottom Hole Pressure (BHP) history match of production well CSP4 shows a significant improvement in the damage zone model in comparison to the base simulation model.

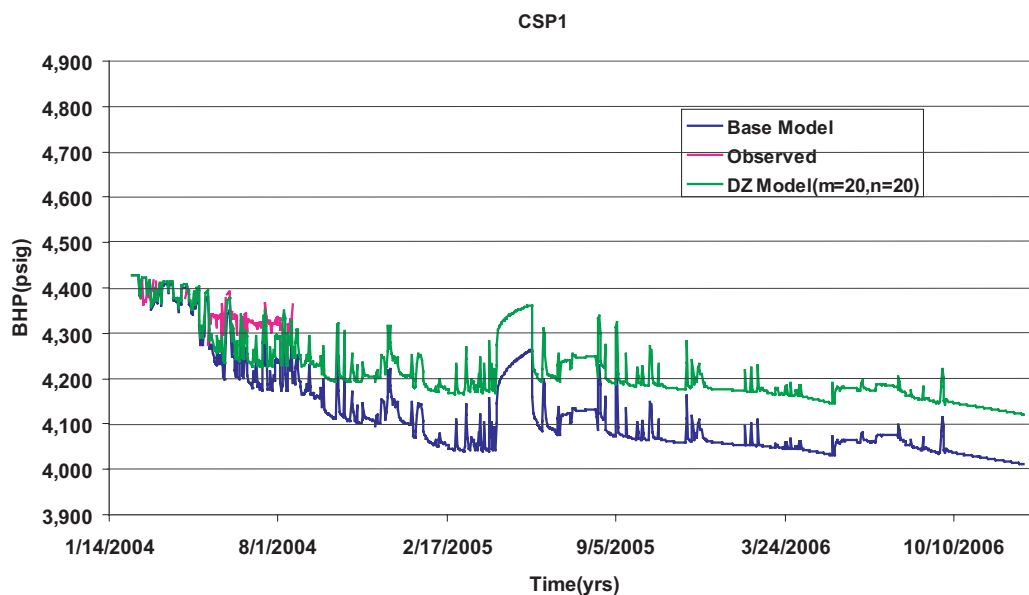


Fig. 5.44: Bottom Hole Pressure (BHP) history match of production well CSP1 shows an improvement with the damage zone model. The mismatch after months of production is related local heterogeneities and aquifer size.

Fig. 5.45 and 5.46 show simulated BHP for the CSP7 and CSP8, which are located to the north of the injectors (Fig. 5.38). From the buildup section of the BHP

response from the wells we can see that the static reservoir pressure of the structure is  $\sim 4450$ psi after a year of production. In well CSP7, the simulation response from the base model is close to the observed response. Also, simulated BHP response from the damage zone model has only a small difference to the base model response, indicating only minor changes between the two models along the path from well CSP7 to the injectors. There is only a minor effect of damage zones because of the absence of major faults on the path. However, well CSP8, which is located in the same platform but slightly north-west of CSP7, shows significant improvement in the BHP response from the damage model in comparison to the base model because this well is connected to the injector area by the NS trending faults with damage zones. Well CSP7 also shows a possible effect of insufficient aquifer support in the latter part of the production (after Jan 2006), resulting in model BHP that are  $\sim 10$ -50 psi lower than observed BHP.

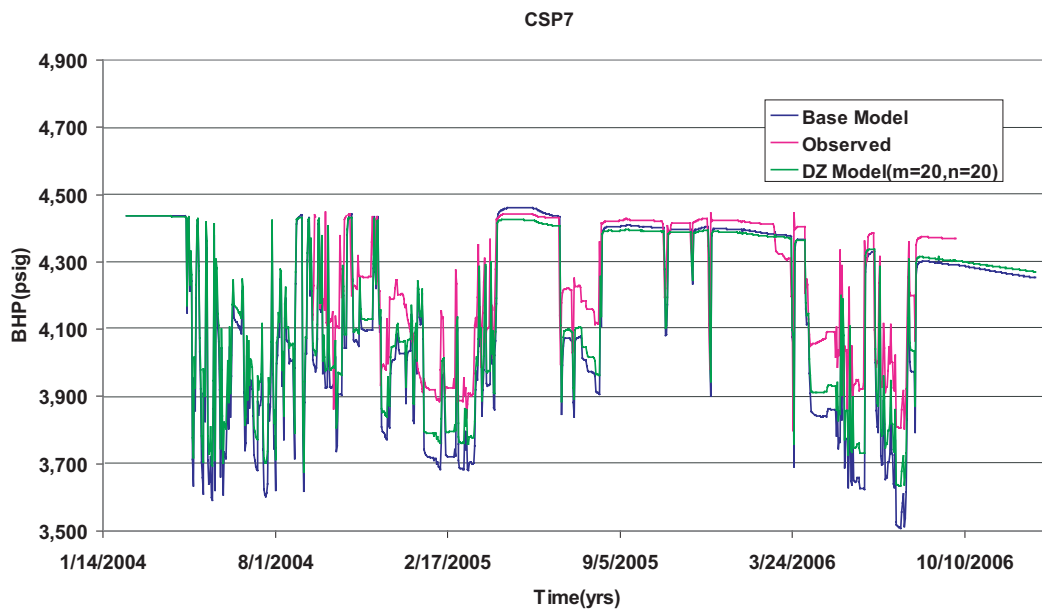


Fig. 5.45: In production well CSP7, BHP response from the damage zone model is close to the base simulation model because well is located in place which is not affected by the damage zone because of smaller faults.

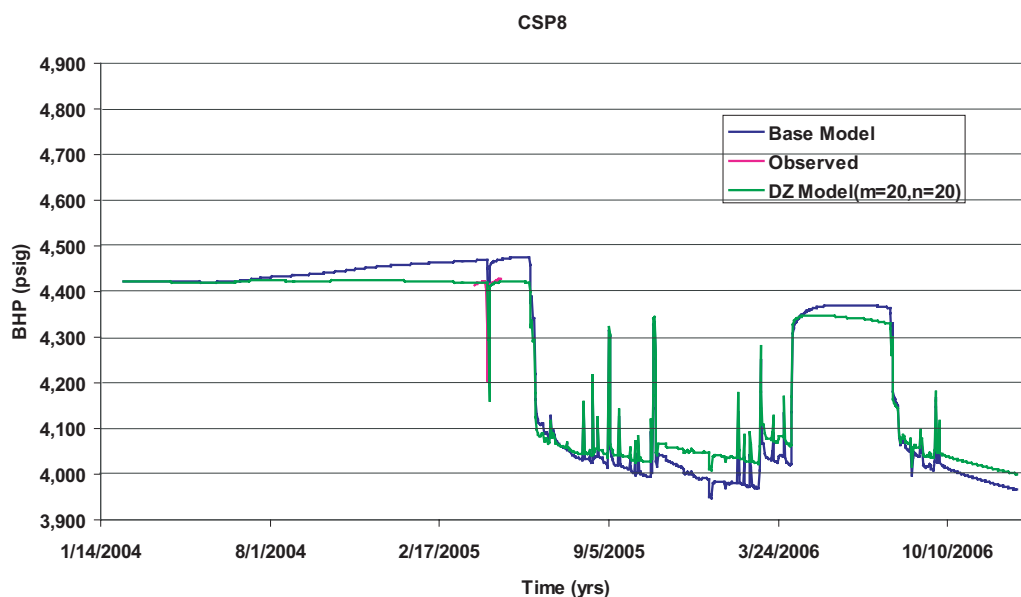


Fig. 5.46: Well CSP8 shows an improved match in history match with the damage zone model comparing to the base simulation model.

Description of history matching of BHP at well locations indicates that including damage zones into the base reservoir simulation model significantly improves the BHP history matching in all the wells. The model with damage zones indicates a depletion of ~40psi in the average reservoir pressure after two years of production (end of 2006). However, in most of the wells observed BHP data shows that the average pressure drop in the reservoir is ~20psi after two years of production, so we believe that the additional pressure drop of ~20psi in the model response may be due to insufficient aquifer size, and the model needs larger aquifer in addition to the damage zone effect to give a better history match in the latter period of production.

### 5.8.2 Water production

In the CS field, the initial water saturation (Fig 5.14) in the reservoir section is 0-30% and most of this is residual water. Detailed relative permeability experiments are not available for this field so there may be some degree of uncertainty in the residual water saturation and water flow. The initial field condensate water to gas ratio was ~2.33 bbls per MMcf of raw gas produced. Thus, the main source of free water

production in the large scale is from the aquifer below the main reservoir. The possible ways by which water can encroach the wells in the early period of production are: perforations very close to the water-gas contact and localized heterogeneities such as active faults connecting the aquifer to wells.

In the wells located on the platform to the north of the injector (Fig. 5.38), the damage zone simulation model has improved the history matching. Fig. 5.47 shows the water production rate from well CSP8. This well started producing water after one and half years (~Jun 2005) of production and afterwards continuously produced ~600-800 bbl/day of water. This well is located close to the flank of the reservoir which may be one of the explanations for large water production. At the initial period of water production both the base and damage zone simulation models over predict the water production. However, with time the water production from the damage zone model matches very well with the observed water production.

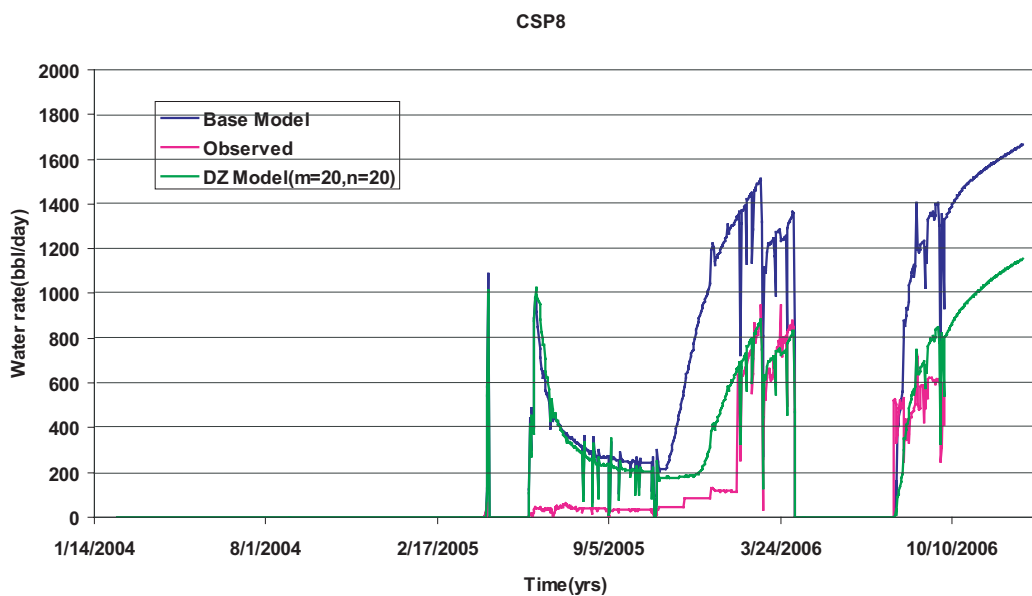


Fig. 5.47: Water production from well CSP8 predicted by the damage zone model has a better match with the observed production but it over estimates the water production at the earlier period.

In well CSP7, water production is comparatively less than CSP8 because this well is at the shallowest part of the structure. It started producing water after just six months

of production but it was controlled. We can see in Fig. 5.48 that in the late period observed water production matches very well with the simulated water production from the damage zone model while the base model slightly over predicts the water production rate.

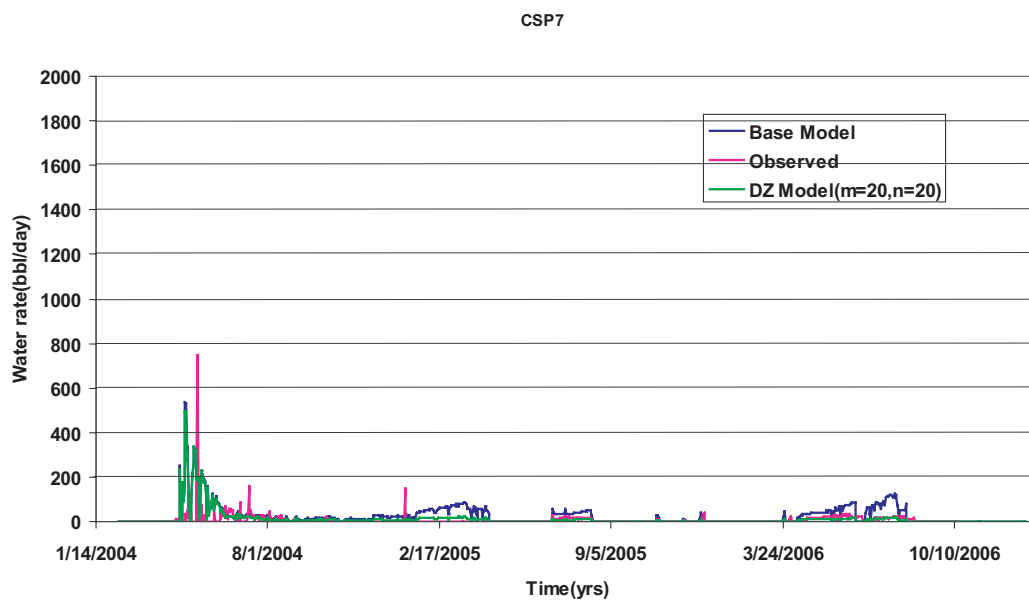


Fig. 5.48: In well CSP7, water production is relatively low than other wells and the response from damage zone model matches very well with the observed production rate.

In the other two wells of this platform, CSP5 and CSP6, water production is relatively low  $\sim 60$  bbl/day and we can see that both the base model and damage zone model match well with the observed water production rate. Fig. 5.49 and 5.50 illustrate the water production history matching from these wells.

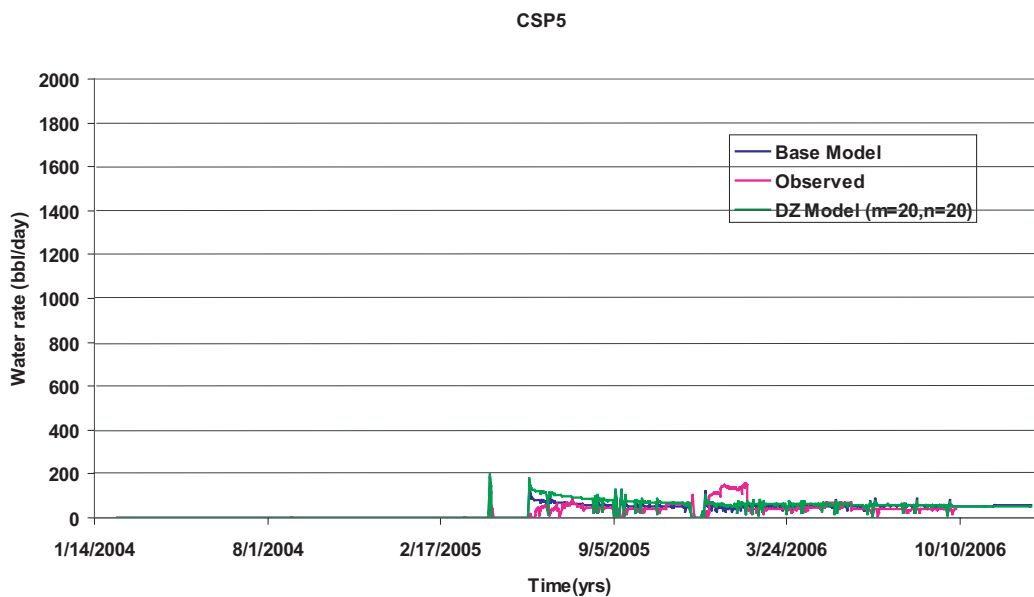


Fig. 5.49: History match of water production from well CSP5 shows a close match by both base and damage zone model.

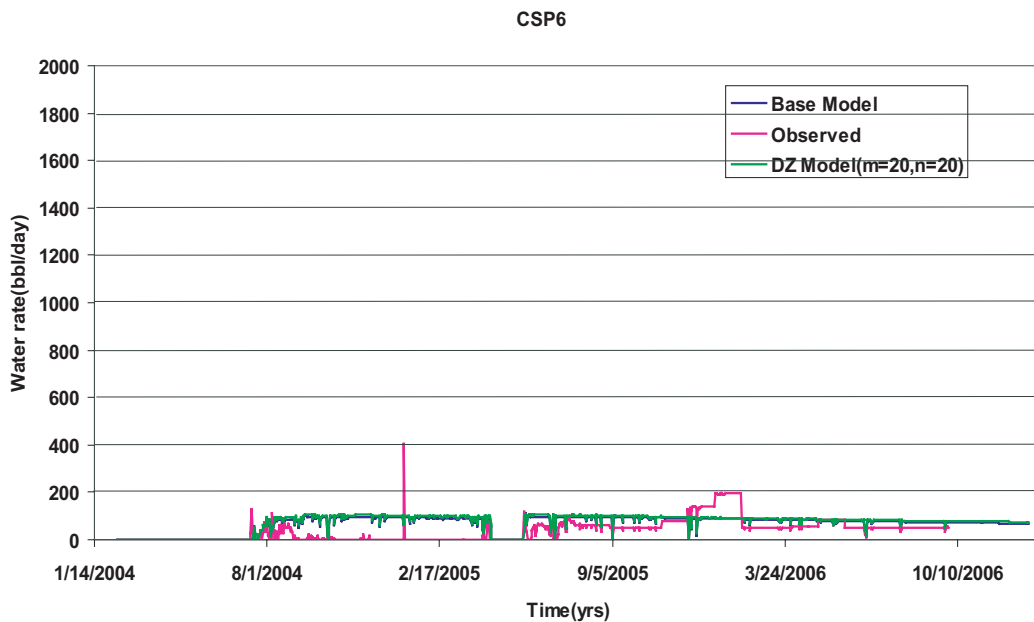


Fig. 5.50: History match of water production from well CSP6 shows a close match by both base and damage zone model. Simulation models over estimate water production at the earlier period.

Among the wells located on the east side structure (Fig. 5.38), wells CSP1 and CSP4 have relatively low water production and we can see in Fig. 5.51 and 5.52 that

history matching in these wells is relatively very good, except some late spikes in well CSP1, which may be due to some local heterogeneities being conductive in the latter stage but not captured in any of the models.

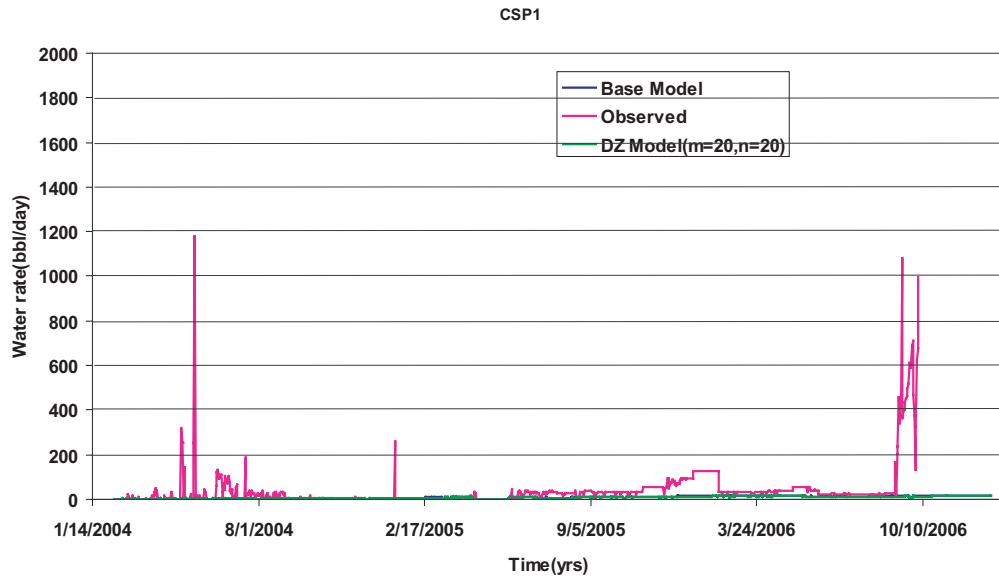


Fig. 5.51: In well CSP1, observed water production shows occasional burst of water from the well, which are not reproduced by the any of the simulation models.

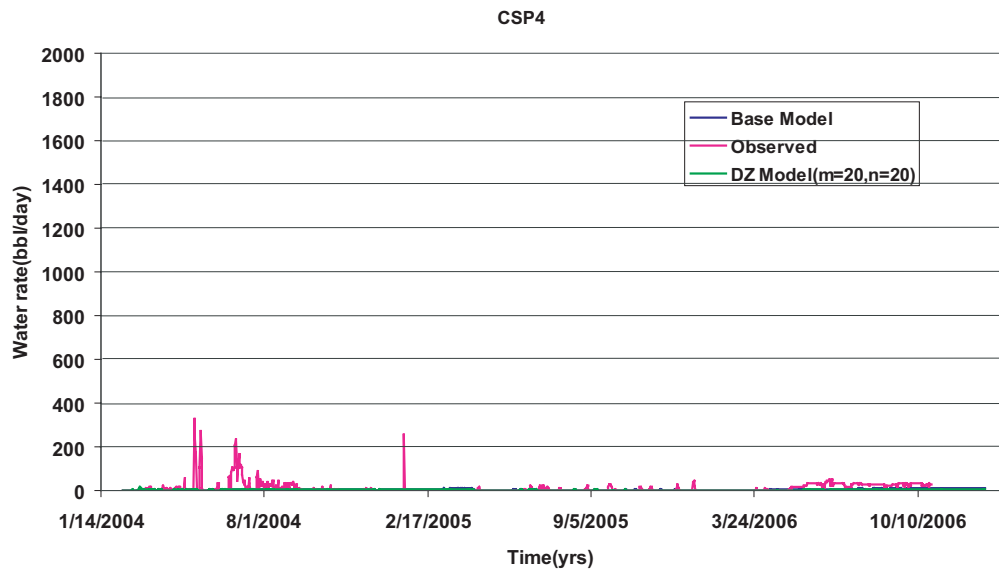


Fig. 5.52: Well CSP4 has low water production and simulation models show the same response.

In well CSP2, observed water production rate is relatively low but giving spikes at late period of production, which is very similar to well CSP1. The simulated response (Fig. 5.53) from both the models over predicts the water production. In the initial period of production, response from the damage zone model is relatively close to the observed water production, but at late periods the base model matches better and the damage model under predicts the water production. The reason for this is unclear. The sudden water production from both the wells, CSP1 and CSP2, may be explained by reactivation of the fault in that area.

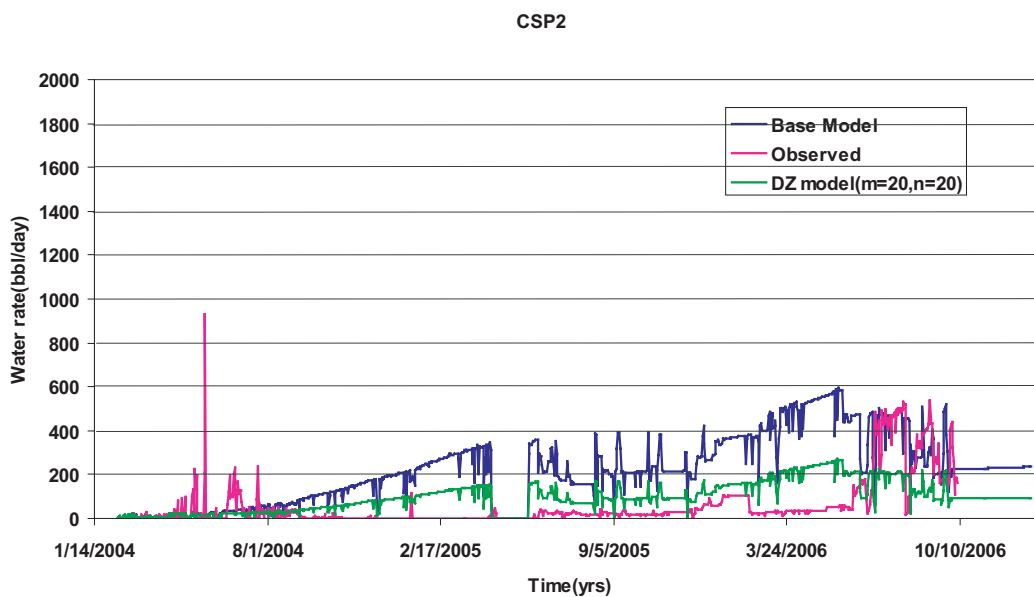


Fig. 5.53: well CSP2 gives occasional high production of water which are not matched by simulation models. The damage zone model matches better with the water production history than the base model.

Well CSP3 started producing water ~1900 bbl/day after one year of production, and the reason behind this is one of the perforations in this well is very close to the oil-water contact and water breakthrough started once the reservoir is slightly depleted. In Fig. 5.54, we can see that both the base model and the damage zone model match the water production trend but under predict the volume of water produced, where the base model is doing relatively better than the damage zone model.



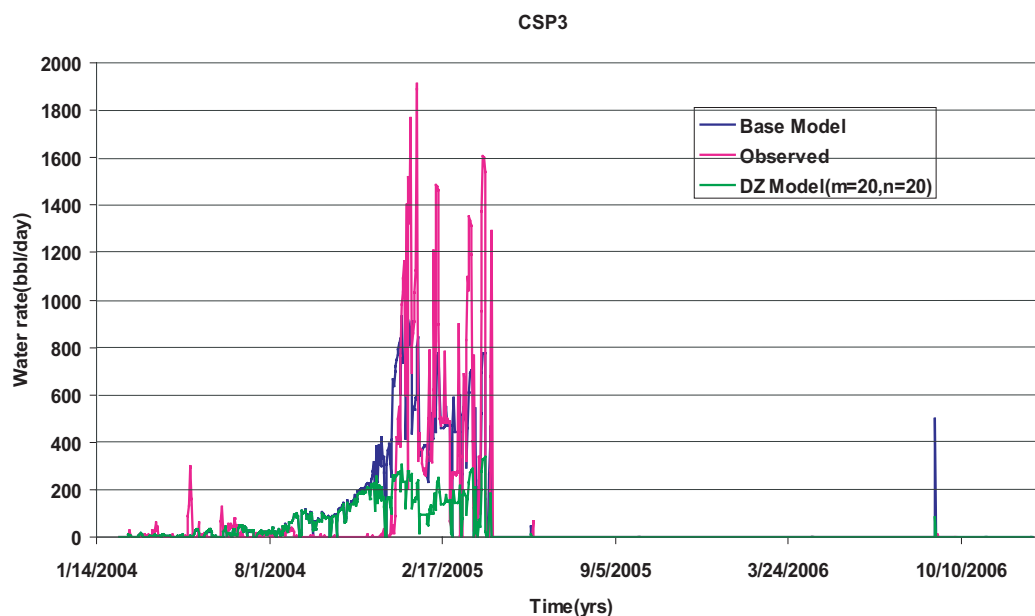


Fig. 5.54: Well CSP3 produces ~1800 bbl of water per day, which is the highest in the CS field among any wells because perforation is close to gas-water contact. Late water production spikes have better match with base model in comparison to the damage zone model.

Fig. 5.55 illustrates cumulative water production from the CS field. The reduced cumulative water production from the damage zone model with respect to the base model can be explained as an increased gravity effect or less coning in the damage zone model because of increased vertical permeability due to damage zones. We can see clearly that the damage zone model is matching better with the observed value than the base model. Thus, the damage zone model has definitely improved the base simulation model by including permeability anisotropy due to damage zones, which guides the pressure distribution and fluid flow in the reservoir. However, we can see that the water production match is still not perfect and the possible reasons are: uncertainty in relative permeability of the water, some localized heterogeneities are missing in the model which are acting as conductive paths, and the uncertainty in the size of the aquifer. The study demonstrates the effect of damage zone in the existing base model, but incorporating the effects of heterogeneity and uncertainty in the base model, in addition to the damage zone, may give a better history matching and prediction capability from the model.

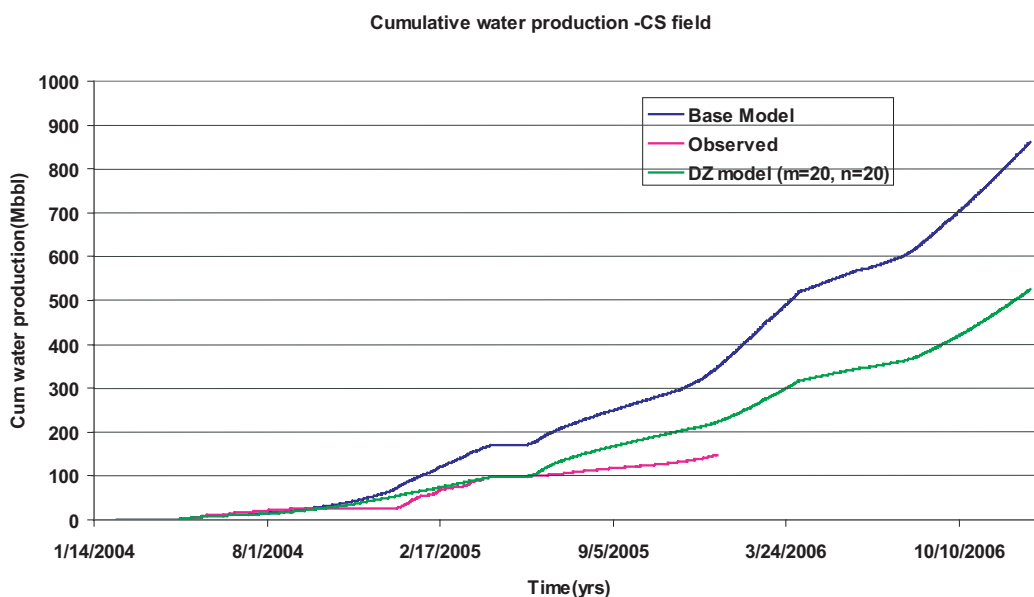


Fig. 5.55: History matching of the cumulative water production from the field indicates a significant improvement using the damage zone model comparing the base model.

### 5.8.3 Uncertainty in the simulation response due to damage zone modeling

In the above sections, history matching of BHP and water production show that the simulation model with damage zones gives a better match when compared to the base simulation model. However, the above study illustrates this on a mean model of 100 equally probable models of the damage zone estimated from the reservoir scale faults. To capture the uncertainty of the damage zone modeling in the simulation response, we simulate 20 of those equally likely damage zone models. While estimating the permeability for the damage zone from these 20 models, we use the same values for  $m$  ( $=20$ ) and  $n$  ( $=20$ ) values that gives the best history match with the mean model.

Fig. 5.56, 5.57, and 5.58 show the BHP of wells CSI3, CSP4, and CSP7 with time. These wells represent the cluster of wells from different parts of the field. In well CSI3, which is a gas injector, the uncertainty range from 20 simulations is  $\sim 30$ psi but all the cases have a better match with the observed values in comparison to the base simulation model. The mean model shows the best match and lies almost at the lower

end of the uncertainty range. Well CSP4, which represents the production well cluster at the west side of the injectors (Fig. 5.38), illustrates that the uncertainty range of simulated BHP from 20 simulations is ~20psi. The best match is again from the mean model which lies at the upper end of the range. In well CSP7, which represents wells north of the injectors (Fig. 5.38) the uncertainty range is narrow (~5-10psi). This narrow uncertainty range indicates less change between the equiprobable models in that area which is consistent because reservoir scale faults on that part of the reservoir are small, producing small damage zones. We know from chapter 4 that smaller damage zones have low standard deviation, hence giving less change between the equiprobable models. Because all these models include an aquifer of the same size and do not include the uncertainty due to the aquifer, the uncertainty range does not increase at the later part of production.

Fig. 5.59 illustrates the uncertainty range from the cumulative water production from the field. The simulation response from all 20 equiprobable models have a better match than the base model. At the early part of production (<1.5 year), the uncertainty range is narrow but at later time, the models behave differently giving an uncertainty range of ~100 Mbbl. The mean model is at the lower end of the range and close to the actual water production but the responses from some of the models are even closer to the observed water production. Overall all the models show improvement from the base case verifying the effect of damage zone in the reservoir.

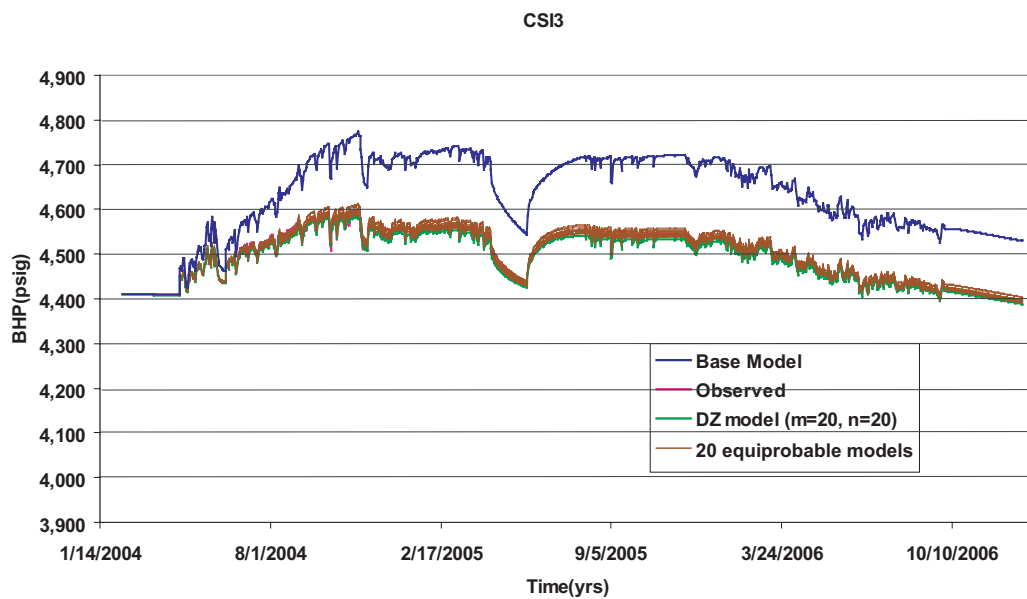


Fig. 5.56: Simulation responses from the 20 equiprobable models with damage zones indicate an uncertainty of ~50 psi but all models matches better with production history in compare to the base model.

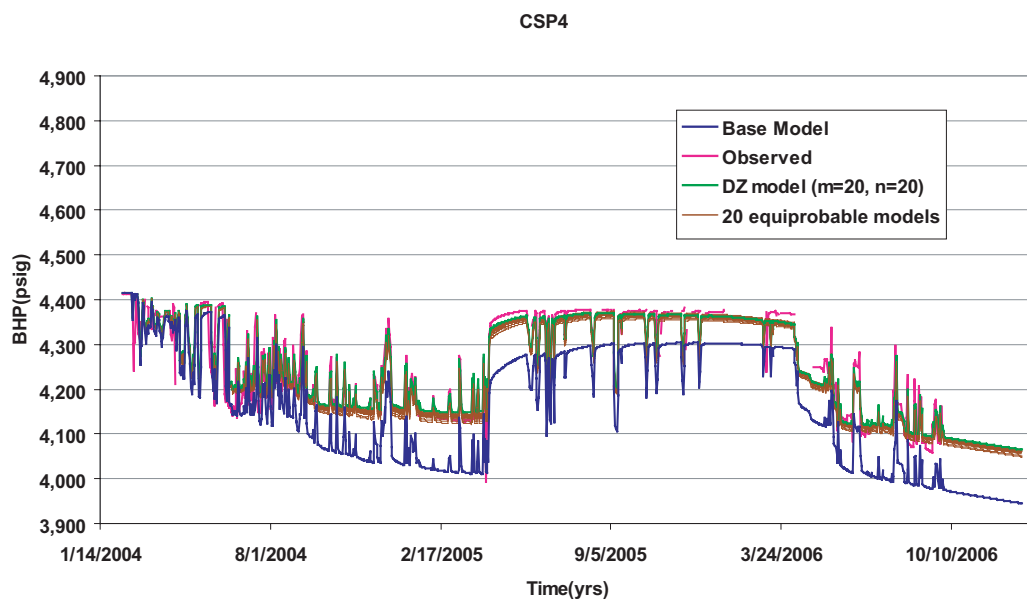


Fig. 5.57: In well CSP4 which is located in the structure east of the injectors, uncertainty from 20 equiprobable simulations is ~40 psi.

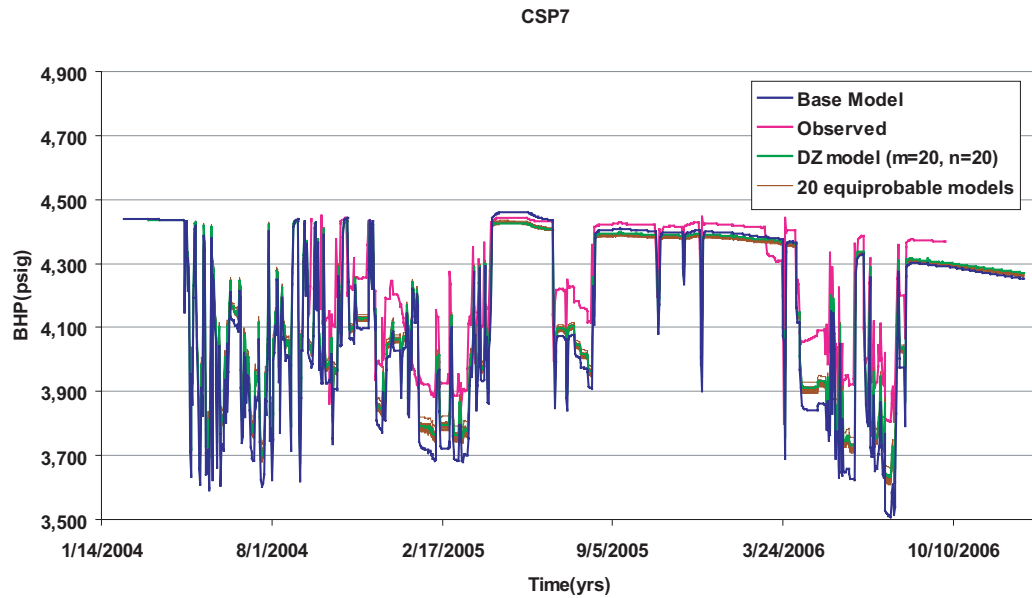


Fig. 5.58: Well CSP7 which is located in the north from the injectors shows a very compact range of uncertainty due to damage zone indicating relatively less change in the base model due to damage zones.

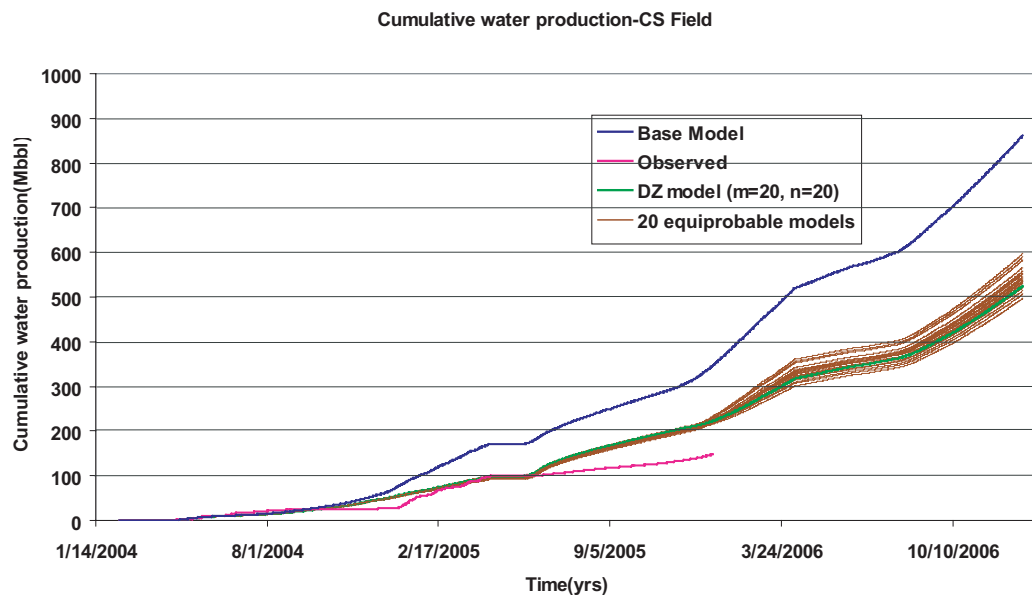


Fig. 5.59: Cumulative water production from the 20 equiprobable damage zone models indicate uncertainty range of ~100 Mbbbl after 3 years of production. The damage zone concept shows a significant improvement in the base model but also shows an increasing range of uncertainty from simulation response with production time.

#### 5.8.4 Uncertainty due to methods of anisotropy distribution in the simulation model

Using the full permeability tensor is the ideal method to distribute anisotropy in the fault-adjacent grid blocks of the simulation model, but the simulator we used can not operate with the full permeability tensor and the simulator provides no good alternative for the full tensor. Previous sections discuss history matching of BHP and water production for the anisotropy distribution method discussed in Eq. 5.10, which is a vector projection of the fault-parallel permeability associated with damage zones to fault-adjacent grid blocks using sine and cosine functions with respect to strike and dip of the fault. This vector projection technique is the arithmetic average approximation between the matrix permeability and the damage zone permeability in X and Y directions in a grid block (Fig. 5.24). Damage zone permeabilities in X and Y directions are estimated using the magnitude of the dot product of full permeability tensor ( $k$ ) and normal vector ( $n$ ) of the grid faces (Eq. 5.13).

$$|k.n|_x = (k_h) \sqrt{(N^2 \cos^2(\omega) + \sin^2(\omega))} \quad (5.13a)$$

$$|k.n|_y = (k_h) \sqrt{(N^2 \sin^2(\omega) + \cos^2(\omega))} , \quad (5.13b)$$

where  $k_h$  is the horizontal permeability of the grid block in the base model,  $\omega$  is the angle of fault from X direction, and N is the fault-parallel permeability multiplier to  $k_h$  in the damage zone.

The vector projection method is easy to implement and it gives reasonable results. However, it may overestimate the permeability in either the Y or X direction for fault orientations with low angle from X or Y axes respectively. This occurs because in these orientations, grid block permeability in Y and X directions are close to the harmonic average of the damage zone permeability in the respective directions and the grid block permeability, but Eqs. 5.10 and 5.11 treat them as an approximation of the arithmetic average. Thus error due to this effect depends on the size of the fault-adjacent grid blocks and orientations of the faults. Larger grid cells tend to show larger

error. However, the error is always restricted within a limited zone of the simulation grid and overall impact on simulation response should be small because in the directions perpendicular to the fault strike, damage zone effect is implemented only in fault-adjacent grid blocks, and next blocks in those directions are unchanged. In this section, we compare the results from Eq. 5.10 with another method to show the effect of different methods of anisotropy distribution in damage zone implementation. The other method is similar to Eq. 5.10 but in this method we do not change the permeability values due to damage zone in Y or X direction for fault orientations 0-20 degrees from X or Y axis respectively, which serves to minimize the error using Eq. 5.10.

Figs. 5.60, 5.61, and 5.62 show the comparison of the BHP responses from wells CSI3, CSP4, and CSP7 from both methods. We can see that the maximum difference in BHP is ~15 psi for producers (CSP4 and CSP7) and ~30 psi for the injector (CSI3). Fig. 5.63 shows a difference of ~50 Mbbl in cumulative water production at the end of two years of production from both the models. Narrow difference in responses (BHP and cumulative water production) from both methods indicates a minimal effect of the error in Eq. 5.10, discussed in the previous paragraph. Overall both methods show a good improvement from the base model, verifying the effect of damage zones in reservoir fluid production behavior.

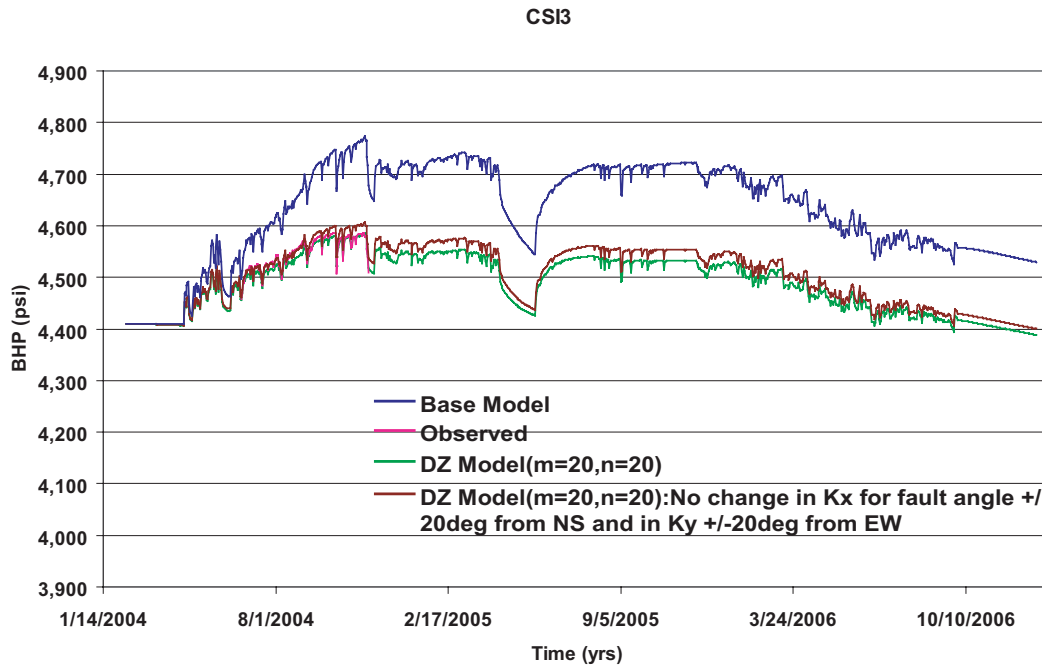


Fig. 5.60: Simulation responses from both anisotropy distribution methods indicate an uncertainty of ~30 psi. Both methods show better history match in comparison to the base model.

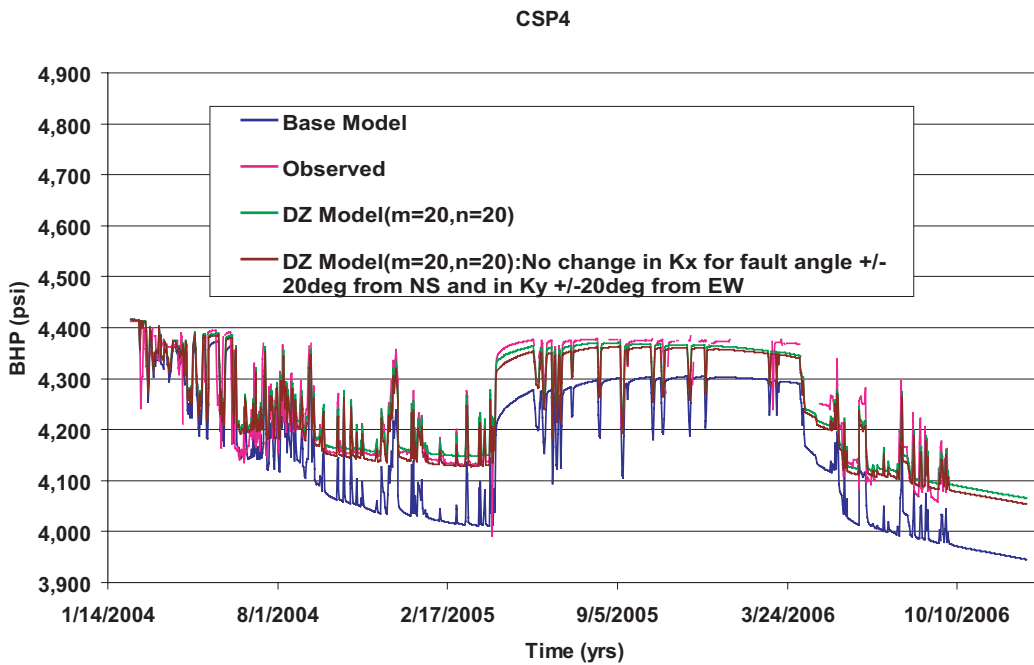


Fig. 5.61: Simulation responses from both anisotropy distribution methods indicate an uncertainty of ~15 psi.



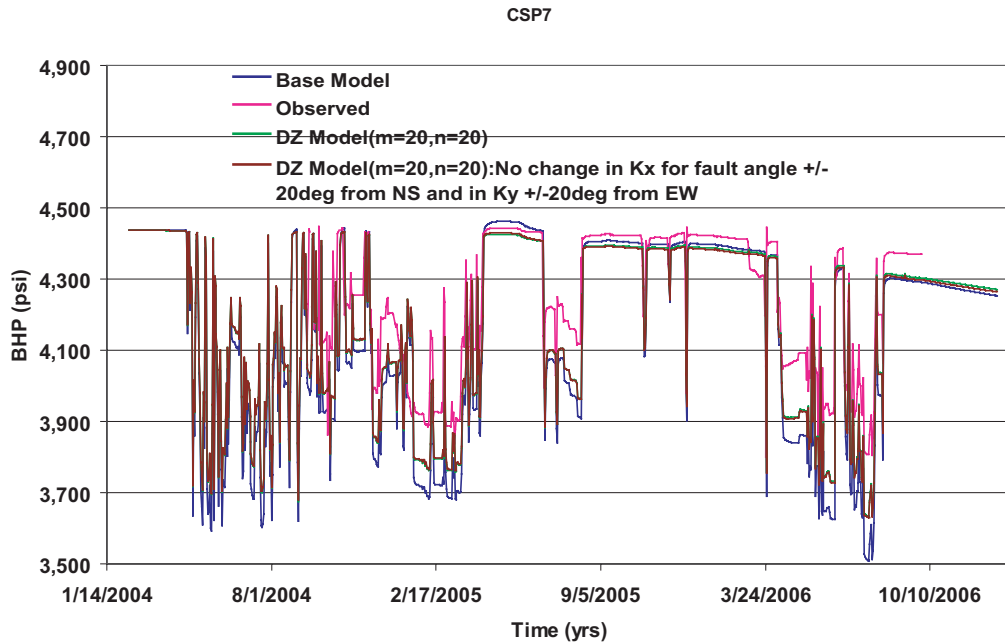


Fig. 5.62: Simulation responses from both anisotropy distribution methods indicate an uncertainty of ~5 psi.

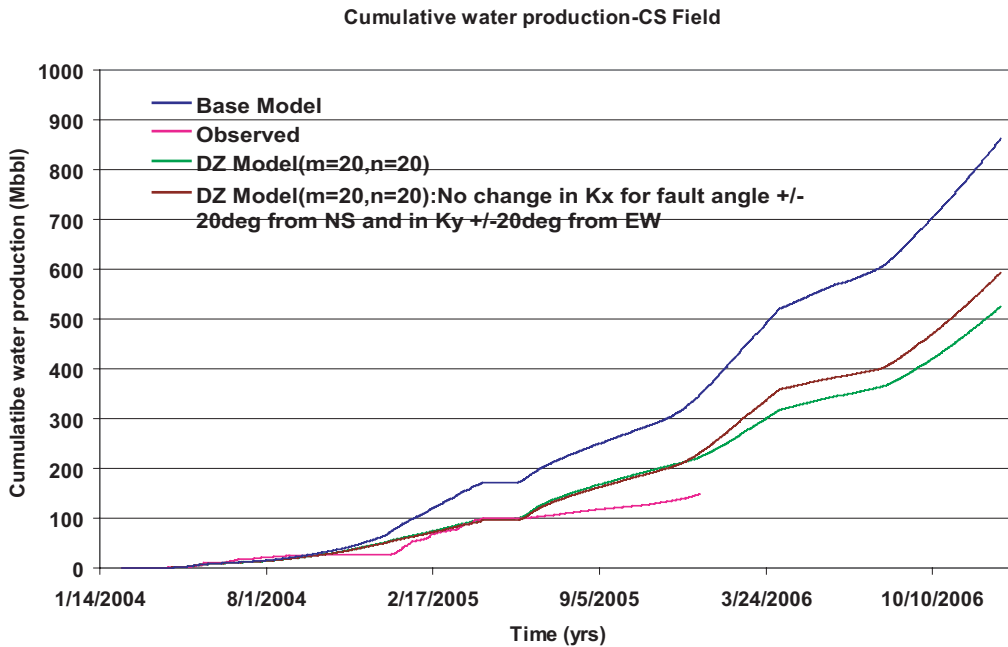


Fig. 5.63: Simulation response from both anisotropy distribution methods indicate difference of ~50 Mbbbl in cumulative water production from the field after a production of two years. Both methods show a good improvement from base model.

### 5.8.5 Uncertainty due to fracture density of damage zone in the simulation model

In the above sections, history matching of BHP and water production uses the value  $m=20$  and  $n=20$  in Eq. 5.11. These parameters scales the average fracture density in the damage zone based on the normalized damage zone intensity parameter defined in Eq. 5.9. As discussed before in this chapter, values of  $m=20$  and  $n=20$  is equivalent to average fracture density  $\sim 2$  fractures/m. To capture the uncertainty in the simulation response due to different average fracture density in the damage zone, we simulate two additional cases  $m=10, n=10$  and  $m=30, n=30$ , which are equivalent to average fracture density range of  $\sim 1.2$  fractures/m and  $2.5$  fractures/m. While estimating the permeability for the damage zone from these models, we use mean NDZI model (Fig. 5.8) and base case anisotropy distribution method (NPF model in X, Y, and Z directions, Fig. 5.29-5.31).

Figs. 5.64, 5.65, and 5.66 show the comparison of the BHP responses from wells CSI3, CSP4, and CSP7 for  $m$  ( $=10, 20, 30$ ) and  $n$  ( $=10, 20, 30$ ). We can see that the maximum difference is  $\sim 30$  psi for producers (CSP4 and CSP7) and  $\sim 60$  psi for the injector (CSI3). Fig. 5.66 shows cumulative water production from the field for these cases, indicating a maximum uncertainty range of  $\sim 100$  Mbbl after a production of 2 years from the reservoir. In all cases, we see a good improvement from the base model, verifying the effect of damage zones in reservoir fluid production behavior.

This uncertainty analysis demonstrates that all the models show significant improvement in the history matching in comparison to the base simulation model. The uncertainty range is fairly compact, which suggests the robustness of the damage zone modeling from rupture propagation technique and its implementation to the simulation model. The difference between simulation responses from the equiprobable models increases with time defining the uncertainty of the damage zone modeling techniques in terms of simulation response.

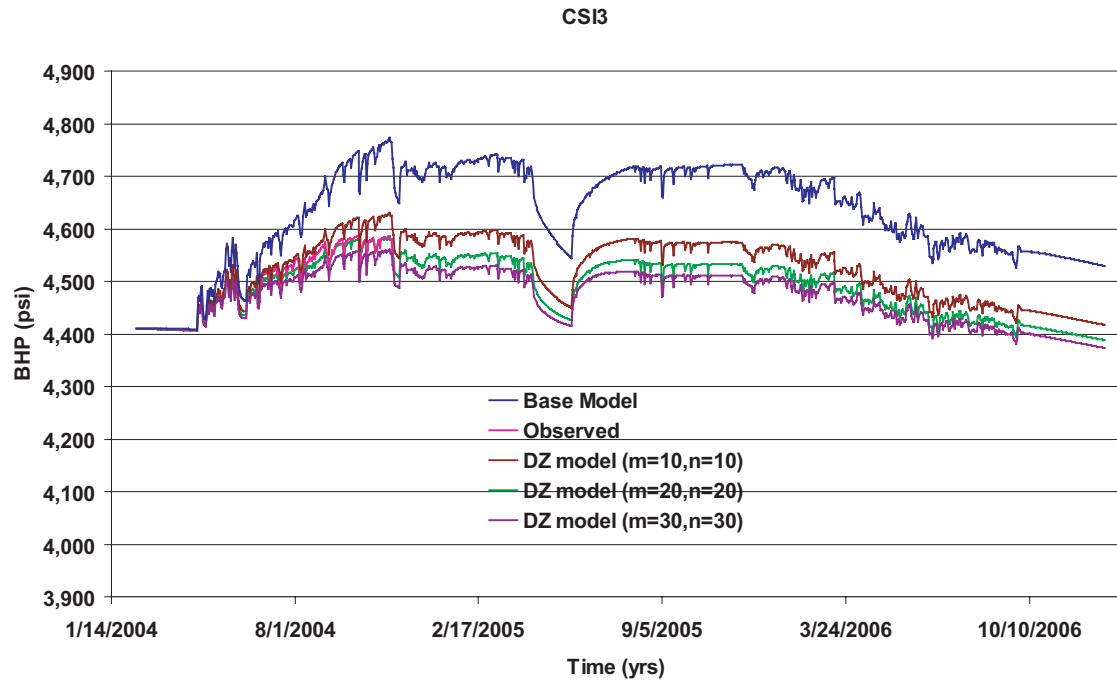


Fig. 5.64: Simulation responses for cases  $m$  ( $=10, 20, 30$ ) and  $n$  ( $=10, 20, 30$ ) indicate an uncertainty of  $\sim 60$  psi. All three methods show better history match from the base model.

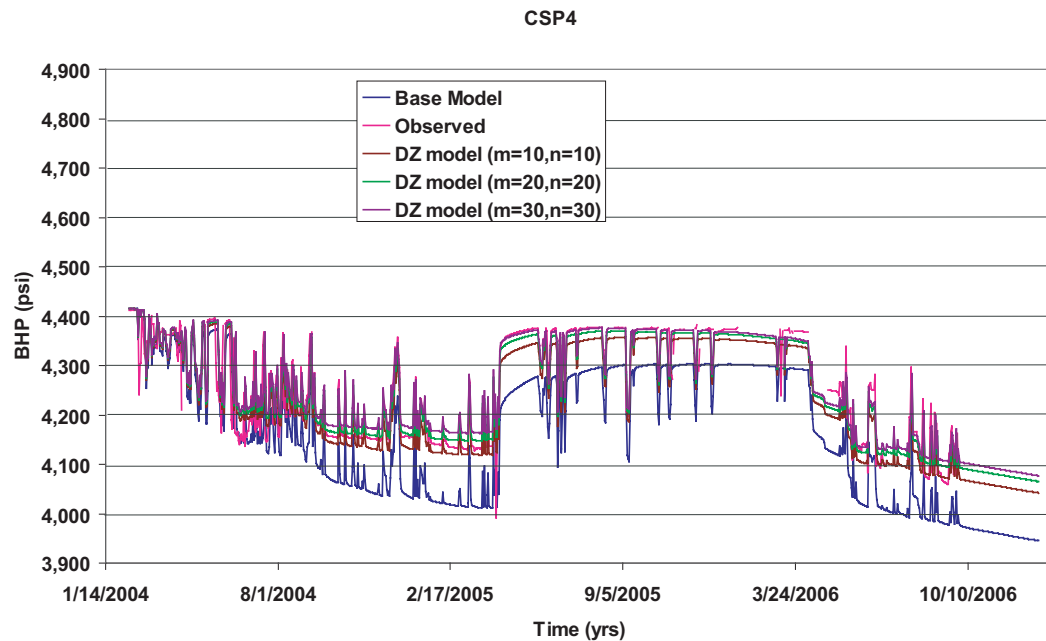


Fig. 5.65: Simulation responses for cases  $m$  ( $=10, 20, 30$ ) and  $n$  ( $=10, 20, 30$ ) indicate an uncertainty of  $\sim 30$  psi.

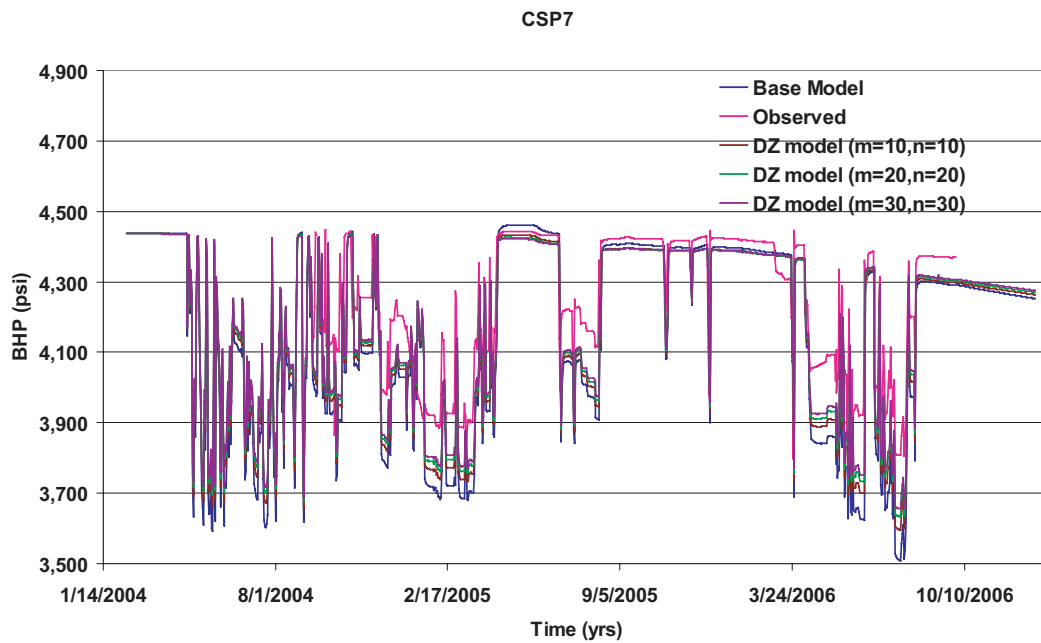


Fig. 5.65: Simulation responses for cases  $m$  ( $=10, 20, 30$ ) and  $n$  ( $=10, 20, 30$ ) indicate an uncertainty of  $\sim 5$  psi.

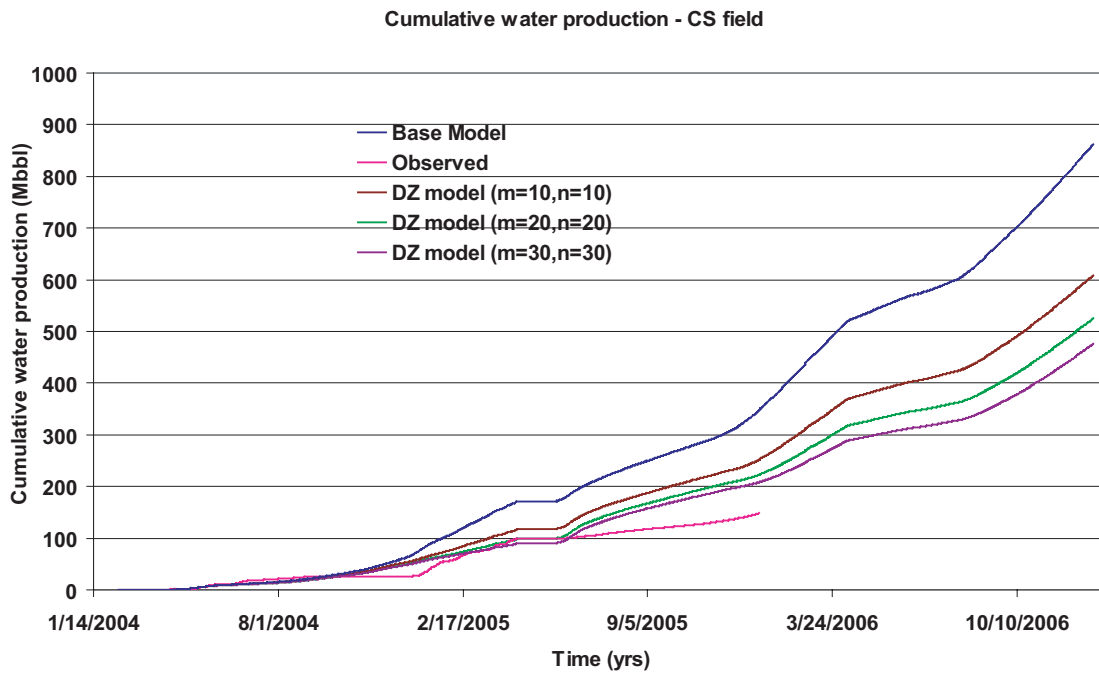


Fig. 5.67: Simulation responses for cases  $m$  ( $=10, 20, 30$ ) and  $n$  ( $=10, 20, 30$ ) indicate an uncertainty range of  $\sim 100$  Mbbbl water production from the field after two years of production.

## 5.9 Discussions and Conclusions

This chapter discusses a methodology to incorporate damage zones into a reservoir simulation model. A fine scale fluid simulation study defines the permeability anisotropy due to damage zones, which suggests increased permeability along the strike of the fault and in the vertical direction, but a negligible effect perpendicular to the fault. We used three steps to implement the effects of damage zones. Strike and dip of the associated faults were used to define the orientation of anisotropy, estimated damage zone widths were normalized by cell volume and area to define the relative effects on grid cells, and history matching was used to define the absolute value of permeability anisotropy in the model. The best fit damage zone model shows a significant improvement in the history matching in all the wells of the field with respect to the base reservoir simulation model with no damage zone. The uncertainty analysis using multiple equiprobable damage zone models indicates a compact range, suggesting a robust modeling and implementation methodology. Also, we found that three independent methods: well scale analysis, fine fluid analysis, and reservoir scale history matching give the consistent result of the effect of damage zone associated with the reservoirs scale faults.

Thus, by this study we successfully demonstrated a workflow to implement damage zones in reservoir simulation models, which should better predict the production behavior. A better prediction by the reservoir model gives a better plan for reservoir development and management, which maximizes the hydrocarbon recovery and minimizes the unwanted surprises such as water production and gas leakage from the field. The study includes all the details to routinely incorporate the methodology for reservoir studies in oil and gas industry. The beauty of this study is most of the parameters used for this methodology are regularly measured in the industry and the simple concepts are easy to implement. However, it is important to understand that suggested workflow is not to model fine scale details of the damage zones in the reservoir simulation model. Rather it shows a conceptual and quantitative understanding of the high permeable zones associated with the reservoir scale faults,

which can potentially provide pathways for reservoir fluids. Also, it is believed that, the aquifer size and localized heterogeneities also affect the production behavior in the later periods of production, though this was not studied here. Quantifying those uncertainties may give a better understanding of the reservoir pressure behavior with time and give an additional confidence in the reservoir model.

## References

- Ahmadov, R., Aydin, A., Karimi-Fard, M., and Durlofsky, L. J., 2007, Permeability upscaling of fault zones in the Aztec Sandstone, Valley of Fire State Park, Nevada, with a focus on slip surfaces and slip bands, *Hydrogeology*, 15, 1239-1250.
- Brown, S.R., and Bruhn, R.L., 1998, Fluid permeability of deformable fracture networks: *Journal of Geophysical Research*, 103(B2), 2489-2500.
- Climont, M., and Sweet, R. A., 1973, Mesh refinement for parabolic equations, *Jour. of Comp. Phy.*, 513-525.
- Corbett, P. W. M., Ringrose, P. S., Jensen, J. L., and Sorbie, K. S., 1992, Laminated Clastic Reservoirs: The interplay of Capillary pressure and Sedimentary Architecture, SPE 24699.
- Durlofsky, L. J., 2003, Upscaling of geocellular models for reservoir flow simulation: A review of recent progress, paper presented at 7<sup>th</sup> International Forum on Reservoir Simulation.
- Flodin, E. A., Aydin, A., Durlofsky, L. J., and Yeten, B., 2001, Representation of fault zone permeability in reservoir flow models, SPE 71617.
- Jourde, H., Flodin, E. A., Aydin, A., Durlofsky, L. J., and Wen, X., 2002, Computing permeability of fault zones in eolian sandstone from outcrop measurements, *AAPG Bulletin*, 86 (7), 1187-1200.
- Karimi-Fard, M., Durlofsky, L. J., and Aziz, K., 2004, An efficient discrete-fracture model applicable for general-purpose reservoir simulators, *SPE Journal*, 227-236 (SPE 88812).
- Koutsabeloulis, N. C., Heffer, K. J., and Wong, S., 1994, Numerical geomechanics in reservoir engineering, *Computer Methods and Advances in Geomechanics*, 2097-2104.
- Lozada, T., Krieger, F., Koelemij, and Jacimovic, I., 2005, ConocoPhillips internal report on the studied field.
- Luthi, S. M., and Souhaite, P., 1990, Fracture apertures from electrical borehole scans, *Geophysics*, V. 55, 821-833.
- Mlacnik, M. J., and Heinemann, Z. E., 2003, Using well windows in full-field reservoir simulation, *SPE Reservoir Evaluation and Engg.*, 6 (4), 275-285.
- Nacul, E. C., 1991, Use of domain decomposition and local grid refinement in reservoir simulation, Ph. D. Dissertation, Dept. of Pet. Engg., Stanford University.

- Pande, G. N., 1980, Numerical simulation of rock behavior: problems and possibilities, *Numerical Methods in Geomechanics*, 4, 1341-1356.
- Pedrosa, O. A., and Aziz, K., 1985, Use of hybrid grid in reservoir simulation, SPE 13507.
- Pickup, G. E., Ringrose, P. S., and Sharif, A., 2000, Steady-state upscaling: From lamina-scale to full-field model, *SPEJ*, 5(2), 208-217.
- Pickup, G. E., and Stephen, K. D., 2000, An assessment of steady-state scale-up for small-scale geological models, *Petroleum Geoscience*, 6, 203-210.
- Ringrose, P. S., Sorbie, K. S., Corbett, P. W. M., and Jensen, J. L., 1993, Immiscible flow behavior in laminated and cross-bedded sandstone, *J. Pet. Sci. & Eng.*, 9, 103-124.
- Rodriguez, J. F., Bombardelli, F. A., Garcia, M. H., Fronthingham, K. M., Rhoads, B. L., and Abad, J. D., 2004, High-resolution numerical simulation of flow through a highly sinuous river reach, *Water Resources Management*, 18, 177-199.
- Soriede, I., & Whitson, C.H., 1992, Peng Robinson predictions for hydrocarbons, CO<sub>2</sub>, N<sub>2</sub> and H<sub>2</sub>S with pure water and NaCl-Brines, *Fluid Phase Equilibria* 77, 217-240.
- Verma, S., and Aziz, K., 1997, A control volume scheme for flexible grids in reservoir simulation, SPE 37999.